Characterisation of Structure-Property Relationships in Novel Chalcogenides Systems

Tigran Simonian, B.A. (Mod.)

Supervisor: Prof. Valeria Nicolosi

School of Chemistry

Trinity College Dublin, the University of Dublin

A thesis submitted in fulfilment of the requirements for the degree of

Doctor of Philosophy

Trinity College Dublin June 2024

I am a patient boy

I wait, I wait, I wait, I wait

My time is like water down a drain

Everybody's moving, everybody's moving

Everybody's moving, moving, moving, moving

Please don't leave me to remain

In the waiting room

– "Waiting Room", *Fugazi*, Fugazi

Take your sweet time

You've taken so long

To make up your mind

It might take your whole life

– "What Went Wrong", *Challenge for a Civilized Society*, Unwound

Declaration

I declare that this thesis has not been submitted as an exercise for a degree at this or any other university and it is entirely my own work.

I agree to deposit this thesis in the University's open access institutional repository or allow the library to do so on my behalf, subject to Irish Copyright Legislation and Trinity College Library conditions of use and acknowledgement.

I consent to the examiner retaining a copy of the thesis beyond the examining period, should they so wish (EU GDPR May 2018).

_____

Tigran Simonian, B.A. (Mod.)

June 2024

Acknowledgements

While this thesis might be under my name, it was not done in a vacuum (or an island, or whatever metaphor you wish to use). I must, first and foremost, thank my supervisor, Prof. Valeria Nicolosi, for the supervision, resources, and support towards this work. It's been a wild couple of years and I have experienced things I never believed I ever would, be it going to random corners of the earth for conferences, or living through a pandemic, and I am ever grateful for the support and encouragement through it all.

Extending on this, I am very thankful to all the members of the Nicolosi group, both past and present, for supporting me in my research. Specifically, I would like to give special thanks to Dr. Ahin Roy, for his training on electron microscopy and density functional theory calculations. Thanks for taking me under your wing and pushing me forward, and I will sorely miss our many coffee-time chats. I would like to extend this thanks also to Clive Downing, for his God-like wisdom on all things microscopy and bikes, for putting up with my nonsense (and vice versa), and for teaching me many a new phrase. Additionally, I would like to thank Dr. Danielle Douglas-Henry for her training on the FIB and Nion UltraSTEM, collaborating on making heterostructures, and for teaching me some Afrikaans which I proceed to butcher, much to her amusement.

I would like to acknowledge the use of the Advanced Microscopy Lab at the Centre for Research on Adaptive Nanostructures and Nanodevices for my research, and would like to thank all the staff and students for their support, training, hours of enlightening conversations, and for making my time in the PhD (and the long days on the microscopes) much more enjoyable.

Over in the States, I would like to thank Prof. James LeBeau for being a wonderful host and mentor during my research placement at MIT. I learnt so much in such a short amount of time (such as the joys of PACBEDs), and would like to extend the thanks to his

group, especially Michael Xu and Colin Gilgenbach, for teaching me mechanical wedge polishing and debugging my messy code. A special thanks is extended to Dr. Aubrey Penn of MIT.nano for her training on their microscopes, for many a lovely coffee chat, and for putting up with my nonsense (I really am full of it, it seems). My time in Boston wouldn't have been nearly as fun if it wasn't for all my wonderful housemates (and of course, Nugs the cat), and so a special thanks goes out to them also.

I'd like to also thank my fellow NPCAMs from the Class of 2019, many of whom (for untold reasons) decided to stay on in academia and embark on PhDs, for providing many a source of joy over the past couple of years. Specifically, I would like to give a shout-out to Dr. Lucia Hughes, my fellow Nicolosi group microscopy student, for the many adventures we've been on worldwide (re: post-conference escapades), and Dr. Áine Coogan for many a discussion on academia, collaborations, and nonsense over a pint. I would also like to thank fellow Nano, Dr. Seán Kavanagh of University College London, for his advice on DFT simulations and his horticultural knowledge.

This work would not have been possible without collaborators, and hence I would like to thank the following: Prof. Zdeněk Sofer and his team in University of Chemistry and Technology, Prague for synthesising the $TlGaSe_2$ materials used in Chapter 3 and performing XRD analysis on them; Prof. Stefano Sanvito of Trinity College Dublin and his team, especially Dr. Rui Dong and Dr. Akash Bajaj, for providing assistance in the DFT calculations by running the electron transport and phonon calculations in Chapter 3; and Prof. Rafael Jaramillo and his team at Massachusetts Institute of Technology for synthesising the $BaZrS_{(3-y)}Se_y$ alloys used in Chapter 5.

Unfortunately, my laptop is nowhere near powerful enough to run the DFT calculations and other simulations used throughout this work, and hence I would like to acknowledge the SFI/HEA Irish Centre for High-End Computing (ICHEC) and Trinity Centre for High Performance Computing (TCHPC) for the provision of computational resources.

I would also like to acknowledge (for fear of death otherwise) the SFI Centre of Doctoral Training in Advanced Microscopy (SFI Award reference: 18/EPSRC-CDT/3581) for the financial support and for allowing me to goof off in the most professional of ways.

Penultimately, I would like to thank my family (my parents, my siblings - David and Emma) and all of my friends, who have been supportive over the past few years, and for putting up with this sometimes cranky, often silly man.

Last, but not least, I would like to thank all the bands and musicians who have been the soundtrack to these past few years, for getting me through some of the best, and sadly also darkest, moments of my life. In no particular order (and most certainly a non-exhaustive list), I would like to thank Fugazi, Unwound, Pavement, Jawbreaker, the Promise Ring, Jets to Brazil, Sonic Youth, Codeine, Pot Valiant, Sunny Day Real Estate, the Van Pelt, Cursive, Shellac, Bedhead, Jimmy Eat World, Weezer, Moss Icon, Indian S

Abstract

As devices become smaller and head towards the atomic limits, minute changes in their structure, in the form of defects, can have an oversized effect on the device properties. This is especially true for novel classes of chalcogenide-based materials, which typically possess weaker bond strengths than their oxide counterparts. As such, careful structure-property relationship establishment is required to fully exploit the material's properties and ensure adequate device's lifetimes and efficiencies.

In this work, several novel chalcogenide systems are investigated through the combination of transmission electron microscopy (TEM) and computational methods such as density functional theory (DFT) calculations. Firstly, the thermoelectric properties of $TlGaSe_2$ were investigated. Stacking faults were seen throughout the samples using scanning TEM (STEM), which were correlated with diffraction measurements and simulations of both. Stacking fault energies were calculated with DFT to be negative, implying that the faults are intrinsic to the system. Due to this, first-principles calculations were more practical to use to qualitatively study the effects of these stacking faults on the thermoelectric properties than physical experimentation. Preliminary results from electron transport studies indicate negligible change with the inclusion of the stacking fault, as to be expected for a thermoelectric material. However, initial phonon band structure calculations indicate a change in phonon frequencies when the stacking faults are included, which may imply a lowering of thermal conductivity.

The lack of control of this stacking order inspired the exploration of chalcogenide van der Waals heterostructures, such as GaS/GaSe heterostructures. DFT simulations predict a Rashba band splitting at the valence band maximum of the structures when spin-orbit coupling effects are included. The size of this splitting, along with the band gap of the structures, is highly dependent on the twist angle between the two monolayers of GaS and

GaSe. These multiple degrees of freedom are highly sought after for optoelectronic and spintronic applications and thus warranted further investigation. Several heterostructures were constructed and imaged. Despite the further sample optimisation required to get to the monolayer limit, the imaging showed successful construction of the heterostructures and plans to probe the band gaps and Rashba splitting using EELS are discussed.

While the systems above are interesting in their own context, they are not yet commercially viable within the short- to medium-term timelines. Hence, the field of chalcogenide perovskites for photovoltaic applications is explored with the $BaZrS_{(3-y)}Se_y$ alloy system. Photoconductivity spectroscopy measurements show a decreasing band gap with increasing Se content, in line with previous and current theoretical studies. Cross-sectional STEM imaging highlights the vast number of in-plane and out-of-plane anti-phase boundaries (APBs) throughout the films. Mapping of the A-site cation distances reveals a tripartite of out-of-plane lattice spacings, which are in line with reflection pairs seen in HRXRD spectra. The lack of strain from the surface of the films to the substrate is indicative of fully relaxed films, where the strain relaxation mechanism is the APBs and the buffered interface with the substrate.

Summary

This thesis discusses several novel chalcogenide systems and the establishment of their structure-property relationships through the means of electron microscopy and computational methods and analysis. Chalcogenides possess a multitude of interesting properties due to their covalent character, but this can cause issues as the weaker bonding can lead to facile device failure, hence the need for careful structure-property investigations.

In this work, the main tools of investigation are transmission electron microscopy (TEM) and density functional theory (DFT) calculations. Throughout each of the main working chapters, the critical and complementary importance of both methods is highlighted and demonstrated. Chapter 1 first introduces the field of chalcogenide materials and the various techniques used throughout. Chapter 2 briefly explains the theory behind each of the methods, up to a level where the reader can appreciate their use in this work. The various sample preparation methods used are described, as are the strengths and weaknesses of DFT and TEM simulations. Sample growth methods employed in this work are also discussed, but the actual growth of the materials is outside the scope of this work.

Chapter 3 details the investigation of the thermoelectric structure-property relationship of $TlGaSe_2$. Imaging of the sample using scanning TEM (STEM) revealed stacking faults throughout the layered system. Diffraction studies and subsequent simulations confirm the existence of these faults. DFT was used to calculate the stacking fault energy for this material, which was revealed to be negative, hence implying that these stacking faults are intrinsic to the system. Due to this, experiments to probe the thermoelectric effect of $TlGaSe_2$ would prove to be too cumbersome, and hence DFT simulations were required to understand the role of these stacking faults in the material's thermoelectric properties. Preliminary electron transport calculations along the stacking direction showed negligible changes when the stacking fault is included. Preliminary phonon studies, however, show

a change in phonon frequencies when the stacking fault was included. Further work is required for conclusive results, but the current analysis is promising and does show a qualitative role of these faults in the thermoelectric properties of $TlGaSe_2$.

Chapter 4 expands on the previous chapter by studying how to control the stacking order of layered materials to construct van der Waals heterostructures. Here, the GaS/GaSe heterostructure system was investigated. First-principles calculations demonstrated a splitting of the valence band maximum of these structures along momentum-space in a process known as Rashba band splitting. An angular dependence of this splitting as well as the band gaps of these structures, highlighted their interest for optoelectronic and spintronic applications. Several heterostructures were constructed using mechanical exfoliation of the layers and investigated using STEM imaging and energy dispersive X-ray (EDX) spectroscopy. While not at the monolayer level, it demonstrated the feasibility of constructing these samples, and plans are discussed on how to measure the band gaps and Rashba splitting of these structures using electron energy loss spectroscopy (EELS).

Chapter 5 discusses the $BaZrS_{(3-y)}Se_y$ chalcogenide perovskite alloy system, which was grown on a $BaZrS_3$ template to force the selenide alloy into a perovskite structure. The act of doing so causes strain due to the lattice spacing difference, which relives themselves through anti-phase boundaries (APBs) and the buffered interface with the $LaAlO_3$ substrate. EDX mapping of the films revealed a constant S/Se ratio throughout the structure in line with the initial growth conditions. STEM imaging revealed that in-plane APBs are predominantly located in the alloy region, while out-of-plane APBs are found mostly in the template region. Mapping of A-site cation distances revealed a tripartite of out-of-plane spacings, which line up with the reflection pairs seen in high-resolution X-ray diffraction (HRXRD) spectra. Photoconductivity spectroscopy measurements confirmed the highly tunable band gaps of the films, in line with previous and current theoretical results, which are ideal for photovoltaic applications.

Finally, Chapter 6 concludes the work with the major findings and discusses the future work planned for these projects.

Publications

Bathe, A. S., Sanz Arjona, A., Regan, A., Wallace, C., Nerney, C. R., O'Donoghue, N., Crosland, J. M., **Simonian, T.**, Walton, R. I., Dunne, P. W. "Solvothermal Synthesis of Soluble, Surface Modified Anatase and Transition Metal Doped Anatase Hybrid Nanocrystals" *RSC Nanoscale Advances 4, 24, 5343-5354* (2022) http://doi.org/10.1039/D2NA00640E

Coogan, Á., Doménech, N.G., McGinley, D., **Simonian, T.**, Rafferty, A., Fedix, Q., Donlan, A., Nicolosi, V. and Gun'ko, Y., "Layered Double Hydroxide/Boron Nitride Nanocomposite Membranes for Efficient Separation and Photodegradation of Water-Soluble Dyes" *Journal of Materials Chemistry A, 11, 12266-12281* (2023) https://doi.org/10.1039/D3TA01581E

Sadeghi, I., Van Sambeek, J., **Simonian, T.**, Xu, M., Ye, K., Cai, T., Nicolosi, V., LeBeau, J. M., Jaramillo, R., "Expanding the Perovskite Periodic Table to Include Chalcogenide Alloys with Tunable Band Gap Spanning 1.5 - 1.9 eV", *Adv. Funct. Mater. 2023, 2304575.* https://doi.org/10.1002/adfm.202304575 (*work forms the basis of Chapter 5*)

Simonian, T., Roy. A, Bajaj, A., Dong, R., Sofer, Z., Sanvito, S., Nicolosi, V., "Elucidating the Role of Stacking Faults in $TlGaSe_2$ on its Thermoelectric Properties", *In Preparation* (*work forms the basis of Chapter 3*)

Sadeghi, I., **Simonian, T.**, Van Sambeek, J., Kamboj, V., Cai, T., Foucher, A.C., Liu, Z., Xu, M., Ye, K., Ross, F.M., Nicolosi, V., LeBeau, J. M., Jaramillo, R., "Epitaxial Hexagonal $BaZrSe_3$ Thin Films with In-Plane Optical Anisotropy made by MBE", *In Preparation*

Awards

M&M 2022 Meeting Award - Physical Sciences, 1st Place Poster Prize, Microscopy and Microanalysis 2022, Portland, Oregon, USA

IMC20 Best Presentation Award - Session PS-02.9 -"Carbon-based/2D Materials" Symposium, 20th International Microscopy Congress 2023, Busan, Republic of Korea

Royal Microscopical Society Travel Bursary, for travel to Materials Research Society (MRS) Fall Meeting 2023, Boston, Massachusetts, USA - Award amount: £ 300

Royal Society of Chemistry Researcher Development and Travel Grant, for travel to Materials Research Society (MRS) Fall Meeting 2023, Boston, Massachusetts, USA - Award amount: £ 500

Nomenclature

BF - Bright Field

CBM - Conduction Band Minimum

CVD - Chemical Vapour Deposition

DF - Dark Field

DFT - Density Functional Theory

DOS - Density of States

EDX - Energy Dispersive X-ray Spectroscopy

EELS - Electron Energy Loss Spectroscopy

FIB - Focused Ion Beam

FFT - Fast Fourier Transform

GGA - Generalised Gradient Approximation

HAADF - High-Angle Angular Dark Field

LDA - Local Density Approximation

MBE - Molecular Beam Epitaxy

PACBED - Position-Average Convergent Beam Electron Diffraction

PDMS - Polydimethylsiloxane

PMMA - Polymethyl Methacrylate

PV - Photovoltaic

SAED - Selected Area Electron Diffraction

SOC - Spin-Orbit Coupling

STEM - Scanning Transmission Electron Microscope

TEM - Transmission Electron Microscope

VBM - Valence Band Maximum

XRD - X-ray Diffraction

Table of contents

List of figures

1

Introduction

These atoms are liars

They do not realize, and we can't blame them.

– "Deep, Deep", *Deathconsciousness*, Have a Nice Life

Many books, review articles, and popular science pieces on the subject of nanoscience often start with a clichéd reference to Richard Feynman's 1959 lecture "There's Plenty of Room at the Bottom" [1]. Although many use creative liberty in interpreting Feynman's words for their own benefit (read basically any recent PhD thesis on the topic of nanoscience, for example), the general synopsis of his lecture is that if we can manipulate matter on the atomic scale, we can use the physics at this scale to build ever denser and sophisticated devices to meet the world's needs (and wants).

To manipulate matter at the atomic scale, we first need to fully understand it. Often, this is summarised in another cliché, this time from Lord Kelvin - "If you can not measure it, you can not improve it" [2]. Again, while overused, it serves to show the importance of thorough material characterisation. This is often done in the micro- and nanoscale via the use of microscopy, such as scanning electron microscopy, atomic force microscopy, etc., and/or spectroscopy, such as energy dispersive X-ray spectroscopy, Raman spectroscopy, Fourier-transformed infrared spectroscopy, etc.

Another reason for the importance of materials characterisation is that, as we get closer to "the bottom", nanoscale, even atomic, defects can have a wildly disproportional influence on the properties of the material. This ultimately will affect the devices the

materials are used in. In the field of material science, these are classed in terms of their dimension. Zero-dimensional (0-D) defects, also known as point defects, can be in the form of vacancies or interstitials in the crystalline lattice. They can affect the size of the band gap in semiconductors [3], or could lead to exotic effects such as superionic conductivity [4, 5]. In terms of mechanical properties, one-dimensional (1-D) line defects, also known as dislocations, can move throughout a material under external load explaining why metals are malleable [6]. Two-dimensional (2-D) planar defects, such as stacking faults and anti-phase boundaries, can increase the brittleness of materials leading to early failure of devices [6, 7].

The exploitation of the properties in novel materials enables innovative device possibilities. Therefore, understanding these various structure-property relationships is vital for the transition of fundamental research into market-ready applications. Despite this, significant knowledge gaps remain for a wide variety of material families, none more so than the chalcogenide-based materials, such as transition metal dichalcogenides (TMDs) or chalcogenide perovskites. The reasons for this range from the difficulties in their synthesis to the difficulties in their characterisation. Therefore, to "fill in" some of these gaps, in this work, several families of novel chalcogenide materials are investigated.

1.1 Chalcogenide-Based Materials

The Group-XVI elements of the periodic table are termed "chalcogens". While there will be no discussion on the origin of the term (or its "correct" pronunciation), it should be noted that although oxygen is part of the chalcogen group, in this work, oxides are often treated as a separate class of materials and the term "chalcogenide" is reserved for sulphides, selenides, and tellurides.

The reason for this is due to the significant change in chemical behaviour and bonding between oxygen and the other chalcogens. Oxygen has a much higher electronegativity (χ = 3.44) than that of the other chalcogenides (χ = 2.58, 2.55, and 2.1 for S, Se, and Te, respectively), and consequently a smaller ionic radius [8]. As such, chalcogenides behave far more covalently and are less closed-packed than oxides, leading to a tendency to crystallize into low-dimensional materials [9]. It should be stressed though that while

they can crystallise into these low dimensions, this effect is not exclusive to chalcogenides; several layered oxides, perovskites, and hydroxides do also exist [10–13].

This low dimensionality of chalcogenides allows for interesting structure-property relationships to emerge. One such example is semiconducting chalcogenide nanoparticles, such as PbS and CdSe, also known as quantum dots. These nanoparticles absorb incoming light which promotes electrons from the valence band to the conduction band, leaving holes behind in the valence band. When the electrons return to their lower-energy ground state, the excess energy from this transition is released as photons of light proportional to the size of the band gap. This band gap size, and hence the wavelength of light emitted, is proportional to the size of the nanoparticle. Since these wavelengths are typically in the visible range, the whole gambit of colours can be produced with these particles, simply by changing their size [14]. This structure-property link can be exploited in a wide range of applications, from solar cells to light-emitting diodes [15]. The reader may have interacted with quantum dots without realizing it, as CdS nanoparticles are the most commonly used material for modern quantum dot displays [14–17]. This discovery was of such great importance that the most recent 2023 Nobel Prize in Chemistry was awarded for the discovery and synthesis of quantum dots [18].

Similarly, two-dimensional chalcogenides exhibit changing material properties as they approach their monolayer limit. An example of this is the TMD, MoS_2. Naturally found, and commercially used as a dry lubricant [19], MoS_2 is a prototypical example of the interesting effects of chalcogen bonding and chemistry. Due to its weak interlayer bonding, MoS_2 can be easily exfoliated, commonly either mechanically [20] or in a liquid [21], and possess a wide variety of tunable optoelectronic properties. MoS_2, for example, is an indirect bandgap semiconductor in the bulk, but in the monolayer regime, it becomes a direct bandgap one [22]. This property can be further exploited by the layering of different chalcogenides nanosheets to create vertical van der Waals heterostructure devices, such as a *pn*-junction by layering MoS_2 onto WSe_2 [23].

The interesting added covalency of chalcogenide-based materials comes at a cost. The weaker bonding allows for the facile formation of chalcogen defects and vacancies, which in turn affects the material properties, and hence potential device applications. These

increased point defects can act as scattering sites which can negatively affect the mobility of charge carriers and exciton populations [24–26], hence affecting optoelectrical performance. Trying to characterise chalcogenide materials also may lead to defect formation, especially in the case of electron microscopy studies [27, 28], hence care needs to be taken. Growth and preparation of chalcogenide materials can also cause some difficulties, as often chalcogen precursor gases such as H_2S and H_2Se can be highly corrosive to the growth chamber [29, 30].

Despite these challenges, chalcogenide materials show great device potential, and hence understanding their structure-property relationships is key to their future applications. Defects in the material can also help to explain their unique properties, as is shown in Chapter 3 of the case of stacking fault-induced thermoelectric effects in $TlGaSe_2$. Defect engineering can also be exploited to observe new physical phenomena, as in Chapter 4 with the Rashba effect in GaS/GaSe heterostructures, or induce and stabilise thermodynamically unstable structures, such as perovskite $BaZrSe_3$ in Chapter 5.

In order to understand these materials and their properties, adequate characterisation tools, such as the electron microscope, are required and are hence heavily exploited in this work.

1.2 Electron Microscopy

Since its invention in 1931 by Max Knoll and Ernst Ruska [31], the electron microscope has been *the* characterisation tool of choice to understand the nanostructure of materials. With its much higher resolving power than that of conventional optical microscopy, electron microscopes allow for the direct imaging of nanoscale features [32]. These powerful abilities accelerated materials discovery and innovation in the 20th century, earning Ruska a Nobel Prize in Physics in 1986 [33].

Feynman, in his aforementioned lecture [1], was infatuated with the idea of pushing electron microscopy to atomic resolution in order to advance material science. Transmission electron microscopy (TEM) is one of the most powerful techniques in materials characterisation which can now achieve this feat and was the main technique used in this work. This method involves the impinging and scattering of highly accelerated electrons,

usually in the tens to hundreds of kV ranges, through a thin sample (< 100 nm thick). From the collection of these scattered electrons, imaging and spectroscopic information can be obtained.

The mode of operation of a TEM is analogous to light microscopy, with parallel illumination of the sample, albeit with electrons instead of photons. This is in contrast to the sister technique, scanning TEM (STEM). Here, the sample is rastered across with a subnanometer-sized probe. Nonetheless, the two techniques are complementary: the former allows for a much greater field of view of the samples, enabling one to characterise sample size, features and crystallinity, while the latter allows for sub-Å imaging of atomic structures, enabling deeper analysis of planar defects, vacancies, interstitials, etc. [34].

It is first important to discuss what defines the resolution of optical systems as this will further illustrate the benefits of TEM compared to other imaging techniques. In optical systems, the resolution is limited by the diffraction effects of the illumination source wavelength and the imperfections (i.e. aberrations) of the lens system. The diffraction-limited resolution is defined by the Rayleigh criterion, which for a circular aperture, relates the resolution, δ, with the wavelength, λ, of the illumination source:

$$\delta \approx \frac{0.61\lambda}{nsin(\beta)} \tag{1.1}$$

where n is the refractive index of the viewing medium and β is the semi-angle of collection of the magnifying lens. For a typical parallel-light illuminated microscope, operated in air, $nsin(\beta)$ can be approximated as unity. Since the smallest wavelength visible to humans is approx. 310 nm [35], the theoretical diffraction-limited resolution of the said microscope is approx. 190 nm.

This resolution can be greatly improved using electrons instead of photons. To appreciate this, first consider that the electrons exhibit wave-particle duality, shown by the de Broglie relation:

$$\lambda = \frac{h}{p} \tag{1.2}$$

where h is Planck's constant and p is momentum. In a TEM, momentum is imparted onto the electrons via an accelerating voltage, V:

$$eV = \frac{1}{2} m_0 v^2 \tag{1.3}$$

where m_0 is the electron rest mass and v is the electron velocity. Through substitution, the relationship between λ and V is given as:

$$\lambda = \frac{h}{\sqrt{2m_0 eV}} \tag{1.4}$$

When taking relativistic terms into account, Equation 1.4 becomes:

$$\lambda = \frac{h}{\sqrt{2m_0 eV\left(1 + \frac{eV}{2m_0 c^2}\right)}} \tag{1.5}$$

where c is the speed of light in a vacuum. For a typical TEM accelerating voltage of 300kV, the de Broglie wavelength equates to 1.97 pm, a 10^6 times improvement in resolution compared to visible light. While this is an impressive increase in resolution, it is not what is achievable, as with any lens system, there are aberrations which limit this. These aberrations in the TEM context are explained later on, in Chapter 2.2.

In order to "see" anything with the microscope, the electrons must scatter off the nuclei and/or electrons of the sample and into a detector, much like how photons scatter off objects and into our optobiological detectors - our eyes. To understand this, first consider that even with the high energy nature of the electrons in a TEM, the vast majority of electrons are scattered in the forward direction, and not back towards the electron source they came from.

Electron scattering can be subdivided into where the scattering occurs and whether there is a momentum transfer from the incident electron to the scattered object. The scattering can be considered elastic, where there is no energy transfer or too small to be detected, or inelastic, where energy transfer, and hence energy loss of the impinging electrons, is large enough to be detected [32]. In the TEM context, large scattering angles occur when the incident electrons scatter off the positively charged atomic nuclei of the sample. However, the majority of electrons travel away from the atomic nuclei and are hence shielded from the intense positive charges, due to electron screening and the inverse square law. This results in smaller scattering angles, which are typically 10-100 mrad for a

100 kV accelerating voltage, and the interference of the electron waves due to the periodic atomic potential leads to diffraction [36]. This variety of scattering modalities and signals produced, as shown in Figure 1.1, means that detector position and design are key to obtaining specific information about the sample, be it for imaging or spectroscopy.

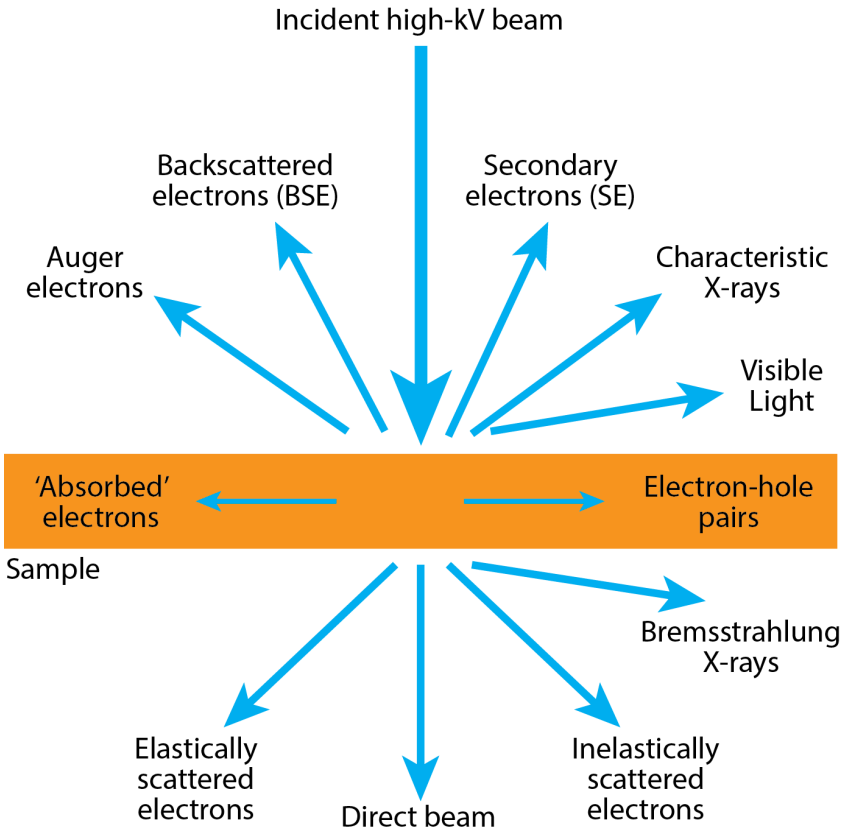

Fig. 1.1 Diagram of pre- and post-sample electron scattering events and signals produced, due to impinging the thin sample with a high-kV electron beam. Reproduced with permission from Springer Nature [32].

To illustrate the concept further, let us simplify and first consider the elastic scattering of an incident electron and an arbitrary, isolated atom, shown in Figure 1.2. The differential cross-section describes the angular distribution of scattering from an atom and is defined as:

$$\frac{d\sigma}{d\Omega} = \frac{1}{2\pi sin(\theta)} \frac{d\sigma}{d\theta} \tag{1.6}$$

where θ is the scattering angle, σ is the scattering cross-section, and Ω is the solid angle of scattering. In the high-angle regime, the electron-nuclei interaction is known as Rutherford scattering and Equation 1.6 can be rewritten as the Rutherford differential cross-section:

$$\frac{d\sigma(\theta)}{d\Omega} = \frac{e^4 Z^2}{16\,(4\pi\epsilon_0 E_0)^2\, sin^4\left(\frac{\theta}{2}\right)} \tag{1.7}$$

where e is the electron charge, Z is the atomic number of the atom, ϵ_0 is the permittivity of free space, and E_0 is the energy of the incident beam [32].

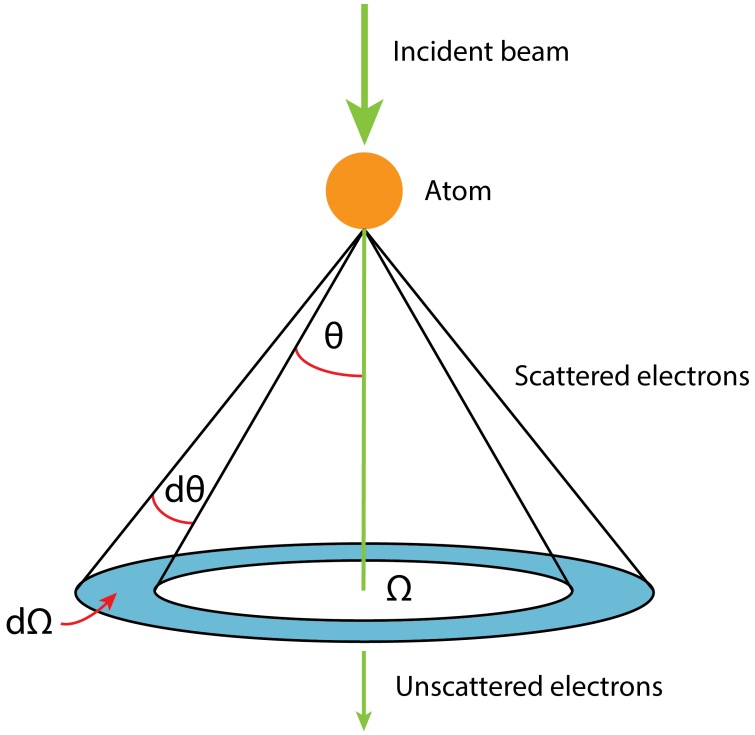

Fig. 1.2 Diagram of electron scattering with a single atom. Electrons are scattered through an angle, θ, with Ω being the solid angle of scattering. An incremental increase in scattering angle, $d\theta$, leads to an incremental increase in the solid angle, $d\Omega$. Reproduced with permission from Springer Nature [32].

A key observation is obtained from Equation 1.7. The probability of electron scattering, i.e. the cross-section, increases if one uses materials with heavier elements or an electron beam with lower energy. For example, when imaging elements with large Z, such as gold, the cross-section will increase by a factor of 100 when compared to low Z elements, such as carbon. Similarly, using electrons of lower energy (by reducing the accelerating voltage) also has the same effect on the cross-section. This phenomenon is exploited in Z-contrast imaging which has been shown to be able to do elemental mapping of a structure and its defects via an imaging mode only [37].

It should be noted, however, that Equation 1.7 is only suitable for large scattering angles; as it neglects electron screening effects which reduce the differential cross-section. Hence, at low angles, Equation 1.7 overestimates the amount of scattering.

Another important issue with Equation 1.7 is that it is a classical approach, neglecting the wave nature of electrons. Fortunately, by taking this into account, the low-angle elastic scattering can be appropriately described, with the high-angle scattering being complementarily described by the Rutherford method. Here, we introduce the atomic scattering factor, $f(\theta)$, which is a measure of the amplitude of an electron wave scattered from an isolated atom (hence $\left|f(\theta)\right|^2$ is proportional to the scattering intensity):

$$f(\theta) = \frac{\left(1+\frac{E_0}{m_0 c^2}\right)}{8\pi^2 a_0}\left(\frac{\lambda}{sin\left(\frac{\theta}{2}\right)}\right)^2 (Z - f_X) \tag{1.8}$$

where a_0 is the Bohr radius and f_X is the scattering factor for X-rays [32]. Equation 1.8 contains components of both elastic nuclear scattering (i.e. from the Z term) and elastic electron-cloud scattering (i.e. from the f_X term), unlike Equation 1.7 which only accounts for the former.

Equation 1.8 is then related to the differential scattering cross-section via the following equation:

$$\left|f(\theta)\right|^2 = \frac{d\sigma(\theta)}{d\Omega} \tag{1.9}$$

While the discussion above has been illustrative and introduces scattering off a single atom in space, it may come as a surprise to the reader to know that real-world materials often contain more than one atom. Hence, for crystalline materials, the approach above is extended via the concept of an atomic structure factor, $F(\theta)$, which is a measure of the electron wave amplitude scattered from the atoms of a unit cell of a crystalline structure. This can consequently be defined as the summation of the atomic scattering factors, $f(\theta)$, of all the i atoms in the unit cell, with fractional atomic coordinates (x_i, y_i, z_i):

$$F(\theta) = \sum_i^\infty f(\theta)_i e^{2\pi i(hx_i + ky_i + lz_i)} \tag{1.10}$$

It is therefore clear from Equation 1.10 that the amplitude of the scattered electron beam is dependent on the type of atom (from the $f(\theta)$ term), the fractional atomic coordinates of the atom (x_i, y_i, z_i) in the structure, and the specific atomic planes (hkl) which make

the structure. How this scattering information is translated into image formation is left for Chapter 2.2.

As was shown in Figure 1.1, as the electrons scatter through the atomic structure of the sample in a TEM, a wide variety of signals can be recorded along with the scattered electrons used to form the images. Spectroscopic techniques, such as energy dispersive X-ray (EDX) spectroscopy and electron energy loss spectroscopy (EELS), can be coupled with the TEM/STEM imaging to allow for chemical [38], plasmonic [39], and phonon maps [40] of the regions of interest, further enabling research into defects and chemical phases. This has led to the TEM being often called a "synchrotron in a microscope" [41].

External inputs, such as voltage biases [42] and strain [43], and environments, such as high temperatures (~1300 °C) [44], gas flows, or liquids [45], can be imposed on the sample and imaged simultaneously with the use of in-situ TEM sample holders in order to monitor chemical kinetics, phase transitions, etc. [46].

1.3 TEM Data Post-Processing & Simulations

As discussed in Chapter 1.2, one can collect an incredible amount of data from TEM experiments. Careful analysis of this data is required to accurately understand the structure-property relationships of the materials under study and to prevent misinterpretation. While the power of the electron microscope cannot be understated, a human's ability to interpret the subsequent images and data can. A common warning in TEM textbooks is to be aware of projection artefacts. For example, there's no such thing (at the time of writing) as a two-headed camel, however, Figure 1.3 may be misinterpreted this way instead of one camel in front of another [32].

Another difficulty humans face is distinguishing minute changes in contrast and displacements, which is important when trying to quantify strain, number of atoms in an atomic column, etc. from TEM images. (Given the number of atomic columns in a typical TEM image, it is also impractical to do by hand). The need for post-processing of images is especially required when imaging novel and/or complicated structures where it is not intuitive as to what one is seeing, or to correlate changes in image contrast with the pres-

ence of defects, etc. This was the case for understanding the lattice expansion due to the presence of anti-phase boundaries in $BaZrS_{(3-y)}Se_y$ alloys in Chapter 5.

Fig. 1.3 Photograph of two camels taken so that, in projection, they appear as one two-headed camel. One needs to take care of these projection artefacts in TEM! Photo courtesy of German Rojas under Creative Commons licence.

Often, this post-processing requires the need to simulate the image taken under the same conditions it was taken. For example, to calculate the thickness of the GaS and GaSe nanosheets in Chapter 4 from their position-averaged convergent beam electron diffraction (PACBED) patterns [47], one needs to simulate the pattern under varying sample thickness to match the experimental patterns.

In order to do so, one needs to, in essence, simulate a TEM on the laptop/PC. However (and perhaps unfortunately for the reader), in order to do that and to understand the limitations of such as scheme, a short primer on the background theory is required. An in-depth analysis of TEM simulations is outside the scope of this work, but should readers wish to learn more about TEM simulations, they are directed to read the extensive "Advanced Computing in Electron Microscopy" by Earl Kirkland [48].

There are two main methods for TEM image simulation. Bloch wave calculations exploit the fact that many samples observed in the TEM are crystalline and hence use that periodicity to efficiently propagate the incoming electron wave through the sample. Nothing in this life is perfect, unfortunately, and so for systems with defects, large unit cells, or aperiodic structures, the Bloch wave method is far too computationally expensive as it

scales with N^3 where N is the number of Bloch waves used [49, 50]. Here, the multislice method excels. By slicing the sample into thin layers along the fast electron direction, and propagating the resultant wave function from one slice to the other, simulating TEM images of almost any system can be routinely done. Both methods have strengths and weaknesses, and these, along with the theory behind the methods, will be further discussed in Chapter 2.2.7.

1.4 Computational Chemistry

Often the atomic models, and hence the atomic potentials, used in TEM simulations come from X-ray diffraction (XRD) data of the bulk thin film or powder. However, as one approaches the length scales required for TEM, the structure of the sample may change due to, for example, surface relaxation effects, defects, etc. and hence these need to be taken into account if one is to extract accurate material property information from the TEM simulations. Conversely, changes in TEM images can help to explain structure-property changes in the material - for example, doping site configuration and EDX concentrations of Sn-doped MoS_2 monolayers can be used to explain the trends in the electronic band structure and exciton shifts [51]. As such the use of computational chemistry and modelling is becoming more ever-present in the field of TEM and materials science, especially with the advent of more powerful computing resources and code packages, such as abTEM, which couple computational chemistry with TEM simulations [52].

Computational modelling of materials and chemical systems is also important as it allows one to understand experimental results such as the measurement of a semiconductor's band gap, to understand chemical processes that may be experimentally difficult to measure, such as transition states [53] or thermoelectric properties such as for $TlGaSe_2$ in Chapter 3. It can also be used to predict new materials and reactions which later experiments can prove to exist in reality [54] (or disprove as fiction).

These computations rely on obtaining the ground-state energy of a system and are based on trying to solve the Schrödinger equation, given here in its many-body time-independent form:

$$\hat{H}\psi(\{\boldsymbol{r}_i, \boldsymbol{R}_I\}) = E\psi(\{\boldsymbol{r}_i, \boldsymbol{R}_I\}) \tag{1.11}$$

where $\boldsymbol{R}_I$ and $\boldsymbol{r}_i$ is the position of the I^{th} nucleus and i^{th} electron, respectively. It should be noted that spin has been neglected in Equation 1.11 (for the benefit of the reader and author), but effects such as spin-orbit coupling, which is key in GaS/GaSe heterostructures will be explained in later in Chapter 4.

$\hat{H}$, in Equation 1.11, is the many-body Hamiltonian operator, which is a summation of kinetic ($\hat{T}$), potential ($\hat{V}$) and Coulombic ($\hat{U}$) operators acting on the wavefunction [53]:

$$\begin{aligned}\hat{H} &= \hat{T}_e + \hat{U}_{e-e} + \hat{V}_{e-nucleus} + \hat{T}_{nucleus} + \hat{U}_{nucleus-nucleus} \\ &= -\frac{\hbar^2}{2m_e}\sum_i \nabla_i^2 + \frac{1}{2}\frac{e^2}{4\pi\epsilon_0}\sum_{i\neq j}\frac{1}{|\mathbf{r}_i - \mathbf{r}_j|} - \frac{e^2}{4\pi\epsilon_0}\sum_{i,I}\frac{Z_I}{|\mathbf{r}_i - \mathbf{R}_I|} - \sum_I \frac{\hbar^2}{2M_I}\nabla_I^2 + \frac{1}{2}\frac{e^2}{4\pi\epsilon_0}\sum_{I\neq J}\frac{Z_I Z_J}{|\mathbf{R}_I - \mathbf{R}_J|}\end{aligned} \tag{1.12}$$

where Z_I and M_I are the charge and mass of the nucleus, respectively, and m_e is the mass of the electron. Unfortunately, for systems containing more than a handful or so interacting electrons and nuclei, directly solving Equation 1.11 for the ground-state energy is, to put it politely, computationally impractical. Consequently, approximations must be taken to achieve this within a reasonable time and computational capability.

One of the first approximations that can be made is known as the Born-Oppenheimer approximation. Made famous by the hit 2023 film "Oppenheimer", this approximation recognises that the mass of the nucleus is much greater than the mass of the electron, and therefore the motion of the nucleus can be negligible compared to that of the electrons [55]. Therefore, by assuming $\frac{1}{M_I}$ becomes very small and ignoring $\hat{T}_{nucleus}$, Equation 1.12 becomes:

$$\hat{H} = -\frac{\hbar^2}{2m_e}\sum_i \nabla_i^2 + \frac{1}{2}\frac{e^2}{4\pi\epsilon_0}\sum_{i\neq j}\frac{1}{|\mathbf{r}_i - \mathbf{r}_j|} - \frac{e^2}{4\pi\epsilon_0}\sum_{i,I}\frac{Z_I}{|\mathbf{r}_i - \mathbf{R}_I|} + E_{nucleus-nucleus} \tag{1.13}$$

where $E_{nucleus\text{-}nucleus}$ is the classical nucleus-nucleus electrostatic term and thus is a constant for a given nucleus.

Another approximation that can be taken is known as the Hartree-Fock approximation. The positions of the nuclei are now known, thanks to the Born-Oppenheimer approximation. Hence, only the electrons are treated like independent, interacting particles occupying single-electron spin-orbitals. Then the energy of the system is minimised using the variation principle by varying the electron orbitals, and the lowest possible energy in this system is known as the Hartree-Fock approximation for the ground-state energy [56, 57].

While $\hat{T}$ and $\hat{V}$ operate on single electrons, $\hat{U}$ involves operating on two different ones. Finding the expectation value of $\hat{U}$ for a pair of electrons leads to two terms known as the Hartree energy, which is the classical electrostatic interaction term:

$$E_H = \frac{1}{2}\sum_{s,t}\int\int \frac{e^2}{4\pi\epsilon_0}\frac{|\phi_s(\mathbf{x}_1)|^2|\phi_t(\mathbf{x}_2)|^2}{|\mathbf{r}_1-\mathbf{r}_2|}d\mathbf{x}_1 d\mathbf{x}_2 \tag{1.14}$$

and the exchange energy, due to the Pauli exclusion principle:

$$E_X = -\frac{1}{2}\sum_{s,t}\int\int \frac{e^2}{4\pi\epsilon_0}\phi_s^*(\mathbf{x}_1)\phi_t(\mathbf{x}_1)\frac{1}{|\mathbf{r}_1-\mathbf{r}_2|}\phi_s(\mathbf{x}_2)\phi_t^*(\mathbf{x}_2)d\mathbf{x}_1 d\mathbf{x}_2 \tag{1.15}$$

While this is an improvement in complexity from Equation 1.13, it does not take electron correlation into account and is still quite computationally expensive as it scales with N^4 where N is the number of basis functions used to describe the system [58, 59]. Accordingly, further approximations are still required to make calculations practical (no surprises here).

However, at this point, a method emerges that balances the need for accuracy of calculations with structures of the size of unit cells and above with computational ability. In its most simple definition, density functional theory (DFT) states that the ground-state energy of a system can be described as a functional of its electron density. This electron density itself can be calculated from self-consistent equations taking into account approximations for exchange and correlation energies [53, 60]. While this will be further explained in Chapter 2.4, doing said methods allows one to accurately calculate, within a reasonable time frame, electronic band structures, electron transport calculations, phonon dispersions, optical properties, etc. Though not without limitations, the power of this

theory cannot be understated and hence landed one of its developers, Walter Kohn, the Nobel Prize in 1998 [61].

1.5 Thesis Outline

The research discussed in this work sets out to "fill in" some of the knowledge gaps that exist in establishing structure-property relationships of chalcogenide materials. Given its above-mentioned utility, (S)TEM was used extensively throughout to characterise the structure of the materials, along with computational modelling to understand the material's properties and how different defects present affect such properties.

Although outside the scope of this work, the different synthesis techniques for the materials used in this work are discussed briefly in Chapter 2.1 to provide the reader with some understanding of the benefits, complexities, and drawbacks of each growth method. The theory of operation and sample preparation methods for TEM are discussed in Chapter 2.2 and Chapter 2.3, respectively. Finally, in Chapter 2.4, the discussion on density functional theory and TEM simulations is extended to provide more context to the reader of the methods used in this work.

Thermoelectricity is explored in Chapter 3, via the study of $TlGaSe_2$. This material is a layered, 2-D semiconductor with anisotropic thermoelectric effects. It has been previously noted that the material is prone to stacking faults along the [001] stacking direction [62, 63], but what has not been established is the relationship between the presence of these faults and the anisotropic thermoelectricity of the material. In Chapter 3, this is explored via the use of TEM and diffraction simulations to understand the structure of the material. To couple this to the properties, density functional theory is used to calculate the stacking fault energy of the materials, along with the phonon dispersions and electron transport calculations of both a pristine and a faulted system.

The ability of controlled stacking of 2-D layers and the effect of twist angles is explored in Chapter 4 with the analysis of GaS/GaSe van der Waals heterostructures. Theorised to possess Rashba splitting [64], where the electronic bands of the material are split along momentum-space rather than energy-space, these heterostructures are assembled and studied with varying twist angle to understand the structural dependence of this effect.

This is done via STEM imaging, coupled with spin-orbit coupled DFT calculations, and the effect is discussed for potential optoelectronic and spintronic applications.

Chapter 5 explores the characterisation of $BaZrS_{(3-y)}Se_y$ alloy chalcogenide perovskite thin films for solar photovoltaics. Adjusting the S/Se ratio as the films are being synthesised allows for precise bandgap engineering, as is confirmed with DFT calculations of the band gaps, but varies the number of planar defects in the materials. These defects are studied via atomic column displacements in both in-plane and out-of-plane film directions, and correlating the results to S/Se ratio of the alloy obtained from EDX.

Finally, Chapter 6 draws conclusions from the previous chapters and discusses the ongoing and future research on the materials in this work. This is then followed by an appendix of additional and supporting data for the various chapters.

References

[1] Richard Feynman. “There’s Plenty of Room at the Bottom”. In: *Engineering and Science* 23.5 (1960), pp. 22–36.

[2] Susan Ratcliffe. “The Practical Applications of Electricity - Lord Kelvin”. In: *Oxford Quotations* (2016).

[3] S.M. Sze and Kwok K. Ng. “Physics of Semiconductor Devices”. In: *Physics of Semiconductor Devices* (2006). DOI: 10.1002/0470068329.

[4] R. M. Sardarli et al. “Superionic conductivity in TlGaTe2 crystals”. In: *Semiconductors* 45.8 (2011), pp. 975–979. DOI: 10.1134/S1063782611080161.

[5] Rauf Sardarly et al. “Superionic Conductivity in One-Dimensional Nanofibrous TlGaTe 2 Crystals”. In: *Japanese Journal of Applied Physics* 50.5S2 (2011), 05FC09. ISSN: 0021-4922. DOI: 10.1143/JJAP.50.05FC09.

[6] Karl W Böer and Udo W Pohl. “Crystal Defects”. In: *Semiconductor Physics*. Vol. 1. 7. Cham: Springer International Publishing, 2018, pp. 529–579. ISBN: 978-3-319-69150-3. DOI: 10.1007/978-3-319-69150-3_15.

[7] Ashfaq Adnan and C. T. Sun. “Evolution of nanoscale defects to planar cracks in a brittle solid”. In: *Journal of the Mechanics and Physics of Solids* 58.7 (2010), pp. 983–1000. ISSN: 0022-5096. DOI: 10.1016/J.JMPS.2010.04.012.

[8] Linus Pauling. *The Nature of the Chemical Bond, An Introduction to Modern Structural Chemistry*. 1960, p. 664. ISBN: 9780801403330.

[9] Michael A. Pell and James A. Ibers. “Layered ternary and quaternary metal chalcogenides”. In: *Chemische Berichte* 130.1 (1997), pp. 1–8. ISSN: 00092940. DOI: 10.1002/cber.19971300102.

[10] Partha Kumbhakar et al. “Emerging 2D metal oxides and their applications”. In: *Materials Today* 45 (2021), pp. 142–168. ISSN: 13697021. DOI: 10.1016/j.mattod.2020.11.023.

[11] Santosh Kumar Radha et al. “Ultrathin 2D-oxides: A perspective on fabrication, structure, defect, transport, electron, and phonon properties”. In: *Journal of Applied Physics* 129.22 (2021), p. 220903. ISSN: 10897550. DOI: 10.1063/5.0051093/158230. arXiv: 2103.12530.

[12] Xiaozong Hu et al. “2D Oxides for Electronics and Optoelectronics”. In: *Small Science* 2.8 (2022), p. 2200008. ISSN: 2688-4046. DOI: 10.1002/SMSC.202200008.

[13] Michelle P. Browne, Zdeněk Sofer, and Martin Pumera. “Layered and two dimensional metal oxides for electrochemical energy conversion”. In: *Energy & Environmental Science* 12.1 (2019), pp. 41–58. ISSN: 17545706. DOI: 10.1039/C8EE02495B.

[14] F. Pelayo García de Arquer et al. “Semiconductor quantum dots: Technological progress and future challenges”. In: *Science* 373.6555 (2021). ISSN: 0036-8075. DOI: 10.1126/science.aaz8541.

[15] Eunjoo Jang and Hyosook Jang. “Quantum Dot Light-Emitting Diodes”. In: *Chemical Reviews* 123.8 (2023), pp. 4663–4692. ISSN: 0009-2665. DOI: 10.1021/acs.chemrev.2c00695.

[16] Aude Bechu et al. “Cadmium-Containing Quantum Dots Used in Electronic Displays: Implications for Toxicity and Environmental Transformations”. In: *ACS Applied Nano Materials* 4.8 (2021), pp. 8417–8428. ISSN: 2574-0970. DOI: 10.1021/acsanm.1c01659.

[17] Mônica A. Cotta. “Quantum Dots and Their Applications: What Lies Ahead?” In: *ACS Applied Nano Materials* 3.6 (2020), pp. 4920–4924. ISSN: 2574-0970. DOI: 10.1021/acsanm.0c01386.

[18] *Nobel Prize for Chemistry 2023, nobelprize.org - https://www.nobelprize.org/prizes/chemistry/2023/summary/.*

[19] Francis Jacob Clauss. *Solid Lubricants and Self-Lubricating Solids*. Academic Press, 1972, p. 260. ISBN: 9780323158220.

[20] Qing Hua Wang et al. “Electronics and optoelectronics of two-dimensional transition metal dichalcogenides”. In: *Nature Nanotechnology 2012 7:11* 7.11 (2012), pp. 699–712. ISSN: 1748-3395. DOI: 10.1038/nnano.2012.193.

[21] Valeria Nicolosi et al. “Liquid exfoliation of layered materials”. In: *Science* 340.6139 (2013), pp. 72–75. ISSN: 10959203. DOI: 10.1126/science.1226419.

[22] Andrea Splendiani et al. “Emerging Photoluminescence in Monolayer MoS 2”. In: *Nano Letters* 10.4 (2010), pp. 1271–1275. ISSN: 1530-6984. DOI: 10.1021/nl903868w.

[23] Rui Cheng et al. “Electroluminescence and photocurrent generation from atomically sharp WSe2/MoS2 heterojunction p-n diodes”. In: *Nano Letters* 14.10 (2014), pp. 5590–5597. ISSN: 15306992. DOI: 10.1021/nl502075n. arXiv: 1403.3447.

[24] Ke Wu et al. “Revealing the Competition between Defect-Trapped Exciton and Band-Edge Exciton Photoluminescence in Monolayer Hexagonal WS2”. In: *Advanced Optical Materials* 10.6 (2022), p. 2101971. ISSN: 2195-1071. DOI: 10.1002/ADOM.202101971.

[25] Jinhua Hong et al. “Exploring atomic defects in molybdenum disulphide monolayers”. In: *Nature Communications 2015 6:1* 6.1 (2015), pp. 1–8. ISSN: 2041-1723. DOI: 10.1038/ncomms7293.

[26] F. Fabbri et al. “Novel near-infrared emission from crystal defects in MoS2 multilayer flakes”. In: *Nature Communications 2016 7:1* 7.1 (2016), pp. 1–7. ISSN: 2041-1723. DOI: 10.1038/ncomms13044.

[27] Jie Jiang et al. “Defect Engineering in 2D Materials: Precise Manipulation and Improved Functionalities”. In: *Research* 2019 (2019). ISSN: 26395274. DOI: 10.34133/2019/4641739.

[28] Y J Zhang et al. “Radiation damage and defect dynamics in 2D WS2: a low-voltage scanning transmission electron microscopy study”. In: *2D Materials* 9.1 (2021), p. 015009. ISSN: 2053-1583. DOI: 10.1088/2053-1583/AC3377.

[29] Kostiantyn V. Sopiha et al. “Chalcogenide Perovskites: Tantalizing Prospects, Challenging Materials”. In: *Advanced Optical Materials* 10.3 (2022), p. 2101704. ISSN: 2195-1071. DOI: 10.1002/ADOM.202101704.

[30] Ida Sadeghi et al. “Making BaZrS3 Chalcogenide Perovskite Thin Films by Molecular Beam Epitaxy”. In: *Advanced Functional Materials* 31.45 (2021), p. 2105563. ISSN: 1616-3028. DOI: 10.1002/ADFM.202105563. arXiv: 2105.10258.

[31] M. Knoll and E. Ruska. “Das Elektronenmikroskop”. In: *Zeitschrift fur Physik* 78.5-6 (1932), pp. 318–339. ISSN: 1434-6001. DOI: 10.1007/BF01342199.

[32] David B. Williams and C. Barry Carter. *Transmission electron microscopy: A textbook for materials science*. 2009, pp. 1–760. ISBN: 9780387765006. DOI: 10.1007/978-0-387-76501-3.

[33] *Enrst Ruska - Facts, nobelprize.org. - https://www.nobelprize.org/prizes/physics/1986/ruska/facts/*. (accessed 2023-09-27).

[34] Rik Brydson, ed. *Aberration-Corrected Analytical Transmission Electron Microscopy*. Wiley, 2011, p. 280. ISBN: 978-1-119-97990-6.

[35] D. H. Sliney. “What is light? the visible spectrum and beyond”. In: *Eye (Basingstoke)* 30.2 (2016), pp. 222–229. ISSN: 14765454. DOI: 10.1038/eye.2015.252.

[36] R.F. Egerton. *Electron Energy-Loss Spectroscopy in the Electron Microscope*. Boston, MA: Springer US, 2011. ISBN: 978-1-4419-9582-7. DOI: 10.1007/978-1-4419-9583-4.

[37] Ondrej L. Krivanek et al. “Atom-by-atom structural and chemical analysis by annular dark-field electron microscopy”. In: *Nature* 464.7288 (2010), pp. 571–574. ISSN: 00280836. DOI: 10.1038/nature08879.

[38] M. Bosman et al. “Two-Dimensional Mapping of Chemical Information at Atomic Resolution”. In: *Physical Review Letters* 99.8 (2007), p. 086102. ISSN: 0031-9007. DOI: 10.1103/PhysRevLett.99.086102.

[39] Jaysen Nelayah et al. “Mapping surface plasmons on a single metallic nanoparticle”. In: *Nature Physics* 3.5 (2007), pp. 348–353. ISSN: 17452481. DOI: 10.1038/nphys575.

[40] F. S. Hage et al. “Phonon Spectroscopy at Atomic Resolution”. In: *Physical Review Letters* 122.1 (2019), p. 016103. ISSN: 0031-9007. DOI: 10.1103/PhysRevLett.122.016103.

[41] L. M. Brown. “A Synchrotron in a Microscope”. In: *Electron Microscopy and Analysis 1997* (2022), pp. 17–22. DOI: 10.1201/9781003063056-4.

[42] C. M. Wang et al. “In situ transmission electron microscopy and spectroscopy studies of interfaces in Li ion batteries: Challenges and opportunities”. In: *Journal of Materials Research* 25.8 (2010), pp. 1541–1547. ISSN: 2044-5326. DOI: 10.1557/JMR.2010.0198.

[43] H. G.F. Wilsdorf. “Apparatus for the Deformation of Foils in an Electron Microscope”. In: *Review of Scientific Instruments* 29.4 (1958), p. 323. ISSN: 0034-6748. DOI: 10.1063/1.1716192.

[44] J. Tijn van Omme et al. “Advanced microheater for in situ transmission electron microscopy; enabling unexplored analytical studies and extreme spatial stability”. In: *Ultramicroscopy* 192 (2018), pp. 14–20. ISSN: 0304-3991. DOI: 10.1016/J.ULTRAMIC.2018.05.005.

[45] Jianbo B Wu et al. “In Situ Environmental TEM in Imaging Gas and Liquid Phase Chemical Reactions for Materials Research”. In: *Advanced Materials* 28.44 (2016), pp. 9686–9712. ISSN: 1521-4095. DOI: 10.1002/ADMA.201602519.

[46] Frances M. Ross and Andrew M. Minor. “In Situ Transmission Electron Microscopy”. In: *Springer Handbooks*. Springer, 2019, pp. 101–187. DOI: 10.1007/978-3-030-00069-1_3.

[47] James M. LeBeau et al. “Position averaged convergent beam electron diffraction: Theory and applications”. In: *Ultramicroscopy* 110.2 (2010), pp. 118–125. ISSN: 03043991. DOI: 10.1016/j.ultramic.2009.10.001.

[48] Earl J. Kirkland. *Advanced Computing in Electron Microscopy*. July. Boston, MA: Springer US, 2010, pp. 1–23. ISBN: 978-1-4419-6532-5. DOI: 10.1007/978-1-4419-6533-2.

[49] Earl J. Kirkland. “On the optimum probe in aberration corrected ADF-STEM”. In: *Ultramicroscopy* 111.11 (2011), pp. 1523–1530. ISSN: 03043991. DOI: 10.1016/j.ultramic.2011.09.002.

[50] Colin Ophus. “A fast image simulation algorithm for scanning transmission electron microscopy”. In: *Advanced Structural and Chemical Imaging* 3.1 (2017), pp. 1–11. ISSN: 21980926. DOI: 10.1186/s40679-017-0046-1. arXiv: 1702.01904.

[51] Mianzeng Zhong et al. “Electronic structure and exciton shifts in Sb-doped MoS2 monolayer”. In: *npj 2D Materials and Applications 2019 3:1* 3.1 (2019), pp. 1–7. ISSN: 2397-7132. DOI: 10.1038/s41699-018-0083-1.

[52] Jacob Madsen and Toma Susi. “The abTEM code: transmission electron microscopy from first principles”. In: *Open Research Europe* 1 (2021), p. 24. DOI: 10.12688/openreseurope.13015.2.

[53] David S. Sholl and Janice A. Steckel. *Density Functional Theory: A Practical Introduction*. John Wiley and Sons, 2009, pp. 1–238. ISBN: 9780470373170. DOI: 10.1002/9780470447710.

[54] Jingming Shi et al. “High-throughput search of ternary chalcogenides for p-type transparent electrodes”. In: *Scientific Reports* 7.1 (2017), pp. 1–13. ISSN: 20452322. DOI: 10.1038/srep43179.

[55] M. Born and R. Oppenheimer. “Zur Quantentheorie der Molekeln”. In: *Annalen der Physik* 389.20 (1927), pp. 457–484. ISSN: 15213889. DOI: 10.1002/andp.19273892002.

[56] D. R. Hartree. “The Wave Mechanics of an Atom with a Non-Coulomb Central Field”. In: *Mathematical Proceedings of the Cambridge Philosophical Society* 24.1 (1928), pp. 89–110. ISSN: 0305-0041. DOI: 10.1017/S0305004100011919.

[57] V. Fock. “Näherungsmethode zur Lösung des quantenmechanischen Mehrkörperproblems”. In: *Zeitschrift für Physik* 61.1-2 (1930), pp. 126–148. ISSN: 14346001. DOI: 10.1007/BF01340294.

[58] J. Almlöf, K. Faegri, and K. Korsell. “Principles for a direct SCF approach to LICAO-MO ab-initio calculations”. In: *Journal of Computational Chemistry* 3.3 (1982), pp. 385–399. ISSN: 0192-8651. DOI: 10.1002/jcc.540030314.

[59] Dieter Cremer and JüRgen Gauss. “An unconventional scf method for calculations on large molecules”. In: *Journal of Computational Chemistry* 7.3 (1986), pp. 274–282. ISSN: 0192-8651. DOI: 10.1002/jcc.540070305.

[60] W. Kohn and L. J. Sham. “Self-consistent equations including exchange and correlation effects”. In: *Physical Review* 140.4A (1965), A1133. ISSN: 0031899X. DOI: 10.1103/PhysRev.140.A1133.

[61] *Walter Kohn - Biography, nobelprize.org - https://www.nobelprize.org/prizes/ chemistry/1998/kohn/biographical/.*

[62] L. Kienle et al. “Real structure of KInS2 polytypes”. In: *Journal of Solid State Chemistry* 177.1 (2004), pp. 6–16. ISSN: 00224596. DOI: 10.1016/S0022-4596(03)00244-5.

[63] D. F. McMorrow et al. “The structure of the paraelectric and incommensurate phases of TlGaSe 2”. In: *Journal of Physics: Condensed Matter* 2.16 (1990), pp. 3699–3712. ISSN: 09538984. DOI: 10.1088/0953-8984/2/16/001.

[64] Wei Wei et al. “Electronic properties of two-dimensional van der Waals GaS/GaSe heterostructures”. In: *Journal of Materials Chemistry C* 3.43 (2015), pp. 11548–11554. ISSN: 20507526. DOI: 10.1039/c5tc02975a.

2

Experimental Techniques

It's the nature of the experiment

It's the patterns of my temperament

It's the nature of the experiment

They're taking me in increments

– "Nature of the Experiment", *A Lesson In Crime*, Tokyo Police Club

This chapter provides an overview of the experimental and modelling techniques used on novel chalcogenide systems. The crystal growth methods and TEM sample techniques for the various systems are discussed. Transmission electron microscopy (TEM) theory, operation, and its various complementary spectroscopic techniques used are outlined and explained. Computational methods of TEM simulations and density functional theory (DFT) concepts and their limitations on material science studies are also briefly explained.

TEM and DFT are further described in the extensive primer textbooks of "Transmission Electron Microscopy" by Williams & Carter [1] and "Density Functional Theory: A Practical Introduction" by Sholl & Steckle [2], should tragically curious readers wish to learn more about them. However, the discussion below is limited to the specific theory required to appreciate the work in the subsequent chapters.

2.1 Sample Growth Methods

While the sample material for this work was provided by collaborators highlighted in the Acknowledgments and the relevant chapters, or purchased from suppliers such as 2D

Semiconductors Inc. as in the case of Chapter 4, it is still important to briefly provide an overview of the different types of growth methods used in this work, highlighting their benefits and complexities.

While sample growth is not the focus of this work, it is still important to briefly provide an overview of the different types of growth methods used in this work, highlighting their benefits and complexities. $TlGaSe_2$, GaS and GaSe, explored in Chapter 3 and 4 respectively, are grown with vacuum melt growth, albeit GaS and GaSe was purchased from 2D Semiconductors Inc. The $BaZrS_{(3-y)}Se_y$ alloy films in Chapter 5 were grown with molecular beam epitaxy.

2.1.1 Bulk Crystal Growth

One of the least complex yet scalable methods that was used in this work is vacuum melt growth. This Bridgman-type method involves the use of stoichiometric amounts of each element in the material of interest, placed inside a sealed quartz tube under vacuum (typically ~ 10^{-3} Pa)[3–5]. The quartz ampoule is then heated to the appropriate temperature, and cooled in a controlled way, resulting in a bulk single crystal ingot [6]. This method is used to synthesise the $TlGaSe_2$ in Chapter 3, which was provided by a collaborator [7], and GaS and GaSe in Chapter 4, which was purchased from 2D Semiconductors, Inc. [8, 9].

Bulk crystal growth methods require further mechanical processing steps to shape the ingot to the required size and, in the case of the material possessing anisotropic properties, crystal direction [10]. However, this method is simpler when compared to the others used in this work, such as molecular beam epitaxial which requires maintaining high vacuum quality and precise epitaxial growth conditions [11].

2.1.2 Thin Film Deposition

Bulk crystal growth is limited to the growth of a single crystal species at a time [10]. Hence, for the growth of nanoscale heterostructure devices such as *pn*-junctions [12], quantum wells [13], etc., alternative material growth methods are employed. For example, many semiconductor devices are constructed via thin film deposition. This process first involves the growth of a suitable substrate through bulk crystal growth methods, then the deposition

of successive layers of material (often in gaseous form) onto a substrate are executed to form a 3D architecture of diodes, wires, transistors, electrodes, etc. [14].

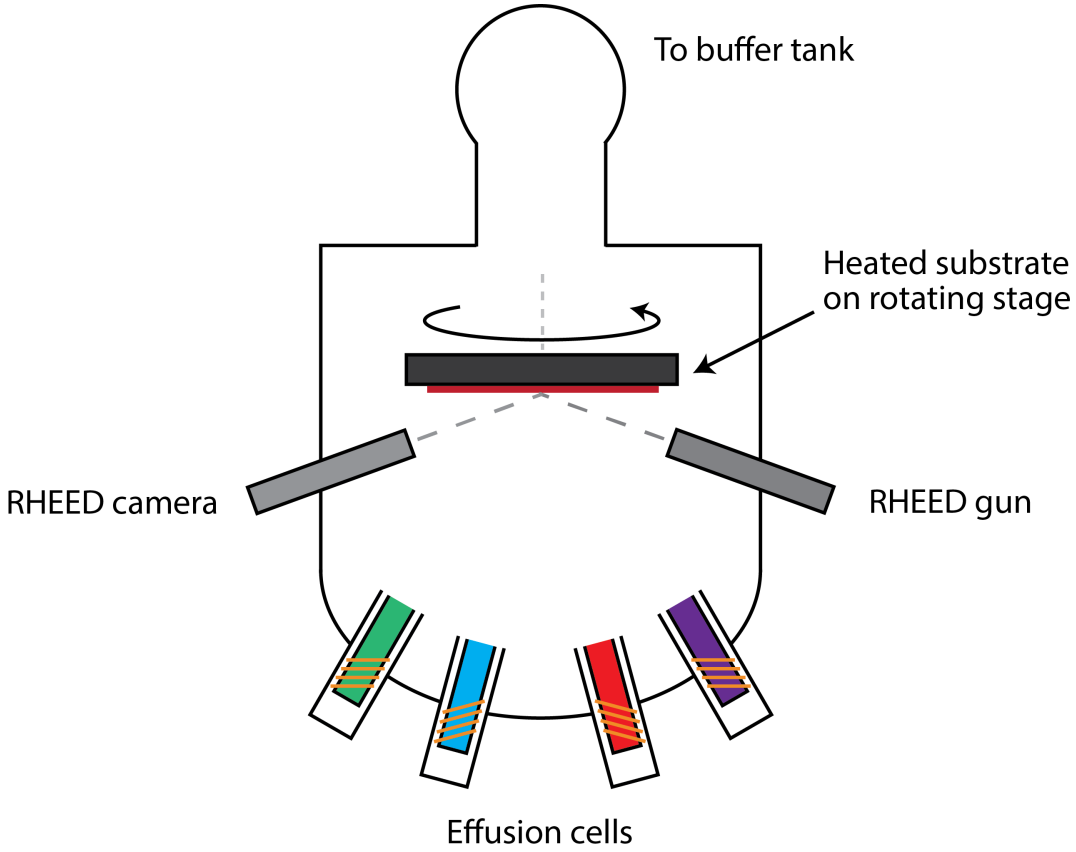

Fig. 2.1 Diagram of a typical molecular beam epitaxy vacuum chamber. Reproduced with permission from Springer Nature [15].

There are multiple techniques that can be used to form these thin films. For the synthesis of $BaZrS_{(3-y)}Se_y$ alloys in Chapter 5, a method known as molecular beam epitaxy (MBE) was used. Here, the substrate and depositing elements are held in an ultra-high vacuum ($< 10^{-7}$ Pa) growth chamber, with the substrate sample stage held at a desired temperature (usually in the hundreds of °C) [11]. The deposition elements are held in individual effusion chambers or electron beam evaporators, as seen in Figure 2.1, and when required are heated into sublimation. These gaseous elements then condense onto the heated substrate, where they can react with each other and form a film and excess gaseous products are collected by a buffer tank. This film growth is then continuously monitored using reflection high-energy electron diffraction (RHEED) inside the chamber, which is sensitive enough to monitor atomic layer-by-layer growth [16].

Using computer-controlled shutters at each cell, precise atomic layer-by-layer growth can be achieved with this method. MBE-grown films are highly pure and conformal

compared to other thin film deposition techniques such as chemical vapour deposition (CVD) as there is no carrier gas for the precursors and the growth is conducted in an ultra-high vacuum environment [17].

However, there are a number of disadvantages to this method. Primarily, due to its high precision, film growth is typically very slow (often < 20 nm/min [15]) compared to other methods such as CVD (typically ~ 200 nm/min [17, 18]), making it impractical for large scale manufacturing. Not only that but maintaining an ultra-high vacuum environment for growth is quite difficult and expensive, further limiting the technique's use to academia rather than to industry.

2.2 Transmission Electron Microscopy

The most versatile tool to investigate the nanostructure of the various material systems utilised in this work was the transmission electron microscope (TEM). This section extends on the discussion in Chapter 1.2 with an explanation of what limits the resolution of a TEM, electron diffraction inside a TEM, image formation, scanning TEM vs conventional TEM, thickness measurements inside the TEM, the complementary spectroscopic techniques (EDX, EELS), TEM image simulation, and the methods of sample preparation for TEM analysis used in this work.

In a TEM, the limiting factors in achieving high resolutions are not due to diffraction, but due to the limitations of the machine itself. To illustrate this, one needs to understand how the various parts of a TEM come together to form an image. A typical TEM vacuum column, as shown in Figure 2.2 consists of an electron gun, where electrons are extracted through the condenser lenses of the illumination system to control the size of the beam. These then scatter through the sample which has been placed in the pole piece gap of the objective lens. This lens focuses the beam onto the sample, and then magnifies the resulting image after the beam has scattered through the sample. Finally, the electrons travel through a series of projection lenses of the imaging system, which further magnify and project the transmitted image onto a screen or camera [1].

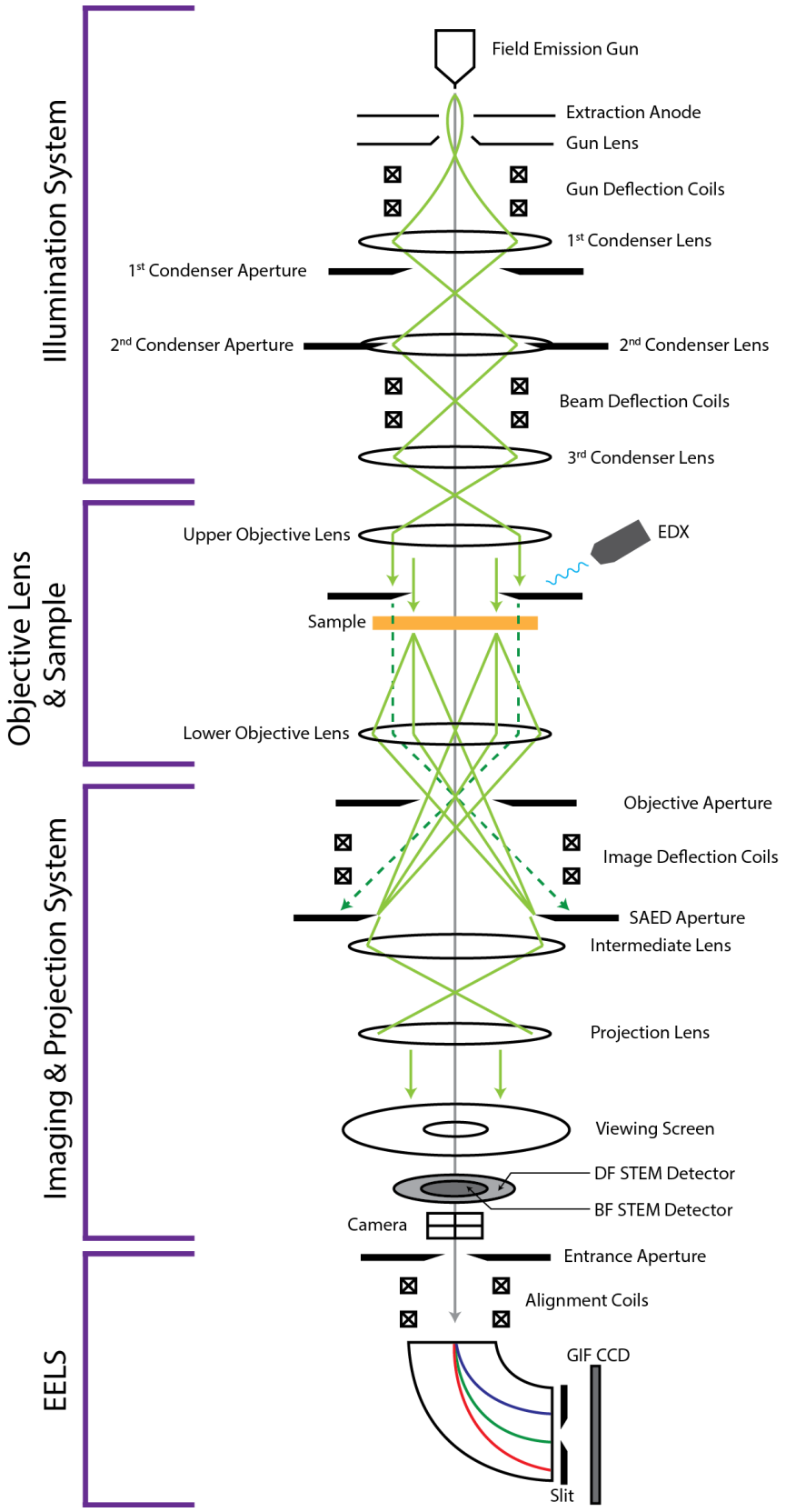

Fig. 2.2 TEM column diagram of a typical (non-aberration corrected) FEI Titan (S)TEM which heavily used throughout this work. The various components are shown, and highlighted in purple are the various major systems that comprise a typical TEM. The electron ray path is in green, and the optic axis is in grey. Adapted with courtesy from Portland State University.

However, nothing is ever so simple. These electromagnetic lenses, just as with optical lenses, are prone to a number of aberrations, with astigmatism, coma, chromatic and spherical aberrations being the main ones.

Astigmatism arises from the structural imperfections of the electromagnetic lens system. Difficulties in forming perfectly cylindrical soft iron pole pieces, along with local variations of the magnetic field due to microstructural inhomogeneities within the soft iron core, lead to the electrons experiencing a non-uniform magnetic field. This causes the electrons to deflect away from their ideal paths. Astigmatism can also arise from apertures not being properly centred around the optic axis. These can be compensated for, both pre- (condenser lens astigmatism) and post-sample (objective lens astigmatism), by using electromagnetic octopoles known as stigmators [1, 19].

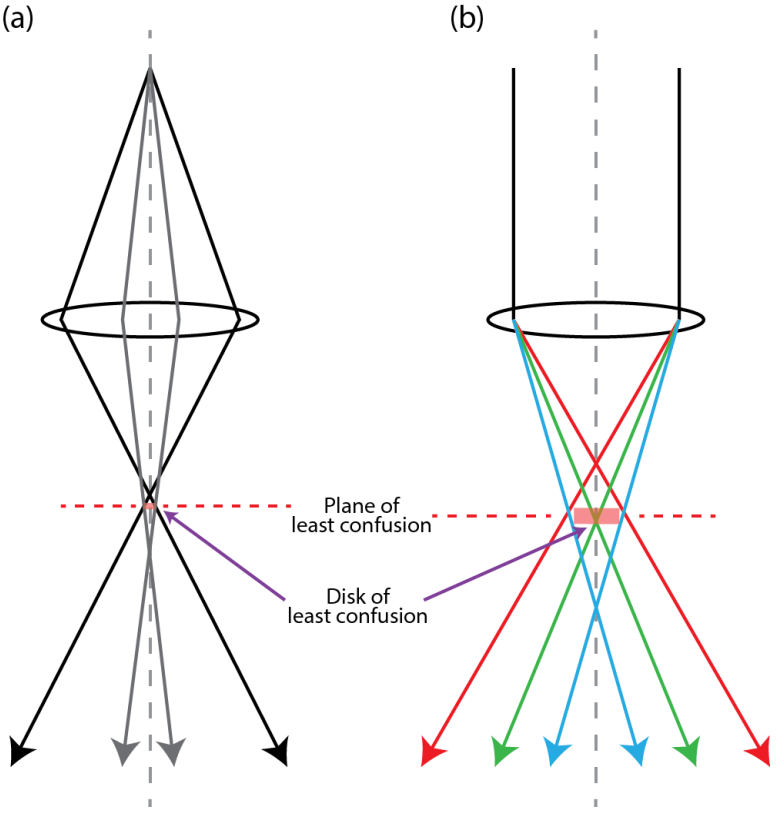

Fig. 2.3 Ray diagrams of (a) spherical aberrations and (b) chromatic aberrations, with the planes and disks of least confusion in each. Reproduced with permission from Springer Nature [1].

Coma is due to electrons originating away from the optic axis, causing the electrons to focus off the optical axis. This is due to either microscope misalignment or lens imperfections, but it can be compensated by using beam deflectors along the TEM column to ensure that the beam is focused back onto the optic axis [1, 19].

As they pass through an electromagnetic lens, electrons at large angles to the optic axis are brought to different focal points compared to electrons travelling at small angles to the optic axis. This is known as spherical aberration, C_s, and results in point objects being imaged as a smeared disk on a "plane of least confusion", as seen in Figure 2.3(a). While this can be corrected for using multipole correctors, for many "uncorrected" systems like the FEI Titan used in this work, C_s is the limiting factor in achieving higher resolutions.

Chromatic aberrations, C_c, on the other hand, are due to the deflection of electrons of different energies. As seen in Figure 2.3(b), these form different focal points for each electron energy and hence lead to a smearing of point objects. This can be corrected for using an electron source with a smaller energy spread, ΔE, such as a (cold) field emission gun (FEG) rather than LaB_6 or tungsten, and/or with a monochromator.

2.2.1 Electron Diffraction

When studying amorphous samples in light microscopy, diffraction blurring is an inconvenience as it is the limiting factor in the microscope's resolution. However, in TEM, diffraction can be exploited to reveal unique characteristics of the sample. As the electron beam passes through the atomic lattice planes of the sample of spacing d_{hkl}, electrons elastically scatter at a variety of angles. However, as shown in Figure 2.4, electrons can constructively interfere with each other if they scatter at the same specific angles, $2\theta_B$, and have a path difference which is an integer number of electron wavelengths, $n\lambda$, i.e. they satisfy Bragg's law:

$$n\lambda = 2d_{hkl}sin(\theta_B) \tag{2.1}$$

This constructive interference forms spots in the back focal plane of the objective lens, which can then be projected onto a screen or camera. These spots form an image in reciprocal space known as a diffraction pattern, which is correlated to the sample's phase, crystal structure, orientation, and defects such as stacking faults and inhomogeneities [1].

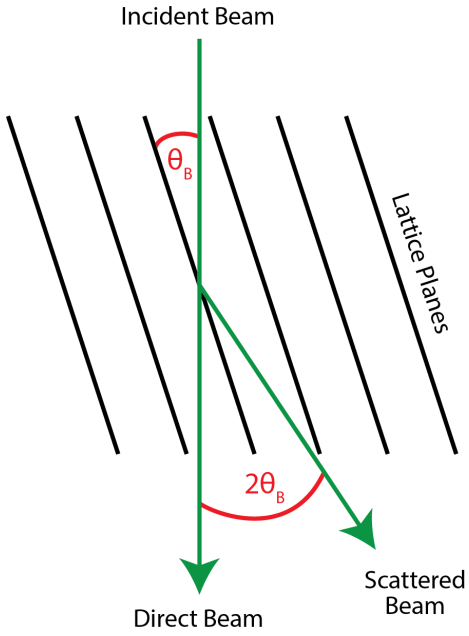

Fig. 2.4 Ray diagram of electron diffraction off a series of lattice planes, where the scattering angle with respect to the incident beam is $2\theta_B$. Reproduced with permission from Springer Nature [1].

2.2.2 Image Formation

In TEM, the illumination system focuses the beam such that the convergence semi-angle, α, is approx. 0 mrad, i.e. the beam is parallel to the optic axis and normal to the sample plane, as shown in Figure 2.7(a). This way, the entire region of interest is illuminated with a parallel beam, similar to a traditional light microscope. As a result, they both share a number of similar main imaging modes. For example, both can produce images in bright field (BF) using the directly transmitted beam, where contrast in the sample is from the attenuation of the beam from more dense parts of the sample, or in dark field (DF) using the scattered beam, where contrast is from the collected scattered beam. Both modes are represented in Figure 2.5 (a) and (b) respectively.

In TEM, this thickness dependence falls under the umbrella term of "amplitude contrast". As was mentioned in Chapter 1.2, the scattering cross-section of the electrons is highly dependent on both the atomic number, Z, of the scattering atom and the thickness of the sample, and hence is termed mass-thickness contrast. This is shown in Figure 2.6 for BF imaging; the higher mass (thicker) areas lead to more off-axis electron scattering than the lower mass (thinner) areas, and hence appear darker in the image.

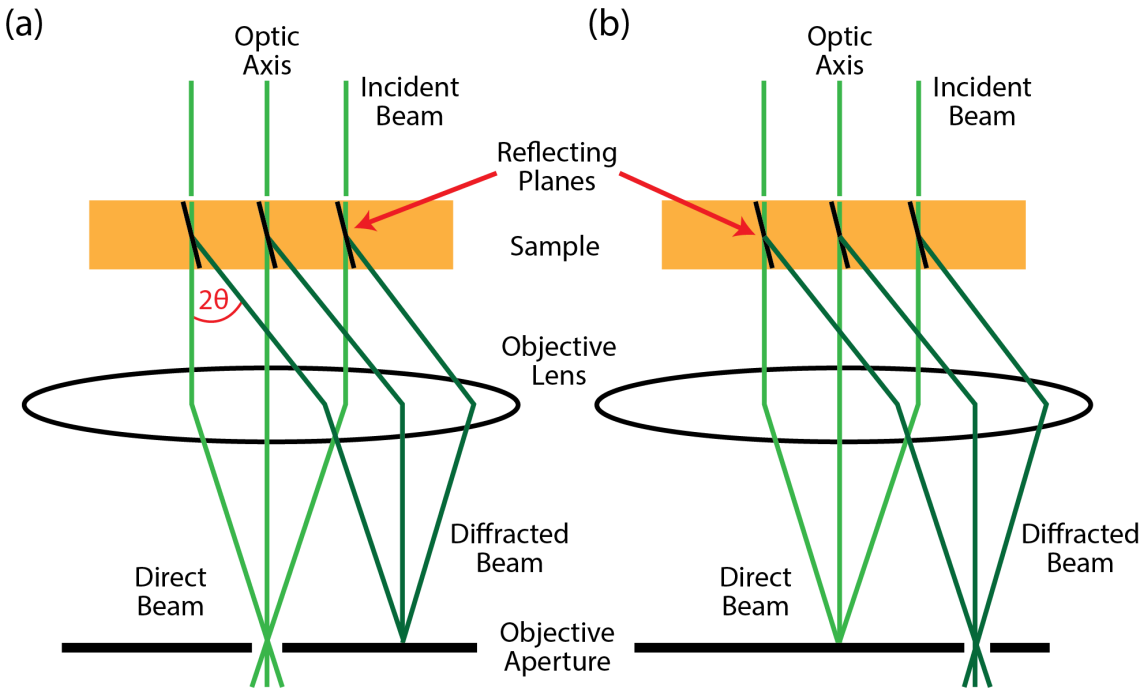

Fig. 2.5 Ray diagram showing how the objective lens and objective aperture are used to form a (a) bright-field (BF) image or a (b) dark-field (DF). Reproduced with permission from Springer Nature [1].

A second contrast mode in amplitude contrast is diffraction contrast. This arises from deviations from the Bragg conditions, and as a result, can generate bend contours in the material [1]. These contrast modes are distinguished by the fact that diffraction contrast changes with sample tilt, but mass-thickness does not.

The other major contrast mode present in both light and electron microscopy is phase contrast imaging. Specifically in TEM, this arises from the differences in the phases of the electrons as they are scattered by the sample. The interference of these electron waves can create a series of fringes in the image which are correlated to the periodicity (i.e. lattice spacings) of the sample. This type of imaging technique is known as high-resolution TEM (HRTEM) and can reveal a large amount of information, such as individual atomic columns and defects [1, 20]. However, it should be stressed that these images are not directly interpretable, as this phase information is a convolution of the exit wave function of the sample and the properties of the microscope, such as its aberrations. Hence, a through focal series (which is a series of images taken at different defocus) and simulations are required to make any quantitive assessments of the sample [1, 20, 21].

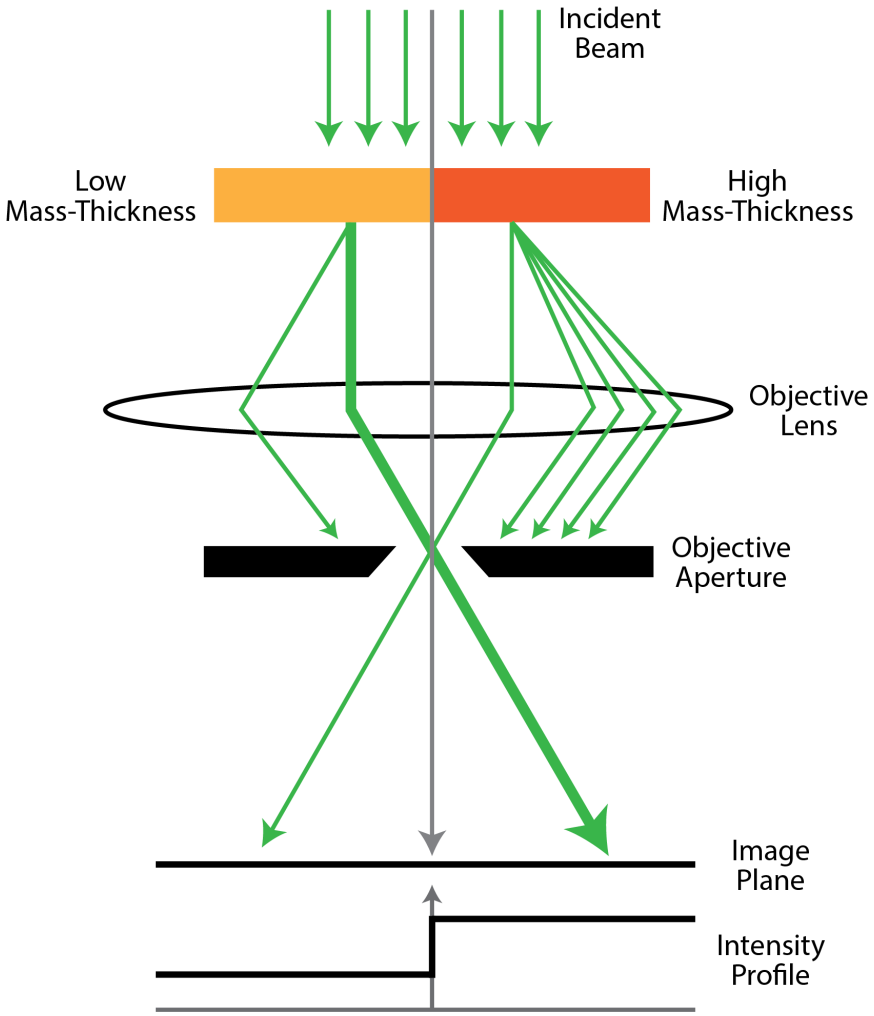

Fig. 2.6 Ray diagram demonstration of mass-thickness contrast, here shown for a BF image. Higher mass and/or thickness will lead to more off-axis scattering, leading to fewer electrons reaching the image plane. Hence, the region appears darker in BF imaging. The converse is true for the lighter and/or thinner regions. Reproduced with permission from Springer Nature [1].

2.2.3 Scanning Transmission Electron Microscopy (STEM)

Rather than illuminating the sample with a parallel beam, as is the case in TEM, in scanning TEM (STEM), the illumination system focuses the electron beam into a probe which then rasters across the sample using scan coils to form an image, as shown in Figure 2.7(b). This way, an image is formed pixel-by-pixel rather than in parallel, in contrary to TEM and the light microscopy analogy.

One of the main benefits of STEM over TEM is that a small sample volume can be illuminated one point at a time, generating a number of signals which can be collected as

the beam rasters across the sample. This way a spectral map of the sample area can be generated at the same time as the image is being taken [1, 19, 20].

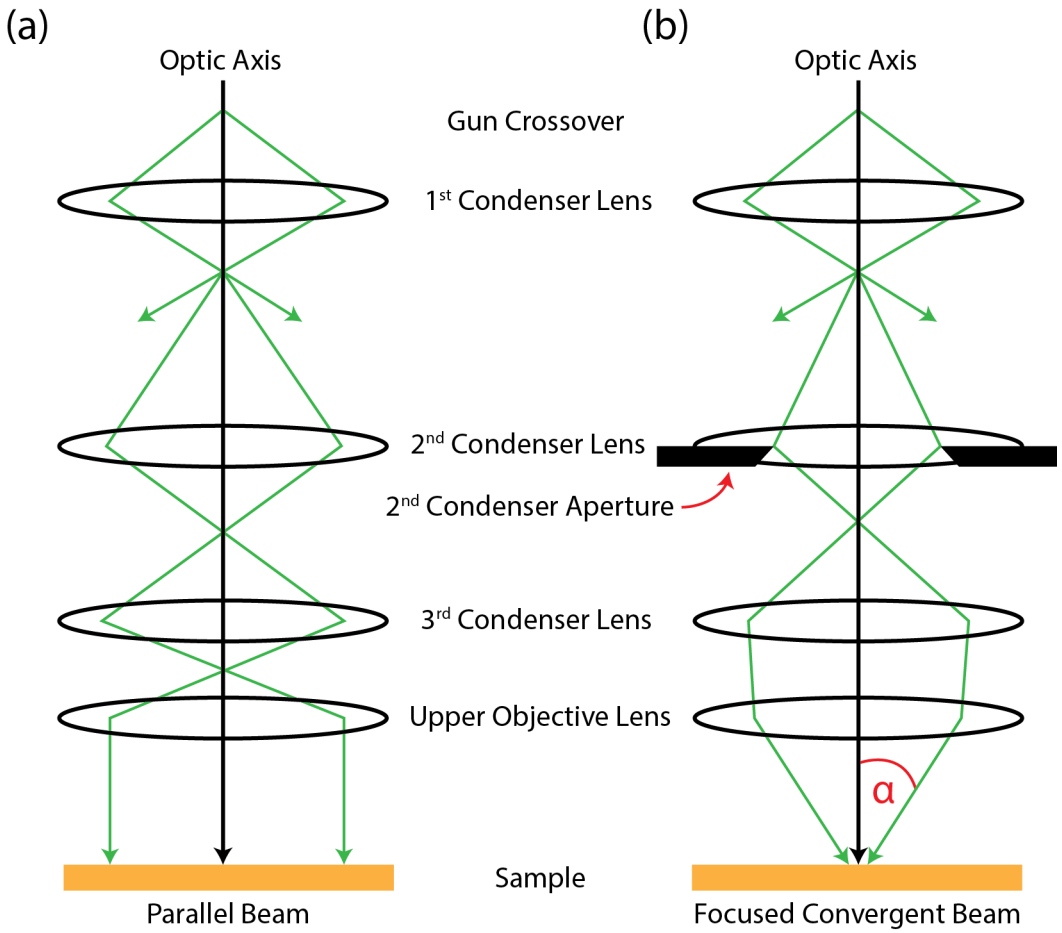

Fig. 2.7 Ray diagram of a typical FEI Titan in (a) parallel TEM mode and (b) convergent STEM mode. Reproduced with permission from Springer Nature [1].

To form images in STEM, transmitted electrons are collected by a number of detectors, each placed to collect a certain electron scattering angle range. A bright field (BF) detector, as seen in Figure 2.8, only collects the (predominately coherent) electrons scattered at relatively small angles. For a convergence semi-angle of 10 mrad and a camera length of 195 mm, such as is the case for the FEI Titan used in Chapter 3 and 4, this is typically 0 - 20 mrad. Electrons scattered at higher angles are incoherent and are collected by annular detectors, such as the annular dark field (ADF) detector. Here, contrast in the images are dominated by diffraction contrast from the Bragg scattering, but depending on the range of collection angles, this contrast can be overlapping with that of Rutherford scattering, making image interpretation difficult. As mentioned in Chapter 1.2, collecting electrons scattered at even greater angles, the effects of Bragg scattering are suppressed, and contrast

from Rutherford scattering dominates. For the case of a convergence semi-angle of 10 mrad and a camera length of 195 mm in the FEI Titan, this is when the collection angles are approx. 40 - 200 mrad, as seen in Figure 2.8. Here, in high-angle annular dark field (HAADF) imaging, the contrast in the image is derived from Z-contrast, where the scattering intensity is proportional to $Z^{\sim 1.7}$, where Z is the atomic number [22–25]. This high atomic sensitivity and direct image interpretation makes HAADF a powerful imaging mode, and hence is used throughout this work.

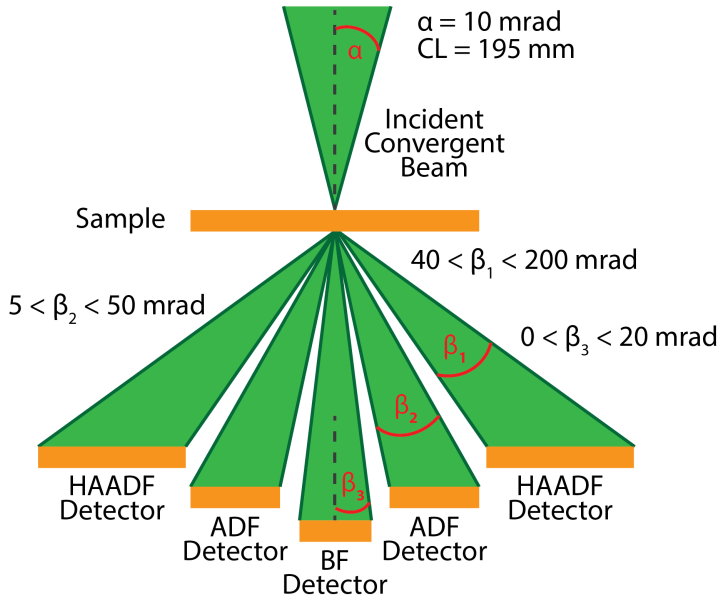

Fig. 2.8 Diagram of BF, ADF and HAADF STEM detectors with collection angles (β) for a convergence semi-angle (α) of 10 mrad and camera length (CL) of 195 mm in a FEI Titan used in Chapter 3 and 4. Reproduced with permission from Springer Nature [1].

2.2.4 Aberration Correction & Resolution Limits

In STEM, the image resolution is determined by the probe size, which in itself is determined by the size of the convergence semi-angle used (set using the condenser apertures) and the aberrations of the system. When C_s dominates, the optimum aperture, α_{opt}, is one for which there is a balance between diffraction broadening at the aperture (minimised via a large aperture) and spherical aberrations (minimised via a small aperture). Therefore, the optimal (circular) aperture can be considered one that allows one wavelength of C_s at its perimeter [26]:

$$\alpha_{\text{opt}} = \left(\frac{4\lambda}{C_s}\right)^{\frac{1}{4}} \tag{2.2}$$

The Rayleigh criterion of Equation 1.1 can be adapted to take into account of this optical aperture condition:

$$\delta \approx \frac{0.61\lambda}{\alpha_{\text{opt}}} \tag{2.3}$$

and hence, substituting Equation 2.2 into Equation 2.3 gives the spherical aberration-limited resolution:

$$\delta \approx 0.43\lambda^{\frac{3}{4}} C_{\text{S}}{}^{\frac{1}{4}} \tag{2.4}$$

For example, according to Equation 1.5, for a typical uncorrected FEI Titan operating at 300 kV, with a C_s of 1.2 mm [27], the optimal C_s-limited resolution at 300 kV is hence approx. 1.3 Å.

While this resolution is sufficient in a number of cases, such as resolving the stacking faults of $TlGaSe_2$ in Chapter 3, in other cases, such as observing the rotational variants and anti-phase boundaries in $BaZrS_{(3-y)}Se_y$ in Chapter 5 and the moiré patterns of GaS/GaSe heterostructures in Chapter 4, sub-angstrom resolution is required.

In order to improve this, it is first important to understand not just the types of aberrations present, as mentioned above, but the different orders of aberrations also. To do this, it is important to consider the wave aberration function, χ. It is defined as the phase shift imparted on a perfect spherical beam arriving at the optic axis as a function of the angle to the optic axis, θ, and azimuthal angle around the optic axis, ϕ [19, 26, 28]:

$$\chi(\theta,\phi) = \frac{2\pi}{\lambda} \sum_{mn} \frac{\theta^{n+1}}{n+1} \left[C_{nm} cos(m\phi) + C_{nm} sin(m\phi) \right] \tag{2.5}$$

where C is the aberration coefficient, n is the radial order of the aberration, m is the azimuthal symmetry. Using the Krivanek notation [29], the first few orders of aberrations are summarised in Table 2.1. For example, defocus is given the notation of $C_{1,0}$ because it is a first order aberration that is symmetric about the optic axis, hence $m = 0$.

Aberration Coefficient	Name
$C_{0,1}$	Image Shift
$C_{1,0}$	Defocus
$C_{1,2}$	Two-Fold Astigmatism
$C_{2,1}$	Axial Coma
$C_{2,3}$	Three-Fold Astigmatism
$C_{3,0} = C_s$	Third-Order Spherical Aberration
$C_{3,2}$	Third-Order Two-Fold Astigmatism
$C_{3,4}$	Four-Fold Astigmatism
$C_{4,1}$	Fourth-Order Axial Coma
$C_{4,3}$	Fourth-Order Three-Fold Astigmatism
$C_{4,5}$	Five-Fold Astigmatism
$C_{5,0}$	Fifth-Order Spherical Aberration
$C_{5,2}$	Fifth-Order Star-Axial Aberration
$C_{5,4}$	Fifth-Order Rosette Aberration
$C_{5,6}$	Six-Fold Astigmatism

Table 2.1 Table of aberration coefficients using Krivanek notation, up to the fifth-order aberrations [19, 29]

These aberrations can be observed by imaging the Ronchigram of the converged probe, which is the disk of undiffracted electrons at the centre of the probe [30]. If there are no aberrations present, the disk would be featureless and "flat" and hence a large aperture can be inserted to use the whole disk to form the probe. As the Ronchigram image is in reciprocal space, this would imply an infinitely small probe. However, in the real world, perfect lenses do not exist and the aberrations of the lenses do add features, as seen in Figure 2.9. This in turn makes the size of the useable featureless area much smaller, which in turn makes the probe larger and hence limits the resolution.

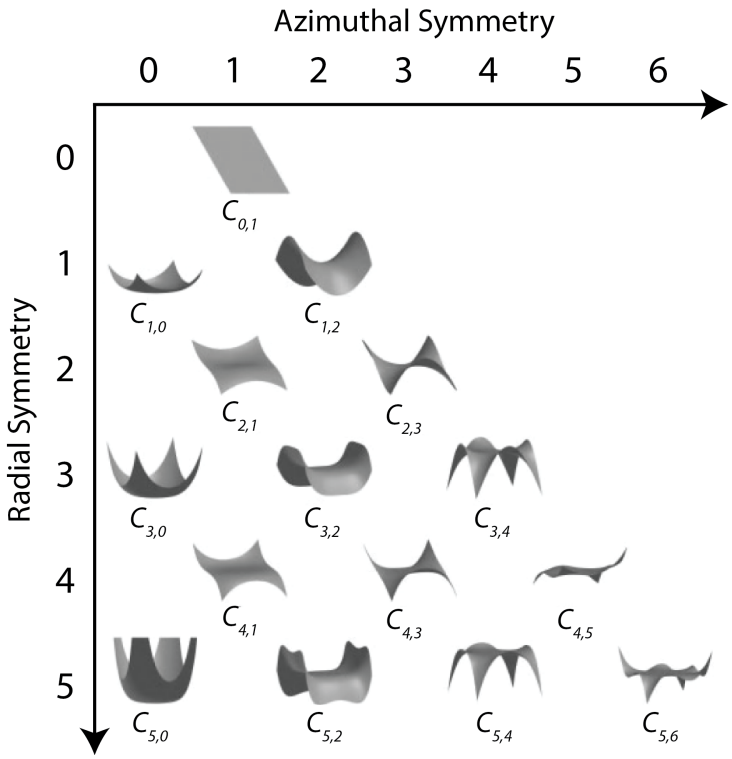

Fig. 2.9 Graphical representation of aberration coefficients, in Krivanek notation and described in Table 2.1, up to the fifth-order. Reproduced with permission from John Wiley and Sons [19].

A trained user can correct the lower order aberrations up to C_s using stigmator coils and beam tilt, such was the case of the FEI Titan in Chapter 3 and Chapter 4, but to correct C_s and the higher order aberrations, as was the case in Chapter 5 on the Thermo Fisher Themis Z and in Chapter 4 on the Nion UltraSTEM 200, the additional functionality of an aberration corrector is required. This is a series of hexapoles [31] or quadrapoles/octopoles [29] placed after the objective lens (to correct the image aberrations in the case of HRTEM) or before the objective lens (to correct the probe aberrations in the case of STEM) to induce a negative aberration to cancel out the aberrations present. Current commercial aberration corrector technology, as seen in the timeline in Figure 2.10, can correct up to and including 5th-order spherical aberrations, allowing for resolutions of sub 50 pm [32, 33] at a 300 kV accelerating voltage. Using advanced pixelated 4DSTEM detectors and post-processing via ptychography, resolutions of 23 pm were achieved approaching the atomic thermal fluctuation limits [34, 35]. However, such advanced techniques and detector technologies were outside the scope of this work.

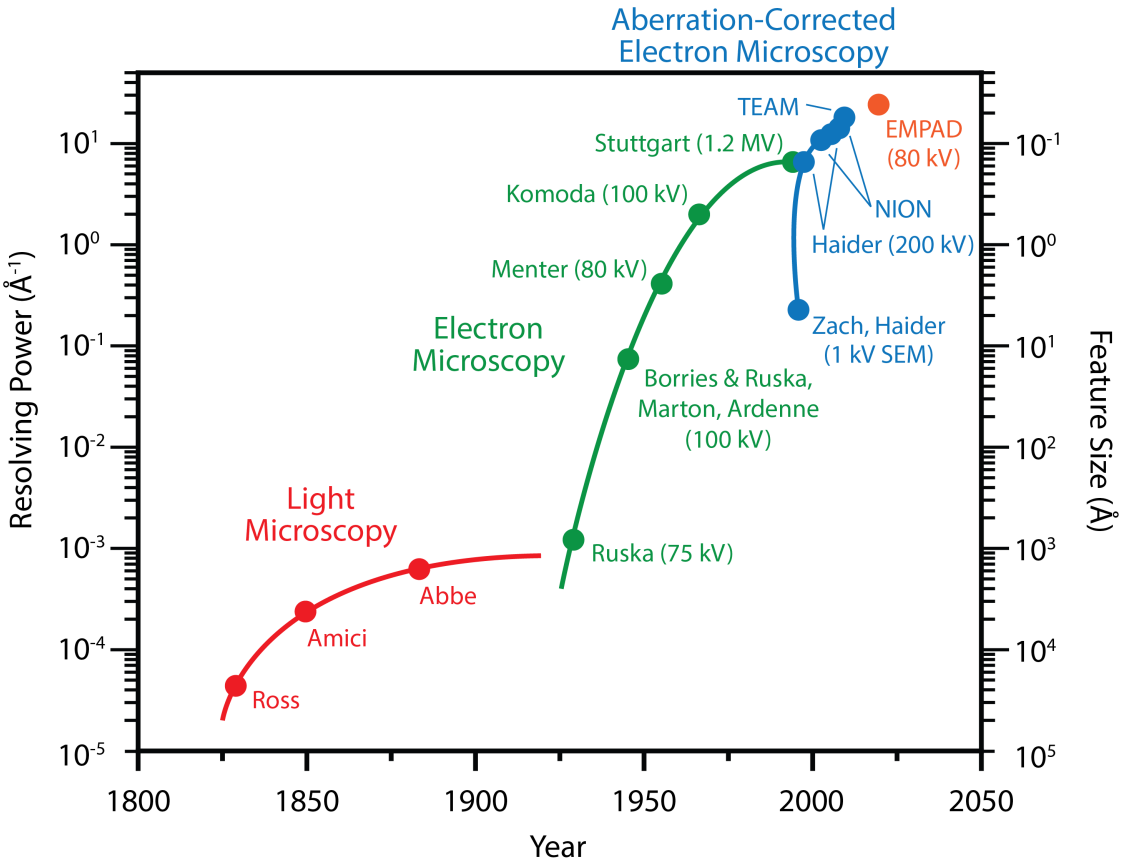

Fig. 2.10 Historical evolution of microscope resolving power, highlighting the different technological era: light, electron, aberration-corrected electron microscopy, and ptychography with the EMPAD pixelated detector [34, 35]. Reproduced with permission from Oxford University Press [36].

2.2.5 Convergence Beam Electron Diffraction (CBED) & Thickness Measurements

As the STEM probe rasters over a sample, not only can the scattered electrons be collected to form images, but the diffraction information from the scattered probe itself can be exploited to obtain additional information about the sample. This converged beam electron diffraction (CBED) pattern has a number of advantages compared to its parallel beam counterpart, selected area electron diffraction (SAED). The latter uses a parallel beam, hence has a fixed incident scattering **k** vector and covers a relatively large sample area (typically ~ 10 μm); the former, on the other hand, uses a converged probe, hence having access to a range of incident **k** vectors and covers much smaller areas (typically ~ 1 - 100 nm) [1]. This focused-probe method hence provides local structural information, such as characterisation of the unit cell of the material [37], strain [38], and charge density [39].

Using direct-electron detectors instead of a standard CCD/CMOS camera [35], the CBED pattern at every position of a STEM raster can be recorded into a large database. This method of recording the x- and y-positions in real-space along with the k_x- and k_y-positions in reciprocal space from the CBED patterns is known as "4D-STEM" [40]. Using this large dataset, one can place arbitrary detectors at any collected angle range, allowing the simultaneous recording and analysis of multiple signals, strain mapping over the whole sample [40], ptychography [34], etc. However, the datasets produced are routinely in the 100s of Gb, if not Tb, hence making data management and processing an additional computational burden to deal with.

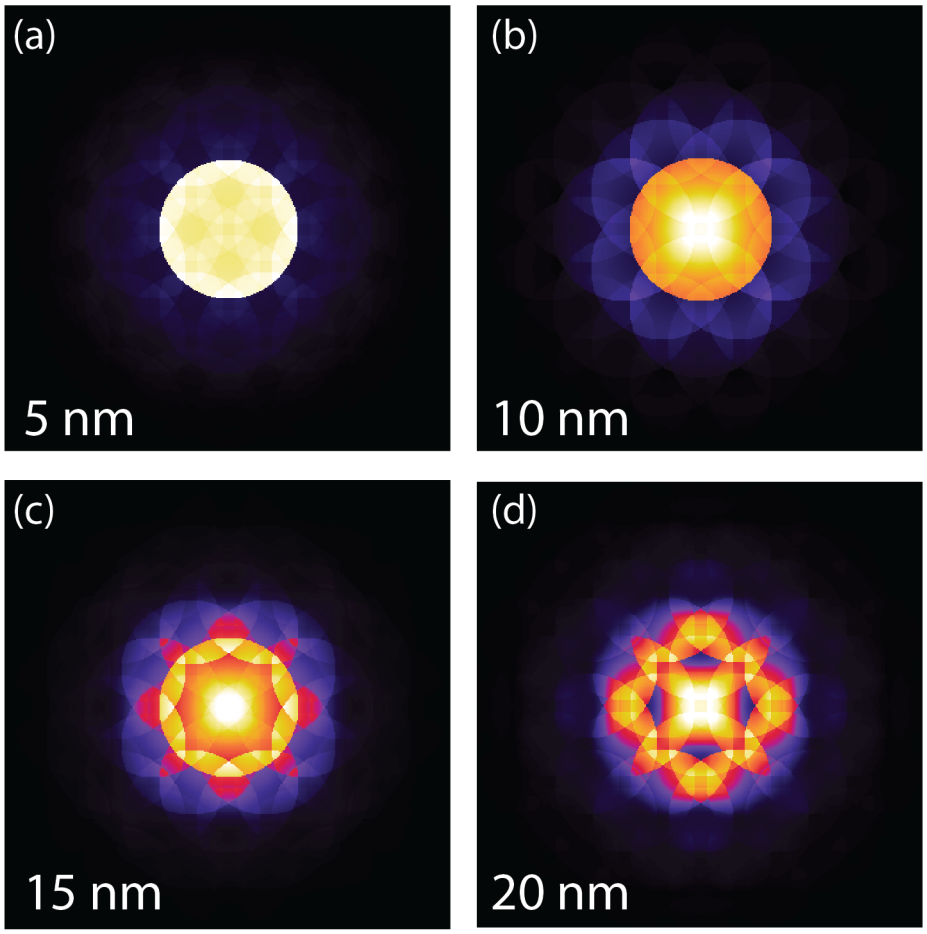

Fig. 2.11 Simulated PACBED patterns of $SrTiO_3$ along the [001] zone axis. The change in the patterns as the thickness increases from (a) 5 nm - (d) 20 nm allows one to measure the thickness of their samples in the TEM. Simulated using a modified version of MBFIT [41]

Thankfully, sample thickness measurements can be performed with CBED on any probe-forming TEM or STEM. Using CBED, instead of the commonly used log-ratio EELS method, for thickness measurements has several advantages. Notably, the inelastic mean free path is often not available for the material one is studying, and hence first needs to be

calculated empirically [42, 43]. EELS measurements require quite thin samples (typically < 50 nm) [44]. However at thinner regions (typically < 20 nm), the log-ratio method becomes highly sensitive to surface plasmons and contamination, hence obscuring results [44, 45]. The disadvantage of using CBED for thickness measurements is that it requires tilting the sample off the zone-axis to a two-beam CBED condition, using lower accelerating voltages, and smaller convergence semi-angles than typically used for atomic-resolution STEM [1, 46]. As a consequence, obtaining thickness measurements and atomic resolution imaging simultaneously is not feasible.

A solution to this is to use the position-averaged CBED (PACBED) method. By setting a large enough exposure on the camera and rastering over the region of interest, one can obtain an averaged CBED pattern which is insensitive to lens aberrations but is highly dependent on sample tilt and thickness, to within ± 10% [46–48]. For example in Figure 2.11, a thickness series of PACBEDs from $SrTiO_3$ is shown. The major benefit of this method is that the STEM imaging conditions do not need to be changed, hence allowing the recording of e.g. an atomic-resolution HAADF image and a PACBED simultaneously. One slight disadvantage is that this method requires comparing the experimental PACBED with simulated ones to determine the thickness. This is remedied by the fact that a full multislice calculation for each thickness is not required: any dynamical wave propagation method is sufficient, and so the Bloch wave method, as mentioned in Chapter 2.2.7, can be efficiently exploited to simulate PACBED patterns.

2.2.6 Spectroscopy & Spectral Imaging

The interaction of electrons with the sample in a TEM produces a wealth of signals from which chemical and defect information can be obtained. The two most common spectroscopic methods in TEM are energy dispersion X-ray spectroscopy (EDX) and electron energy loss spectroscopy (EELS). By using STEM instead of TEM, point-by-point imaging of a sample area can be performed to form a spectral image along with a (annular) BF/DF image of the sample, providing both chemical and structural information simultaneously.

EDX relies on the principle that the primary electrons from the beam can ionise electrons in the inner electronic shells of atoms, promoting the system to a higher energy level

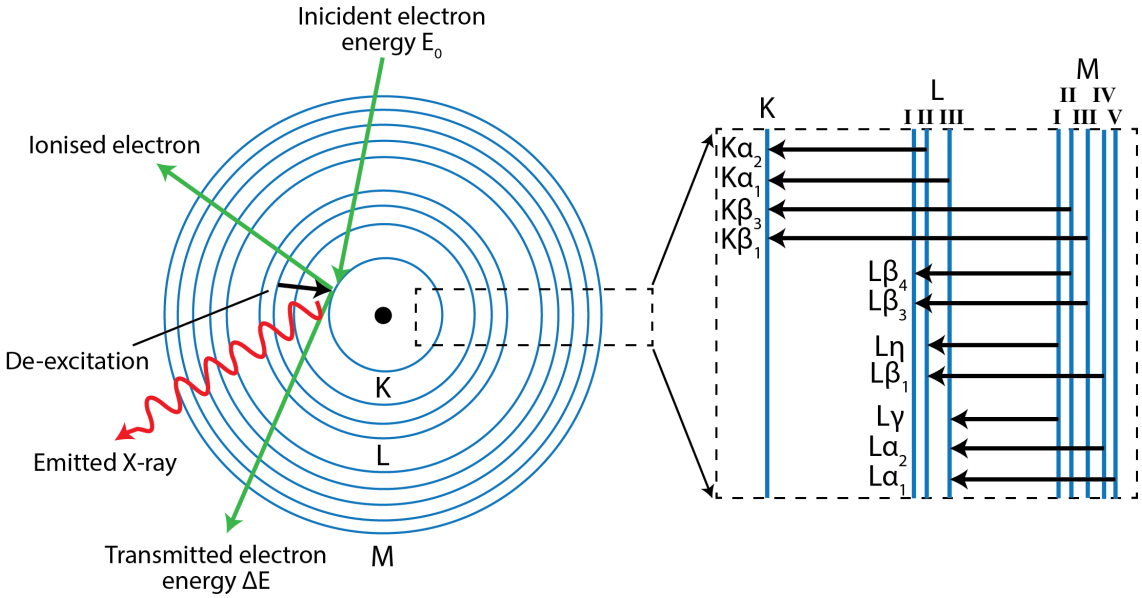

Fig. 2.12 Diagram of the X-ray emission mechanism of an atom from an incident electron. The ionisation of a K-shell electron results in the emission of a Kα X-ray when de-excitation occurs. Reproduced with permission from John Wiley and Sons [19].

and leaving behind a hole in that shell. As electrons from higher levels drop to fill the vacant hole and return the system to its ground state, the excess energy from this transition, equal to the energy difference of the levels, is often released in the form of a photon. This energy difference is often within the X-ray range and is characteristic of the atom, hence allowing for elemental characterisation.

To denote which shell has undergone ionisation, the nomenclature of *K*, *L*, *M*, *N*, etc. from the innermost shell outwards is used, with the subscripts' α, β, γ, etc., and 1, 2, 3, etc. to denote the transition, as seen in Figure 2.12. For example, in the case of $BaZrS_{(3-y)}Se_y$ in Chapter 5, if an electron from the K-shell of a barium atom is ionised and the hole left behind is filled by an electron from the higher energy *L*-shell, the energy difference is approx. 32 keV, which is emitted as a characteristic X-ray denoted as K_α [49].

This ability to detect the characteristic X-rays produced makes elemental identification trivial (for the most part). However, there are a number of limitations to EDX. For sufficiently robust samples such as $SrTiO_3$ and GaAs [50, 51], atomic resolution EDX mapping can now be routinely done, especially now with abberation-corrected systems [19, 52]. However, quantitative analysis is not as routine due to the complexing of elastic and thermal scattering, especially with thicker samples, which produces a highly non-linear response to the density of atoms located under the probe. This phenomenon is known as

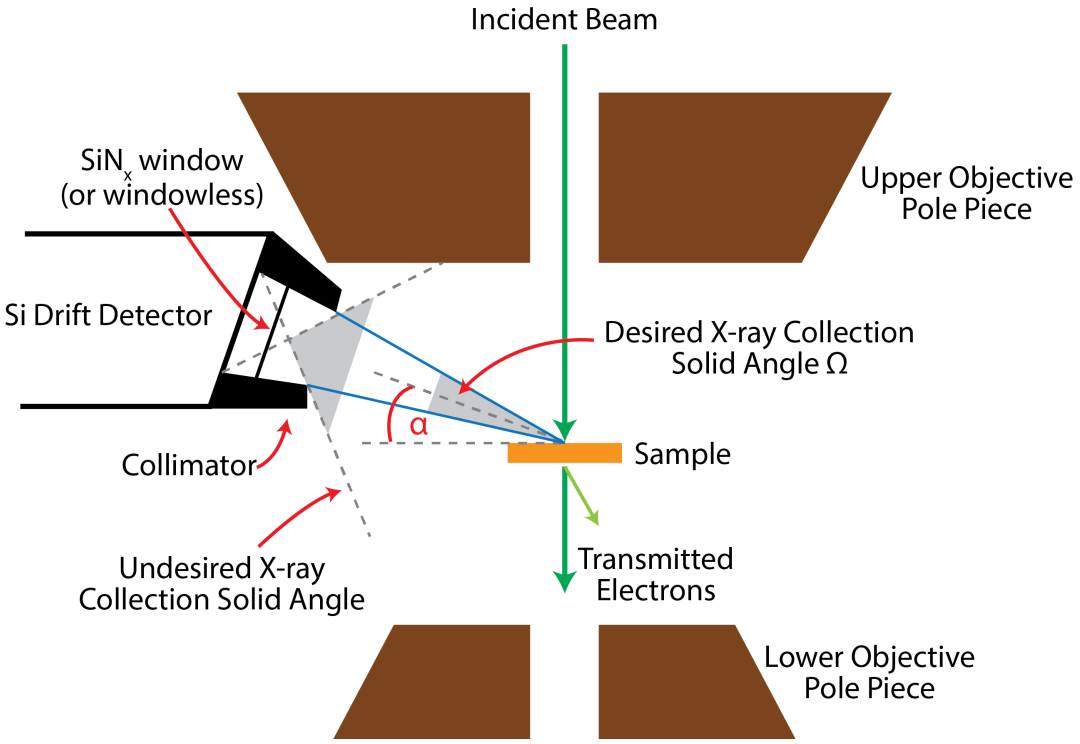

Fig. 2.13 Schematic of objective lens pole piece gap of a TEM with the EDX detector inserted. Here, a modern silicon drift detector is shown, as well as the collection solid angle, Ω, and the X-ray take-off angle, α, from the sample. Reproduced with permission from Springer Nature [1].

"electron channelling" and is typically alleviated by tilting the sample slightly to an off-axis position, at the cost of resolving clear atomic columns [53].

The detector geometry also limits the benefits of EDX. As shown in Figure 2.13, the detector is positioned as close to the sample stage as possible to collect as many X-rays as possible. However, only a certain percentage of X-rays will be collected by the detector. This makes reliably detecting lighter elements, such as N, difficult due to their relatively weak signals. This can be improved by the addition of multiple EDX detectors in order to increase the solid angle of collection [54]. However, for quantification of these lighter elements, a large beam current and long probe dwell times are still required to increase the signal-to-noise ratio, hence leading to potential sample damage [1, 52].

EELS can act as a complementary technique to help alleviate some of the issues with EDX. As the electron beam interacts with the inner shell electrons of an atomic species, not only does it promote an electron to a higher energy state, but the energy imparted to this transition is also equal to the energy loss of the impinging electron. Hence, this energy loss is characteristic of that element. These energy-loss electrons scatter at small angles

(approx. < 10 mrad), which can then be collected by a spectrometer at the end of the TEM column. This spectrometer separates the electrons according to their kinetic energies, as shown at the bottom of Figure 2.2, which produces a spectrum showing the number of electrons (i.e. the scattered intensity) as a function of their decrease in kinetic energy [44].

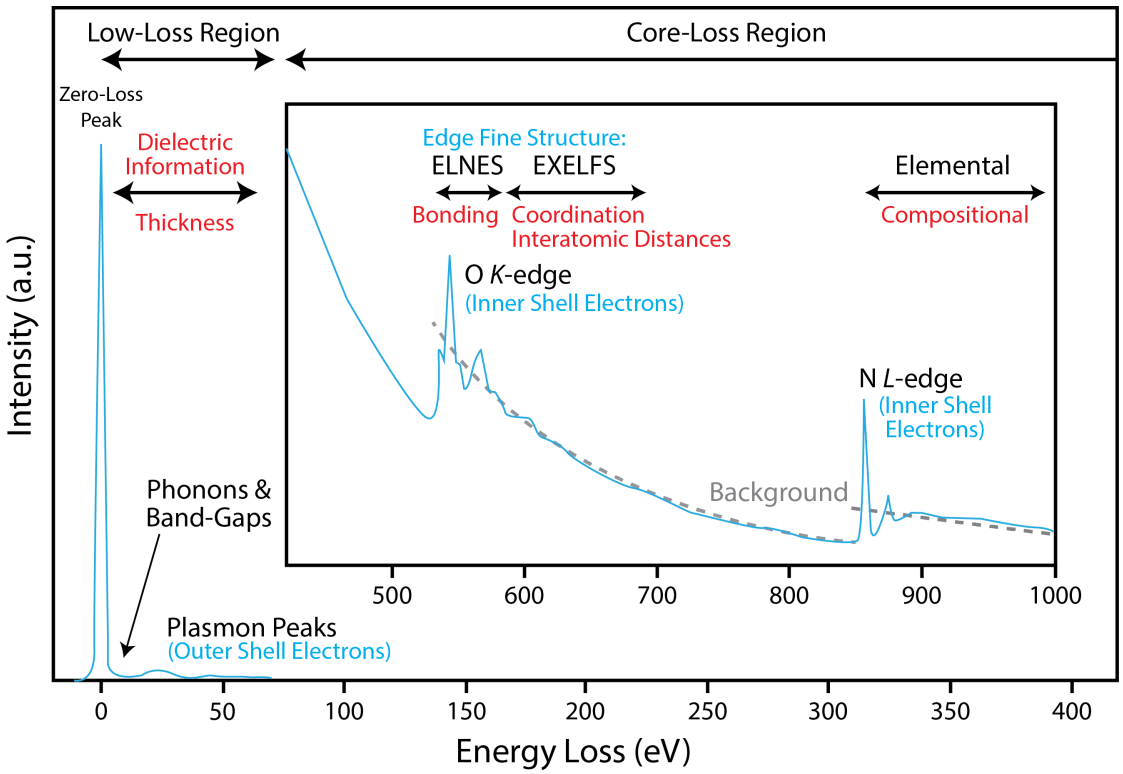

Fig. 2.14 Typical EELS spectrum of a sample, showing the zero-loss peak (ZLP), core-loss and low-loss regions. Various information which can be gathered from the spectrum is highlighted, such as energy loss near edge structure (ELNES) and extended energy loss fine structure (EXELFS). Insert y-axis scale is magnified 100x to highlight core-loss features. Adapted with courtesy from Peter Hadley, TU Graz [55].

Because of the collection of typically 20-50% of the energy loss electrons into the spectrometer, the signal from the characteristic edges from lighter elements, such as Li or B, is much stronger than that of X-rays detected from the EDX detector, which is typically less than 10% of the X-rays produced by the sample [44].

These characteristic "core loss" edges are not only signals that can be detected. The primary beam electrons can also scatter off the outer shell electrons. This scattering may involve multiple atoms, leading to an oscillation of the valence electron density known as a plasmon. These plasmon peaks are seen near the zero (energy) loss peak (ZLP) of the unscattered electrons. In semiconductors, not only are these plasmons present, but the valence band electrons can transition to the conduction band, resulting in a peak near the

ZLP that is at the same energy as the size of the material's band gap. However, often careful background subtraction and the use of a monochromator is required to reveal this weak signal. Furthermore, some commercial monochromators can achieve energy resolutions of approx. 5 meV, allowing for the measurements of phonon modes from planar defects and single atoms [56, 57]. These spectral features are summarised in Figure 2.14, however, these advanced methods are outside the scope of this work.

Much like EDX, EELS too has several limitations. A major limitation is in the range of energy loss that it can detect, as most commercial EELS spectrometer detectors can typically only detect up to approx. 3000 eV [58, 59]. This means while it can detect *K*-loss edges for many lighter elements and the *L*-loss edges up to some d-block elements, it will not be able to detect the high energy *K*-loss edges of heavier elements such as Au, Pt, etc. Some recent work has achieved detection of, for example, Ti *K*-loss edges at approx. 5000 eV using direct electron detectors [58, 60], but the ability to achieve the wide energy ranges of EDX is still currently out of reach.

EELS also has more stringent sample requirements than EDX. While in EDX samples can be approximately 100 nm thick and still be able to resolve atomic columns of different elements [50], for EELS a sample thickness of less than 50 nm is required due to plural scattering in the sample obscuring the loss edges. This adds further background that needs to be deconvolved from the spectrum in order to resolve the spectral edges [44].

In summary, both EDX and EELS provide complementary spectroscopic data and the use of both techniques is often required to fully characterise and quantify material properties. For example, in Chapter 5, EDX and EELS were used to measure and quantify the ratio of S to Se in the $BaZrS_{(3-y)}Se_y$ alloy systems. In Chapter 4, EDX was used to highlight the layers of the GaS/GaSe heterostructure and to highlight the contamination from the flake transfer process.

2.2.7 Bloch Wave & Multislice Simulations

As mentioned in Chapter 1.3, analysis of the data obtained from TEM is required to obtain features and to prevent misinterpretation. Oftentimes, this requires simulating the whole image to extract data or to confirm the structure of a novel system.

To begin with TEM simulations, some definitions are required. A crystalline material is thought of as a periodic array of positive atomic nuclei potential wells, while the electrons of the TEM beam are described by an electron wavefunction, $\psi(\mathbf{r})$, where $\mathbf{r} = (x, y, z)$. The challenge is how to calculate the change to the wavefunction from the surface plane to the exit plane of the sample, as from the exit wave, the image of the sample can be reconstructed.

In all elastic scattering TEM simulation methods, for the fast electrons along the optical axis, z, this evolution of the electron wavefunction is described by the Schrödinger equation, here shown in its time-independent form:

$$\left[-\frac{\hbar^2}{2m}\nabla^2 - eV(x,y,z)^2\right]\psi(\mathbf{r}) = E\psi(\mathbf{r}) \tag{2.6}$$

where $\hbar = \frac{h}{2\pi}$, h is Planck's constant, m is the relativistic mass of the electron, e is the charge of the electron, E is the kinetic energy of the electron and $-eV$ is the potential energy of the electron, where V is the potential of the atoms in the sample.

The two main methods of performing TEM simulations are Bloch wave calculations and the multislice method. The former expands the electron wavefunction as a sum of plane waves in a periodic potential, known as Bloch waves, which satisfy Equation 2.6 inside the sample:

$$\psi(\mathbf{r}) = \sum_j \alpha_j b_j(\mathbf{k}_j, \mathbf{r}) \tag{2.7}$$

where α_j is a weighting coefficient, $b(\boldsymbol{k}_j, \boldsymbol{r})$ are Bloch waves, and $\mathbf{k}_j$ are the scattering wave vectors.

For a perfect crystal, the Bloch waves have solutions with the same periodicity and symmetry as that of the crystalline lattice. Therefore, the Schrödinger equation in Equation 2.6 can be approximated by a set of linear equations. Then, the set of functions of Equation 2.7, known as a basis set, is calculated by computing the eigenvectors and eigenvalues for these linear equations up to some maximum scattering vector $\mathbf{k}_{max}$. Next, for each required initial condition, such as different STEM probe positions on the sample surface, the weighting coefficients, α_j, for each element of the Bloch wave basis set is calculated. Finally, the resulting electron wavefunction can be computed everywhere (including the

exit surface of the sample). This is a highly efficient method for small, highly-symmetric perfect crystals. However, for larger crystals, crystals with defects, and/or many probe positions, this method is extremely inefficient since the computational time scales with N^3, where N is the number of Bloch waves used in the basis set or the number of beams/probe positions [21, 61].

The more efficient and universal method of TEM simulations is the mulitslice method. Here, the sample is divided into many thin slices along the optical axis direction. Each slice is thin enough to be treated as a phase shift grating for the electron wavefunction due to the projected atomic potential of all the atoms in the slice. The diffracted beams are then propagated through free space to the next slice, and the process is repeated [21]. This is expressed in the following equation:

$$\psi_{n+1}(\mathbf{r}) = \left[\psi_n(\mathbf{r}) \otimes P_{n+1}(\mathbf{r})\right] q_{n+1}(\mathbf{r}) \tag{2.8}$$

where $P_{n+1}(\mathbf{r})$ is the propagation function, $q_{n+1}(\mathbf{r})$ is the phase grating, and $\otimes$ denotes a convolution. This method can be performed in a number of ways, e.g. in reciprocal space with the use of fast Fourier transforms (FFTs), and hence is much faster than the Bloch wave method for larger crystals. Using the FFT approach, the calculation speed greatly improves, with computer time scaling with $Nlog_2N$, where N is the number of Fourier components used. Another benefit of this method is that each slice is independent of all other slices, so both the slice thickness and propagation function may vary from one slice to another, allowing for the modelling of point defects, for example.

However, the multislice method can also be inefficient for very large scales, such as modelling whole nanoparticles, and hence the use of the recently developed PRISM algorithm may be of interest [61, 62], however, that is outside the scope of this work.

2.3 TEM Sample Preparation

There are a number of variables which can affect the data one obtains from the TEM, such as vibrational instabilities, stray electromagnetic fields, aberration correction, etc. Many of these variables can be corrected by, for example, proper TEM room design to cancel

the stray fields and vibrations [63, 64] and/or post-processing of data to remove sample drift, shearing [65, 66], etc. However, how the sample is prepared for TEM is also just as important, and different methods have both benefits and limitations. Herein, the different TEM sample preparation techniques that were used in this work are discussed.

2.3.1 Drop-Cast Method

The simplest method undertaken, as was the case in Chapter 3, was the drop-cast method [1]. As shown in Figure 2.15, the method proceeds as follows: the bulk crystal is crushed up into a fine powder with an agate mortar and pestle, where the crystal is sandwiched between sheets of filter paper to prevent contamination of and from the mortar. Next the powder is dispersed in a transfer medium such as water or isopropyl alcohol (IPA), depending on the sample. Next, the solution is ultrasonicated to further break down the samples into smaller and thinner pieces. Finally, the solution is dropped using a pipette onto a TEM grid, typically covered in a form of carbon film, be it lacey or holey carbon (PELCO NetMesh^{TM}, Ted Pella, Inc.). Alternatively, the powder can be finely sprinkled onto the grid, thus avoiding the use of a transfer medium.

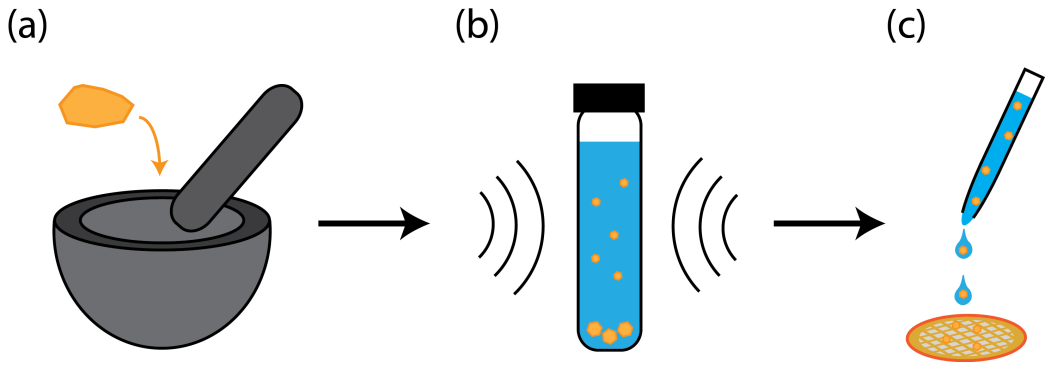

Fig. 2.15 Drop-cast method for TEM sample preparation. The sample material is crushed into a fine powder (a), then dispersed in a solvent and ultrasonicated to further thin and/or delaminate the sample (b). Finally, sample supernatant is placed onto a TEM grid with a carbon coating using a pipette (c).

The benefit of this method is its simplicity: without the use of expensive and/or specialized equipment, a TEM sample grid can be prepared in a matter of minutes. For layered van der Waals materials, liquid phase exfoliation of the layers is possible if the surface energy of the material is similar to that of the solvent [67–69]. Hence, plan-view TEM images of 2D materials can be routinely performed.

However, its simplicity is also its downfall; while many grids can be prepared in a matter of minutes, it may take hours to search each grid square for a suitably thin material at a required orientation to image. With an additional centrifugation step to size select the sample required, this variance in thickness can be minimised. However, once the sample has been drop-cast onto the grid, there is no further post-processing of the thickness of the flakes/fragments of the sample, unlike in other methods. There are also issues of hydrocarbon contamination from the solvents used, which require further baking or plasma cleaning to remove, and of mechanical stress on the sample, which may induce unwanted structural changes, such as defects or slip planes.

2.3.2 Mechanical Wedge Polishing

For more thickness and orientation control, the mechanical wedge polishing of Chapter 5 was used. As shown in Figure 2.16, the sample material is either placed onto or grown onto a substrate, such as Si, $SrTiO_2$, $LaAlO_3$, etc. and sectioned into small ~ 2 mm x 2 mm squares. These squares are glued such that the samples are sandwiched inwards facing each other.

The square sandwiches are now further sectioned into ~ 1 mm x 2 mm pieces and attached to the polishing arm of a polishing wheel. Using diamond lapping films of ever smaller grit size, the sample is polished until it is approximately 50 μm thick. Water or IPA is used as the lubricant, and the lapping films are continuously cleaned with lens wipes to remove any cutting residue from damaging the newly polished sample surface.

The polishing arm is then tilted, and a wedge is formed until Fresnel fringes at the tip of the wedge can be seen in an optical microscope. This indicates that the wedged area is typically < 1 μm thick. The wedging angle is dependent on the sample; smaller wedging angles of < 2° are desirable as more thin area is available to image and a smaller thickness gradient in the final lamella; on the other hand, it suffers the drawback of poorer structural integrity, and can not work well with more brittle substrates such as $LaAlO_3$ [70].

The lamella is then attached to a slotted TEM grid using epoxy, and placed into an ion milling machine to thin the lamella down to be electron transparent. Here, Ar ions are fired at the sample at a choice of angles and kV (typically 1 - 10 kV) to thin the sample

further and sputter away any amorphous material that may have built up over time, such as carbon residue [71].

While mechanical polishing is far more time-consuming than drop-casting, it provides far more control of the sample's orientation (especially for thin films grown on substrates) and thickness hence reducing the "needle in the haystack" approach of finding a suitable flake on a drop-cast TEM grid. However, this method also has a number of downsides. Firstly, it is quite wasteful, as many lens wipes, several diamond lapping films, and up to a litre or so of lubricant could be used to prepare a single lamella. Secondly, while the polishing wheel is relatively accessible to most, an ion mill can be prohibitively costly to many research groups. Finally, the method requires a significant amount of starting material, and hence may not be suitable in cases where sample material is scarce.

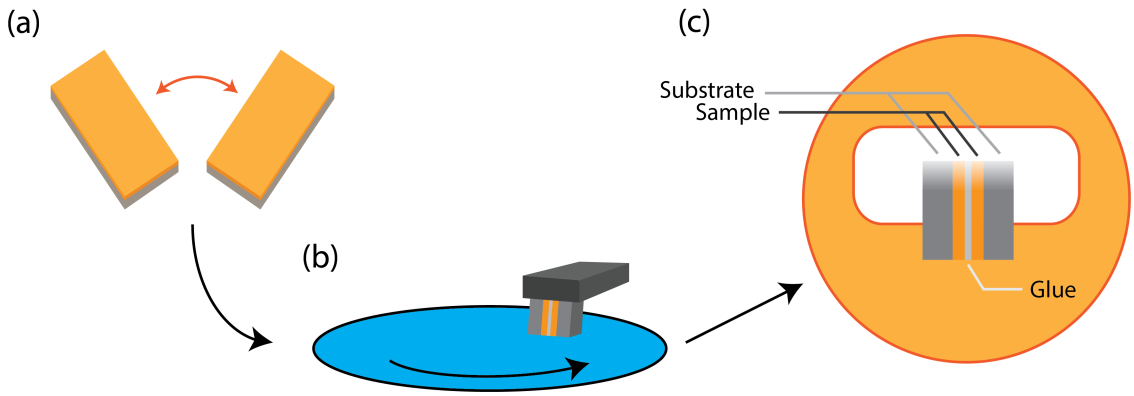

Fig. 2.16 Mechanical wedge polishing method for TEM sample preparation. The sample material is sectioned into small mm sized pieces and sandwiched together with an appropriate adhesive (a), then polished and wedged on a polishing wheel with diamond lapping films (b). The final TEM grid (before ion mill polishing) is shown in (c).

2.3.3 Focused Ion Beam (FIB) Milling

For cases where not much of the sample is available and/or the sample is sensitive, mechanical polishing might not be appropriate. In this situation, focused ion beam (FIB) milling may be a better option, as was the case in Chapter 4. In this situation, Ga^+ ions are accelerated and focused into a fine probe, with probe sizes of < 2.5 nm, allowing for precise sputtering of material. Coupled to the FIB system is often a scanning electron microscopy (SEM) electron column, allowing for simultaneous imaging and milling.

Here, as shown in Figure 2.17, the sample area of interest is first protected from milling by depositing a platinum protection layer on top. This is achieved by flowing a platinum

organometallic gas near the area of interest, then using the electron and ion beams to raster over the area to ionise the gas and deposit the Pt. Trenches are then milled on both sides of the area of interest, and an undercut is milled to expose the lamella. A tungsten micro-manipulator is then moved into view and welded onto the lamella with the platinum gas source. The other side of the lamella is then cut to free the lamella from the sample.

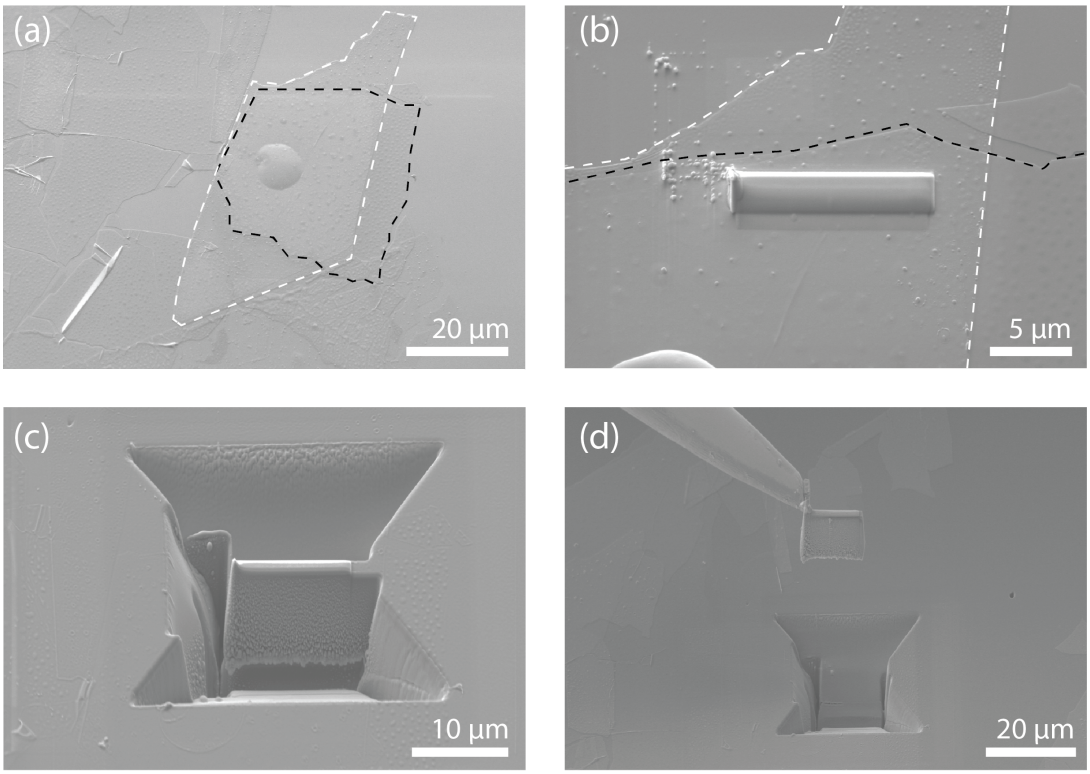

Fig. 2.17 SEM images of preparation of a cross-sectional TEM lamella for the GaSe/GaS van der Waals heterostructure in Chapter 4. The flake is located (a) and a Pt protection layer is deposited on the area of interest (b). Side trenches (c) are milled away with the Ga^+ ion beam of the FIB, then a tungsten needle (d) is attached to the lamella and is lifted out. It is then attached to a FIB grid post on a TEM grid and thinned until suitable for TEM imaging. The white dotted lines represent the top GaSe flake of the heterostructure, and the black dotted lines represent the bottom GaS flakes.

The lamella is then welded onto a post of a TEM grid, and the sides of the lamella are thinned with ever-decreasing kV and current. For example, for the heterostructure cross-sections in Chapter 4, 30 kV with 2 nA was used for trenching, and 240 pA, 120 pA, 50 pA and 20 pA currents for sample thinning. This is done to thin the sample while avoiding localised heating or Ga^+ ion implantation, which could affect the local microstructure by forming defects.

Finally, the grid is transferred to a Fischonne Nanomill, which is an Ar-source ion mill for final thinning. The Nanomill operates at lower accelerating voltages than that of a typical FIB, and Ar ions are lighter and hence have a much smaller scattering cross-section than that of Ga^+ ions. Therefore, the Nanomill is used to remove any surface damage and contamination caused by the FIB process [72].

FIB lamella preparation is a highly precise TEM sample preparation technique, which can provide high-quality samples of a desired orientation (unlike drop-casting) and even thickness across the lamella (unlike in mechanical wedge polishing). However, a typical FIB-SEM system can cost nearly as much as a typical TEM system and hence can be prohibitively expensive to most research groups and centres.

2.4 Density Functional Theory

As was mentioned in Chapter 1.4, by using electron densities and appropriate approximations for the exchange and correlation energies, one can use density functional theory (DFT) to simulate a variety of materials and chemical systems within reasonable computational times and resources. The fundamentals of DFT are briefly discussed (the author cannot stress enough the word "briefly") below to illustrate to the reader the strengths and limitations of this method and its use in this work.

2.4.1 Hohenberg-Kohn Theorems

Building on top of the Born-Oppenheimer and Hartree-Fock approximations, as mentioned in Chapter 1.4, the fundamentals of DFT were first established by Honhenberg and Kohn in the form of two theorems [73]:

> Theorem 1: It is impossible that two external potentials $V_{ext}(\boldsymbol{r})$ and $V'_{ext}(\boldsymbol{r})$, whose difference is not a constant, to give the same ground-state energy distribution $\rho(\mathbf{r})$

In other words, the ground-state energy density $\rho(\boldsymbol{r})$ uniquely determines the external potential, $V_{ext}(\boldsymbol{r})$. This in turn determines the many-body wavefunction, ψ, and the ground-

state energy, E_0. The non-constant condition for the external potential is there since adding a constant to the potential does not change the ground-state wavefunction or energy.

Theorem 1 implies that the ground-state energy can be expressed as:

$$E_0 = \int V_{ext}(\mathbf{r})\rho(\mathbf{r})d\mathbf{r} + F[\rho(\mathbf{r})] \tag{2.9}$$

where $F[\rho(\mathbf{r})]$ is a general functional of $\rho(\mathbf{r})$ representing the expectation value of the total kinetic and electron-electron interaction energies when the ground-state density is $\rho(\mathbf{r})$. This means specifying $\rho(\mathbf{r})$ uniquely determines $F[\rho(\mathbf{r})]$, and hence E_0.

The second theorem extends this definition further for a system of N electrons:

> Theorem 2: E_0 for a given $V_{ext}(\boldsymbol{r})$ is correctly obtained by minimising the functional $E_0[\rho(\mathbf{r})] = \int V_{ext}(\mathbf{r})\rho(\mathbf{r})d\mathbf{r} + F[\rho(\mathbf{r})]$ with respect to $\rho(\mathbf{r})$ for a fixed $V_{ext}(\boldsymbol{r})$ and fixed N. The minimised $\rho(\mathbf{r})$ gives the correct electronic density of the ground-state.

$F[\rho(\mathbf{r})]$ can therefore be expressed as the sum of the kinetic energy, Hartree energy (from Equation 1.14), exchange energy (from Equation 1.15) and correlation energy. The latter two energies can be expressed as one term known as the exchange-correlation energy E_{xc}, and hence the total energy of the ground-state can be expressed as:

$$E_0 = \int V_{ext}(\mathbf{r})\rho(\mathbf{r})d\mathbf{r} + T[\rho(\mathbf{r})] + E_H[\rho(\mathbf{r})] + E_{xc}[\rho(\mathbf{r})] \tag{2.10}$$

2.4.2 Kohn-Sham Equation

There are three important points to be made about Equation 2.10. Firstly, that while the Hohenberg-Kohn theorems show that the ground-state electronic density can be used to calculate the properties of the system, it does not actually show how to calculate the ground-state electronic density. Secondly, that $E_{xc}[\rho(\mathbf{r})]$ is simply the part of the total energy that is not accounted for by the other terms. Finally, $T[\rho(\mathbf{r})]$ is defined to be the kinetic energy of a system of non-interacting electrons having a density distribution $\rho(\mathbf{r})$, as described by Kohn and Sham [74].

Therefore, using these points, one can establish a method of calculating the ground-state energy. If the charge density for a system of N independent electrons can be calculated as:

$$\rho(\mathbf{r}) = \sum_{i=1}^{N} |\phi_i(\mathbf{r})|^2 \tag{2.11}$$

where $\phi_i(\mathbf{r})$ are the Kohn-Sham orbital wavefunctions. The kinetic energy (in Dirac notation) is then given by:

$$T[\rho(\mathbf{r})] = -\frac{\hbar^2}{2m} \sum_{i}^{N} \langle \phi_i | \nabla^2 | \phi_i \rangle \tag{2.12}$$

where m is the mass of the electrons. The Hartree energy can then be defined in terms of $\rho(\mathbf{r})$:

$$E_H = \frac{e^2}{4\pi\epsilon_0} \int\int \frac{1}{2} \frac{\rho(\mathbf{r})\rho(\mathbf{r}')}{|\mathbf{r}-\mathbf{r}'|} d\mathbf{r} d\mathbf{r}' \tag{2.13}$$

As such, the total energy can be written as:

$$E = \int V_{ext}(\mathbf{r})\rho(\mathbf{r}) d\mathbf{r} + T[\rho(\mathbf{r})] + G[\rho(\mathbf{r})] \tag{2.14}$$

where $G = E_H + E_{xc}$. As stated in Theorem 2, when Equation 2.14 is subject to the constraint of:

$$\int \rho(\mathbf{r}) d\mathbf{r} = N \tag{2.15}$$

the ground state energy can be calculated by minimising the total energy with respect to $\rho(\mathbf{r})$:

$$\frac{\delta E}{\delta \rho(\mathbf{r})} = \mu \tag{2.16}$$

where μ is the Lagrange undetermined multiplier (note to reader: do not worry, μ as it will disappear soon).

Equation 2.16 must be true for any arbitrary $\delta\rho(\mathbf{r})$ in order to satisfy Equation 2.15. Therefore, the ground-state condition is:

$$\frac{\delta T}{\delta \rho(\mathbf{r})} + \frac{\delta G}{\delta \rho(\mathbf{r})} + V_{ext}(\mathbf{r}) = \mu \tag{2.17}$$

An effective potential, $V_{eff}(\mathbf{r})$, can be defined to be the sum of $V_{ext}(\mathbf{r})$ and $\frac{\delta G}{\delta \rho(\mathbf{r})}$, hence:

$$\frac{\delta T}{\delta \rho(\mathbf{r})} + V_{eff}(\mathbf{r}) = \mu \tag{2.18}$$

However, for non-interacting electrons, E_H and E_{xc} vanish, leaving $G = 0$, and hence the minimum condition is left as:

$$\frac{\delta T}{\delta \rho(\mathbf{r})} + V_{ext}(\mathbf{r}) = \mu \tag{2.19}$$

Equation 2.19 shows that the ground-state density of an interacting system of electrons with effective potential $V_{eff}(\mathbf{r})$ is the same as the ground-state density of a non-interacting system of single particle electrons with an external potential $V_{ext}(\mathbf{r})$. Therefore, the ground-state density for the interacting electron system can be obtained by solving the Schrödinger equation for a non-interacting system:

$$\left[-\frac{\hbar^2}{2m}\nabla^2 + V_{eff}(\mathbf{r})\right]\phi_i(\mathbf{r}) = \epsilon_i \phi_i(\mathbf{r}) \tag{2.20}$$

where $V_{eff}(\mathbf{r}) = V_{ext}(\mathbf{r}) + V_H[\rho(\mathbf{r})] + V_{xc}[\rho(\mathbf{r})]$. Equation 2.20 is called the Kohn-Sham equation, and once solved, the electron density can then be calculated using Equation 2.11 [75].

2.4.3 Exchange-Correlation Energy, E_{xc}

It can be seen from Equation 2.20 that E_{xc} is the difference between the energy of the interacting many-body system and that of the independent particle system, with the electron-electron interaction replaced with E_H. The issue in solving the Kohn-Sham equation, and hence one of DFT's major limitations, is that the exact form of E_{xc} is not known. Therefore, suitable approximations must be used for it to obtain (reasonably) accurate results. Two of the most common types of approximations for this include the local density approximation (LDA), and the generalised gradient approximation (GGA) [76].

Local Density Approximation (LDA)

While $E_{xc}[\rho(\mathbf{r})]$ for the whole system is not known exactly, it is almost exactly known for a uniformed electron gas [74]. The exchange-correlation energy per electron as a function of density, $\epsilon^0_{xc}(\rho)$, does not depend on the position in a uniform electron gas. Therefore, it is reasonable to assume that for a non-uniform system where $\rho(\mathbf{r})$ does depend on position, at every point $\mathbf{r}$ there is exchange-correlation energy given by $\rho(\mathbf{r})\epsilon^0_{xc}(\rho(\mathbf{r}))$. Thus, E_{xc} can be expressed as:

$$E^{LDA}_{xc}[\rho(\mathbf{r})] = \int \rho(\mathbf{r})\epsilon^0_{xc}(\rho(\mathbf{r}))d\mathbf{r} \tag{2.21}$$

LDA works well for weakly correlated systems such as metals [74]. However, it is not appropriate in stronger correlated systems or ones with inhomogeneous electron densities, such as molecules or transition metal oxides [77].

General Gradient Approximation (GGA)

Another common approximation, GGA, follows on from LDA and tries to address its limitations. Rather than a purely local approximation, it is a semi-local approximation where the exchange-correlation energy is a functional of both the charge density and its gradient:

$$E^{GGA}_{xc}[\rho(\mathbf{r})] = \int \rho(\mathbf{r})\epsilon^{GGA}_{xc}(\rho(\mathbf{r}), |\nabla\rho(\mathbf{r})|)d\mathbf{r} \tag{2.22}$$

This general functional appears in many forms, with one of the most common forms being the Perdew-Burke-Ernzerhof (PBE) formulation [78]. It itself is based on the local spin density approximation of the system and only adds energetically significant corrections to the non-local gradient.

For systems where the density changes slowly, GGA is quite a good approximation to use. However, for systems with abrupt changes such as layered van der Waals materials, the systems are modelled less well and thus corrections may have to be used [79, 80], as is the case for the GaS/GaSe heterostructures in Chapter 4.

Hybrid Functionals

Both LDA- and GGA-based exchange-correlation functionals are heavily used throughout literature and can provide excellent structural relaxation at little computational cost. However, they struggle with calculating accurate electronic band structures and often underestimate the size of the band gap in semiconductors. Fortunately, these functionals can be "mixed" with a percentage of Hartree-Fock exchange energy, from Equation 1.15, to account for these underestimations of electronic properties. For example, the Heyd-Scuseria-Ernzerhof (HSE) functional uses a portion of the Hartree-Fock exchange energy for short-range interactions, while also using the PBE functional for long-range interactions as well as the correlation energy [81, 82].

This does considerably increase the computational cost and time of running these calculations, often requiring the use of a supercomputing cluster, as the Hartree-Fock part of the calculation scales with N^4, where N is the number of basis functions used to describe the system, rather than N^3 as is the case with PBE-GGA [83, 84]. As such, depending on the system under study, these hybrid functional calculations can take more than eight times longer than that of PBE calculations to complete [85]. However, in return for this added time cost is added accuracy. For example, for the bulk GaS calculations in Chapter 4, PBE calculations underestimated the experimental band gap by over 1 eV, while HSE06 calculations underestimated it by ~ 0.3 eV. If more accuracy is required then using different functionals or changing the amount of Hartree-Fock exchange is mixed into the functional, at the cost of more computational power. In this work, this was not required and the level of accuracy provided by HSE06 hybrid functionals was sufficient to characterise the electronic band structures of the chalcogenide systems.

2.4.4 Pseudopotentials & DFT Codes

The accuracy of a DFT calculation is not only determined by the functional used to express the exchange-correlation energy, but how one describes the charge densities in the first place. For example, one can describe every electron in each atom of the system, typically done in so-called "all-electron" DFT codes. While these are the most accurate descriptions of the electronic structures to be used in DFT, they are very computationally expensive,

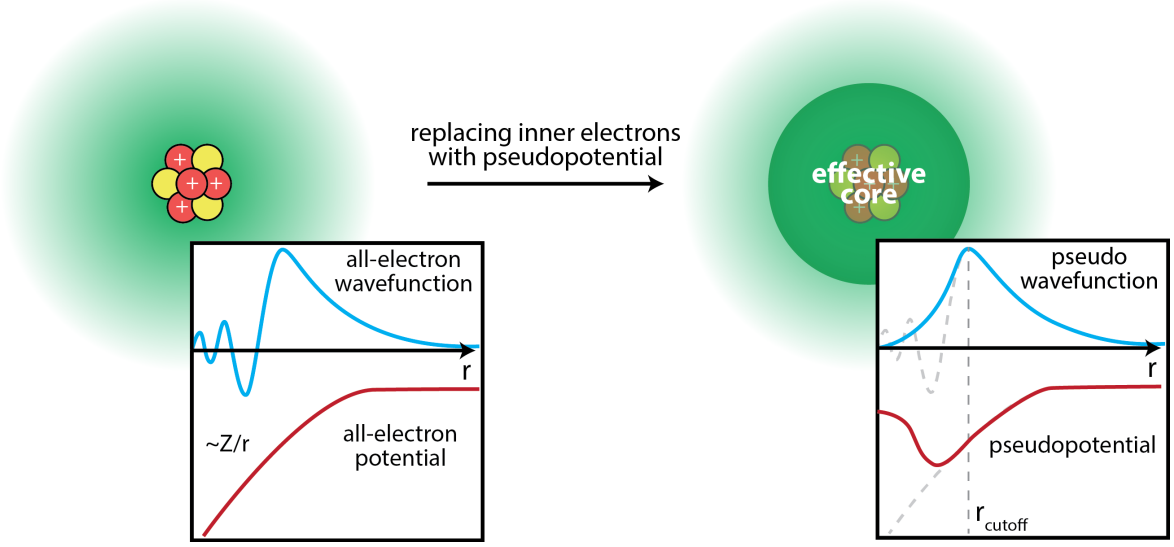

Fig. 2.18 Diagram of the pseudopotential method of representing the core-charge region of an atom with an effective core charge. This simplifies the electron wavefunction with a pseudo wavefunction, allowing for routine DFT calculations. Adapted from Edvin Fako, WikiMedia Commons, under a Creative Commons licence [87].

especially with larger systems. Therefore, in order to be able to run calculations in a reasonable timeframe, it is more efficient to describe the core electrons differently from the valence electrons. The core electrons do not contribute to chemical bonding directly and are far lower in energy than those of the valence electrons, hence describing them using a different basis allows for reduced computational complexity. These descriptions of the electron potentials are known as pseudopotentials [2, 86]. The repulsive core-region charge can be described up to a cut-off radius with a pseudopotential, with the rest of the electron wavefunction for the atom described by the valence electrons, as shown in Figure 2.18.

Pseudopotentials are used in all DFT calculations in this work, but not all pseudopotentials are the same, nor are the DFT codes used. For example, the *Vienna Ab-Initio Simulation Package* (VASP) code used in this work is based on the plane-wave basis formalism [88]. Here, the system under study is treated as periodic and is described with a Bloch wave basis set up to some cut-off, similar to the method in Chapter 2.2.7 for simulating TEM images. However, the electron wavefunctions are highly oscillatory near the nucleus, as seen in Figure 2.18, and hence would require very large basis sets and high sampling meshes to be able to accurately describe this. The use of pseudopotentials allows for a large reduction in the size of the basis required [86]. However, the use of a plane-wave

description of the basis also limits the size of the calculation, as the calculations scale with N^3, where N here is the number of atoms [89]. This is important to note as these types of codes are typically not suitable to calculate effects such as electron transport through a system, as was done Chapter 3, or aperiodic systems like molecules [90]. Strictly confined basis orbitals, which are set to zero beyond a certain radius, are used instead to achieve this. Codes such as the *Spanish Initiative for Electronic Simulations with Thousands of Atoms* (SIESTA) package used in Chapter 3 to calculate the electron transport properties of $TlGaSe_2$, use this method which allows for linear scaling of computational complexity, at the cost of some accuracy [90, 91].

2.4.5 Self-Consistency Calculations

The reader may be frustrated with reading so much theory up to this point (and the author also hopes that they can sympathise with him having to put all this into practice throughout this work). Therefore, to summarise, a typical DFT calculation cycle works in the following steps, which is also illustrated in the flowchart of Figure 2.19:

1. Assume an initial density $\rho_{\text{int}}(\mathbf{r})$
2. Use $\rho_{\text{int}}(\mathbf{r})$ to calculate V_H and V_{xc}, and hence V_{eff}
3. Solve the Kohn-Sham equation of Equation 2.20 to obtain Kohn-Sham orbitals ϕ_{i} and their energies ϵ_{i}
4. Calculate the output density $\rho_{\text{out}}(\mathbf{r})$ using Equation 2.11
5. Repeat 1-5 with $\rho_{\text{out}}(\mathbf{r})$ until self-consistency has approached i.e. until $\rho_{\text{int}}(\mathbf{r}) = \rho_{\text{out}}(\mathbf{r})$ to within a specific tolerance
6. Use the final self-consistent $\rho_{\text{out}}(\mathbf{r})$ to compute the ground-state energy E_0 and hence, other properties of the system under study

2.4.6 Limitations of DFT

Despite the merits of DFT, it is not a panacea and has several limitations. As hinted above, careful choice in exchange-correlation functionals and choice of pseudopotentials are key

and hence, convergence testing is required for each system under study [2]. For example, if one is studying van der Waals materials, then one needs to include corrections into the functional to account for the weak interlayer forces [79]. If there are transition metals or f-block elements in the system, then the careful choice of pseudopotentials which account for the spin and magnetisation from the unpaired electrons in the valence shells is critical [92]. Many modern functionals include more empirical corrections, which, while it helps to increase computational speed, undermines the *ab-initio* aspect of DFT [93].

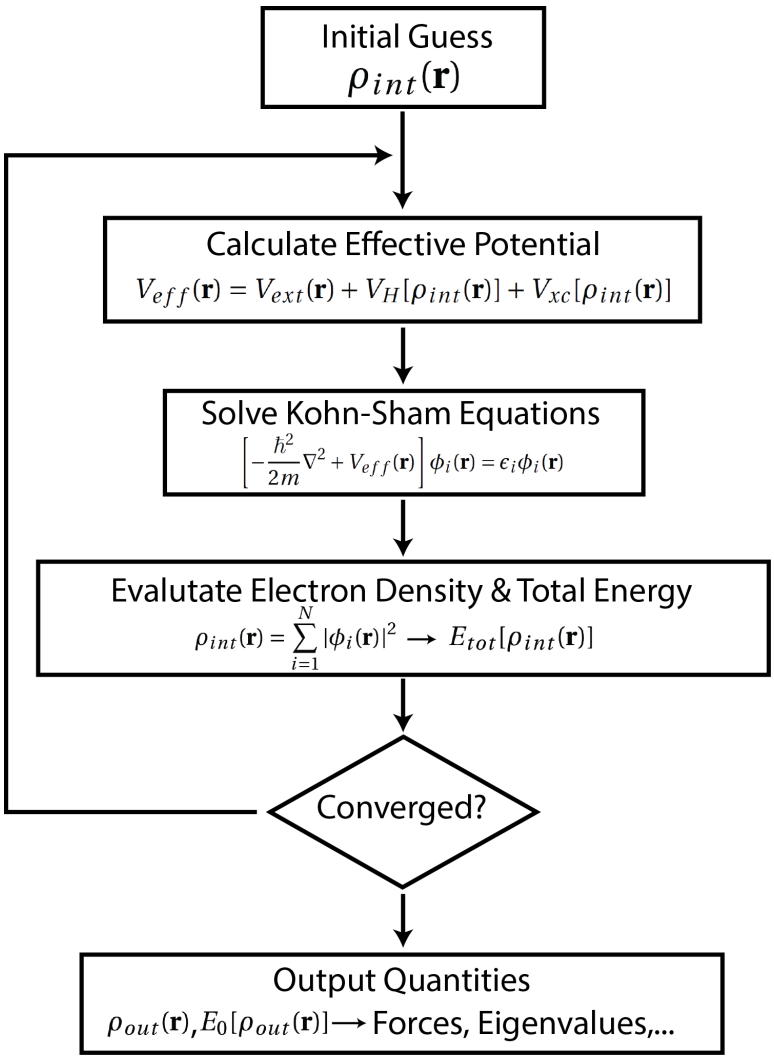

Fig. 2.19 Flowchart of a typical DFT self-consistency calculation. Reproduced with permission from Springer Nature [94].

DFT codes have no prior knowledge as to what the actual minimum energy state of a system should be; it simply tries to minimise the energy of the system to a point where the electron density is converged to within a set tolerance, as shown in Figure 2.19. As a result, the initial input structure may be converged into a local minimal in the potential energy

surface, rather than the true global minimum. Some recent codes try to mitigate this issue by performing a series of quick calculations to sample the full potential energy surface, and hence determine the true minimum [95]. Despite this, the lack of a priori confidence in the calculation is a fundamental constraint of DFT.

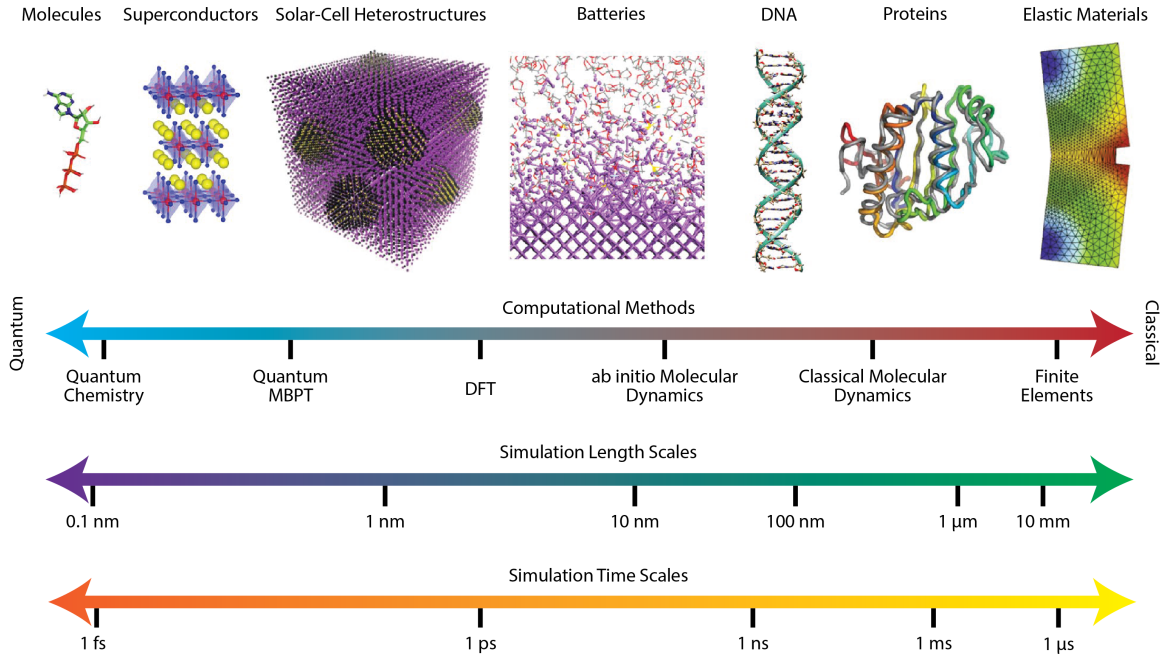

Fig. 2.20 Overview of different computational chemistry methods, with typical system sizes, length scales, and time scales shown. Reproduced with permission from Springer Nature [96].

Another limitation of DFT is that it has no input for environmental factors such as temperature. The calculations are performed under the assumption that the system is at 0 K, and hence, while one can find the true converged ground state energy of the system using the above technique, it may not be a thermodynamically stable structure at room temperature [2]. Using statistical mechanics and time-dependent DFT, this can be achieved via ensembles but at an extremely high computational cost and at extremely short time scales, typically less than 1 ns [97], as seen in Figure 2.20. Hence, many simulations which study diffusion or run at temperatures above 0 K are performed by adding more classical mechanics via molecular dynamics [98].

Ultimately, the size and accuracy of a DFT calculation is determined by the size of the computer you have access to (and the patience one has to debug all the errors). DFT is used throughout this work to calculate several material properties of the various chalcogenide systems under study, such as band gaps, electron transport and phonon dispersions.

However, the limitations of DFT are also noted throughout, often the limitation being that the systems under study are far too large for the DFT codes and the supercomputing cluster to handle.

References

[1] David B. Williams and C. Barry Carter. *Transmission electron microscopy: A textbook for materials science*. 2009, pp. 1–760. ISBN: 9780387765006. DOI: 10.1007/978-0-387-76501-3.

[2] David S. Sholl and Janice A. Steckel. *Density Functional Theory*. Hoboken, NJ, USA: John Wiley & Sons, Inc., 2009, pp. 1–235. ISBN: 9780470447710. DOI: 10.1002/9780470447710.

[3] Wei Liu et al. "Crystallographic, magnetic and electronic structures of a new layered ferromagnetic compound Cr2Ge2Te6". In: *Journal of Physics: Condensed Matter* 7.1 (1995), p. 69. ISSN: 0953-8984. DOI: 10.1088/0953-8984/7/1/008.

[4] M. Benabdeslem et al. "Diffusion of Zn in CuInSe2 bulk crystals". In: *Journal of Crystal Growth* 274.1-2 (2005), pp. 144–148. ISSN: 0022-0248. DOI: 10.1016/J.JCRYSGRO.2004.09.085.

[5] Shu Min Tan et al. "Electrochemistry of layered GaSe and GeS: applications to ORR, OER and HER". In: *Physical Chemistry Chemical Physics* 18.3 (2016), pp. 1699–1711. ISSN: 1463-9084. DOI: 10.1039/C5CP06682D.

[6] R. K. Crouch, W. J. Debnam, and R. Ryan. "Vacuum tight quartz ampoule for bridgman growth of crystals with interface demarcation". In: *Journal of Crystal Growth* 56.1 (1982), pp. 215–216. ISSN: 0022-0248. DOI: 10.1016/0022-0248(82)90031-8.

[7] Zdeněk Sofer. *Personal Communcation*. 2020.

[8] *GaSe Crystal | 2D Semiconductors*.

[9] *GaS Crystal | 2D Semiconductors*.

[10] Peter Capper. “Bulk Crystal Growth – Methods and Materials”. In: *Springer Handbook of Electronic and Photonic Materials*. Boston, MA: Springer US, 2006, pp. 231–254. DOI: 10.1007/978-0-387-29185-7_12.

[11] John Orton and Tom Foxon. *Molecular Beam Epitaxy: A Short History*. Oxford University Press, 2015. ISBN: 9780191748844. DOI: 10.1093/ACPROF:OSO/9780199695829.001.0001.

[12] S. S. Ang. “Electrical characteristics of epitaxial pn junction diodes fabricated on germanium-boron-doped silicon”. In: *Journal of Applied Physics* 78.2 (1995), pp. 1322–1326. ISSN: 0021-8979. DOI: 10.1063/1.360305.

[13] Mark Fox and Radu Ispasoiu. “Quantum Wells, Superlattices, and Band-Gap Engineering”. In: *Springer Handbook of Electronic and Photonic Materials*. Boston, MA: Springer US, 2006, pp. 1021–1040. DOI: 10.1007/978-0-387-29185-7_42.

[14] Kumar Shubham and Ankaj Gupta. *Integrated Circuit Fabrication*. CRC Press, 2021. ISBN: 9781003178583. DOI: 10.1201/9781003178583.

[15] William Nunn, Tristan K. Truttmann, and Bharat Jalan. “A review of molecular-beam epitaxy of wide bandgap complex oxide semiconductors”. In: *Journal of Materials Research* 36.23 (2021), pp. 4846–4864. ISSN: 20445326. DOI: 10.1557/s43578-021-00377-1.

[16] Ayahiko Ichimiya and Philip I. Cohen. *Reflection High-Energy Electron Diffraction*. Cambridge University Press, 2004. DOI: 10.1017/CBO9780511735097.

[17] Navneet Kumar et al. “Growth Inhibition to Enhance Conformal Coverage in Thin Film Chemical Vapor Deposition”. In: *Journal of the American Chemical Society* 130.52 (2008), pp. 17660–17661. ISSN: 0002-7863. DOI: 10.1021/ja807802r.

[18] M. Aliofkhazraei and N. Ali. “Fabrication of Micro/Nanostructured Coatings by CVD Techniques”. In: *Comprehensive Materials Processing* 7 (2014), pp. 85–117. DOI: 10.1016/B978-0-08-096532-1.00706-8.

[19] Rik Brydson, ed. *Aberration-Corrected Analytical Transmission Electron Microscopy*. Wiley, 2011, p. 280. ISBN: 978-1-119-97990-6.

[20] John C. H. Spence. *High-Resolution Electron Microscopy*. Fourth Edi. Vol. 8. 9. Oxford University Press, 2013. ISBN: 9780199668632. DOI: 10.1093/acprof:oso/9780199668632.001.0001.

[21] Earl J. Kirkland. *Advanced Computing in Electron Microscopy*. July. Boston, MA: Springer US, 2010, pp. 1–23. ISBN: 978-1-4419-6532-5. DOI: 10.1007/978-1-4419-6533-2.

[22] Max T. Otten. "High-Angle annular dark-field imaging on a tem/stem system". In: *Journal of Electron Microscopy Technique* 17.2 (1991), pp. 221–230. ISSN: 0741-0581. DOI: 10.1002/jemt.1060170209.

[23] P. Hartel, H. Rose, and C. Dinges. "Conditions and reasons for incoherent imaging in STEM". In: *Ultramicroscopy* 63.2 (1996), pp. 93–114. ISSN: 03043991. DOI: 10.1016/0304-3991(96)00020-4.

[24] Ondrej L. Krivanek et al. "Atom-by-atom structural and chemical analysis by annular dark-field electron microscopy". In: *Nature* 464.7288 (2010), pp. 571–574. ISSN: 00280836. DOI: 10.1038/nature08879.

[25] Michael M.J. Treacy. "Z Dependence of Electron Scattering by Single Atoms into Annular Dark-Field Detectors". In: *Microscopy and Microanalysis* 17.6 (2011), pp. 847–858. ISSN: 1431-9276. DOI: 10.1017/S1431927611012074.

[26] S. J. Pennycook et al. "Scanning transmission electron microscopy for nanostructure characterization". In: *Scanning Microscopy for Nanotechnology: Techniques and Applications*. Springer New York, 2007, pp. 152–191. ISBN: 0387333258. DOI: 10.1007/978-0-387-39620-0_6.

[27] J. M. LeBeau et al. "New Approach to Quantitative ADF STEM". In: *EMC 2008 14th European Microscopy Congress 1–5 September 2008, Aachen, Germany*. Springer Berlin Heidelberg, 2009, pp. 129–130. DOI: 10.1007/978-3-540-85156-1_65.

[28] Earl J. Kirkland. "On the optimum probe in aberration corrected ADF-STEM". In: *Ultramicroscopy* 111.11 (2011), pp. 1523–1530. ISSN: 03043991. DOI: 10.1016/j.ultramic.2011.09.002.

[29] O. L. Krivanek, N. Dellby, and A. R. Lupini. “Towards sub-Å electron beams”. In: *Ultramicroscopy* 78.1-4 (1999), pp. 1–11. ISSN: 03043991. DOI: 10.1016/S0304-3991(99)00013-3.

[30] J. A. Lin and J. M. Cowley. “Calibration of the operating parameters for an HB5 STEM instrument”. In: *Ultramicroscopy* 19.1 (1986), pp. 31–42. ISSN: 03043991. DOI: 10.1016/0304-3991(86)90005-7.

[31] Max Haider et al. “A spherical-aberration-corrected 200 kV transmission electron microscope”. In: *Ultramicroscopy* 75.1 (1998), pp. 53–60. ISSN: 03043991. DOI: 10.1016/S0304-3991(98)00048-5.

[32] Rolf Erni et al. “Atomic-Resolution Imaging with a Sub-50-pm Electron Probe”. In: *Physical Review Letters* (2009). ISSN: 0031-9007. DOI: 10.1103/PhysRevLett.102.096101.

[33] Shigeyuki Morishita et al. “Attainment of 40.5 pm spatial resolution using 300 kV scanning transmission electron microscope equipped with fifth-order aberration corrector”. In: *Microscopy* 67.1 (2018), pp. 46–50. ISSN: 20505701. DOI: 10.1093/jmicro/dfx122.

[34] Zhen Chen et al. “Electron ptychography achieves atomic-resolution limits set by lattice vibrations”. In: *Science* 372.6544 (2021), pp. 826–831. ISSN: 0036-8075. DOI: 10.1126/science.abg2533.

[35] Hugh T. Philipp et al. “Very-High Dynamic Range, 10,000 Frames/Second Pixel Array Detector for Electron Microscopy”. In: *Microscopy and Microanalysis* 28.2 (2022), pp. 425–440. ISSN: 1431-9276. DOI: 10.1017/S1431927622000174. arXiv: 2111.05889.

[36] Harald H. Rose. “Historical aspects of aberration correction”. In: *Journal of Electron Microscopy* 58.3 (2009), pp. 77–85. ISSN: 0022-0744. DOI: 10.1093/JMICRO/DFP012.

[37] A. G. Jackson. “Identification of the Laue zone number in hcp systems in convergent beam electron diffraction”. In: *Ultramicroscopy* 32.2 (1990), pp. 181–182. ISSN: 0304-3991. DOI: 10.1016/0304-3991(90)90036-L.

[38] Valerie Randle, Ian Barker, and Brian Ralph. “Measurement of lattice parameter and strain using convergent beam electron diffraction”. In: *Journal of Electron Microscopy Technique* 13.1 (1989), pp. 51–65. ISSN: 1553-0817. DOI: 10.1002/JEMT.1060130108.

[39] J. M. Zuo et al. “Direct observation of d-orbital holes and Cu-Cu bonding in Cu2O”. In: *Nature 1999 401:6748* 401.6748 (1999), pp. 49–52. ISSN: 1476-4687. DOI: 10.1038/43403.

[40] Colin Ophus. “Four-Dimensional Scanning Transmission Electron Microscopy (4D-STEM): From Scanning Nanodiffraction to Ptychography and Beyond”. In: *Microscopy and Microanalysis* 2019 (2019), pp. 563–582. ISSN: 14358115. DOI: 10.1017/S1431927619000497.

[41] Yoichiro Ogata et al. “Refinement of the crystal structural parameters of the intermediate phase of h-BaTiO 3 using convergent-beam electron diffraction”. In: *Acta Crystallographica Section A Foundations of Crystallography* 60.6 (2004), pp. 525–531. ISSN: 0108-7673. DOI: 10.1107/S0108767304016307.

[42] Alan J. Craven et al. “Accurate measurement of absolute experimental inelastic mean free paths and EELS differential cross-sections”. In: *Ultramicroscopy* 170 (2016), pp. 113–127. ISSN: 0304-3991. DOI: 10.1016/J.ULTRAMIC.2016.08.012.

[43] Keiichiro Oh-ishi and Tetsu Ohsuna. “Inelastic mean free path measurement by STEM-EELS technique using needle-shaped specimen”. In: *Ultramicroscopy* 212 (2020), p. 112955. ISSN: 0304-3991. DOI: 10.1016/J.ULTRAMIC.2020.112955.

[44] R.F. Egerton. *Electron Energy-Loss Spectroscopy in the Electron Microscope*. Boston, MA: Springer US, 2011. ISBN: 978-1-4419-9582-7. DOI: 10.1007/978-1-4419-9583-4.

[45] T. Malis, S. C. Cheng, and R. F. Egerton. “EELS log-ratio technique for specimen-thickness measurement in the TEM”. In: *Journal of Electron Microscopy Technique* 8.2 (1988), pp. 193–200. ISSN: 1553-0817. DOI: 10.1002/JEMT.1060080206.

[46] James M. LeBeau et al. “Position averaged convergent beam electron diffraction: Theory and applications”. In: *Ultramicroscopy* 110.2 (2010), pp. 118–125. ISSN: 03043991. DOI: 10.1016/j.ultramic.2009.10.001.

[47] James M. LeBeau et al. “High-angle scattering of fast electrons from crystals containing heavy elements: Simulation and experiment”. In: *Physical Review B* 79.21 (2009), p. 214110. ISSN: 1098-0121. DOI: 10.1103/PhysRevB.79.214110.

[48] J. A. Pollock et al. “Accuracy and precision of thickness determination from position-averaged convergent beam electron diffraction patterns using a single-parameter metric”. In: *Ultramicroscopy* 181 (2017), pp. 86–96. ISSN: 0304-3991. DOI: 10.1016/J.ULTRAMIC.2017.05.001.

[49] Günter Zschornack. *Handbook of X-Ray Data*. Berlin, Heidelberg: Springer Berlin Heidelberg, 2006, pp. 1–969. ISBN: 978-3-540-28618-9. DOI: 10.1007/978-3-540-28619-6.

[50] A. J. D’Alfonso et al. “Atomic-resolution chemical mapping using energy-dispersive x-ray spectroscopy”. In: *Physical Review B - Condensed Matter and Materials Physics* 81.10 (2010), pp. 2–5. ISSN: 10980121. DOI: 10.1103/PhysRevB.81.100101.

[51] Leslie J. Allen et al. “Chemical mapping at atomic resolution using energy-dispersive x-ray spectroscopy”. In: *MRS Bulletin* 37.1 (2012), pp. 47–52. ISSN: 0883-7694. DOI: 10.1557/mrs.2011.331.

[52] Stephen J. Pennycook and Peter D. Nellist. *Scanning Transmission Electron Microscopy*. Ed. by Stephen J. Pennycook and Peter D. Nellist. New York, NY: Springer New York, 2011, p. 282. ISBN: 978-1-4419-7199-9. DOI: 10.1007/978-1-4419-7200-2.

[53] NR Lugg et al. “What Does Quantitative Mean In Atomic-Resolution EDS STEM?” In: *Microscopy and Microanalysis* 21.S3 (2015), pp. 1075–1076. ISSN: 1431-9276. DOI: 10.1017/S1431927615006169.

[54] Nestor J. Zaluzec. “Quantitative Assessment and Measurement of X-ray Detector Performance and Solid Angle in the Analytical Electron Microscope”. In: *Microscopy and Microanalysis* 28.1 (2022), pp. 83–95. ISSN: 14358115. DOI: 10.1017/S143192762101360X.

[55] *Electron Energy Loss Spectroscopy - EELS - http://lampx.tugraz.at/ hadley/ss2/ quasiparticles/eels/eels.php*. (accessed 2023-10-15).

[56] Xingxu Yan et al. “Single-defect phonons imaged by electron microscopy”. In: *Nature* 589.7840 (2021), pp. 65–69. ISSN: 1476-4687. DOI: 10.1038/s41586-020-03049-y.

[57] Mingquan Xu et al. “Single-atom vibrational spectroscopy with chemical-bonding sensitivity”. In: *Nature Materials* 22.May (2023). ISSN: 1476-1122. DOI: 10.1038/s41563-023-01500-9.

[58] Ian MacLaren et al. “EELS at very high energy losses”. In: *Microscopy* 67.September 2017 (2018), pp. i78–i85. ISSN: 20505701. DOI: 10.1093/jmicro/dfx036.

[59] Gatan Inc. *GIF Continuum and Continuum S Advanced Systems for EELS & EFTEM - datasheet*. 2020.

[60] Masashi Watanabe et al. “Development of a High Electron Energy-loss Spectrometry System for Advanced Scanning Transmission Electron Microscopy”. In: *Microscopy and Microanalysis* 28.S1 (2022), pp. 2644–2647. ISSN: 1431-9276. DOI: 10.1017/s1431927622010029.

[61] Colin Ophus. “A fast image simulation algorithm for scanning transmission electron microscopy”. In: *Advanced Structural and Chemical Imaging* 3.1 (2017), pp. 1–11. ISSN: 21980926. DOI: 10.1186/s40679-017-0046-1. arXiv: 1702.01904.

[62] Luis Rangel DaCosta et al. “Prismatic 2.0 - Simulation software for scanning and high resolution transmission electron microscopy (STEM and HRTEM)”. In: *Micron* 151.August (2021), p. 103141. ISSN: 09684328. DOI: 10.1016/j.micron.2021.103141.

[63] A. Muller and J. Grazul. “Optimizing the environment for sub-0.2 nm scanning transmission electron microscopy”. In: *Journal of Electron Microscopy* 50.3 (2001), pp. 219–226. ISSN: 00220744. DOI: 10.1093/jmicro/50.3.219.

[64] David A. Muller et al. “Room design for high-performance electron microscopy”. In: *Ultramicroscopy* 106.11-12 SPEC. ISS. (2006), pp. 1033–1040. ISSN: 03043991. DOI: 10.1016/j.ultramic.2006.04.017.

[65] Xiahan Sang and James M. LeBeau. “Revolving scanning transmission electron microscopy: Correcting sample drift distortion without prior knowledge”. In: *Ultramicroscopy* 138 (2014), pp. 28–35. ISSN: 18792723. DOI: 10.1016/j.ultramic.2013.12.004.

[66] Lewys Jones et al. “Smart Align-a new tool for robust non-rigid registration of scanning microscope data”. In: *Advanced Structural and Chemical Imaging* 1.1 (2015), pp. 1–16. ISSN: 21980926. DOI: 10.1186/s40679-015-0008-4.

[67] Jonathan N. Coleman et al. “Two-dimensional nanosheets produced by liquid exfoliation of layered materials”. In: *Science* 331.6017 (2011), pp. 568–571. ISSN: 00368075. DOI: 10.1126/science.1194975.

[68] Jonathan N. Coleman. “Liquid exfoliation of defect-free graphene”. In: *Accounts of Chemical Research* 46.1 (2013), pp. 14–22. ISSN: 00014842. DOI: 10.1021/ar300009f.

[69] Valeria Nicolosi et al. “Liquid exfoliation of layered materials”. In: *Science* 340.6139 (2013), pp. 72–75. ISSN: 10959203. DOI: 10.1126/science.1226419.

[70] Hao Li and L. Salamanca-Riba. “The concept of high angle wedge polishing and thickness monitoring in TEM sample preparation”. In: *Ultramicroscopy* 88.3 (2001), pp. 171–178. ISSN: 03043991. DOI: 10.1016/S0304-3991(01)00079-1.

[71] Lynnette D. Madsen, Louise Weaver, and Sissel N. Jacobsen. “Influence of material properties on TEM specimen preparation of thin films”. In: *Microscopy Research and Technique* 36.5 (1997), pp. 354–361. ISSN: 1059910X. DOI: 10.1002/(SICI)1097-0029(19970301)36:5<354::AID-JEMT2>3.0.CO;2-L.

[72] Paul E. Fischione et al. “A Small Spot, Inert Gas, Ion Milling Process as a Complementary Technique to Focused Ion Beam Specimen Preparation”. In: *Microscopy and Microanalysis* 23.4 (2017), pp. 782–793. ISSN: 14358115. DOI: 10.1017/S1431927617000514.

[73] P. Hohenberg and W. Kohn. “Inhomogeneous electron gas”. In: *Physical Review* 136.3B (1964), B864. ISSN: 0031899X. DOI: 10.1103/PhysRev.136.B864.

[74] W. Kohn and L. J. Sham. “Self-consistent equations including exchange and correlation effects”. In: *Physical Review* 140.4A (1965), A1133. ISSN: 0031899X. DOI: 10.1103/PhysRev.140.A1133.

[75] John M. Wills et al. “Density Functional Theory and the Kohn–Sham Equation”. In: *Springer Series in Solid-State Sciences*. Vol. 167. Springer Science and Business Media Deutschland GmbH, 2010, pp. 7–19. DOI: 10.1007/978-3-642-15144-6_2.

[76] David S. Sholl and Janice A. Steckel. *Density Functional Theory: A Practical Introduction*. John Wiley and Sons, 2009, pp. 1–238. ISBN: 9780470373170. DOI: 10.1002/9780470447710.

[77] K. Held et al. "LDA+DMFT Investigations of Transition Metal Oxides and f-Electron Materials". In: Springer, Berlin, Heidelberg, 2003, pp. 267–286. DOI: 10.1007/978-3-540-44838-9_19.

[78] John P. Perdew, Kieron Burke, and Matthias Ernzerhof. "Generalized gradient approximation made simple". In: *Physical Review Letters* 77.18 (1996), pp. 3865–3868. ISSN: 10797114. DOI: 10.1103/PhysRevLett.77.3865.

[79] Stefan Grimme. "Accurate description of van der Waals complexes by density functional theory including empirical corrections". In: *Journal of Computational Chemistry* 25.12 (2004), pp. 1463–1473. ISSN: 01928651. DOI: 10.1002/jcc.20078.

[80] Irina V. Lebedeva et al. "Comparison of performance of van der Waals-corrected exchange-correlation functionals for interlayer interaction in graphene and hexagonal boron nitride". In: *Computational Materials Science* 128 (2017), pp. 45–58. ISSN: 09270256. DOI: 10.1016/j.commatsci.2016.11.011. arXiv: 1708.01504.

[81] Jochen Heyd, Gustavo E. Scuseria, and Matthias Ernzerhof. "Hybrid functionals based on a screened Coulomb potential". In: *The Journal of Chemical Physics* 118.18 (2003), pp. 8207–8215. ISSN: 0021-9606. DOI: 10.1063/1.1564060.

[82] John P. Perdew, Matthias Ernzerhof, and Kieron Burke. "Rationale for mixing exact exchange with density functional approximations". In: *The Journal of Chemical Physics* 105.22 (1996), pp. 9982–9985. ISSN: 0021-9606. DOI: 10.1063/1.472933.

[83] J. Almlöf, K. Faegri, and K. Korsell. "Principles for a direct SCF approach to LICAO-MO ab-initio calculations". In: *Journal of Computational Chemistry* 3.3 (1982), pp. 385–399. ISSN: 0192-8651. DOI: 10.1002/jcc.540030314.

[84] Dieter Cremer and JüRgen Gauss. "An unconventional scf method for calculations on large molecules". In: *Journal of Computational Chemistry* 7.3 (1986), pp. 274–282. ISSN: 0192-8651. DOI: 10.1002/jcc.540070305.

[85] Jong Won Song and Kimihiko Hirao. “Efficient method of evaluation for Gaussian Hartree-Fock exchange operator for Gau-PBE functional”. In: *Journal of Chemical Physics* 143.2 (2015), p. 24102. ISSN: 10897690. DOI: 10.1063/1.4923264/825094.

[86] Kurt Lejaeghere et al. “Reproducibility in density functional theory calculations of solids”. In: *Science* 351.6280 (2016). ISSN: 0036-8075. DOI: 10.1126/science.aad3000.

[87] Edvin Fako. *Pseudopotential - Wikimedia Commons*.

[88] G. Kresse and J. Furthmüller. “Efficient iterative schemes for ab initio total energy calculations using a plane wave basis set”. In: *Physical Review B - Condensed Matter and Materials Physics* 54.16 (1996), pp. 11169–11186. ISSN: 1550235X. DOI: 10.1103/PhysRevB.54.11169.

[89] D. R. Bowler and T. Miyazaki. “O(N) methods in electronic structure calculations”. In: *Reports on Progress in Physics* 75.3 (2012), p. 036503. ISSN: 0034-4885. DOI: 10.1088/0034-4885/75/3/036503. arXiv: 1108.5976.

[90] José M. Soler et al. “The SIESTA method for ab initio order-N materials simulation”. In: *Journal of Physics: Condensed Matter* 14.11 (2002), pp. 2745–2779. ISSN: 0953-8984. DOI: 10.1088/0953-8984/14/11/302. arXiv: 0111138 [cond-mat].

[91] Otto F. Sankey and David J. Niklewski. “Ab initio multicenter tight-binding model for molecular-dynamics simulations and other applications in covalent systems”. In: *Physical Review B* 40.6 (1989), pp. 3979–3995. ISSN: 0163-1829. DOI: 10.1103/PhysRevB.40.3979.

[92] Christoph R. Jacob and Markus Reiher. “Spin in density-functional theory”. In: *International Journal of Quantum Chemistry* 112.23 (2012), pp. 3661–3684. ISSN: 0020-7608. DOI: 10.1002/qua.24309. arXiv: 1206.2234.

[93] Michael G. Medvedev et al. “Density functional theory is straying from the path toward the exact functional”. In: *Science* 355.6320 (2017), pp. 49–52. ISSN: 0036-8075. DOI: 10.1126/SCIENCE.AAH5975.

[94] José Coutinho. “Density Functional Modeling of Defects and Impurities in Silicon Materials”. In: *Lecture Notes in Physics*. Vol. 916. Springer Verlag, 2015, pp. 69–127. ISBN: 9784431557999. DOI: 10.1007/978-4-431-55800-2_2.

[95] Irea Mosquera-Lois et al. “Identifying the ground state structures of point defects in solids”. In: *npj Computational Materials* 9.1 (2023), p. 25. ISSN: 2057-3960. DOI: 10.1038/s41524-023-00973-1. arXiv: 2207.09862.

[96] Steven G. Louie et al. “Discovering and understanding materials through computation”. In: *Nature Materials* 20.6 (2021), pp. 728–735. ISSN: 1476-1122. DOI: 10.1038/s41563-021-01015-1.

[97] Mohammad Zarshenas et al. “Room-temperature diffusion of metal clusters on graphene”. In: *Physical Chemistry Chemical Physics* 23.23 (2021), pp. 13087–13094. ISSN: 1463-9076. DOI: 10.1039/D1CP00522G.

[98] M. Sri Harish and Puneet Kumar Patra. “Temperature and its control in molecular dynamics simulations”. In: *Molecular Simulation* 47.9 (2021), pp. 701–729. ISSN: 0892-7022. DOI: 10.1080/08927022.2021.1907382. arXiv: 2006.02327.

3

Investigation of the Thermoelectric Structure-Property Relationship of $TlGaSe_2$

You, what do you own the world?

How do you own disorder? Disorder?!

– "Toxicity", *Toxicity*, System of a Down

After outlining the various projects in this work and the concepts required to understand such projects, attention is now turned to the first of the novel chalcogenide materials investigated. In this chapter, the layered 2-D material $TlGaSe_2$ is introduced and characterised via (scanning) transmission electron microscopy (STEM) and selected area electron diffraction (SAED) patterns. Stacking faults are seen throughout the material and confirmed via simulations of the SAED patterns and STEM images. The stacking fault energy and the role of these faults in the thermoelectric properties of the material are investigated via density functional theory (DFT) calculations. Preliminary results from electron transport and phonon band structure calculations are presented, as are the ongoing plans for this project.

The majority of the work in this Chapter was performed by the author, however the growth and XRD analysis of the $TlGaSe_2$ crystals was performed by a collaborator (Zdenek

Sofer, University of Chemistry and Technology Prague), as well as the electron transport and phonon dispersion calculations (Rui Dong & Akash Bajaj, Trinity College Dublin).

3.1 Introduction

When electrical devices are under load, the resistivity of the circuit leads to a conversion of some electrical energy into heat. In some cases, this is intentional and beneficial, such as an electric kettle or a toaster. In most other cases, this excess energy consumption is environmentally and economically unsustainable. The waste heat is, at best, a nuisance (such as the overheating laptop used to prepare this thesis). At worst, it is detrimental, if not fatal, to a device's performance, especially as devices such as transistors are approaching the atomic scale. In order to tackle these issues, research has increased into thermoelectric materials and their subsequent devices. These materials have low thermal conductivity, but yet possess high electrical conductivity, allowing for the conversion of excess heat energy into electrical energy and hence leading to high device efficiencies [1–4].

The performance of thermoelectric materials is compared via the dimensionless figure of merit *ZT*, which is defined as:

$$ZT = \frac{S^2\sigma}{\kappa}T \tag{3.1}$$

where S is the Seebeck coefficient ($V\,K^{-1}$), σ is the electrical conductivity ($(\Omega\cdot m)^{-1}$), κ is the thermal conductivity ($W\,(m\cdot K)^{-1}$), and T is the temperature (K) [5]. For context, bulk Si has a *ZT* of approximately 0.01 due to its high thermal and electrical conductivity [6]. The family of Bi_xTe_y nanowires and their alloys are the most commonly studied high *ZT* materials, with *ZT*'s ranging from ~0.8 - 1.5 at room temperature [7].

Another material that shows promising thermoelectric capabilities is the $TlGaSe_2$ ternary chalcogenide. This layered, monoclinic *p*-type semiconductor is of interest for optoelectronic devices as it has a band gap of ~ 1.95 - 2.2 eV which is in the near-IR range [8–13] which could be used for near-IR spectroscopy of deep space astronomical bodies such as cool stars [14, 15] (Here, "cool" is defined as temperature, not popularity, however the two are not mutually exclusive).

$TlGaSe_2$ consists of $GaSe_4$ tetrahedra linked together by common chalcogen atoms to form Ga_4Se_{10} complexes, as seen in Figure 3.1. These then form layers parallel to the (001) plane, and each layer is turned at a 90° angle relative to the previous one, forming trigonal cavities where Tl^+ ions reside [13, 16, 17].

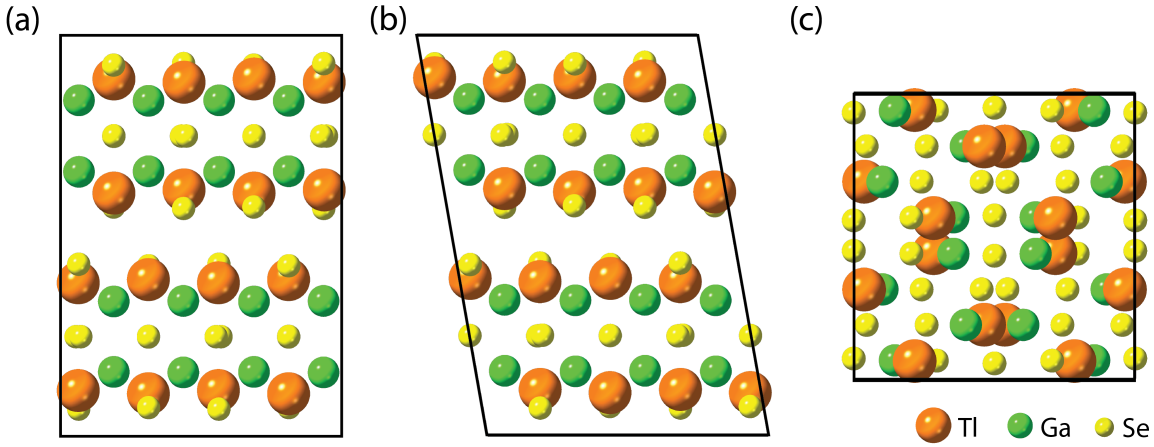

Fig. 3.1 Unit cell of $TlGaSe_2$ along the (a), (b) and (c) lattice directions.

$TlGaSe_2$ has been shown to possess impressive thermoelectric properties [10]. Theoretical studies have shown that $TlGaSe_2$ possesses a ZT of ~0.8 at room temperature [18]. This value quickly diminishes due to the presence of Se vacancies [18]. However, unlike many thermoelectric materials currently available, thin film production of $TlGaSe_2$ has been reported [19], opening the door for $TlGaSe_2$-based thermoelectric devices to be manufactured at scale.

The weakly covalent layered nature of the material means that it is susceptible to planar defects such as stacking faults [18, 20, 21]. However, this layered nature is also attributed to the material's highly anisotropic properties, such as much higher electrical conductivity in-plane than out-of-plane, along the [001] stacking direction [11]. The presence of stacking faults in other layered materials dampens the thermal conductivity in the [001] stacking direction [22–24], such as in the $(BiS)_{1.18}(TiS_2)_2$ where the faults reduce the thermal conductivity but preserve the electron mobility [25]. Another example is $In_2Ge_2Te_6$ where stacking faults are seen throughout, with perfect stacking rarely seen, leading to the low thermal conductivity of the material [26]. It is assumed that a similar situation is present in $TlGaSe_2$ [13, 18]. However, to date, no such comprehensive structure-

property investigation has been conducted. Hence, if one wanted to develop devices with $TlGaSe_2$, it is important to establish this thermoelectric relationship.

Here, the layered nature of $TlGaSe_2$ is characterised via STEM imaging and diffraction studies. The stacking faults in the material, as seen in selected area electron diffraction (SAED) patterns and high-angle annular dark field (HAADF)-STEM imaging, are correlated with simulations, along with calculations of the stacking fault energy to determine the nature of the planar defects. The thermoelectric properties are qualitatively probed using electron transport calculations and phonon band structure simulations of both the bulk system and one of with a stacking fault. Preliminary results from both are presented, as well as discussions on the future optimisation of these calculations.

3.2 Methods

High purity elements (Tl (99.99%), Ga (99.9999%) and Se (99.9999%)) from Wuhan Xinrong New Materials, China, were used to synthesise bulk $TlGaSe_2$. Stoichiometric amounts of the elements, corresponding to 20 g of $TlGaSe_2$, were placed into a quartz ampoule (25 mm x 120 mm, 3 mm wall thickness) and melt sealed under vacuum (~ 10^{-3} Pa) using a diffusion pump. The ampoule was then heated to 850 °C using a heating rate of 1 °C min^{-1}, held at that temperature for 5 hrs, and then cooled to room temperature at a rate of 0.2 °C min^{-1}. X-ray diffraction (XRD) was performed using a Bruker D8 Discover diffractometer on a silicon holder with a Cu Kα source. The measured range was 5-90 °2θ, with a step size set to 0.012 °2θ and at a rate of 0.2 s per step.

TEM samples were prepared via the drop-cast method as mentioned in Chapter 2.3. Single crystals of the material were placed between several sheets of filter paper and were ground up with an agate mortar and pestle into a fine powder, then dispersed in isopropyl alcohol (IPA). Samples were drop-cast onto copper, 400-grid lacey carbon TEM grids (Ted Pella, Inc.), with subsequent baking in a vacuum oven at approx. 80 °C for 24 hrs. HAADF-STEM imaging and SAED patterns were performed on an uncorrected FEI Titan operating at 300 kV. HAADF-STEM imaging was performed with a convergence angle of 10 mrad and a collection angle range of 40 - 200 mrad. The probe current was approx. 20 pA and imaging was performed with a 10 μs dwell time (except Figure 3.4(a) which had a dwell

time of 16μs) with 1024×1024 pixels. Sample drift in Figure 3.3(b) was reduced by taking an 11 image stack of the same area, and then aligning the images using rigid registration methods in the SmartAlign plug-in for Digital Micrograph [27, 28].

For all simulations, the stacking faults of $TlGaSe_2$ were formed using the ATOMMAN python package [29], using the stacking fault descriptions in Equations 3.2 and 3.3. ReciPro was used to simulate the diffraction patterns [30]. Multislice simulations of HAADF-STEM images were performed via the abTEM code [31, 32], with roughly similar parameters as the imaging conditions of the reference images to provide a qualitative understanding of the structure.

DFT calculations of the electronic band structures and stacking fault energies were performed via the Vienna ab-initio Simulation Package (VASP) code with projector augmented wave (PAW) pseudopotentials [33, 34]. Atomic structures were optimised using the PBE functional [35] and a Hellman-Feynman force criterion of 10^{-2} eV/Å. Calculations of the band structures and stacking fault energy were performed with a cutoff energy of 400 eV. A 6×6×4 k-point grid was used in all calculations.

DFT-level quantum transport calculations were carried out on the relaxed structures using the semiclassical Boltzmann transport formalism via the BoltzTraP code [36], which interfaced with the SIESTA package [37]. Here, the probability distribution of the position and momentum of an electron gas due to an applied field, such as an electric field, is calculated, from which a number of transport properties can be established [36, 38]. BoltzTraP was used to compute the Seebeck coefficients and the conductivities at ambient temperature under the constant relaxation-time (τ) approximation, for both with and without the stacking fault. Note that under the constant relaxation-time approximation, only the Seebeck coefficient is independent of the relaxation time. Thus, for conductivities, σ/τ is reported instead.

The pseudopotentials for use within SIESTA were generated using the ATOM program [39]. Numerical atomic orbitals (NAOs) were used as the basis set within SIESTA, where a *spd*-basis was used for Tl while only a *sp*-basis was used for Ga and Se. The cutoff radii were carefully chosen to reproduce the valence band structure of bulk $TlGaSe_2$ as benchmarked

using the all-electron FHI-AIMS code [40]. All DFT calculations in SIESTA were performed at the PBE-GGA level of theory [35].

Computing the energy eigenvalues as inputs to the BoltzTraP code was performed on the relaxed structures using a 13×13×13 k-mesh. The real-space grid resolution for the electron density was set at a plane-wave energy cutoff of 400 Ry, where 1 Ry ~ 13.6 eV. The self-consistent-field (SCF) convergence was achieved when the maximum difference across all elements of the density matrix was below $1x10^{-5}$. The original k-mesh was interpolated onto a mesh 31 times as dense using BoltzTraP for computation of all the transport coefficients.

Phonon dispersions for a periodic system can be determined from second-order interatomic force-constant matrices which describe the change in the force on a given atom in response to the displacement of another atom from its equilibrium position. A simple method for computing these force-constant matrices is to perform small displacements of atoms and compute the resultant forces, hence building up the required derivatives using finite differences. These matrices can be transformed to a dynamical matrix for a given phonon wavevector **q**, which captures the wavelength and propagation of the atomic-displacement wave. Finally, from this dynamical matrix, the phonon frequencies and eigenvectors can be calculated [41–44].

For the phonon calculations, all of the structural optimisation and force calculations were performed with the CP2K software package [45] at the PBE-GGA level of theory [35], including Grimme's D3 van der Waals corrections [46]. A triple-zeta polarized MOLOPT basis set and a 600 Ry of plane-wave cutoff were used for all atomic species. Phonon dispersion and density of states were calculated using the finite difference method implemented in the Phonopy package [43, 44] using CP2K-computed energies. A 3×3×2 supercell is used for bulk $TlGaSe_2$, and a 3×3×1 supercell is used for stacking fault. Such supercells were used to evaluate the second-order force constants with atomic displacements of 0.01 Å.

3.3 Results & Discussion

3.3.1 Characterisation of Stacking Faults in $TlGaSe_2$

Bulk crystals of $TlGaSe_2$ were structurally analysed via XRD, as seen in Figure 3.2(a), confirming its monoclinic crystal structure (space group *C12/c1*; ICSD - 17397) [47], with lattice parameters of $a = b = 10.772$ Å, c = 15.636 Å, and $\beta = 100.06°$. The 64-atom unit cell consists of Ga_4Se_{10} units, each containing four corner-sharing $GaSe_2$ tetrahedra, forming layers. In each unit cell, there are two layers aligned parallel to the (001) plane, and perpendicular to the [114] direction. These layers are connected only by Tl^+ ions located in the centre of Se_6 trigonal cavities between the layers [17, 20, 21, 48].

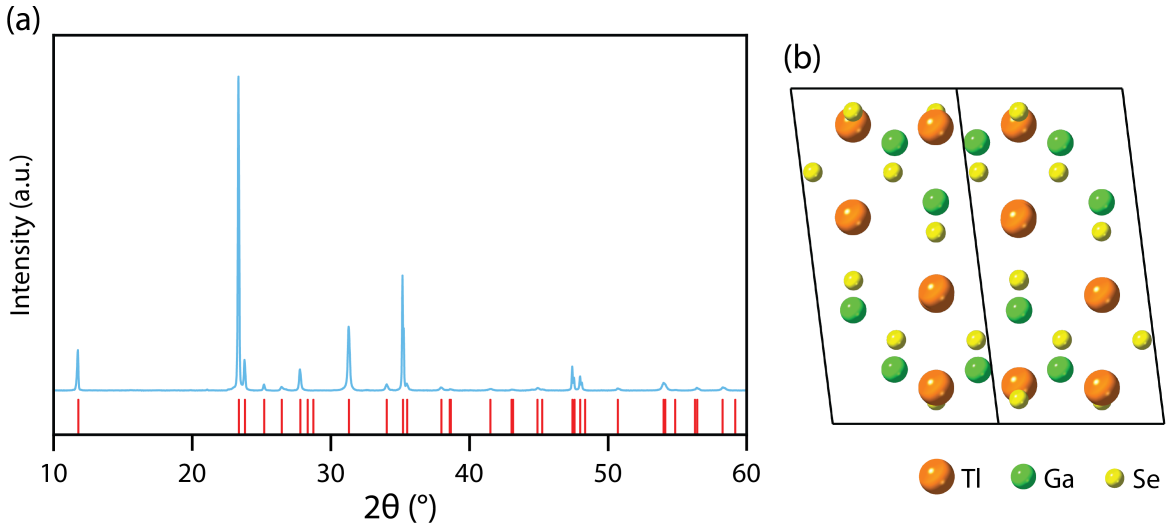

Fig. 3.2 (a) XRD pattern of $TlGaSe_2$ (blue), along with appropriate fitting of the structure (red) from ICSD - 17397. (b) Unit cell of $TlGaSe_2$, shown along $[1\bar{1}0]$ zone axis to highlight its monoclinic and layered structure.

Figure 3.3(a) shows a HAADF-STEM image of a typical region of $TlGaSe_2$ along the $[1\bar{1}0]$ zone axis, with a highlighted section of the same sample at a higher magnification in Figure 3.3(b). Following along the stacking direction, indicated by the [001] arrow in Figure 3.3(b), reveals large numbers of stacking faults throughout the sample. Multislice simulations of the sample, seen in the top left corner of Figure 3.3(b), also confirm the stacking fault nature of the sample.

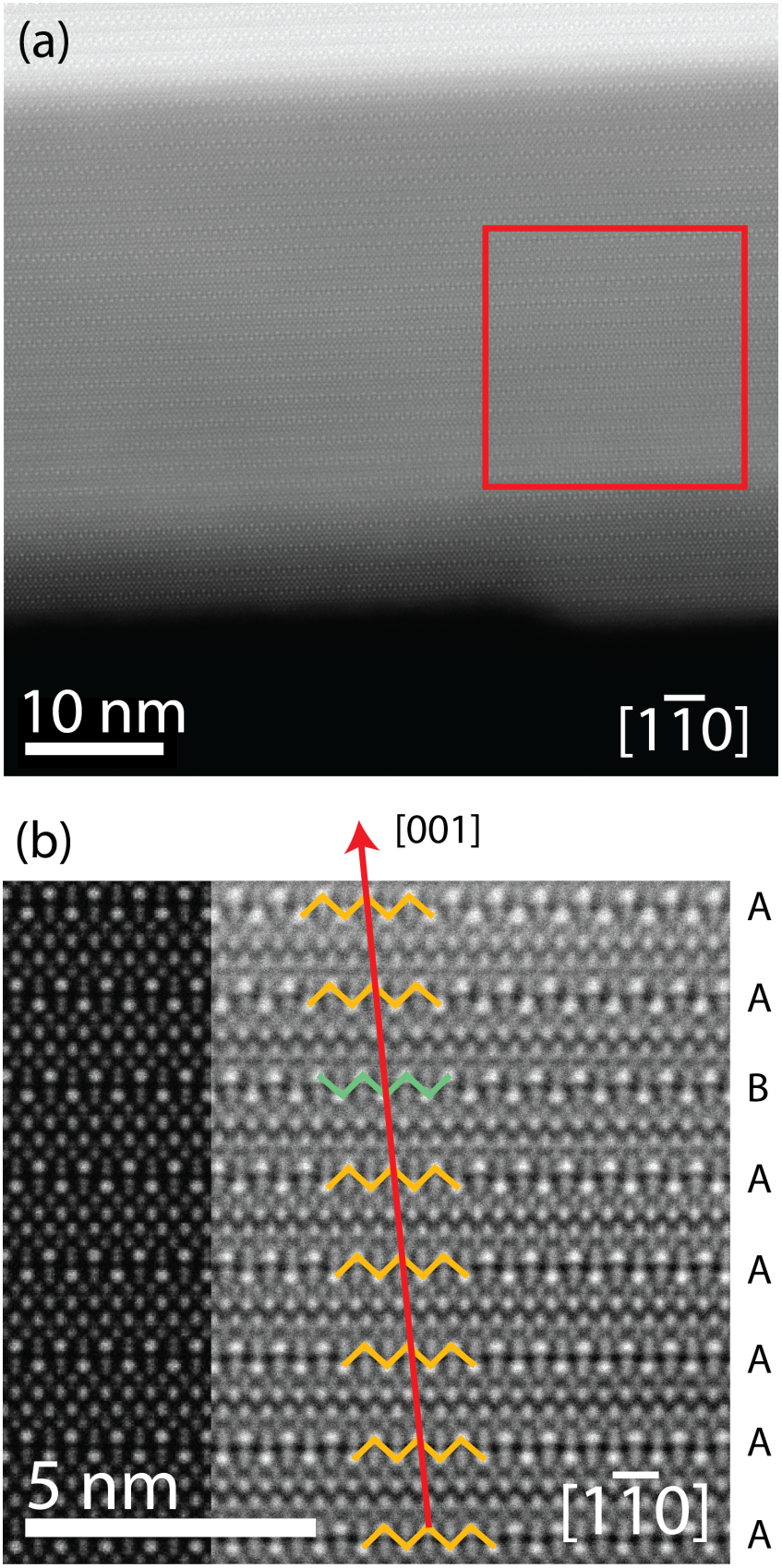

Fig. 3.3 HAADF-STEM image (a) of $TlGaSe_2$ along the [1$\bar{1}$0] zone axis, with a magnified region in (b). Red arrow is along the [001] direction, highlighting the stacking fault along the *c*-axis. The zigzags are on the Tl atomic columns, where orange indicates bulk stacking and green indicates a stacking fault. The stacking order in (b) is shown along the right-hand side. Multislice simulation of the structure is shown along the left-hand side.

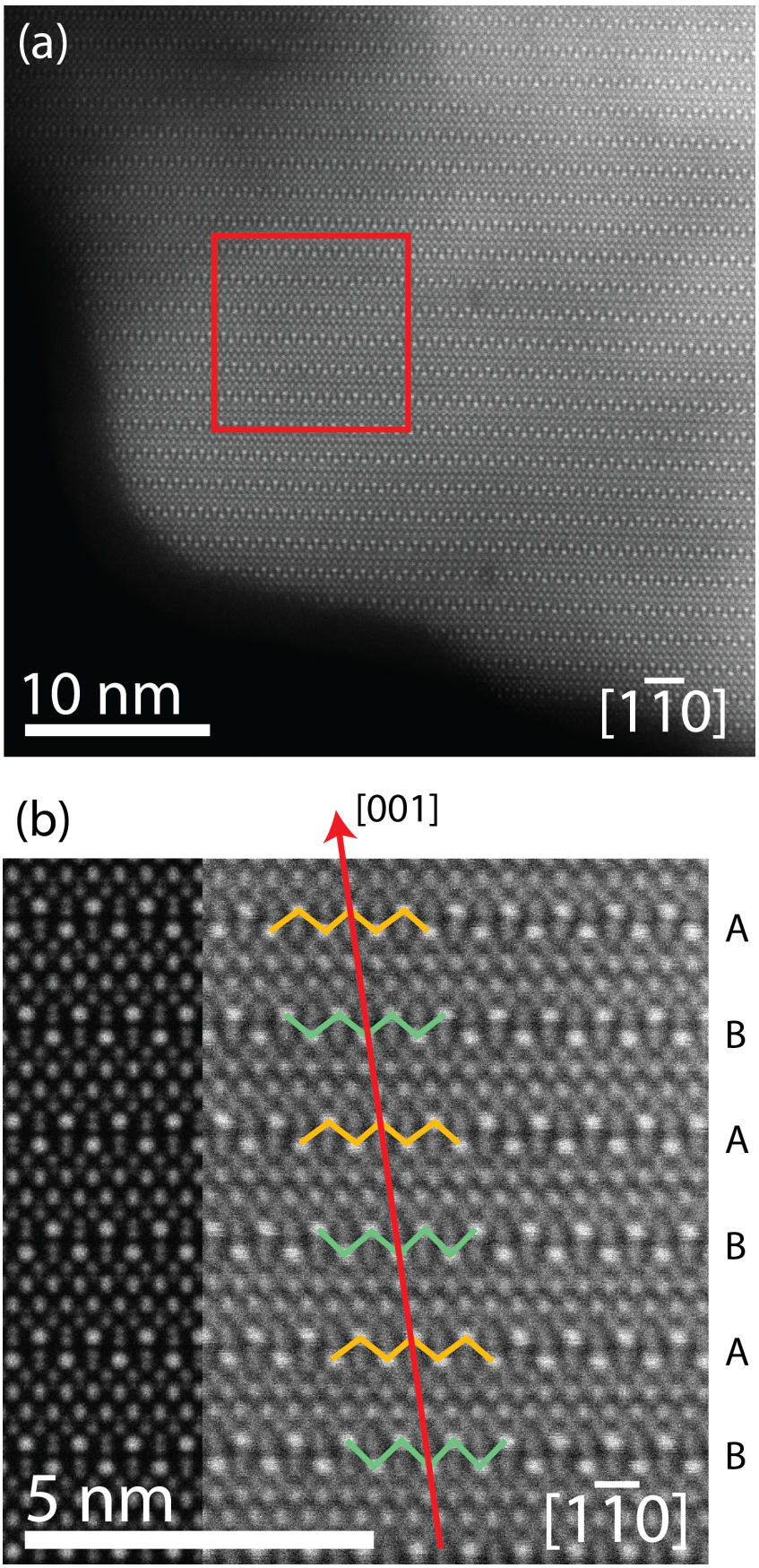

Fig. 3.4 HAADF-STEM image (a) of another $TlGaSe_2$ sample along the [1$\bar{1}$0] zone axis, with a magnified region in (b). The red arrow is along the [001] direction, highlighting the stacking faults along the *c*-axis. The zigzags are on the Tl atomic columns, where orange indicates bulk stacking and green indicates a stacking fault. The stacking order in (b) is shown along the right-hand side. Multislice simulation of the structure is shown along the left-hand side.

Similar HAADF-STEM analysis can be seen on another sample in Figure 3.4 showing a more varied stacking order. Initial observations from several TEM samples highlight no long-range ordering of the layers, however as shown in Figure 3.3(b) and Figure 3.4(b), some short-range order does exist in line with previous reports [20, 21]. Similar layered chalcogen thermoelectric materials such as $In_2Ge_2Te_6$ also shows this property [26].

As mentioned in Chapter 1, the covalent bonding nature of chalcogenide-based materials often leads to the facile formation of defects. As such, care must be taken to minimise this damage through the use of low acceleration voltages of < 80 kV (to minimise knock-on damage) [49, 50] and/or low electron fluence of < 10^6 e^- $Å^{-2}$ (to minimise ionisation effects) [51–54]. In the electron microscopy community, electron fluence is often referred to as "electron dose" [55]. Despite the misnomer, this is the term that will be used hereafter. $TlGaSe_2$ was robust enough that adequate signal-to-noise HAADF imaging could be performed at electron doses of up to 10^6 e^- $Å^{-2}$, as shown in Table 3.1, despite the high accelerating voltage of 300 kV. In fact, Figure 3.3(b) is an 11 image stack that was recorded and aligned with rigid registration, leading to enhanced signal-to-noise [27]. However, beam damage is still prevalent in the sample, as can be seen by the dark spots in the structure in Figure 3.4(a) where the beam was parked momentarily longer than the 16 μs dwell time at that location to adjust alignments.

Units = e^- $Å^{-2}$	Figure 3.3		Figure 3.4	
	(a)	(b)	(a)	(b)
e^- Dose	2.64×10^5	6.10×10^5	3.12×10^5	1.27×10^6
Total e^- Dose (single frame)	2.77×10^{11}	6.40×10^{11}	3.27×10^{11}	1.33×10^{12}
Total e^- Dose (multi-frame)		7.04×10^{12}		

Table 3.1 Table of electron doses and electron dose per image frame for the HAADF-STEM images in Figure 3.3 and 3.4. The total electron dose for multi-frame image stack used in Figure 3.3(b) is also highlighted.

In spite of the relative robustness of the material to the imaging conditions it was subjected to, sample contamination was an issue, especially when attempting thickness measurements through PACBED patterns for the multislice calculations. The low baking temperature of 80°C was used in the sample preparation as the material was observed

to be heat-sensitive. Other sample cleaning methods such as plasma or ozone cleaning damaged the material irreversibly, even at the lowest system settings available to the author. Collection of PACBED patterns was attempted as described in Chapter 2.2.7. The FEI Titan used in these experiments has a CCD-based camera and therefore, in order to resolve the PACBED with sufficient dynamic range to compare to simulations, long camera exposure times are required (5 - 10 seconds). To simplify the PACBED simulations, an area of the sample where no stacking faults were present was rastered over using the same dwell time as for the HAADF-STEM imaging. However, this area is typically only a few unit cells wide, and thus the electron dose increases significantly [55]. The long exposure time required for the CCD camera means that a significant amount of hydrocarbon contamination builds up on the area, along with beam damage, highly obscuring the recorded PACBED patterns. Therefore, the sample thickness for the multislice simulations was set to 20 nm and the simulations are to be thought of as a qualitative confirmation of the observed stacking faults.

For $TlGaSe_2$ polytypes, such as $KInS_2$ [21], stacking faults can exist between unit cells along the [001] stacking direction due to the weak interlayer bonding. They appear in one of two forms: *AA* and *AB*, as seen in Figure 3.5. The *AA*-stacking can be described as a pseudotranslation of a layer along the [110] direction:

$$s_1 = \frac{1}{4}a + \frac{1}{4}b \tag{3.2}$$

where a and b are the lattice parameters. The *AB*-stacking is a 90° rotation of a layer about the $[1\bar{1}4]$ direction. Conveniently, this can also be considered a pseudotranslation along the [110] direction [21]:

$$s_2 = \frac{1}{4}a - \frac{1}{4}b \tag{3.3}$$

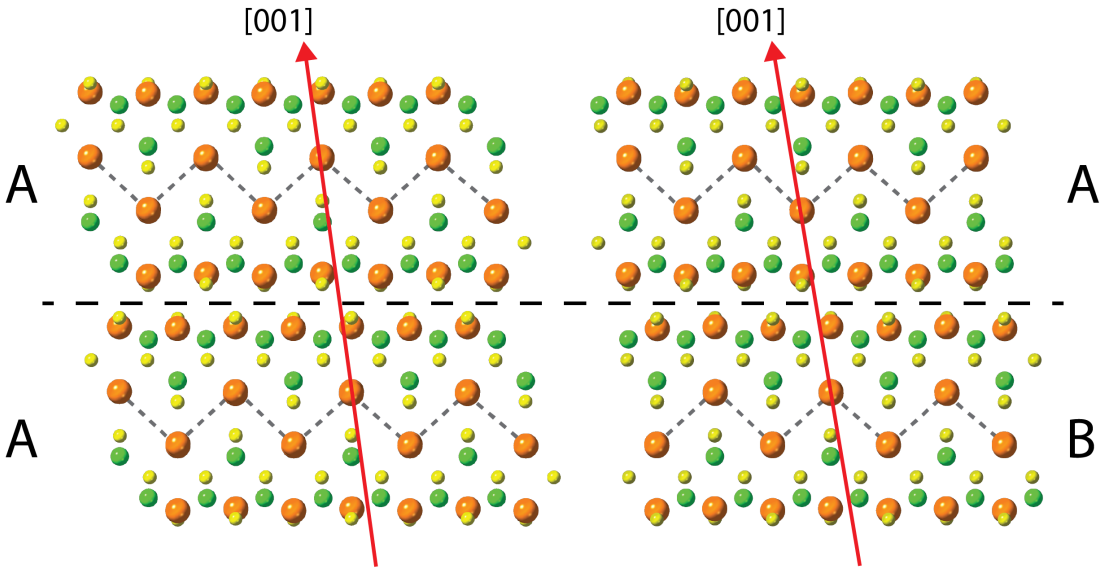

Fig. 3.5 *AA*- and *AB*-stacking of $TlGaSe_2$ seen along $[1\bar{1}0]$ zone axis. Red arrows showing the [001] direction and polyhedra around $GaSe_2$ units are shown to highlight the stacking order.

Streaks in the SAED patterns of $TlGaSe_2$, as can be seen in Figure 3.6(a), are observed when the sample was orientated to be viewed along on the $[1\bar{1}0]$ zone axis. This diffuse streaking is seen along the (hhl) direction, where h = odd [20]. The presence of these streaks can indicate the presence of stacking faults in the structure, which appear as additional spots around the Bragg spots [54]. Interestingly, as the number of stacking faults increases, the number of additional spots increase as the diffuse intensities are split symmetrically around the positions of the Bragg intensities with $h\bar{h}l$. However, low numbers of stacking faults imply extended local domains where domains are of either *AA*- or *AB*-stacking, which lead to the smearing or streaking of the spots along the c^* direction [21, 56]. The lack of fully continuous streaks, as seen in Figure 3.6(a), implies some short-range order to the stacking of the layers in this part of the sample [20].

To confirm this, the SAED pattern in Figure 3.6(a) was taken from the area shown in Figure 3.3(a). A $TlGaSe_2$ model consisting of the stacking order in Figure 3.3(a) was created and used to simulate a SAED pattern using diffraction simulations. The model parameters are shown in Chapter A in the CIF file format [57]. As shown in Figure 3.6(b), the presence of streaking is along the same directions in both cases [20, 21, 56]. For comparison, a SAED pattern using the same parameters is shown in Figure 3.6(c) for the bulk structure, showing a lack of streaking.

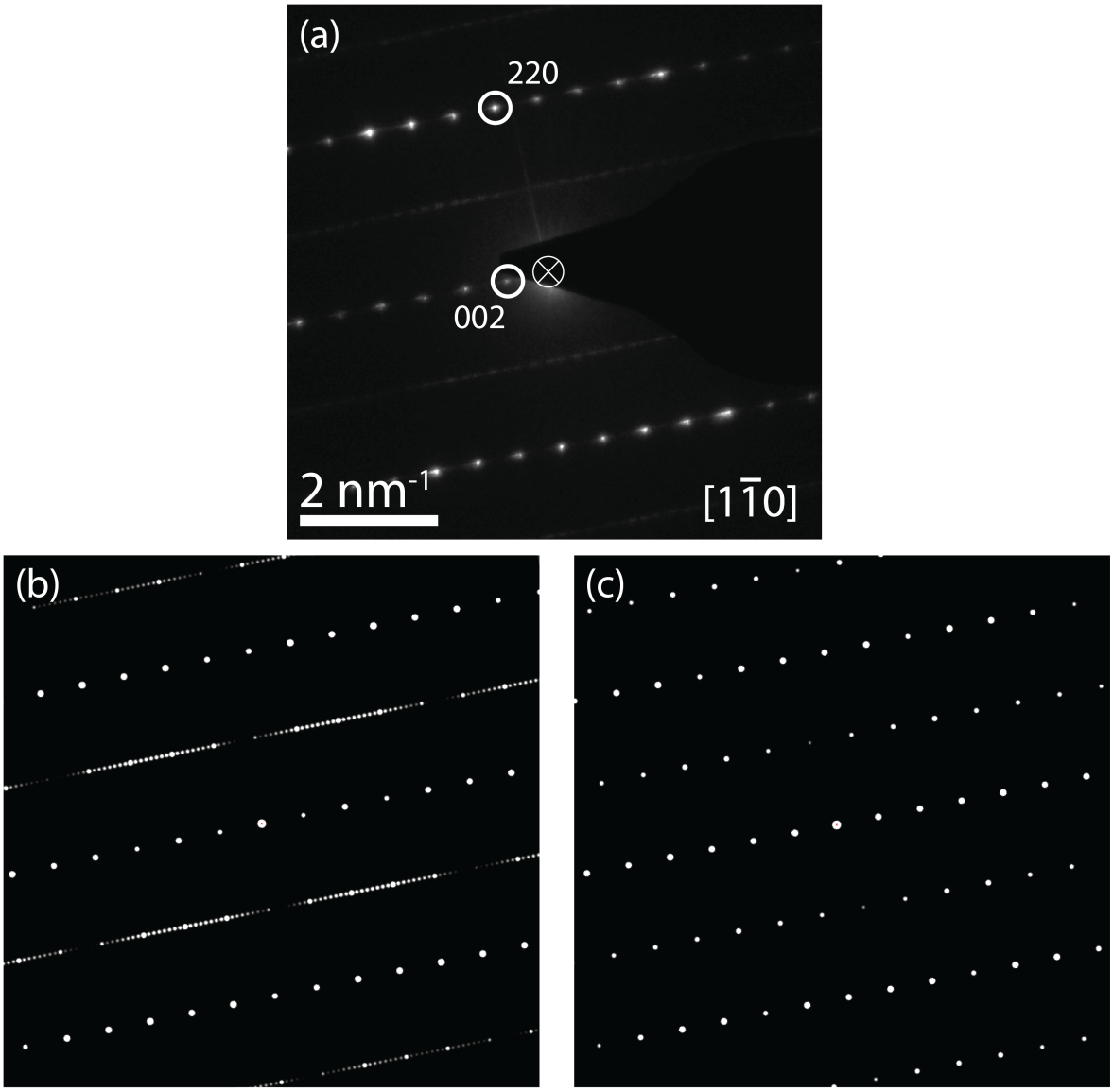

Fig. 3.6 (a) Selected area electron diffraction (SAED) pattern of $TlGaSe_2$ along [1$\bar{1}$0] zone axis. The circle with a cross indicates the central beam, which has been covered by the beam blocker. Dynamical diffraction simulation along the same zone axis and same scale of the structure in the experimental SAED (b) and of bulk stacking order (c).

The effect of stacking faults on the electronic band structure of $TlGaSe_2$ was investigated using PBE-GGA level calculations. A high symmetry k-path was chosen which went through the Γ-point of the complex monoclinic Brillouin zone of $TlGaSe_2$ [58], as seen in Figure 3.7, and this was used for both bulk (i.e. *AA*) and *AB*-stacking configurations. The resulting electronic band structures are shown in Figure 3.8.

The number of bands for the *AB*-stacking configuration, seen in Figure 3.8(b), is twice that of the *AA*-stacking configuration, as the structure has double the number of atoms in the simulation cell. Band unfolding methods could be used for the *AB*-stacking, to highlight the changes in the band structures [59]. However, the primary interest here is

the changes to the band gap due to the introduction of stacking faults, and as such, band unfolding was not deemed necessary.

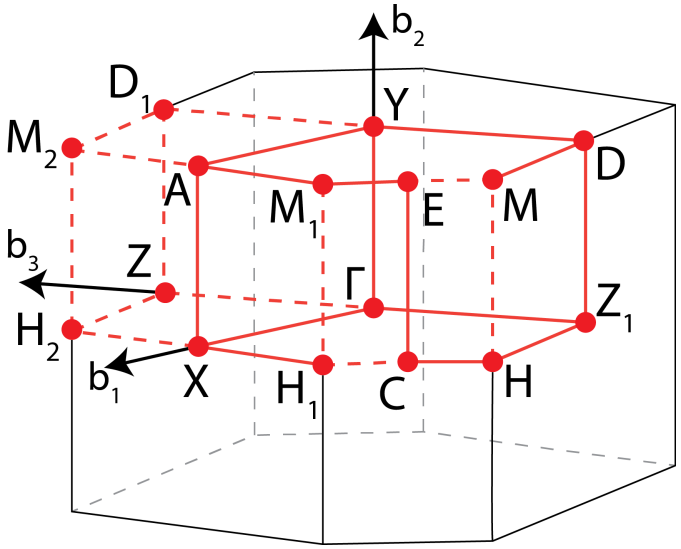

Fig. 3.7 Brillouin zone of monoclinic $TlGaSe_2$, with high symmetry points and reciprocal lattice vectors labelled. Reprinted from *Computational Materials Science*, 49, W. Setyanwan & S. Curtarolo, "High-throughput electronic band structure calculations: Challenges and Tools", Copyright (2010), with permission from Elsevier [58].

The *AA* and *AB*-stacked structures both have, effectively, the same direct band gaps, with a value of 1.337 eV for the bulk *AA*-stacking and 1.177 eV for the *AB*-stacking. There is disagreement in the literature on what the actual size of the band gap is for $TlGaSe_2$, with experimental values ranging from 1.95 - 2.2 eV [9–13], as well as if it is direct or not. In any case, the band gaps from Figure 3.8 are underestimated due to the use of the PBE functional [60–63]. The difference between the bandgaps is also negligible as PBE-GGA calculations of the band gap have a large standard deviation of approximately 1 eV, rendering the 0.15 eV difference between the two systems insignificant [60].

While it is clear that these stacking faults are ubiquitous and that they have little effect on the electronic band structure, it is not clear whether they are intrinsic (i.e. appear from the growth stage) or extrinsic (i.e. whether they can/were induced) stacking faults. In order to investigate this, the stacking fault energy was calculated using the following equation:

$$\gamma_{SFE} = \frac{E_{bulk} - E_{fault}}{2A} \tag{3.4}$$

where E_{bulk} is the ground state energy of the bulk system, E_{fault} is the ground state energy of the faulted system, and A is the area of the stacking fault. Since the stacking faults happen

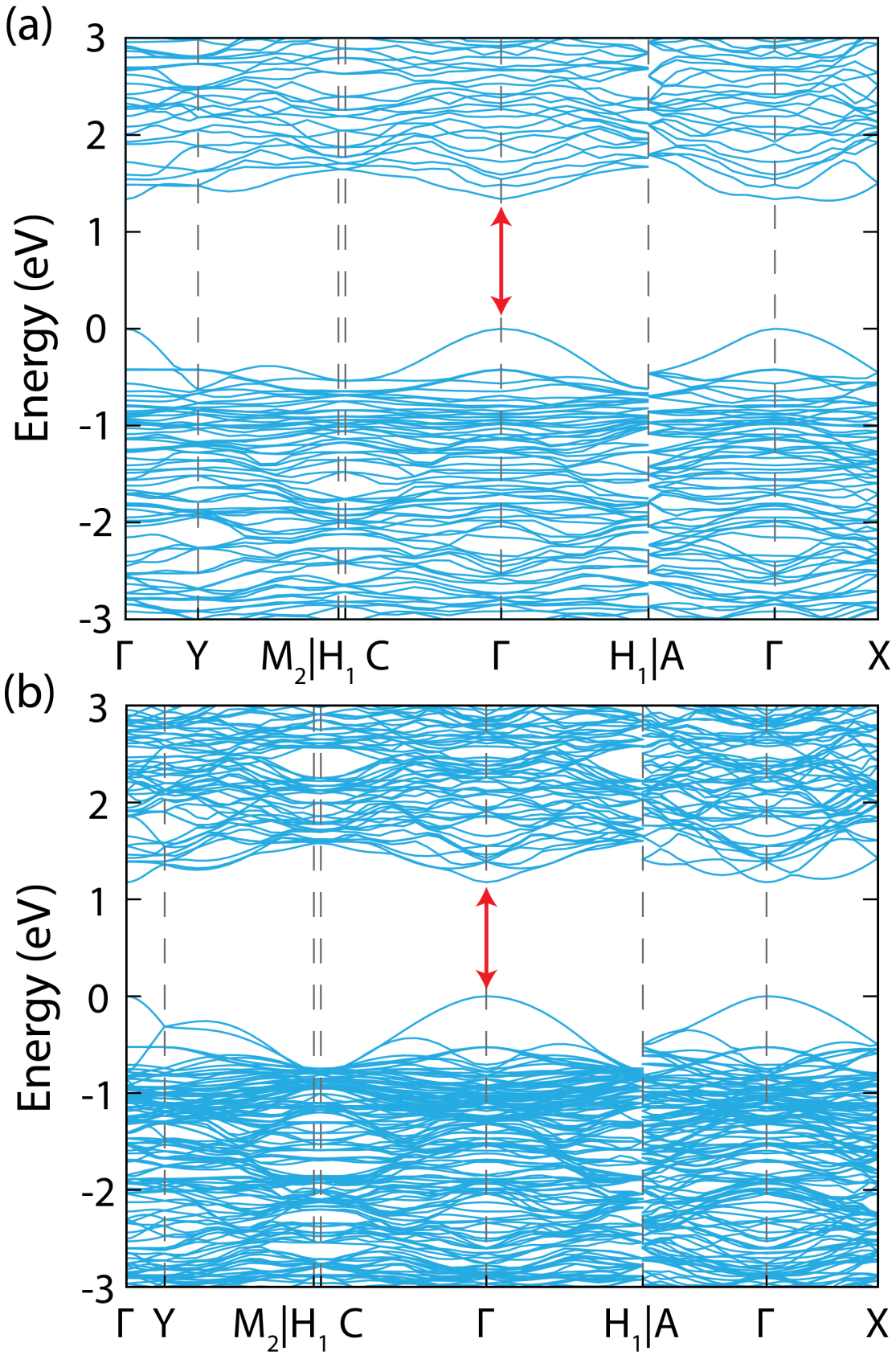

Fig. 3.8 Electronic band structures of *AA*-type stacking of TlGaSe2 (a) and *AB*-stacking (b) using the PBE-GGA functional.

between unit cells, the area of the (001) plane of a unit cell is taken to be *A*. The ground state energy per unit cell of bulk stacking order (*AA*) and a fully defaulted (*AB*) system were calculated, with the resulting stacking fault energies summarised in Table 3.2. The stacking fault energy was determined to be -25.46 mJ m^{-2}, which is remarkable as negative stacking fault energies are only typically only seen in high entropy alloys [64–68]. For additional context, gold is known to readily form stacking faults and has a low stacking fault energy of < 35 mJ m^{-2} [69]. Similarly, brass has a low stacking fault energy of ~ 7 mJ m^{-2} [70]. 2D materials such as graphene show a stacking fault energy of 55 mJ m^{-2} [71].

	AA (Bulk)	AB	AAB
PBE [eV/unit cell]	-234.75962	-234.57563	-234.57615
γ_{SFE} [mJ m^{-2}]		-25.46	-25.37

Table 3.2 Table of energies per unit cell for the bulk (*AA*), *AB*-, and *AAB*-stacking of $TlGaSe_2$, and stacking fault energies for the *AB* and *AAB*-type structures, calculated using DFT [35].

This negative stacking fault energy in $TlGaSe_2$ implies that the stacking faults are intrinsic to the material. However, to establish whether an equilibrium stacking fault distance may exist, an *AAB*-ordered structure was also trailed, with the results summarised in Table 3.2. The negative value and negligible change in the stacking fault energy to -25.37 mJ m^{-2} suggests that there is no equilibrium distance between the faults [64, 66]. The negative stacking fault energy also implies that stacking faults can be easily induced into the system, either through external stimuli or due to the aggressive nature of the TEM sample preparation with a mortar and pestle. Regardless, while short-range domains have been observed in the HAADF-STEM imaging and SAED studies, stacking faults are calculated to be omnipresent in $TlGaSe_2$, which can help explain why no long-range stacking order was observed in the experimental data or previous studies [20, 21].

3.3.2 Preliminary Thermoelectric Studies of $TlGaSe_2$

As shown by the experimental data and the calculations of the stacking fault energies in the previous section, the intrinsic nature of the stacking faults in $TlGaSe_2$ poses an issue when trying to perform thermoelectric studies on the material. A large enough

section of $TlGaSe_2$ that possess no stacking faults is required to perform electrical and thermal conductivity measurements in order to establish the role of stacking faults on the thermoelectric properties. However, due to the intrinsic nature of the faults, growing such a section or having a priori knowledge of which part of the sample is defect-free is not practical or achievable at the time of writing. It is still vital to establish the thermoelectric relationship if the material is to transition to market-ready applications. Therefore, as it was impractical to do so experimentally, the electrical transport and phonon dispersion of $TlGaSe_2$, both with and without stacking faults, were compared via DFT calculations.

It is important to note to the reader that the calculations in this section were outside the scope of the author's remit, and hence were performed on behalf of the reader by collaborators (Akash Bajaj & Rui Dong, Trinity College Dublin).

The Seebeck coefficient is the magnitude of the induced thermoelectric voltage across a material at a given temperature difference [72]. The calculated Seebeck coefficient components at 300 K of both the bulk (*AA*-stacking) and faulted (*AB*-stacking) systems along the [001] stacking direction are shown in Figure 3.9. At the charge neutrality point of 0 eV, there is a slight decrease in Seebeck coefficients from the bulk state (1221 μV K^{-1}) when the stacking faults are introduced (1125 μV K^{-1}).

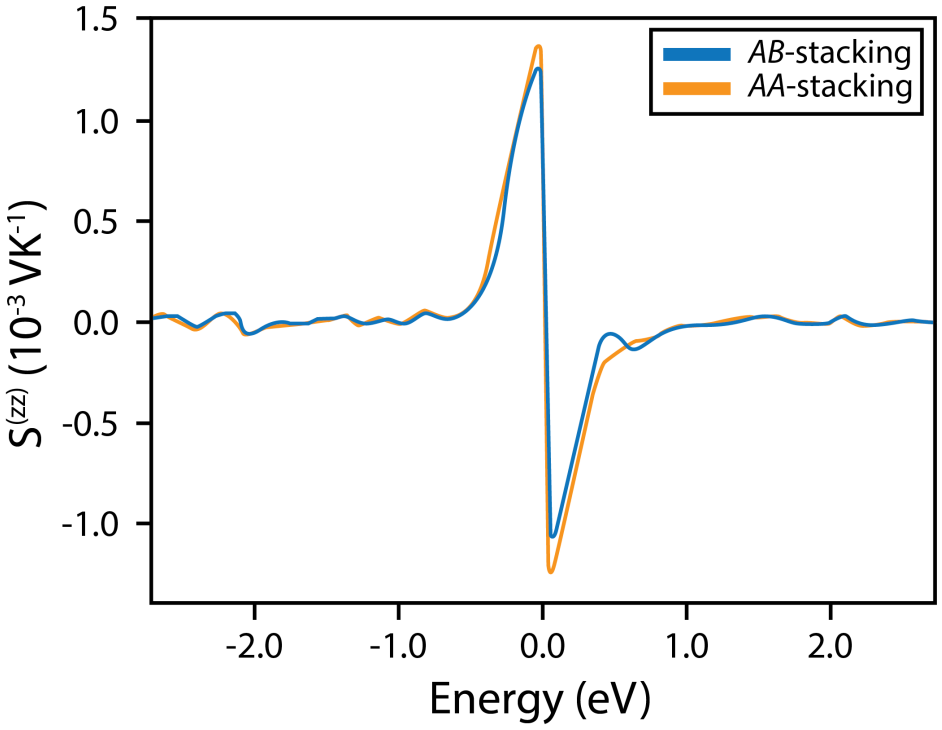

Fig. 3.9 Seebeck coefficient components of $TlGaSe_2$ along the [001] stacking direction at 300 K for *AB*-(blue) and *AA*-stacking (orange) orders.

Many thermoelectric materials consist of centrosymmetric space groups, allowing for isotropic thermoelectric properties and hence the Seebeck coefficient is a single number for a given temperature. However, for non-centrosymmetric space groups and those which possess anisotropic thermoelectric properties, such as 2-D layered materials, the Seebeck coefficient is decomposed into its tensor components [73, 74]. As the stacking faults are along the [001] stacking direction, we are primarily concerned with studying the *zz*-components of the Seebeck coefficient tensor. There are negative Seebeck coefficient values for the *xx*- and *yy*-components, as seen in Table 3.3, as well as some residual negative off-diagonal components.

w/o SF (μV K^{-1})	x	y	z
x	-1047	0	-53
y	0	-1125	0
z	-154	0	1221

w/ SF (μV K^{-1})	x	y	z
x	-1047	0	-53
y	0	-1125	0
z	-154	0	1221

Table 3.3 Seebeck coefficients for $TlGaSe_2$ without and with a stacking fault at 300 K when simulating along the [001] stacking direction of the system. These values are obtained at the charge neutrality point of 0 eV.

For a fair comparison between anisotropic thermoelectric materials, one should consider the symmetry of the material and the direction of measurement. These conditions further illustrate the difficulty in experimentally measuring the thermoelectric properties of $TlGaSe_2$, and hence the required use of computational modelling for this study. Frustratingly, many literature reports on non-centrosymmetric thermoelectric materials simply provide a single value for the Seebeck coefficient, which they calculate as a third of the trace of the Seebeck coefficient tensor, making fair comparisons with other material systems difficult [74, 75]. Nonetheless, $TlGaSe_2$ shows high Seebeck coefficients along the [001] stacking direction when compared to similar layered materials such as $NaSbSe_2$, where $S^{(zz)} = 500\ \mu V\ K^{-1}$ [76].

There are other caveats that should be discussed with these preliminary Seebeck coefficient results. Notably, these calculations were performed under the assumption that the system is undoped, which is not the case as previous experimental results show that $TlGaSe_2$ is a *p*-type semiconductor [12, 13, 77]. Non-doped calculations were therefore first

trialled to establish the correct calculation parameters required before performing doped calculations and work on this is ongoing.

The sign of the Seebeck coefficient is an indication of the type of doping in the semiconductor [36, 78]. When experimental doping values are included, the charge neutrality point would shift into the valence bands and the values of the coefficient would hence be positive, implying *p*-type conductivity. From Figure 3.9, it can be seen that the values would be significantly reduced and be far more similar. This further implies that the stacking fault has a negligible role in the Seebeck coefficient along the [001] stacking direction.

The lack of significant change in the electric properties with the introduction of stacking faults can also be seen in the electrical conductivity coefficient component along the [001] stacking direction at 300 K in Figure 3.10. The band gaps of both structures are smaller than their experimentally measured values of ~ 2.1 eV [10, 13, 79] due to the use of the PBE-GGA functionals in these calculations [63], as was also shown in Figure 3.8. Despite this, there is negligible change around the valence band maximum of the electrical conductivity with the introduction of stacking faults into $TlGaSe_2$.

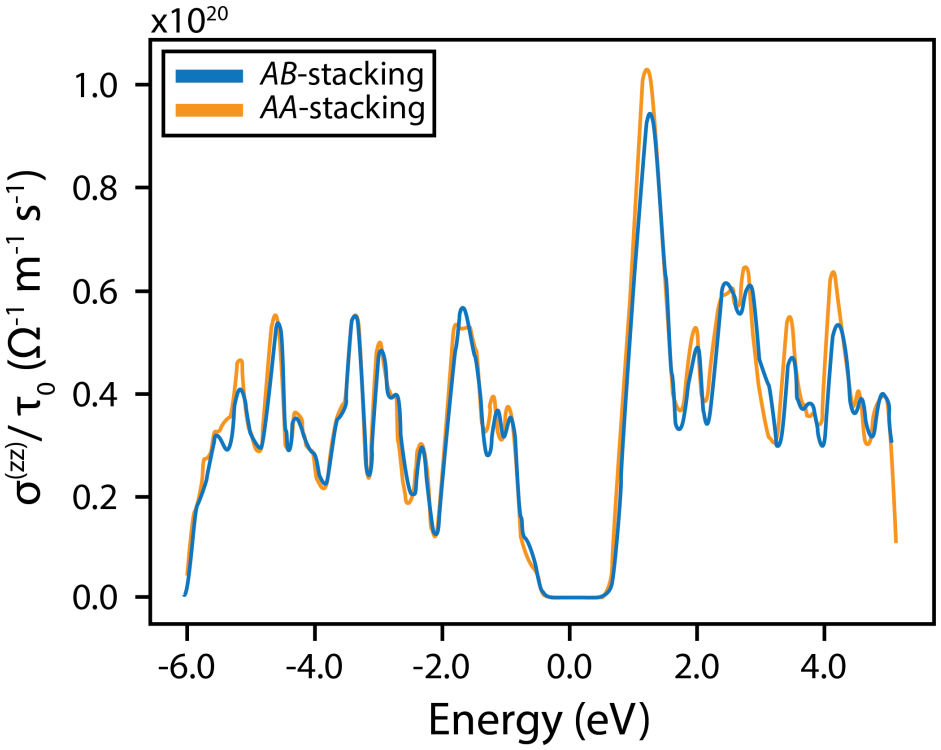

Fig. 3.10 Electrical conductivity (in the constant relaxation-time approximation) coefficient components of $TlGaSe_2$ along the [001] stacking direction for *AB*-(blue) and *AA*-stacking (orange) orders.

The numerator of the thermoelectric figure of merit ZT, shown in Equation 3.1, can be used as a measure of the thermoelectric power of a material. This is a useful measurement as measuring thermal transport properties experimentally can be quite non-trivial, especially for 2-D materials [75, 80–83]. Figure 3.11 highlights the thermoelectric power factor components of $TlGaSe_2$ both with and without a stacking fault. While there is some change at the valence band maximum with the introduction of the stacking faults, the effect is insignificant when in comparison to the introduction of Se vacancies [18]. The variation may also be due to numerical error carried over from the Seebeck coefficient and electrical conductivity calculations, and hence, further optimisation of both is required to remove these errors.

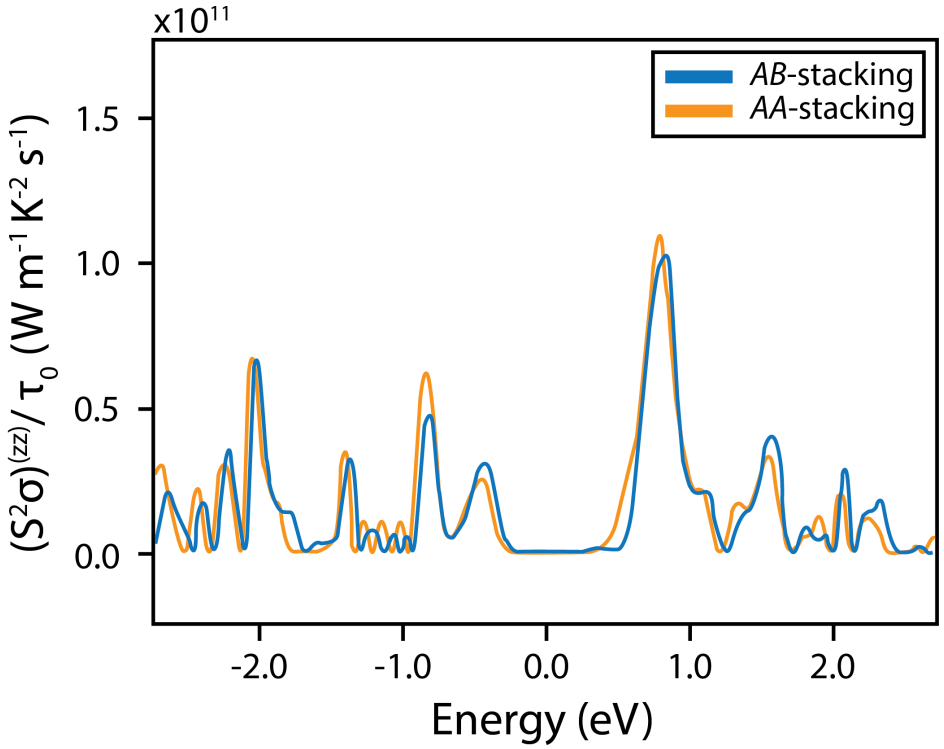

Fig. 3.11 Thermoelectric power factor components of $TlGaSe_2$ along the [001] stacking direction for *AB*-(blue) and *AA*-stacking (orange) orders.

To understand how the phonons, and ultimately the thermal properties, are affected by the presence of the stacking fault, a series of phonon dispersions were calculated. Using the high-symmetry points of the $TlGaSe_2$ Brillouin zone in Figure 3.7, the phonon dispersions along high-symmetry paths on the *xy*-, *xz*-, and *yz*-planes are shown in Figures 3.12, 3.13 and 3.14, respectively.

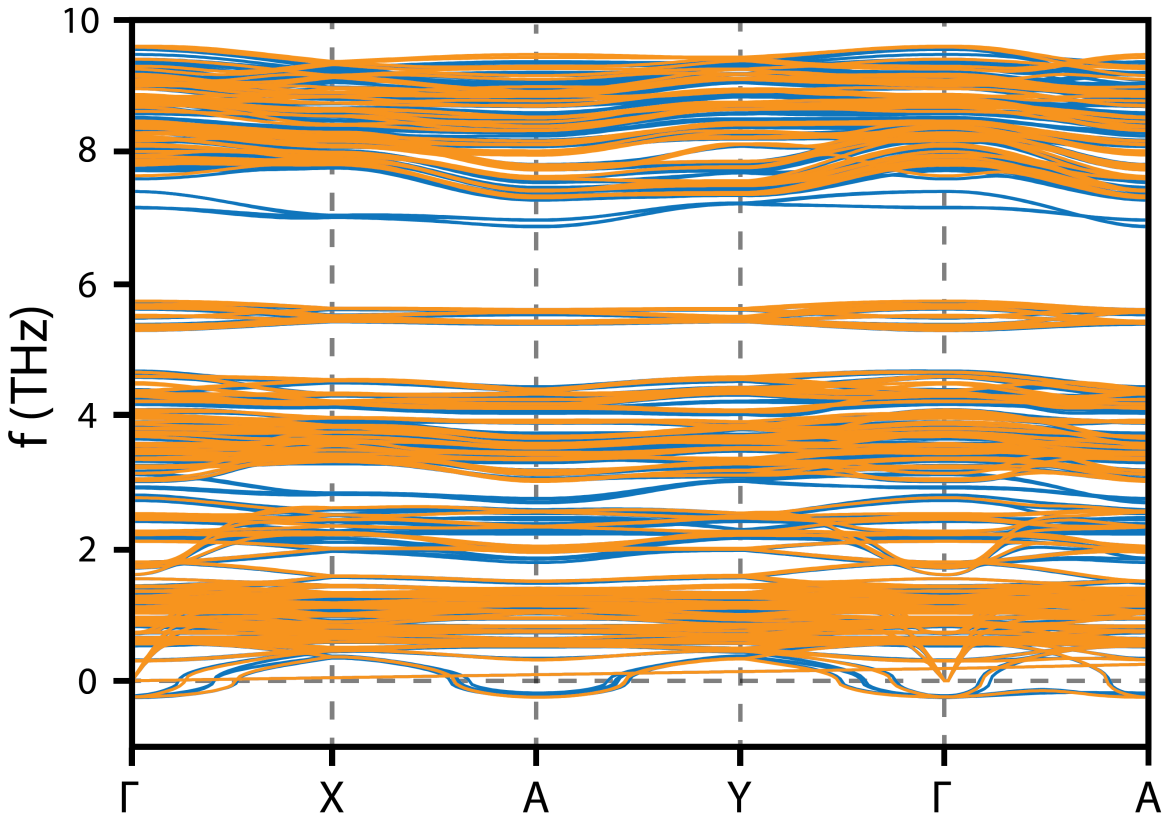

Fig. 3.12 Phonon dispersion along high-symmetry points on the *xy*-plane of the $TlGaSe_2$ reciprocal lattice in Figure 3.7 for *AB*-(blue) and *AA*-stacking (orange) orders.

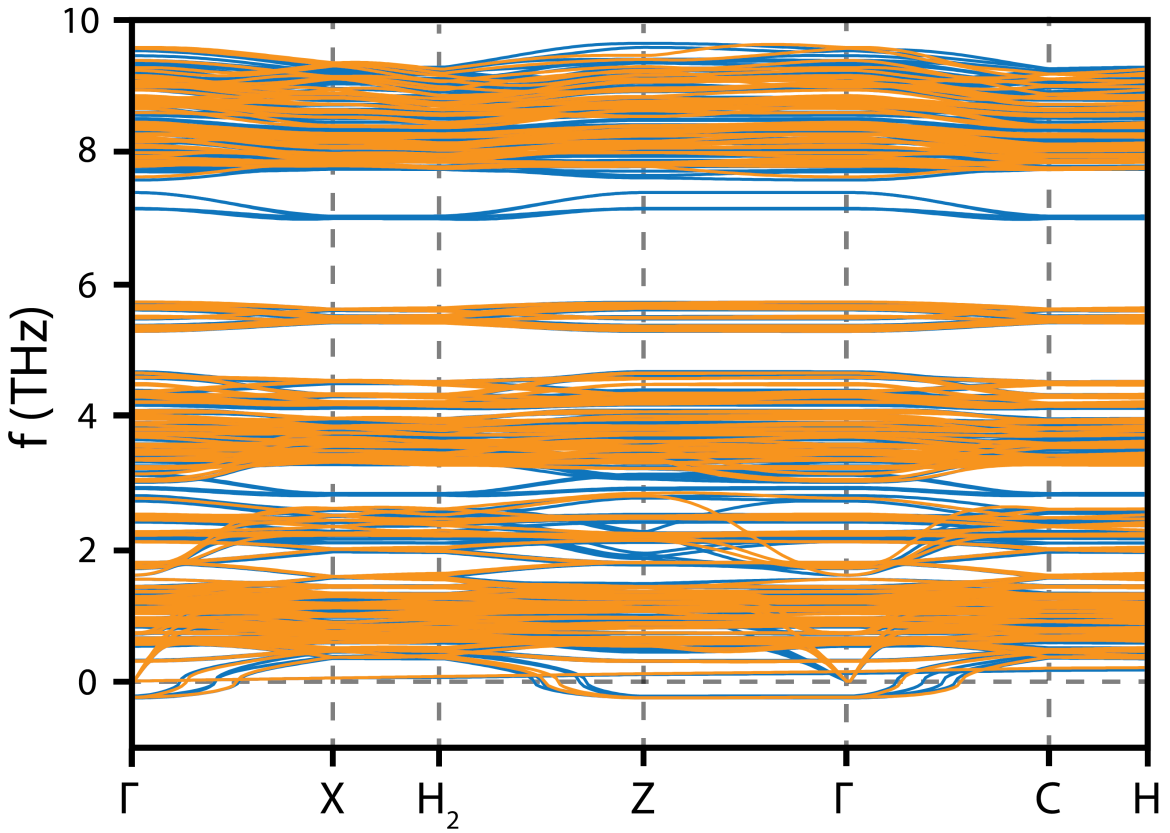

Fig. 3.13 Phonon dispersion along high-symmetry points on the *xz*-plane of the $TlGaSe_2$ reciprocal lattice in Figure 3.7 for *AB*-(blue) and *AA*-stacking (orange) orders.

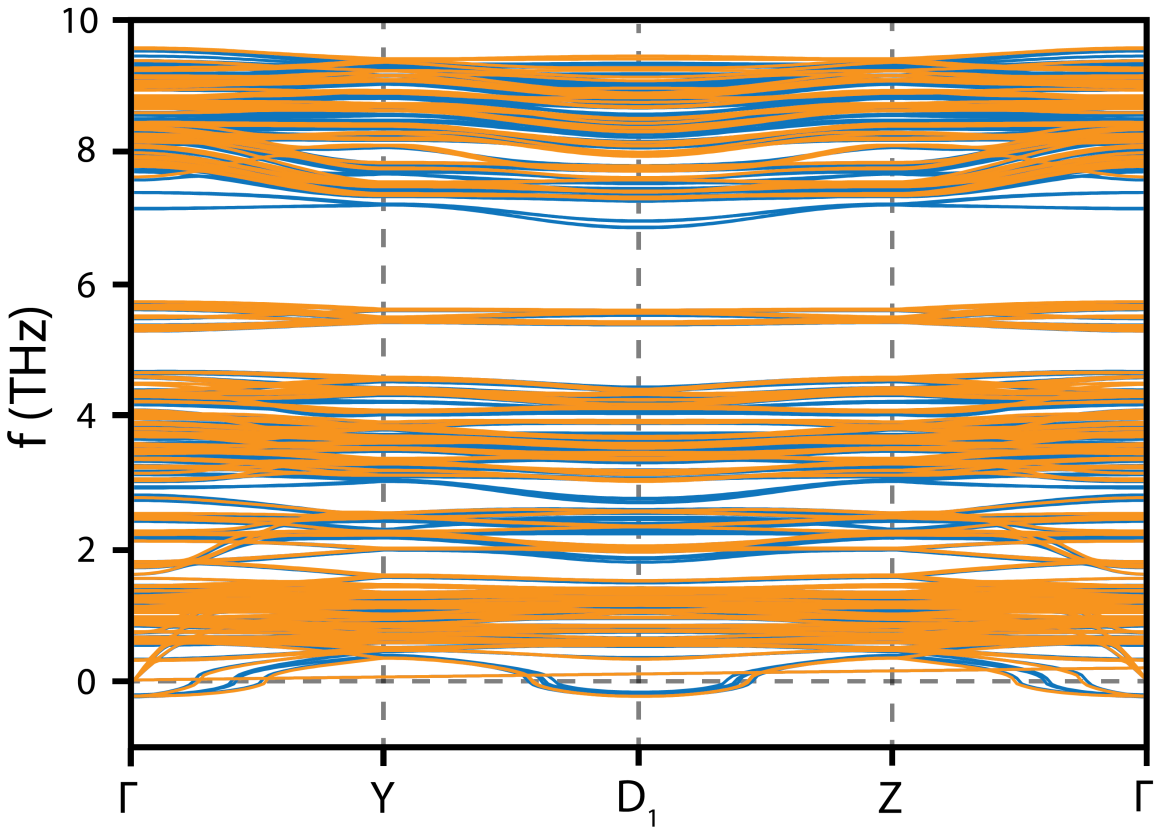

Fig. 3.14 Phonon dispersion along high-symmetry points on the *yz*-plane of the $TlGaSe_2$ reciprocal lattice in Figure 3.7 for *AB*-(blue) and *AA*-stacking (orange) orders.

A number of key observations can be made from this data. Notably, for the most part, the phonon frequencies and bands in both the bulk and defected systems are the same. Interestingly, there are additional modes at ~ 3 and ~ 7 THz when the stacking fault is included, which are not present in the bulk structure. These observations are more clearly seen in the total phonon density of states (DOS) in Figure 3.15.

The presence of these modes may have arisen from the suppression of certain modes from the bulk state when the stacking fault is induced due to increased scattering [22, 84, 85]. However, the lack of significant change in the phonon DOS in Figure 3.15, bar the presence of these new modes, does not make this conclusion obvious. Careful analysis and assignment of the bands is required in order to fully understand the nature of these modes.

As can also be seen in these phonon dispersions and DOS is the evidence of negative phonon frequencies at certain high-symmetry points, especially at the Γ point. Phonon frequencies are given by the square root of the eigenvalues of the dynamical matrix, and hence the presence of negative phonon frequencies may be an indication of system in-

stability [86]. However, both systems have very similar negative phonon frequencies, and hence it is believed that their presence is due to calculation error.

As mentioned in Chapter 2.4, DFT scales with N^3 where N is the number of basis functions used to descibe the system. Therefore, to reduce computational costs, the tilt of the c lattice vector was fixed such that it was precisely 1/4 of the a lattice vector, allowing for the reduction of the unit cell due to symmetry. However, this may have led to the structure not being fully relaxed before applying the finite displacements treatment to calculate the phonon frequencies, resulting in the appearance of negative phonons in both systems. Work is underway to alleviate this via the use of the original cells in the calculations. The use of a larger supercell and larger displacement values may also improve accuracy for the other phonon bands but at a large computational cost.

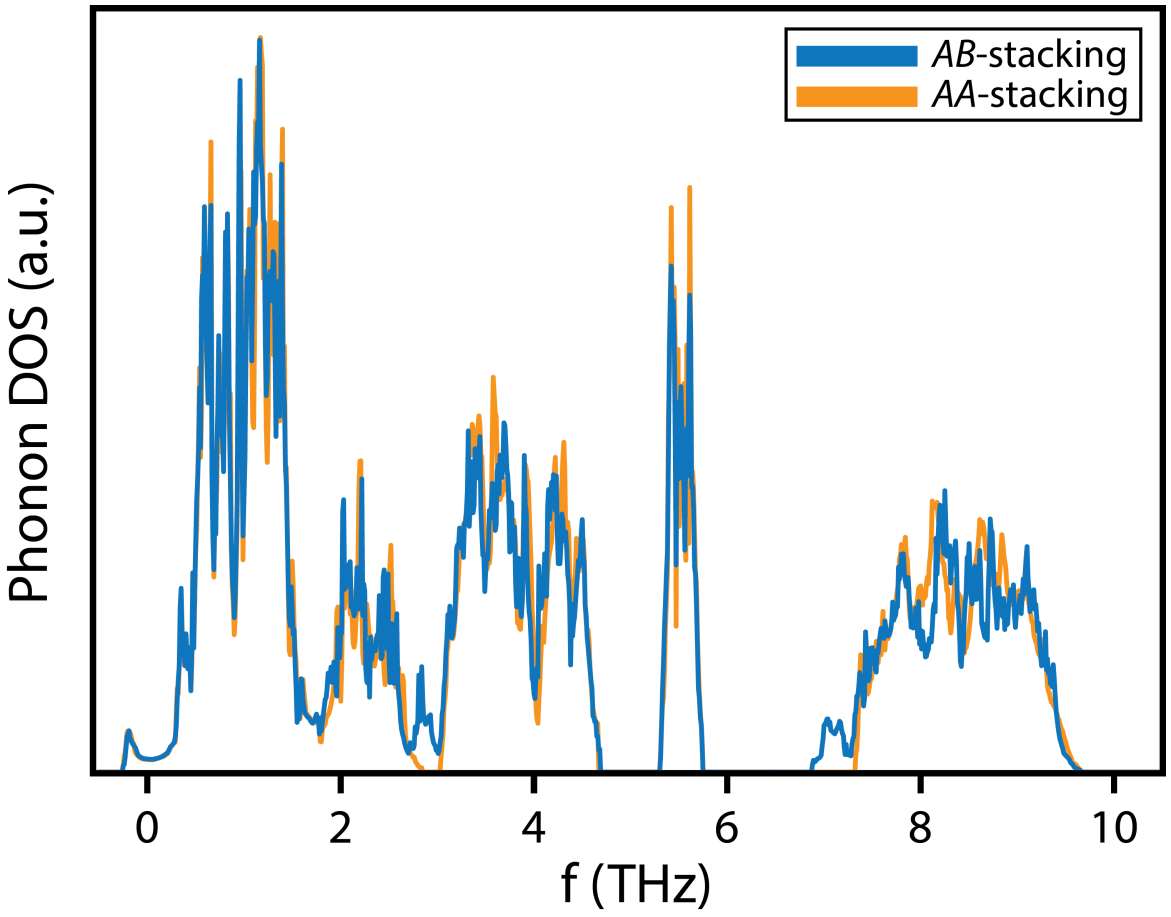

Fig. 3.15 Total phonon density of states of $TlGaSe_2$ for *AB*-(blue) and *AA*-stacking (orange) orders.

Nonetheless, the presence of these modes at ~ 3 and ~ 7 THz does imply that the stacking faults do have an effect on the vibrational properties, and hence the thermal properties, of the system. This is in contrast to the electrical transport calculations which showed

a lack of change when the stacking faults are included. However, further optimisation of both sets of calculations is required before a definitive conclusion on the role of the stacking faults on the thermoelectric properties of $TlGaSe_2$ can be established.

3.4 Conclusions

The novel layered ternary chalcogenide $TlGaSe_2$ was structurally characterised via the use of TEM-based methods and its thermoelectric properties were probed via the use of DFT calculations. HAADF-STEM imaging and SAED patterns of the material revealed the ubiquitous nature of stacking faults throughout the system, which was confirmed via the use of multislice and diffraction simulations. Short-range domains of stacking order were observed, but DFT calculations showed that the stacking faults are intrinsic to the material, confirming the lack of long-range stacking order.

Due to this intrinsic property of the stacking faults, it was deemed more practical to perform DFT calculations to understand their role in the thermoelectric properties of the material rather than via experimentation. Preliminary electrical transport calculations reveal negligible change to the Seebeck coefficient or electrical conductance of the material along the [001] stacking direction when stacking faults are introduced. However, phonon dispersions of the bulk and faulted system show an introduction of phonon frequencies at about ~ 3 and ~ 7 THz when stacking faults are introduced. This may imply the suppression of phonon modes, and hence of thermal transport properties, when stacking faults are present. The presence of negative phonon frequencies for both systems indicates calculation errors, and hence further optimisations of these calculations, along with the electrical transport calculations, are required before a qualitative conclusion can be made. Regardless, it can be seen that the stacking faults do possess some role in the thermoelectric properties of $TlGaSe_2$, and further analysis of this is required before such a material can progress to devices and commercial applications.

References

[1] Dan Zhao et al. “Ionic thermoelectric gating organic transistors”. In: *Nature Communications 2017 8:1* 8.1 (2017), pp. 1–7. DOI: 10.1038/ncomms14214.

[2] Xiaojian Liao et al. “Extremely low thermal conductivity and high electrical conductivity of sustainable carbonceramic electrospun nonwoven materials”. In: *Science Advances* 9.13 (2023). ISSN: 2375-2548. DOI: 10.1126/sciadv.ade6066.

[3] Jose Manuel Sojo Gordillo et al. “Recent advances in silicon-based nanostructures for thermoelectric applications”. In: *APL Materials* 11.4 (2023), p. 40702. ISSN: 2166532X. DOI: 10.1063/5.0134208/2884093.

[4] Hao Deng, Bohang Nan, and Guiying Xu. “Innovative Design of Bismuth-Telluride-Based Thermoelectric Transistors”. In: *Materials 2023, Vol. 16, Page 5536* 16.16 (2023), p. 5536. ISSN: 1996-1944. DOI: 10.3390/MA16165536.

[5] Hiroki Yoshihama and Hiromasa Kaneko. “Design of thermoelectric materials with high electrical conductivity, high Seebeck coefficient, and low thermal conductivity”. In: *Analytical Science Advances* 2.5-6 (2021), pp. 289–294. ISSN: 2628-5452. DOI: 10.1002/ansa.202000114.

[6] Allon I. Hochbaum et al. “Enhanced thermoelectric performance of rough silicon nanowires”. In: *Nature* 451.7175 (2008), pp. 163–167. ISSN: 00280836. DOI: 10.1038/nature06381.

[7] Jiangtao Wei et al. “Review of current high-ZT thermoelectric materials”. In: *Journal of Materials Science* 55.27 (2020), pp. 12642–12704. ISSN: 15734803. DOI: 10.1007/s10853-020-04949-0.

[8] A. M. Panich. “Electronic properties and phase transitions in low-dimensional semiconductors”. In: *Journal of Physics Condensed Matter* 20.29 (2008). ISSN: 09538984. DOI: 10.1088/0953-8984/20/29/293202.

[9] S Duman and B Gürbulak. “ Urbach Tail and Optical Absorption in Layered Semiconductor TlGaSe 2(1- x) S 2 x Single Crystals ”. In: *Physica Scripta* 72.1 (2005), pp. 79–86. ISSN: 0031-8949. DOI: 10.1238/physica.regular.072a00079.

[10] H.T. Shaban. “Characterization of TlGaSe2 single crystals”. In: *Physica B: Condensed Matter* 405.8 (2010), pp. 1951–1954. ISSN: 09214526. DOI: 10.1016/j.physb.2009.08.018.

[11] Simon Johnsen et al. “Thallium chalcogenide-based wide-band-gap semiconductors: TlGaSe 2 for radiation detectors”. In: *Chemistry of Materials* 23.12 (2011), pp. 3120–3128. ISSN: 08974756. DOI: 10.1021/cm200946y.

[12] Shengxue Yang et al. “Ultrathin ternary semiconductor TlGaSe2 phototransistors with Broad-spectral response”. In: *2D Materials* 4.3 (2017). ISSN: 20531583. DOI: 10.1088/2053-1583/aa80c7.

[13] Asuman Cengiz et al. “Origin of the optical absorption of TlGaSe2 layered semiconductor in the visible range”. In: *Semiconductor Science and Technology* 33.7 (2018). ISSN: 13616641. DOI: 10.1088/1361-6641/aac97b.

[14] F. Quinlan et al. “A 12.5 GHz-spaced optical frequency comb spanning >400 nm for near-infrared astronomical spectrograph calibration”. In: *Review of Scientific Instruments* 81.6 (2010), p. 63105. ISSN: 00346748. DOI: 10.1063/1.3436638/352762. arXiv: 1002.4354.

[15] Tobias Wilken et al. “A spectrograph for exoplanet observations calibrated at the centimetre-per-second level”. In: *Nature* 485.7400 (2012), pp. 611–614. ISSN: 1476-4687. DOI: 10.1038/nature11092.

[16] Kyeong Ae Yee and Thomas A. Albright. “Bonding and Structure of TlGaSe”. In: *Journal of the American Chemical Society* 113.17 (1991), pp. 6474–6478. ISSN: 15205126. DOI: 10.1021/ja00017a018.

[17] F. A. Mikailov et al. “Phase transitions and metastable states in TlGaSe2”. In: *Phase Transitions* 76.12 (2003), pp. 1057–1064. DOI: 10.1080/01411590310001603690.

[18] Murat Çaydaşı et al. “A Study of Thermoelectric Performance of TlGaSe 2 Layered Dichalcogenides from First-Principles Calculations: Vacancy Defects Modeling and Engineering”. In: *physica status solidi (b)* 259.1 (2022), p. 2100409. ISSN: 0370-1972. DOI: 10.1002/pssb.202100409.

[19] I. M. Ashraf et al. “Development and characterization of TlGaSe2 thin film-based photodetector for visible-light photodetector applications”. In: *Optical Materials* 103.December 2019 (2020), p. 109834. ISSN: 09253467. DOI: 10.1016/j.optmat.2020.109834.

[20] D. F. McMorrow et al. “The structure of the paraelectric and incommensurate phases of TlGaSe 2”. In: *Journal of Physics: Condensed Matter* 2.16 (1990), pp. 3699–3712. ISSN: 09538984. DOI: 10.1088/0953-8984/2/16/001.

[21] L. Kienle et al. “Real structure of KInS2 polytypes”. In: *Journal of Solid State Chemistry* 177.1 (2004), pp. 6–16. ISSN: 00224596. DOI: 10.1016/S0022-4596(03)00244-5.

[22] Junqin Li et al. “Stacking Fault-Induced Minimized Lattice Thermal Conductivity in the High-Performance GeTe-Based Thermoelectric Materials upon Bi2Te3 Alloying”. In: *ACS Applied Materials and Interfaces* 11.22 (2019), pp. 20064–20072. ISSN: 19448252. DOI: 10.1021/acsami.9b04984.

[23] Eli Sutter et al. “Stacking Fault Induced Symmetry Breaking in van der Waals Nanowires”. In: *ACS Nano* 16 (2022), 21199–21207. DOI: 10.1021/acsnano.2c09172.

[24] K. Vuttivorakulchai, M. Luisier, and A. Schenk. “Effect of stacking faults and surface roughness on the thermal conductivity of InAs nanowires”. In: *Journal of Applied Physics* 124.20 (2018). ISSN: 10897550. DOI: 10.1063/1.5051677.

[25] Chunlei Wan et al. “Nanoscale stacking faults induced low thermal conductivity in thermoelectric layered metal sulfides”. In: *Applied Physics Letters* 100.10 (2012), pp. 0–4. ISSN: 00036951. DOI: 10.1063/1.3691887.

[26] Robin Lefèvre et al. “Layered tellurides: stacking faults induce low thermal conductivity in the new In2Ge2Te6 and thermoelectric properties of related compounds”. In: *Journal of Materials Chemistry A* 5.36 (2017), pp. 19406–19415. ISSN: 2050-7488. DOI: 10.1039/C7TA04810F.

[27] Lewys Jones et al. “Smart Align-a new tool for robust non-rigid registration of scanning microscope data”. In: *Advanced Structural and Chemical Imaging* 1.1 (2015), pp. 1–16. ISSN: 21980926. DOI: 10.1186/s40679-015-0008-4.

[28] Xiahan Sang and James M. LeBeau. “Revolving scanning transmission electron microscopy: Correcting sample drift distortion without prior knowledge”. In: *Ultramicroscopy* 138 (2014), pp. 28–35. ISSN: 18792723. DOI: 10.1016/j.ultramic.2013.12.004.

[29] Lucas M. Hale, Zachary T. Trautt, and Chandler A. Becker. “Evaluating variability with atomistic simulations: the effect of potential and calculation methodology on the modeling of lattice and elastic constants”. In: *Modelling and Simulation in Materials Science and Engineering* 26.5 (2018), p. 055003. ISSN: 0965-0393. DOI: 10.1088/1361-651X/AABC05.

[30] Yusuke Seto and Masahiro Ohtsuka. “ReciPro: free and open-source multipurpose crystallographic software integrating a crystal model database and viewer, diffraction and microscopy simulators, and diffraction data analysis tools”. In: *Journal of Applied Crystallography* 55.2 (2022), pp. 397–410. ISSN: 1600-5767. DOI: 10.1107/S1600576722000139.

[31] Jacob Madsen and Toma Susi. “The abTEM code: transmission electron microscopy from first principles”. In: *Open Research Europe* 1 (2021), p. 24. DOI: 10.12688/openreseurope.13015.2.

[32] Earl J. Kirkland. *Advanced Computing in Electron Microscopy*. July. Boston, MA: Springer US, 2010, pp. 1–23. ISBN: 978-1-4419-6532-5. DOI: 10.1007/978-1-4419-6533-2.

[33] G. Kresse and J. Furthmüller. “Efficient iterative schemes for ab initio total energy calculations using a plane wave basis set”. In: *Physical Review B - Condensed Matter*

and Materials Physics 54.16 (1996), pp. 11169–11186. ISSN: 1550235X. DOI: 10.1103/PhysRevB.54.11169.

[34] G. Kresse and D. Joubert. "From ultrasoft pseudopotentials to the projector augmented wave method". In: *Physical Review B* 59.3 (1999), pp. 1758–1775. ISSN: 0163-1829. DOI: 10.1103/PhysRevB.59.1758.

[35] John P. Perdew, Kieron Burke, and Matthias Ernzerhof. "Generalized gradient approximation made simple". In: *Physical Review Letters* 77.18 (1996), pp. 3865–3868. ISSN: 10797114. DOI: 10.1103/PhysRevLett.77.3865.

[36] Georg K.H. Madsen, Jesús Carrete, and Matthieu J. Verstraete. "BoltzTraP2, a program for interpolating band structures and calculating semi-classical transport coefficients". In: *Computer Physics Communications* 231 (2018), pp. 140–145. ISSN: 0010-4655. DOI: 10.1016/J.CPC.2018.05.010. arXiv: 1712.07946.

[37] José M. Soler et al. "The SIESTA method for ab initio order-N materials simulation". In: *Journal of Physics: Condensed Matter* 14.11 (2002), pp. 2745–2779. ISSN: 0953-8984. DOI: 10.1088/0953-8984/14/11/302. arXiv: 0111138 [cond-mat].

[38] Jasprit Singh. *Modern Physics for Engineers*. Wiley, 1999. ISBN: 9780471330448. DOI: 10.1002/9783527617685.

[39] S Froyen et al. *ATOM documentation - https://docs.siesta-project.org/projects/atom/en/latest/index.html*. (accessed 2023-11-10).

[40] Volker Blum et al. "Ab initio molecular simulations with numeric atom-centered orbitals". In: *Computer Physics Communications* 180.11 (2009), pp. 2175–2196. ISSN: 0010-4655. DOI: 10.1016/J.CPC.2009.06.022.

[41] K. Parlinski, Z. Q. Li, and Y. Kawazoe. "First-Principles Determination of the Soft Mode in Cubic ZrO2". In: *Physical Review Letters* 78.21 (1997), pp. 4063–4066. ISSN: 0031-9007. DOI: 10.1103/PhysRevLett.78.4063.

[42] Jonathan M. Skelton et al. "Lattice dynamics of the tin sulphides SnS 2 , SnS and Sn 2 S 3 : vibrational spectra and thermal transport". In: *Physical Chemistry Chemical Physics* 19.19 (2017), pp. 12452–12465. ISSN: 1463-9076. DOI: 10.1039/C7CP01680H.

[43] Atsushi Togo. “First-principles Phonon Calculations with Phonopy and Phono3py”. In: *Journal of the Physical Society of Japan* 92.1 (2023). ISSN: 0031-9015. DOI: 10.7566/JPSJ.92.012001.

[44] Atsushi Togo et al. “Implementation strategies in phonopy and phono3py”. In: *Journal of Physics: Condensed Matter* 35.35 (2023), p. 353001. ISSN: 0953-8984. DOI: 10.1088/1361-648X/acd831. arXiv: 2301.05784.

[45] Thomas D. Kühne et al. “CP2K: An electronic structure and molecular dynamics software package - Quickstep: Efficient and accurate electronic structure calculations”. In: *The Journal of Chemical Physics* 152.19 (2020), p. 194103. ISSN: 0021-9606. DOI: 10.1063/5.0007045. arXiv: 2003.03868.

[46] Stefan Grimme. “Accurate description of van der Waals complexes by density functional theory including empirical corrections”. In: *Journal of Computational Chemistry* 25.12 (2004), pp. 1463–1473. ISSN: 01928651. DOI: 10.1002/jcc.20078.

[47] W. Henkel et al. “High-pressure Raman study of the ternary chalcogenides TlGaS2, TlGaSe2, TlInS2, and TlInSe2”. In: *Physical Review B* 26.6 (1982), p. 3211. ISSN: 01631829. DOI: 10.1103/PhysRevB.26.3211.

[48] Range Klaus-Jürgen, Gunther Mahlberg, and Sigrid Obenland. *Hochdruckphasen von TlAlSe2 und TlGaSe2 mit TlSe-Struktur*. 1977. DOI: 10.1515/znb-1977-1129.

[49] Toma Susi, Jannik C. Meyer, and Jani Kotakoski. “Quantifying transmission electron microscopy irradiation effects using two-dimensional materials”. In: *Nature Reviews Physics* 1.6 (2019), pp. 397–405. ISSN: 2522-5820. DOI: 10.1038/s42254-019-0058-y.

[50] Rik Brydson, ed. *Aberration-Corrected Analytical Transmission Electron Microscopy*. Wiley, 2011, p. 280. ISBN: 978-1-119-97990-6.

[51] Yi Jiang et al. “Electron ptychography of 2D materials to deep sub-ångström resolution”. In: *Nature* 559.7714 (2018), pp. 343–349. ISSN: 0028-0836. DOI: 10.1038/s41586-018-0298-5.

[52] Gerardo Algara-Siller et al. “The pristine atomic structure of MoS2 monolayer protected from electron radiation damage by graphene”. In: *Applied Physics Letters* 103.20 (2013), p. 203107. ISSN: 00036951. DOI: 10.1063/1.4830036/130097. arXiv: 1310.2411.

[53] Recep Zan et al. “Control of Radiation Damage in MoS 2 by Graphene Encapsulation”. In: *ACS Nano* 7.11 (2013), pp. 10167–10174. ISSN: 1936-0851. DOI: 10.1021/nn4044035.

[54] David B. Williams and C. Barry Carter. *Transmission electron microscopy: A textbook for materials science*. 2009, pp. 1–760. ISBN: 9780387765006. DOI: 10.1007/978-0-387-76501-3.

[55] Tiarnan Mullarkey et al. “Using Your Beam Efficiently: Reducing Electron Dose in the STEM via Flyback Compensation”. In: *Microscopy and Microanalysis* 28.4 (2022), pp. 1428–1436. ISSN: 14358115. DOI: 10.1017/S1431927621013908. arXiv: 2107.02066.

[56] A G Fitzgerald and M Mannami. “Electron Diffraction From Crystal Defects: Fraunhofer Effects From Plane Faults”. In: *Proceedings of the Royal Society of London. Series A, Mathematical and Physical Sciences* 293.1433 (1966), pp. 169–180. ISSN: 00804630.

[57] S. R. Hall and B. McMahon, eds. *International Tables for Crystallography*. Vol. G. International Tables for Crystallography. Chester, England: International Union of Crystallography, 2006. ISBN: 978-1-4020-5411-2. DOI: 10.1107/97809553602060000107.

[58] Wahyu Setyawan and Stefano Curtarolo. “High-throughput electronic band structure calculations: Challenges and tools”. In: *Computational Materials Science* 49.2 (2010), pp. 299–312. ISSN: 09270256. DOI: 10.1016/j.commatsci.2010.05.010. arXiv: 1004.2974.

[59] Bonan Zhu, Seán R Kavanagh, and David Scanlon. “easyunfold: A Python package for unfolding electronic band structures”. In: *Journal of Open Source Software* 9.93 (2024), p. 5974. ISSN: 2475-9066. DOI: 10.21105/joss.05974.

[60] Pedro Borlido et al. “Exchange-correlation functionals for band gaps of solids: benchmark, reparametrization and machine learning”. In: *npj Computational Materials* 6.1 (2020), p. 96. ISSN: 2057-3960. DOI: 10.1038/s41524-020-00360-0.

[61] Jason M. Crowley, Jamil Tahir-Kheli, and William A. Goddard. “Resolution of the Band Gap Prediction Problem for Materials Design”. In: *The Journal of Physical Chemistry Letters* 7.7 (2016), pp. 1198–1203. ISSN: 1948-7185. DOI: 10.1021/acs.jpclett.5b02870.

[62] John P. Perdew et al. “Restoring the density-gradient expansion for exchange in solids and surfaces”. In: *Physical Review Letters* 100.13 (2007). DOI: 10.1103/PhysRevLett.100.136406. arXiv: 0711.0156v3.

[63] Jochen Heyd, Gustavo E. Scuseria, and Matthias Ernzerhof. “Hybrid functionals based on a screened Coulomb potential”. In: *The Journal of Chemical Physics* 118.18 (2003), pp. 8207–8215. ISSN: 0021-9606. DOI: 10.1063/1.1564060.

[64] Zongrui Pei et al. “Hidden Effects of Negative Stacking Fault Energies in Complex Concentrated Alloys”. In: *Physical Review Letters* 126.25 (2021), p. 255502. ISSN: 0031-9007. DOI: 10.1103/PhysRevLett.126.255502.

[65] Norihiko L. Okamoto et al. “Size effect, critical resolved shear stress, stacking fault energy, and solid solution strengthening in the CrMnFeCoNi high-entropy alloy”. In: *Scientific Reports* 6.1 (2016), pp. 1–10. ISSN: 2045-2322. DOI: 10.1038/srep35863.

[66] Mulaine Shih et al. “Stacking fault energy in concentrated alloys”. In: *Nature Communications 2021 12:1* 12.1 (2021), pp. 1–10. ISSN: 2041-1723. DOI: 10.1038/s41467-021-23860-z.

[67] Shijun Zhao et al. “Local-environment dependence of stacking fault energies in concentrated solid-solution alloys”. In: *npj Computational Materials* 5.1 (2019), pp. 1–7. ISSN: 2057-3960. DOI: 10.1038/s41524-019-0150-y.

[68] A. J. Zaddach et al. “Mechanical Properties and Stacking Fault Energies of NiFeCrCoMn High-Entropy Alloy”. In: *Journal of The Minerals, Metals & Materials Society* 65.12 (2013), pp. 1780–1789. ISSN: 1047-4838. DOI: 10.1007/s11837-013-0771-4.

[69] Anuj Goyal et al. “The influence of alloying on the stacking fault energy of gold from density functional theory calculations”. In: *Computational Materials Science* 188 (2021), p. 110236. ISSN: 0927-0256. DOI: 10.1016/J.COMMATSCI.2020.110236.

[70] Ehab El-Danaf, Surya R. Kalidindi, and Roger D. Doherty. “Influence of grain size and stacking-fault energy on deformation twinning in fcc metals”. In: *Metallurgical and Materials Transactions A* 30.5 (1999), pp. 1223–1233. ISSN: 1073-5623. DOI: 10.1007/s11661-999-0272-9.

[71] Songsong Zhou et al. “van der Waals bilayer energetics: Generalized stacking-fault energy of graphene, boron nitride, and graphene/boron nitride bilayers”. In: *Physical Review B* 92.15 (2015), p. 155438. ISSN: 1098-0121. DOI: 10.1103/PhysRevB.92.155438.

[72] Lidong Chen, Ruiheng Liu, and Xun Shi. “General principles of thermoelectric technology”. In: *Thermoelectric Materials and Devices*. Elsevier, 2021, pp. 1–18. ISBN: 978-0-12-818413-4. DOI: 10.1016/B978-0-12-818413-4.00001-6.

[73] Robert E. Newnham. *Thermoelectricity*. Oxford University Press, 2004, pp. 234–242. ISBN: 9780198520757. DOI: 10.1093/oso/9780198520757.001.0001.

[74] Jing Wu et al. “Perspectives on Thermoelectricity in Layered and 2D Materials”. In: *Advanced Electronic Materials* 4.12 (2018), p. 1800248. ISSN: 2199-160X. DOI: 10.1002/aelm.201800248.

[75] Myoung-Jae Lee et al. “Thermoelectric materials by using two-dimensional materials with negative correlation between electrical and thermal conductivity”. In: *Nature Communications* 7.1 (2016), p. 12011. ISSN: 2041-1723. DOI: 10.1038/ncomms12011.

[76] Aditya Putatunda et al. “Thermoelectric properties of layered NaSbSe 2”. In: *Journal of Physics: Condensed Matter* 30.22 (2018), p. 225501. ISSN: 0953-8984. DOI: 10.1088/1361-648X/aabf5b.

[77] G. Makhnovets et al. “Phase diagram and specific band gap features of novel TlGaSe2: Zn+2(Cd+2, Hg+2) crystals”. In: *Journal of Alloys and Compounds* 768 (2018), pp. 667–675. ISSN: 09258388. DOI: 10.1016/j.jallcom.2018.07.282.

[78] Joseph R. Sootsman, Duck Young Chung, and Mercouri G. Kanatzidis. “New and Old Concepts in Thermoelectric Materials”. In: *Angewandte Chemie International Edition* 48.46 (2009), pp. 8616–8639. ISSN: 1433-7851. DOI: 10.1002/anie.200900598.

[79] G Abdullaicva. “Band Structure of TIGaSe2”. In: 41 (1983).

[80] T. Serkan Kasirga. “Thermal Conductivity Measurements in 2D Materials”. In: *SpringerBriefs in Applied Sciences and Technology*. Springer, 2020, pp. 11–27. DOI: 10.1007/978-981-15-5348-6_2.

[81] Huanyu Dai and Ridong Wang. “Methods for Measuring Thermal Conductivity of Two-Dimensional Materials: A Review”. In: *Nanomaterials* 12.4 (2022), p. 589. ISSN: 2079-4991. DOI: 10.3390/nano12040589.

[82] Nicolas Morell et al. “Optomechanical Measurement of Thermal Transport in Two-Dimensional MoSe 2 Lattices”. In: *Nano Letters* 19.5 (2019), pp. 3143–3150. ISSN: 1530-6984. DOI: 10.1021/acs.nanolett.9b00560. arXiv: 1905.00764.

[83] Mohammad Hassan Kalantari and Xian Zhang. “Thermal Transport in 2D Materials”. In: *Nanomaterials* 13.1 (2022), p. 117. ISSN: 2079-4991. DOI: 10.3390/nano13010117.

[84] Li Xie et al. “Stacking faults modulation for scattering optimization in GeTe-based thermoelectric materials”. In: *Nano Energy* 68 (2020), p. 104347. ISSN: 22112855. DOI: 10.1016/j.nanoen.2019.104347.

[85] Xingxu Yan et al. “Single-defect phonons imaged by electron microscopy”. In: *Nature* 589.7840 (2021), pp. 65–69. ISSN: 1476-4687. DOI: 10.1038/s41586-020-03049-y.

[86] Martin T. Dove. *Introduction to Lattice Dynamics*. Cambridge University Press, 1993. ISBN: 9780521392938. DOI: 10.1017/CBO9780511619885.

4

Assembly and Study of GaS/GaSe van der Waals Heterostructures

And I know

There's something down there, sugar soul

Back to the cross, a twisted lane

There something down there, Sugar Kane

– "Sugar Kane", *Dirty*, Sonic Youth

In the previous chapter, the stacking faults of $TlGaSe_2$ were studied, and their role in the material's thermoelectric properties was established. While this material has been shown to contain a plethora of interesting physics and material properties, its practical real-world use is limited as thallium and its compounds are highly toxic [1, 2]. It is often dubbed "the poisoner's poison" and there are calls to prohibit the use of thallium entirely due to its toxicity and lack of any clear biological benefit [3].

Nonetheless, the intrinsic nature of the stacking faults of layered $TlGaSe_2$ raises an interesting question: what if one were to be able to control the stacking of these layered materials? In the previous few years, the world of van der Waals heterostructures and twisted structures has been opening up new devices, such as vertical LEDs [4], and phenomena, such as superconductivity in twisted bilayer graphene [5].

In this chapter, these novel concepts are explored through the medium of GaS/GaSe heterostructures. These layered 2-D materials individually possess ideal optoelectronic

properties [6, 7], which are enhanced when coupled to other 2-D material systems such as MoS_2 [8] or graphene [9]. When layered together, these GaS/GaSe heterostructures are theorised to have interesting physics phenomena, such as the presence of Rashba effect [10] which would be of interest in spintronic applications. Here, the bulk and monolayer electronic properties of GaS and GaSe are studied via DFT simulations, along with a study of the angle dependence between monolayer GaS and monolayer GaSe on band structure changes. Experimentally, several twisted heterostructure systems are prepared and studied in TEM, in both plan-view and cross-section, in order to correlate the ab-initio simulation results. Finally, the trials and tribulations of this work are discussed, as are the future plans for this project.

4.1 Introduction

Since the discovery of graphene [11] and its ability to possess very different properties than in its bulk form, there has been intensive research focus on exfoliating other layered materials and establishing their novel structure-property relationships. As was mentioned in Chapter 1, many of these layered materials are chalcogens due to loosening in covalent bond strengths as compared to oxides, allowing them to crystallise into layers held together with van der Waals forces. As such, some of the most intensively researched van der Waals materials include MoS_2 [12, 13], WSe_2 [13–15], In_2Se_3 [16, 17], SnSe [18, 19], Bi_2Se_3 [20–22], etc.

This ability to exfoliate layered materials down to monolayers allows for the ability to assemble devices without having to construct them via epitaxy or lithography. Many scientists have started to play with these "2-D Legos" to construct devices such as LEDs [4, 23, 24], transistors [25–27], photodetectors [28–32], pressure sensors [33–35], biosensors [36, 37], etc.

These van der Waals heterostructures can be constructed in a number of ways. The 2-D layers can be exfoliated from their bulk crystals via mechanical exfoliation [11, 38] or via liquid phase exfoliation [39, 40], and then transferred onto other flakes via a viscoelastic stamp [41–43] or transfer polymer such as polymethyl methacrylate (PMMA) [44–47]. However, there are issues of hydrocarbon contamination between the layers that must be

considered [48], and the multistep process means its scalability is currently limited. These heterostructures can also be grown in-situ, but growth and epitaxial conditions must be considered, thus arbitrary stacking is not yet trivial [49–53].

Recently, it was discovered that a heterostructure's properties are not simply just due to the arbitrary stacking of the layers. Breaking away from its initial Lego analogy, it was found that the complex interplay of the interlayer coupling, lattice reconstruction and twist angle between the layers can result in new and exotic phenomena. For example, graphene is a zero-band gap semiconductor with extremely high thermal and electrical transport characteristics. When two graphene monolayers are in contact at an angle of approx. 1.1° and cooled to approx. 2 K, the bilayer exhibits superconductivity effects [5].

This new field of studying how the relative angle between vertically stacked 2-D materials affects the electronic properties of the heterostructure has been termed "twistronics" [54, 55]. The resulting phenomena can be so dramatically different to the non-twisted structure that the angles are termed "magic" [5, 56, 57]. These twisted structures have been shown to exhibit phenomena such as superconductivity [5, 56–58], ferromagnetism [57, 59], moiré excitons [60–63], quantum Hall effects [64–67], etc. Even a single twisted 2-D layer in an otherwise 3-D bulk structure can dramatically change the electronic band structure and phenomena of the system [68]. The wealth of physical phenomena and potential device applications for twistronics hence requires further study.

Here, the layered 2-D monochalcogenides GaS and GaSe are studied, along with GaS/-GaSe heterostructures. Bulk GaS and GaSe have band gaps of 2.53 eV [69] and 2 eV [70], respectively, which increase to 3.2 eV and 3.3 eV [71–73], respectively, in the monolayer limit. These band gaps make GaS and GaSe ideal for optoelectronic devices operating in the visible and UV-ranges [6, 72, 74]. As shown in Figure 4.1, GaS and GaSe have hexagonal structures, and both possess similar lattice parameters of $a = b = 3.585$ Å [6, 75, 76] and $a = b = 3.752$ Å [8, 77], respectively. This slight lattice mismatch allows for the formation of a moiré superlattice even without twisting, which can dramatically alter the electronic band structure of the heterostructure [78, 79]. By controlling the twist angle, one can in theory control these changes and hence make bespoke devices which exhibit exotic features. Indeed, recent preliminary DFT studies of GaS/GaSe heterostructures demonstrate the

presence of Rashba spin splitting effects which can be used for spintronic applications [10]. Spintronic devices differ from traditional electronic devices in that the electron spins are also used, allowing for a further degree of freedom which can be used for more efficient data storage and transfer [80].

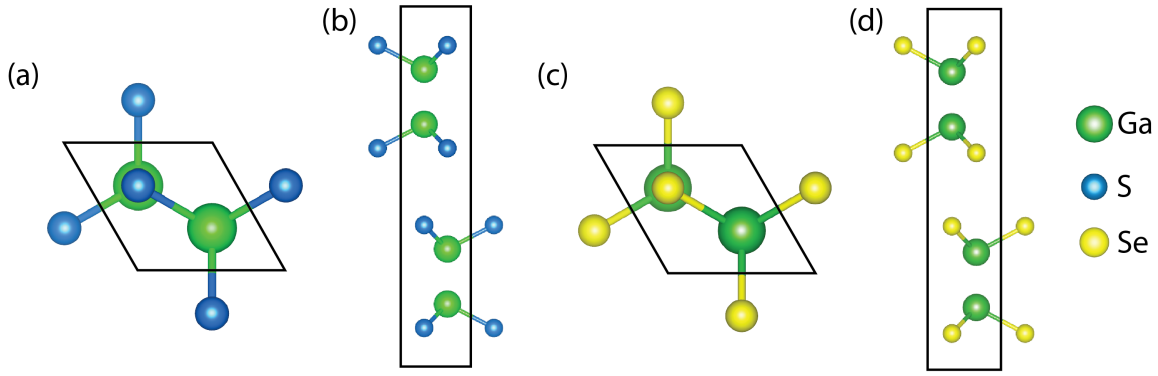

Fig. 4.1 GaS (a,b) and GaSe (c,d) unit cells in a 2H stacking configuration, projected along the *c*- (a,d) and *a*-axes (b,d). Unit cells are shown in black. Structures were visualised using the VESTA software package [81].

In this work, GaS/GaSe heterostructures are investigated both theoretically and experimentally. First-principles calculations are performed on both the bulk structure and the monolayers of GaS and GaSe, along with calculations of the angular dependence of a monolayer GaS/GaSe heterostructure on the band structure. Several heterostructures are constructed via mechanical exfoliation and are characterised using HAADF-STEM and EDX. Preliminary experimental results of the plane-view and cross-sections of the heterostructures are shown and future work on this project is also discussed.

4.2 Methods

All DFT calculations were performed via the VASP code with projector augmented wave (PAW) pseudopotentials [82, 83]. Atomic structures were optimised using the PBE functional [84] and a Hellman-Feynman force criterion of 10^{-3} eV/Å. DFT typically struggles to accurately describe dispersion forces, such as van der Waals interactions, and hence a dispersion correction is included to take this into account. Here the D3 dispersion correction of Grimme et al. [85, 86] was used in the structural relaxation and was found to be the best compromise of accuracy and speed [87]. Band structure calculations were subsequentially performed using the PBE and HSE06 functional [88]. A 8×8×2 k-point grid was used in the

bulk GaS and GaSe calculations, while a 8×8×1 grid was used for the monolayers. In all cases, a cutoff energy of 500 eV for the plane wave basis set was used for the band structure calculations such that the calculations were converged to within 1 meV per atom. This cut-off energy was increased to 650 eV for the structural relaxation to avoid Pulay stress [89]. It should also be noted that for the monolayers, 20 Å of vacuum was added to the cells along the *c*-axis to prevent fictitious interactions between the slabs.

To calculate and study the electronic band structures of GaS/GaSe heterostructures, a number of limitations had to be considered. Firstly, the VASP code used in this work is based on a plane-wave basis set formulation [82], as mentioned in Chapter 2.4, and hence relies on periodic boundary conditions. This can be achieved by having perfect lattice matching between the two layers of the heterostructures [90]. However, this results in very large unit cells, as seen in Table 4.1. Since DFT scales with N^3 where N is the number of basis functions used to describe the system [91–94], as mentioned in Chapter 2.4.3, these calculations would too large to calculate given limited computational resources available to the author (and time on earth). For accurate electronic band structures, as is required to investigate the Rashba splitting effects, the situation is further exacerbated if one were to perform HSE06 calculations, where part of the calculation scales with N^4 [88, 95, 96]. Linear scaling plane-wave methods such as those implemented in the ONETEP code can be used to calculate structures up to at least 14,000 atoms, but at the reduction of band structure accuracy [97]. However, the ONETEP code was not available to the author at the time of writing, and hence other calculation methods were sought after.

To maintain periodic boundary conditions while reducing calculation overheads, the coincidence lattice theory approach was used [98–100]. Briefly, consider two 2D monolayers, **A** and **B**, which are described by basis vectors ($\mathbf{a_1}$, $\mathbf{a_2}$) and ($\mathbf{b_1}$, $\mathbf{b_2}$), respectively. Any arbitrary superlattice of **A** can be defined by two new linearly independent basis vectors $\mathbf{A_1}$ and $\mathbf{A_2}$, as seen in Figure 4.2 [101]:

$$\begin{aligned} \mathbf{A_1} &= n_1\mathbf{a_1} + n_2\mathbf{a_2} \\ \mathbf{A_2} &= n_3\mathbf{a_1} + n_4\mathbf{a_2} \end{aligned} \tag{4.1}$$

where n_x are integer indices which uniquely describe the superlattice. Similarly, for **B**:

$$\begin{aligned} \mathbf{B_1} &= m_1\mathbf{b_1} + m_2\mathbf{b_2} \\ \mathbf{B_2} &= m_3\mathbf{b_1} + m_4\mathbf{b_2} \end{aligned} \tag{4.2}$$

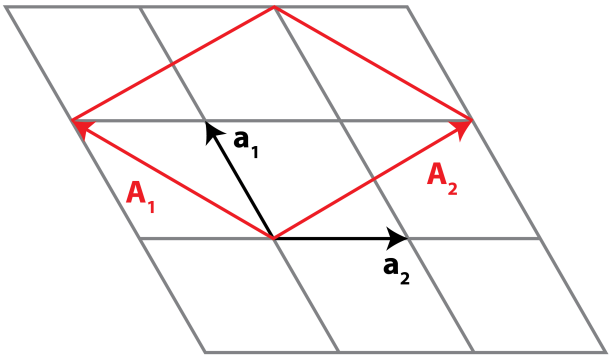

Fig. 4.2 Diagram of supercell construction (in red), with basis vectors $\mathbf{A_1}$ and $\mathbf{A_2}$, from a hexagonal unit cell (in grey) with basis vectors $\mathbf{a_1}$ and $\mathbf{a_2}$. Here, the supercell has indices of [2, 1, -1, 1]. Adapted from [101] under a Creative Commons (CC-BY) licence.

If $\mathbf{A_1} = \mathbf{B_1}$ and $\mathbf{A_2} = \mathbf{B_2}$, then the two monolayers share a common superlattice. By introducing a pre-defined length and angle tolerance, this condition can still hold and reduce the number of atoms in the supercell, but at the cost of the introduction of strain to the structure [98, 101]. This approach can be justified, as the transfer process of 2D materials often leaves some residual strain from folds, wrinkles and bubbles in the sheets [102–104].

A series of different heterostructures were constructed using coincidence lattice theory via the Hetbuilder software package to study the effect of twist angle on the electronic band structure, as seen in Figure 4.3, with the number of atoms shown in Table 4.1 [98, 105]. The structures range from ε-phase at 0° to β-phase at 60°, at 30° intervals, with the strain in each structure shown in Table 4.1. The structures are the ones closest to the desired angle, with a minimal amount of atoms. However, this results in large in-plane strain in the structures of up to 4%, as shown in Table 4.1. Strain can affect the electronic band structures, and hence can be used as a mechanism for engineering a desired band gap, for example [106–109]. Strain in twisted van der Waals structures is relieved through atomic reconstruction in the saddle points between the AA and AB domains for twist angles of $< 10°$ [110–115]. However,

the structures chosen are far too small for these effects to be observed. Instead, it may be more accurate to think of these structures, and their subsequent calculated electronic band structures, as localised domains in their full lattice-matched supercell indicated by their twist angle [116]. Herein, the structures will be referred to by their twist angle, with the caveat that they may not entirely represent the full twisted structure.

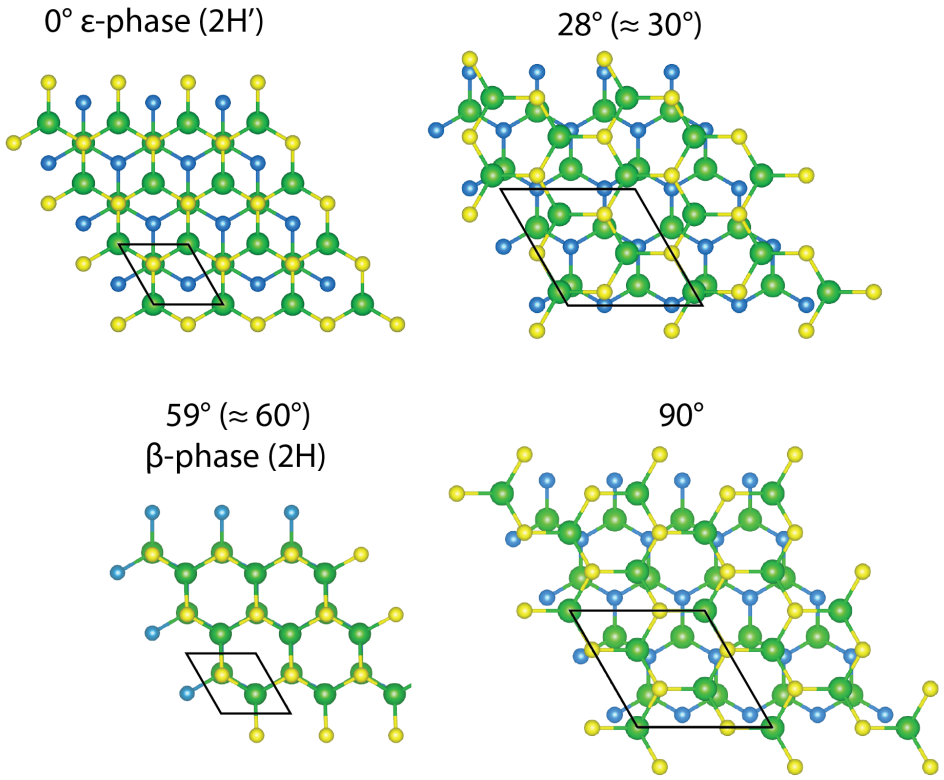

Fig. 4.3 GaS/GaSe heterostructures at different twist angles that were used for DFT calculations. Projection is along the *c*-axis with Ga = green, S = blue, and Se = yellow. Unit cells are shown in black. Structures were visualised using the VESTA software package [81].

	Atoms/unit cell (PLM)	Atoms/unit cell (CLT)	Strain (%)
0°	4052	8	1.9
28° (~30°)	1984	28	4
59° (~60°)	4052	8	1.9
90°	2788	28	4

Table 4.1 Table of GaS/GaSe heterostructures at various twist angles using in DFT calculations. Atoms per unit cell of structure, either with perfect lattice matching (PLM) or coincidence lattice theory (CLT), are highlighted, along with the strain of the CLT-based structures chosen for calculations in this work.

The DFT calculations for the heterostructures followed the same parameters as for the monolayers, including the use of a 8×8×1 k-point grid. However, for the heterostructures with larger numbers of atoms (i.e. the 30° and 90° heterostructures), a smaller 4×4×1 k-point grid was used in order to be able to run the calculations. At least 20 Å of vacuum was added to the cells along the *c*-axis to prevent fictitious interactions between the slabs. The relaxed structural file for each heterostructure is shown in Appendix B. Electronic band structures were plotted with Sumo command-line package [117], while the spin textures were plotted using the PyPROCAR Python package [118]. Analysis of angle dependence on the electronic band structures was performed with the Origin graph plotting software.

Bulk GaS and GaSe were purchased from 2D Semiconductors, Inc., and mechanically exfoliated using low-tack, minimal-residue adhesive tape (Nitto BT-150E-CM). To examine the exfoliated flakes and construct the heterostructures, a low-cost deterministic transfer stage and optical microscope was established using parts from AliExpress and ThorLabs [43], as seen in Figure 4.4. The exfoliated bottom flake is transferred onto a Si substrate that had a 100 nm SiO_2 layer on the surface and then placed onto the rotating stage under the microscope. The thickness of the flakes is approximated from their colour and contrast on the SiO_2 [75], and a chosen flake is focused into view of the microscope. The top flake is exfoliated onto a polydimethylsiloxane (PDMS)-based viscoelastic stamp (GelPak WF x4 6.0 mil) [43]. This stamp is then attached to the end of a glass slide using regular adhesive tape and subsequently attached to the adjustable height stage of the transfer set-up. The flakes are aligned to the desired angle and location, and the top flake is slowly lowered until both are in focus. The top stage is then raised slowly, such that the air/stamp interface can be seen slowly moved over the heterostructure over the course of a few minutes, depending on the size of the flake.

To examine the heterostructures in cross-section, an additional hBN layer was placed onto of the heterostructure. This was done with the idea that this layer would minimise oxidation before preparing a TEM lamella in a FIB, and that it would minimise surface damage from the FIB process. Any layered material could be used for this, such as graphene, but hBN was available to the author at the time and hence its use herein. The heterostructure underwent vacuum baking at approx 100°C for 72 hours in a repurposed precision ion

polishing system (Gatan). Lamella preparation proceeded as mentioned in Chapter 2.3 on a Zeiss Auriga FIB-SEM at 30 kV with 2 nA for trenching and 240 pA, 120 pA, 50 pA and 20 pA currents for sample thinning. Final thinning was performed in a Fischone NanoMill at 800 V and 80 pA. HAADF-STEM imaging was performed on an uncorrected FEI Titan operating at 300 kV with a convergence angle of 10 mrad and a collection angle range of 40 - 200 mrad. EDX spectral mapping was performed in the FEI Titan with a Bruker Quantax XFlash 6T-30 30 mm^2 EDX detector with a beam current of approx. 500 pA and a dwell time of 1 second.

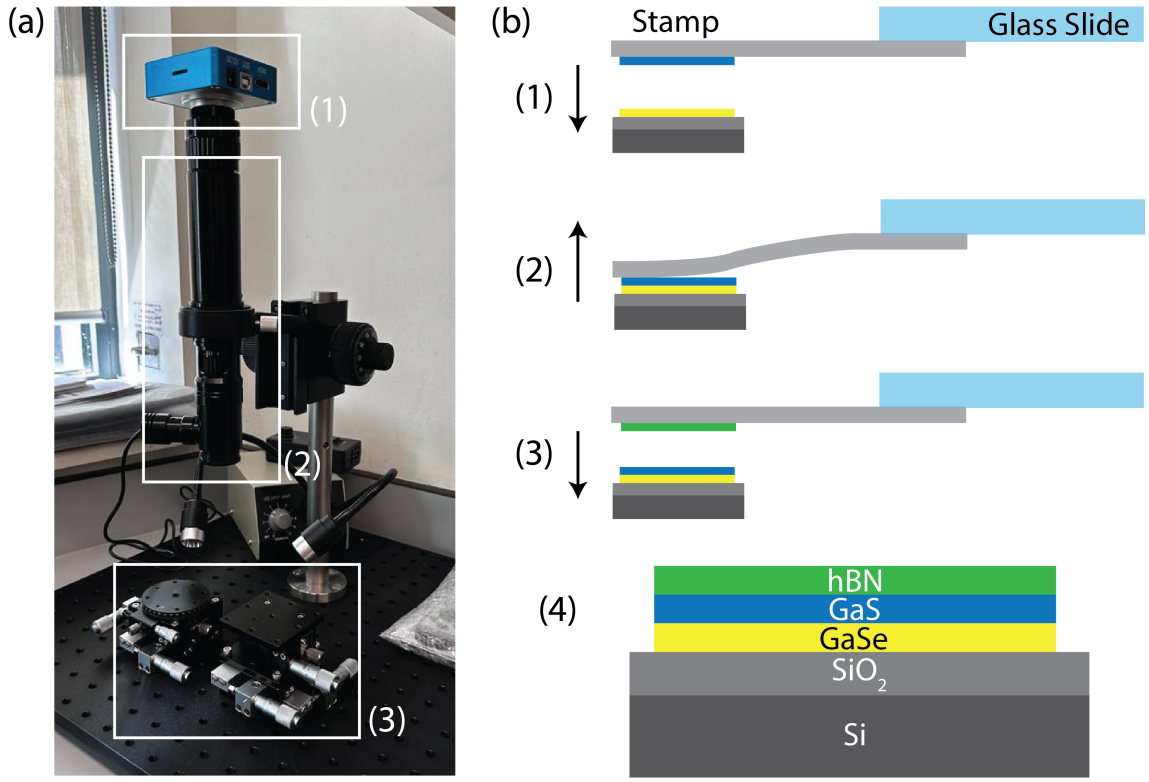

Fig. 4.4 (a) Photograph of low-cost van der Waals flake transfer station, with the camera (1), optics and in-line lighting (2), and adjustable stages (3) highlighted. (b) Schematic of typical transfer process where (1) the top flake attached to the stamp is slowly brought into contact with the bottom flakes and substrate, and (2) slowly removed to ensure successful transfer. The process is repeated for another flake (3). A typical heterostructure is shown in (4).

Plan-view samples of the heterostructures were constructed in a similar fashion as above, except on a SiN_x TEM grid (Ted Pella) and no hBN capping layer was applied. The grids also underwent vacuum baking at approx 100°C for 72 hours. Initial sample checks and PACBED pattern collection was performed on a FEI Titan operating at 300 kV, while HAADF-STEM imaging was performed on an aberration-corrected Nion UltraSTEM 200

operating at 200 kV. Estimation of the thickness of the flakes was performed by capturing PACBED patterns in the FEI Titan, as described in Chapter 2.2.5, and compared to simulations using a modified version of the MBFIT software package [119, 120]. The beam was continuously rastered over an area of interest with a 2 μs dwell time and a probe current of approx. 20 pA, while the CCD camera (Gatan Ultrascan) was exposed for 5 seconds for each PACBED pattern. HAADF-STEM imaging was performed with a convergence angle of 27 mrad, a probe current of approx. 35 pA and a dwell time of 2 μs. Sample charging and drift effects were minimised by subsequent non-rigid registration post-processing of image stacks using SmartAlign software plug-in for Digital Micrograph [121]. For GaSe, 20 images were collected, while for GaS and the GaS/GaSe heterostructure, 50 images were collected each.

4.3 Results & Discussion

4.3.1 First-Principles Analysis of GaS, GaSe, & GaS/GaSe Heterostructures

Previously reported theoretical studies on GaS/GaSe heterostructures reported electronic band splitting around the Γ point when spin-orbit coupling (SOC) effects were considered in the calculations [10]. SOC is the interaction between the spin angular momentum and the orbital angular momentum of the electrons due to the magnetic field of the protons in the nucleus [122, 123]. This perturbs the electronic wavefunctions and hence redefines the energy levels of the electrons. While all elements will have some SOC correction to their band structure, the effect is far more striking for heavier elements and hence for accurate band structure calculations, many transition metals and f-block elements require the inclusion of SOC [124]. SOC not only contributes to a shift in the energies of the electronic bands, but it can also lead to the breaking of degeneracy, leading to fine and hyperfine spectra [122].

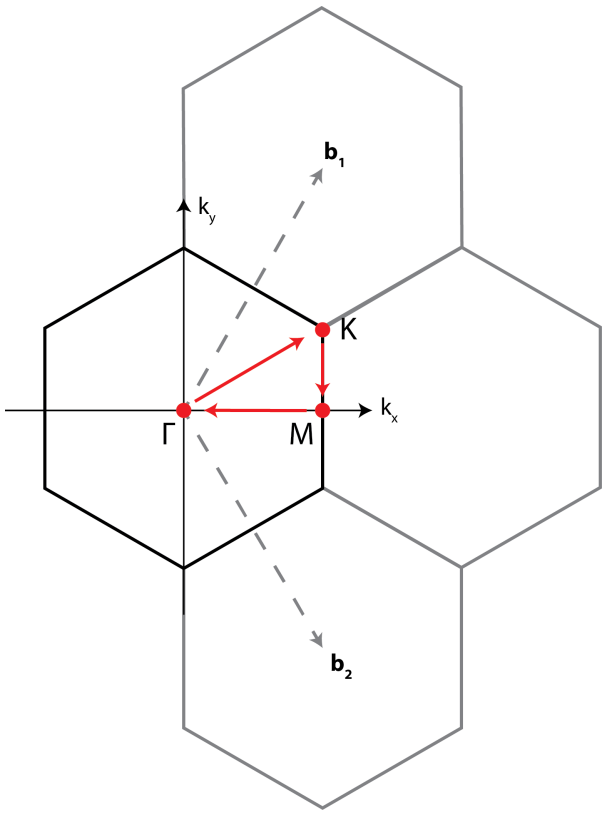

Fig. 4.5 Brillouin zone of a 2-D hexagonal lattice (black) with reciprocal lattice basis vectors $\mathbf{b_1}$ and $\mathbf{b_2}$. The symmetry points Γ (0,0,0), K ($\frac{1}{3}b$,$\frac{1}{3}b$,0) and M ($\frac{1}{2}b$,0,0) are shown, where b is the reciprocal lattice vector. The high symmetry path of Γ-M-K-Γ is also shown [125].

This is not the only type of band splitting to occur in materials. For systems with broken inversion symmetry, SOC can lead to the phenomenon known as the Rashba effect. Here, spin-degenerate pairs of parabolic bands are split energetically and shifted oppositely along the wave-vector **k**, depending on the spin direction [126, 127]. For bands at the Fermi level of a semiconductor, this type of splitting may affect the electronic properties of the material and potentially provide an extra degree of freedom for use in spintronics. Therefore, the electronic band structures with and without SOC are calculated for all the structures under this study to search for evidence and effects of Rashba splitting.

Electronic band structure analysis of the bulk GaS and GaSe were first performed in order to appreciate any changes in band structures later on when studying the monolayers of each and of their heterostructures. Both GaS and GaSe are hexagonal space groups, hence their reciprocal lattice is also a hexagon. As such, all the band structures shown throughout this work follow the high symmetry path of Γ-M-K-Γ [125], shown in Figure 4.5.

Figures 4.6 and 4.7 show the band structures of bulk GaS and GaSe, respectively, each with and without SOC corrections, as well as their density of states (DOS). Calculations for bulk GaS show an indirect band gap of 2.305 eV, with a negligible change to 2.307 eV when SOC is included.

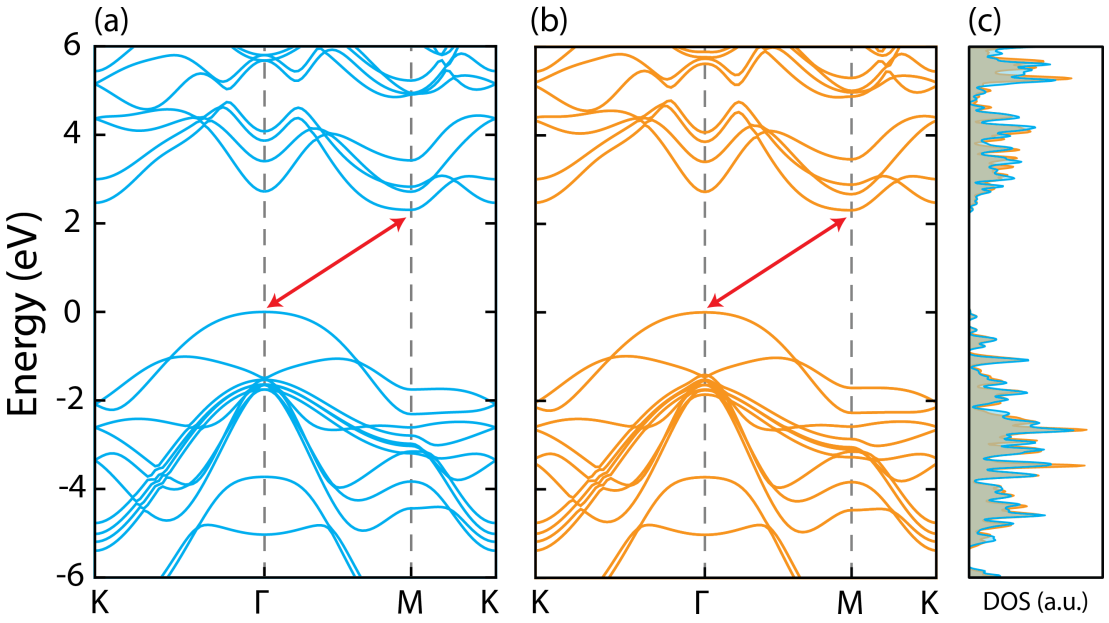

Fig. 4.6 Electronic band structure of bulk GaS, both with (a) and without (b) SOC corrections. The DOS of both are overlaid in (c) highlighting the lack of significant change in the DOS when SOC is included. Red arrows in (a) and (b) indicate the indirect band gap.

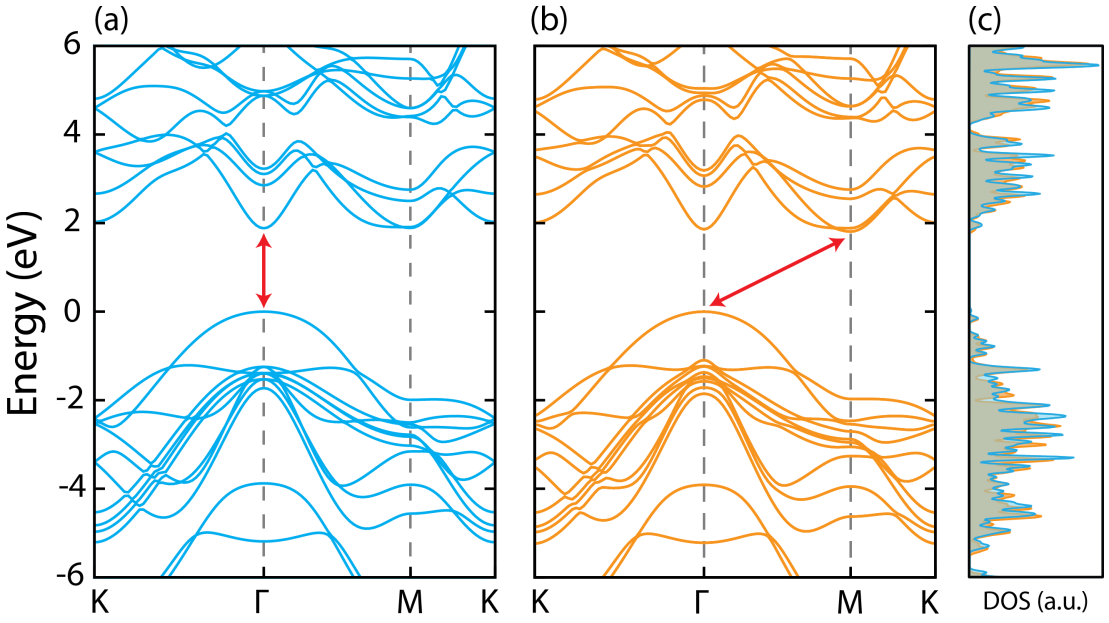

Fig. 4.7 Electronic band structure of bulk GaSe, both with (a) and without (b) SOC corrections. The DOS of both are overlaid in (c) highlighting the lack of significant change in the DOS when SOC is included. Red arrow in (a) indicates the direct band gap, but in (b) the arrow indicates an indirect band gap when SOC is included.

These values are close to experimental values of 2.53 eV [69]. However, as shown in the DOS, little to no band splitting is evident, especially near the Fermi level at the Γ point. GaSe shows a different story: it demonstrates a direct band gap at the Γ point of 1.883 eV, which becomes an indirect band gap of 1.808 eV when SOC is included. This latter band gap is close to the experimental results of an indirect 2 eV band gap [70], highlighting the importance of SOC inclusion.

The electronic band structures of monolayer GaS and GaSe show a number of key differences to their bulk phases, as shown in Figures 4.8 and 4.9 respectively. In line with previous theoretical studies [71], the band gaps are larger when SOC is included, at 3.342 eV and 3.082 eV, respectively. While all the band gaps are indirect, the valence band maximum (VBM) is not at the Γ point like in the bulk; instead, it is along the Γ-*M* path for GaS and the Γ-*K* path for GaSe. The conduction band minimum (CBM) is at the *M* point in monolayer GaS, just like in bulk GaS and GaSe, but for monolayer GaSe, it is at the Γ point.

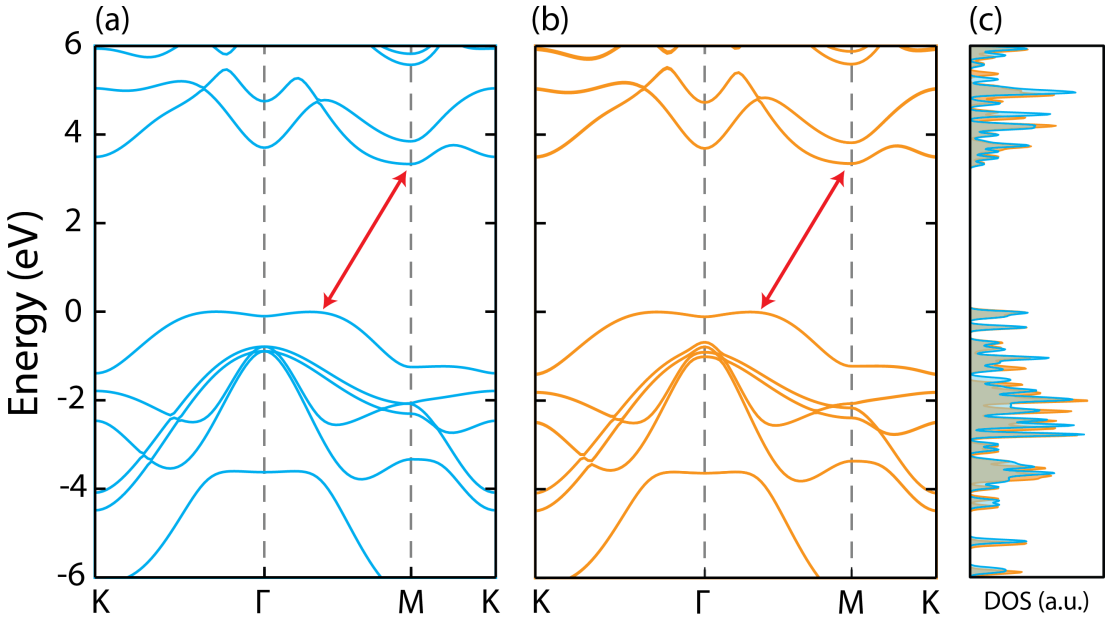

Fig. 4.8 Electronic band structure of monolayer GaS, both with (a) and without (b) SOC corrections. The DOS of both are overlaid in (c) highlighting the lack of significant change in the DOS when SOC is included. Red arrows in (a) and (b) indicate the indirect band gap.

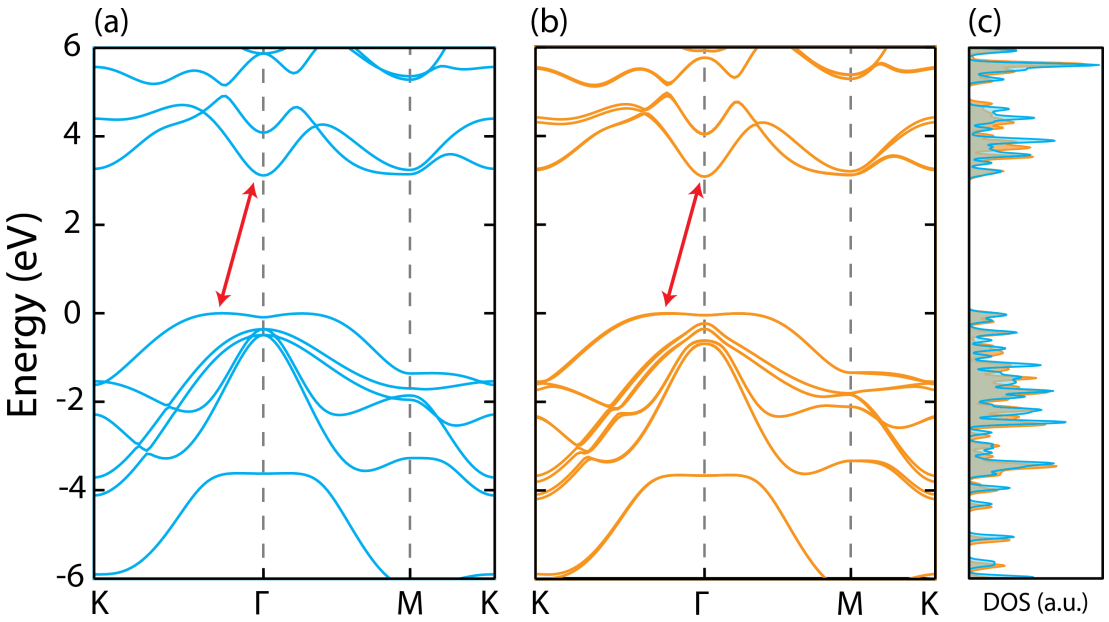

Fig. 4.9 Electronic band structure of monolayer GaSe, both with (a) and without (b) SOC corrections. The DOS of both are overlaid in (c) highlighting the lack of significant change in the DOS when SOC is included. Red arrows in (a) and (b) indicate the indirect band gap.

Due to the broken inversion symmetry of being a monolayer, the inclusion of SOC leads to some band splitting in both monolayer GaS and GaSe [128]. The splitting is only along the Γ-*K* path for both and the energy difference of the split bands is small, with 5 meV for the GaS monolayer and 8 meV for the GaSe monolayer. In theory, these energies are just about large enough to detect using angle-resolved photoemission spectroscopy (ARPES) at a synchrotron facility, but these experiments are non-trivial and outside the scope of this work [129]. One could also use the high spatial resolution of STEM and highly monochromated electron beam which can achieve energy resolutions of 5 meV to map out the changes in the DOS using EELS [130]. However, in reality, it might not be clear if these are measurable differences, and the gap between the split bands may diminish by using higher level (and more complex) computational chemistry methods such as *GW* calculations, as mentioned in Chapter 2.4. However, these types of calculations are outside the scope of this work.

The four GaS/GaSe heterostructures shown in Figure 4.3 underwent a similar computational treatment. Figure 4.10 shows the band structure for the β-phase stacking of the heterostructure, with twist angle = 0°. Even at the energy scale in Figure 4.10(b), it is clear that the splitting of the bands is much larger than that of either monolayer GaS

or GaSe. The band gap of this heterostructure, which is 2.403 eV when including SOC, is larger than either individual bulk material, but smaller than either individual monolayer. Curiously, when the VBM is zoomed into in Figure 4.11, one can see that the band splitting is asymmetric along the Γ-K and Γ-M paths.

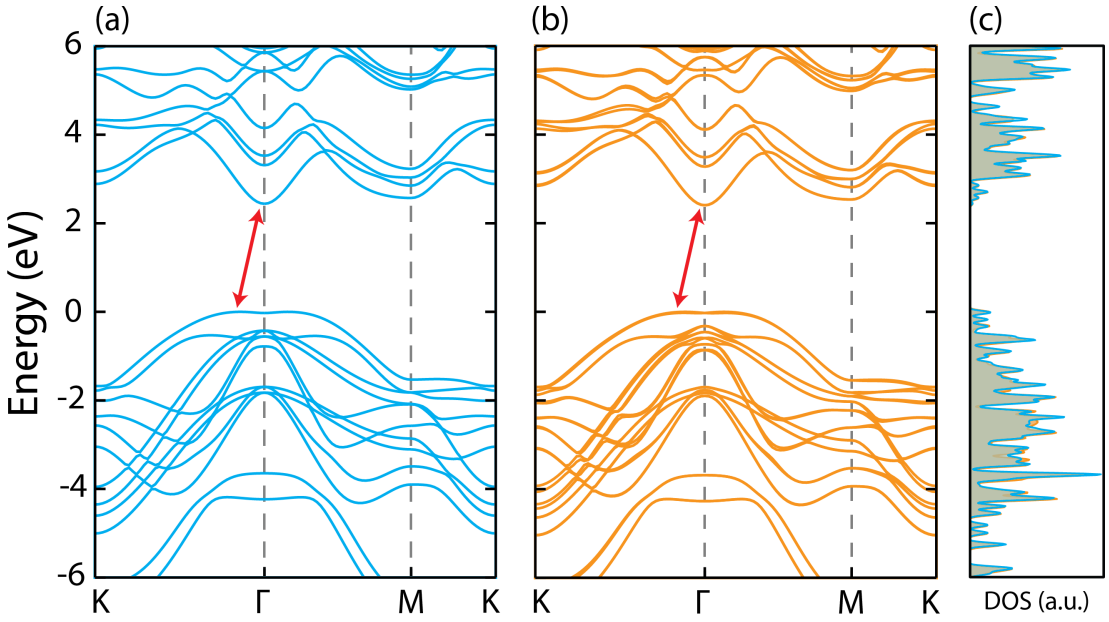

Fig. 4.10 Electronic band structure of GaS/GaSe heterostructure with 0° twist angle, both with (a) and without (b) SOC corrections. The DOS of both are overlaid in (c). Red arrows in (a) and (b) indicate the indirect band gap.

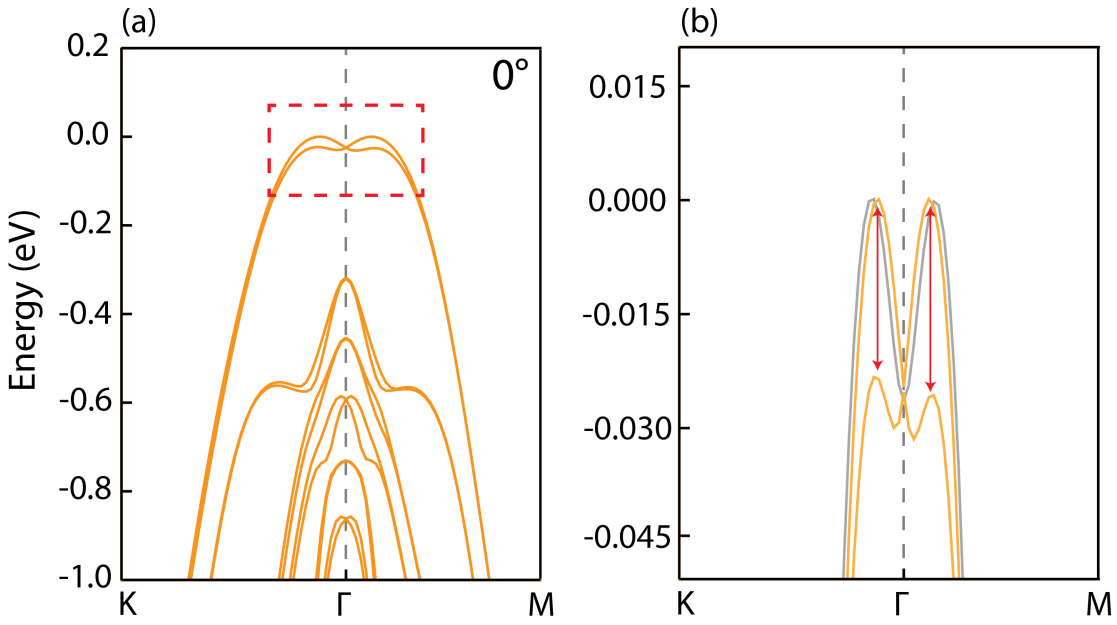

Fig. 4.11 Close-up electronic band structure around the VBM of the GaS/GaSe heterostructure with 0° twist angle and SOC. In (b), the asymmetric Rashba splitting energies along both paths are shown, while the grey band is the non-SOC VBM of the system.

This Rashba splitting energy along the Γ-*K* and Γ-*M* paths is measured for all four heterostructures in Figure 4.3 and are plotted in Figure 4.12. While these values come from PBE-level band structure calculations, there are three striking features to be obtained from this plot. Firstly that the splitting can be controlled with the twist angle, unlike monolayer GaS and GaSe where it is fixed. There is a sinusoidal change in splitting energy with twist angle along the Γ-*K* path, from a peak of 21.6 meV at 0° to a minimum of 10.5 meV at 30°, and then returns to a similar starting value of 22.3 meV at 60°. Along the Γ-*M* path, there is a similar but smaller sinusoidal trend. The values peak at 0° (21.6 meV) and 60° (22.3 meV) twist angles, and have troughs at 30° (19.1 meV) and 90° (18.9 meV) twist angles. These values are smaller than those reported for other systems such as BiTeI (~ 100 meV) [131], $PtBi_2$ (~ 160 meV) [132], and $CsPbF_3$ (~ 44 meV) [133]. However, it should be noted that those works are on bulk phase materials; for heterostructures, recent studies predicted that $MoTe_2/PtS_2$ would have the highest van der Waals heterostructure Rashba splitting energy of ~ 120 meV, but no experimental work has been performed on this system to date [134].

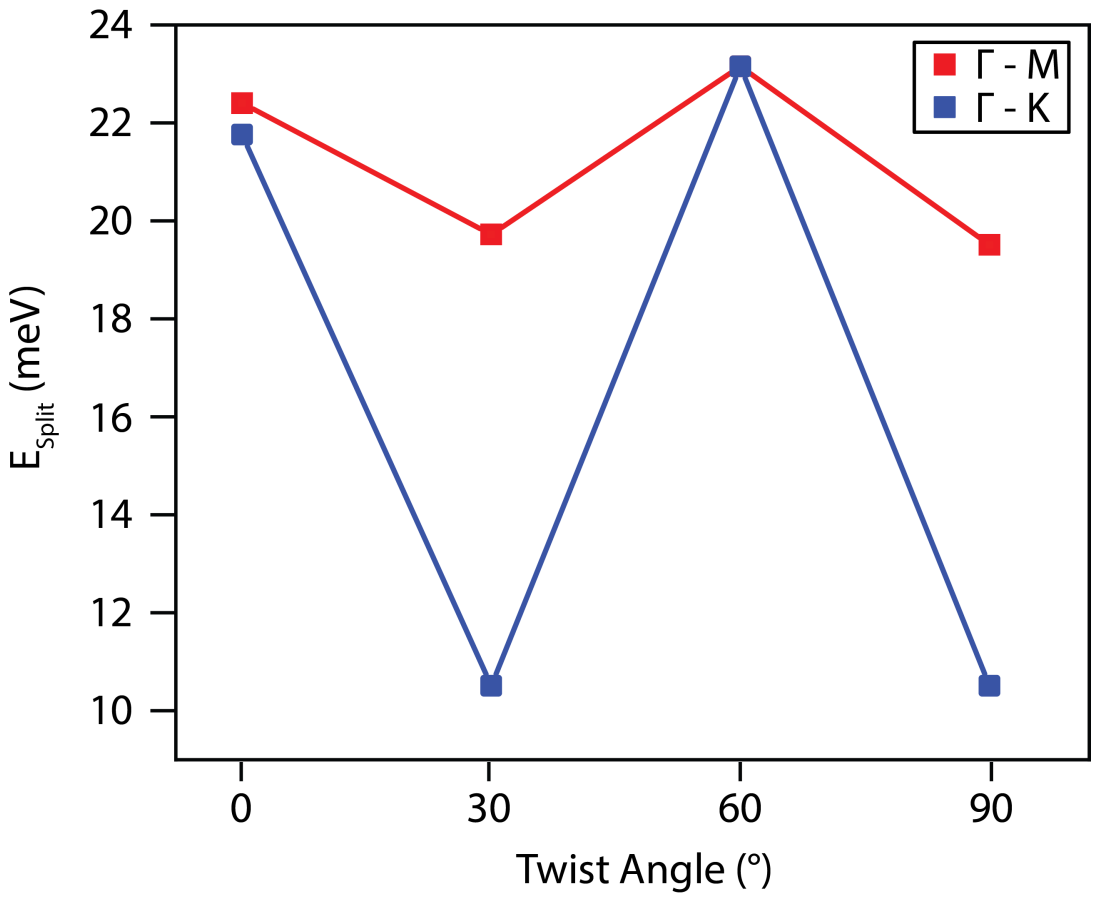

Fig. 4.12 Plot of Rashba splitting energy for the Γ-*K* (blue) and Γ-*M* paths (red) against the twist angle of GaS/GaSe heterostructures.

Nonetheless, these two degrees of freedom are of great interest for spintronic applications. With the use of an electric field to manipulate both spin states at varying amounts, twice as much data could be stored within a given space [80, 135, 136].

To investigate the effects of the twist angle on the band gap, the DOS for all four heterostructures are plotted in Figure 4.13. Each DOS is plotted with the same scaling, which highlights the smaller DOS for 0° and 60° heterostructures. This is due to the smaller number of atoms in their unit cells, as per Table 4.1. For the 30° and 90° heterostructures, however, there is the appearance of states near the conduction band, which would decrease the band gap for these structures. These states appear to be mostly coming from the GaSe rather than GaS monolayer, as shown by the Ga-*sp* and Se-*sp* orbitals in the partial density of states (PDOS) in Figure 4.14, but it is not clear why they are not present at 0° and 60°.

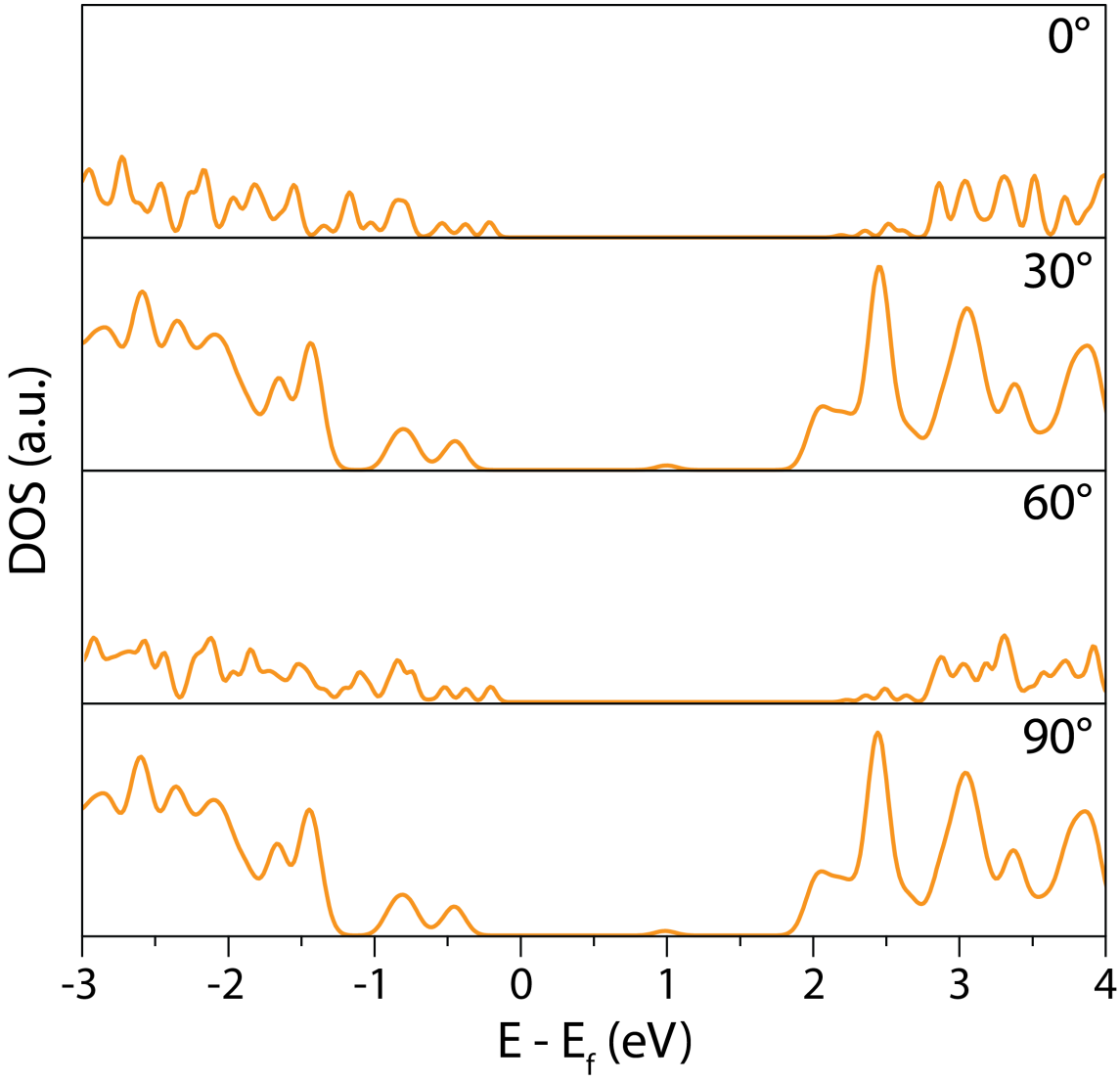

Fig. 4.13 Density of states (DOS) for the GaS/GaSe heterostructures from HSE06 calculations.

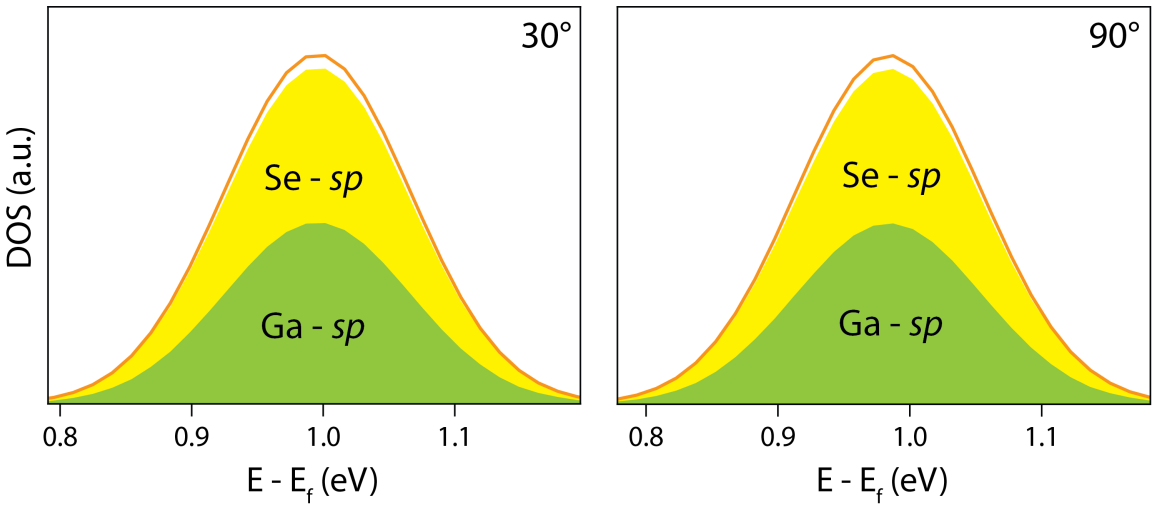

Fig. 4.14 Partial density of states (DOS) of the mid-band gap states for the 30° and 90° GaS/GaSe heterostructures from HSE06 calculations. Scaling is the same for 30° and 90°, and Ga-*sp* and Se-*sp* states are shown as a proportion of the total DOS for the peak.

Regardless, the predicted band gaps of the different heterostructures are plotted in Figure 4.15 and also show a similar trend to the Rashba splitting energies along the Γ-*K* path. There is a sinusoidal relationship between the twist angle and the size of the band gaps, from the peaks of 1.47 eV to troughs of 0.68 eV in the PBE level of theory and when SOC is included. A similar relationship is seen when using HSE06 functionals, with peaks of 2.41 eV and troughs of 1.41 eV. This angle-dependence of the band gap is not an exclusive feature of GaS/GaSe heterostructures as previous reports on MoS_2/graphene [137], WSe_2/WS_2 [138], $MoSe_2/CrI_3$ [139], and InSe/WTe_2 heterostructures [140], and twisted bilayer MoS_2 [141] all demonstrate this phenomenon. However, the band gaps of these structures differ at most by 0.5 eV with twist angle [140]. To the best of the author's knowledge, such a drastic change in band gaps with twist angle in GaS/GaSe has not been previously reported. This added third degree of freedom shows that GaS/GaSe heterostructures are well-suited for potential spintronic applications. This excellent tunability and wide range of band gaps also allow for bespoke optoelectronic applications by simply adjusting the twist angle, rather than growing $GaS_{(1-x)}Se_x$ alloys [142].

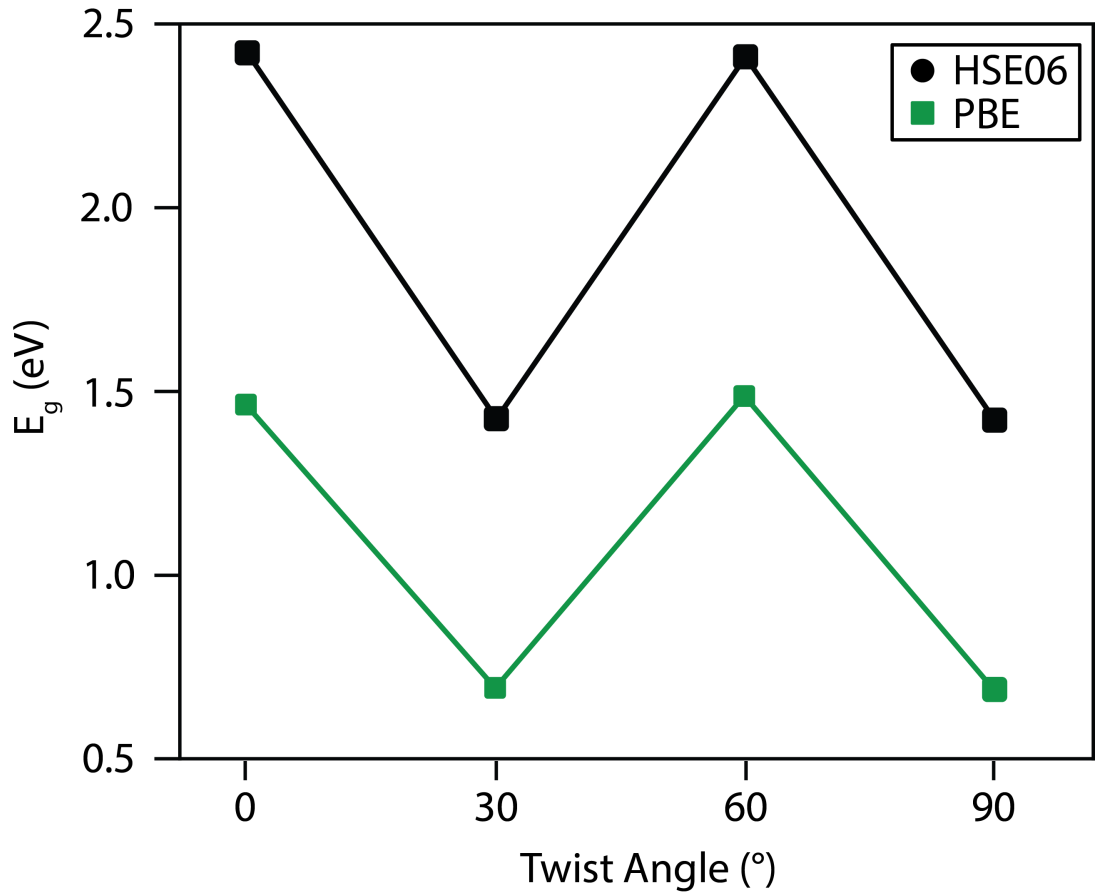

Fig. 4.15 Plot of band gap energy against the twist angle of GaS/GaSe heterostructures, with both PBE (green) and HSE06 (black) derived values shown.

It should be important to reiterate here that while these trends are significant and show great promise for applications, they may not fully represent the effects that would be present in an experimental-produced heterostructure. As mentioned in the Methods, the supercells used for each twist angle may instead be a domain in a larger supercell of that same angle, due to the large reduction in atoms in the unit cell and the strain introduced from coincidence lattice theory [98]. Whether the results from these simulations can be extended to the full lattice-matched twisted heterostructures remains to be seen, either through theory, as simulations with larger supercells were not possible with the resources available to the author, or experiments, via spectral imaging of a heterostructure through STEM-EELS [143].

Nonetheless, in order to confirm that the band splitting is indeed due to the Rashba effect, a constant energy surface calculation of the GaS/GaSe heterostructure band structure at 0° twist angle is performed in Figure 4.16 at 0.5 eV below the Fermi level. The spin texture components along *x*, *y* and *z* axes all show two concentric circular Fermi contours

on which the spins of the electronic states are tangential. The in-plane spin components, S_x and S_y, are perpendicular to the crystal momentum. The out-of-plane component, S_z, is completely absent. This results in the clockwise curling of one of the bands and counter-clockwise for the other, which is confirmation of the existence of Rashba splitting [133, 144–148].

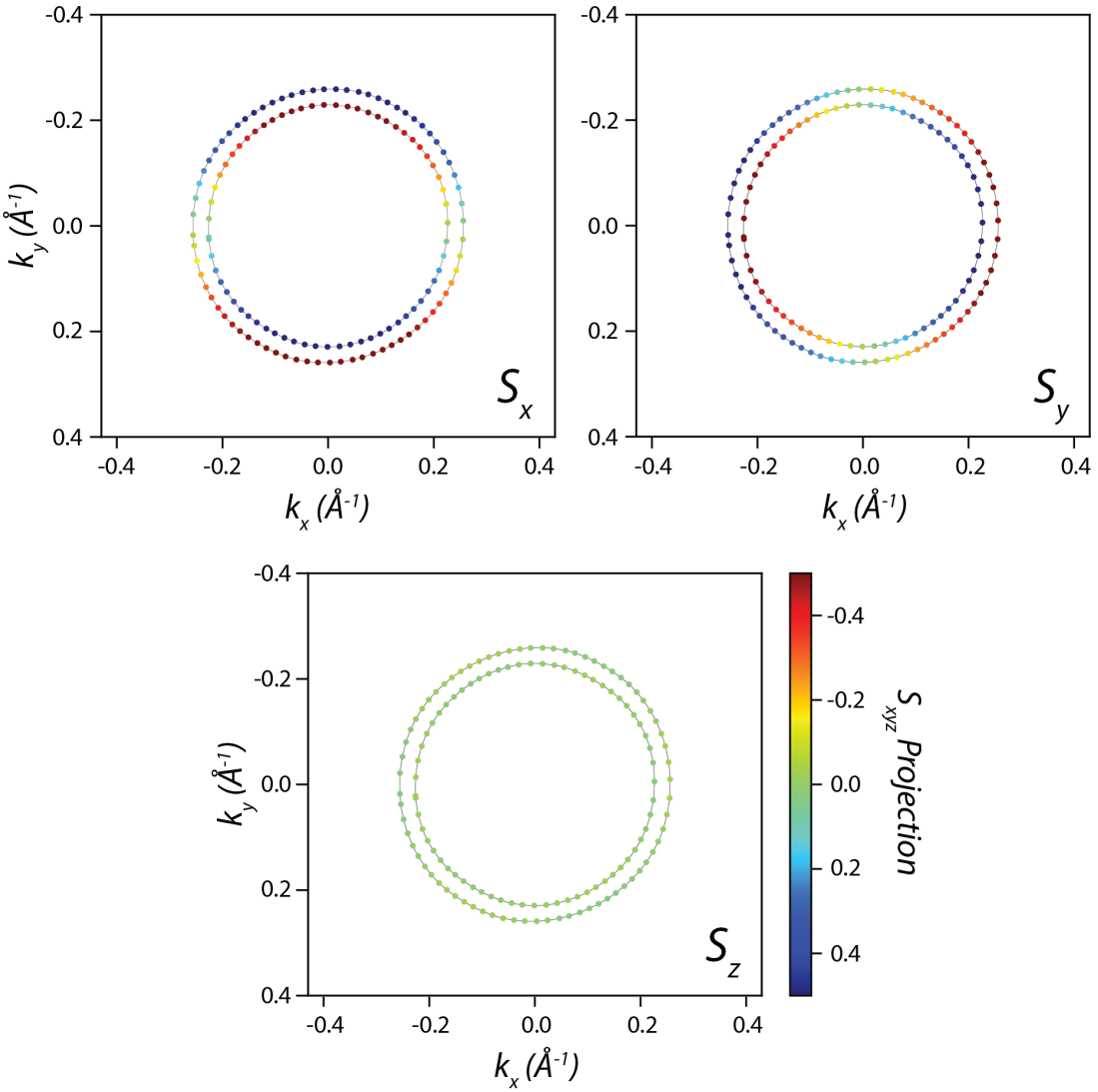

Fig. 4.16 Spin texture components of GaS/GaSe heterostructure at 0° twist angle at the constant energy surface of E_f - 0.5 eV.

4.3.2 Preliminary Experimental Results of GaS/GaSe Heterostructures

A series of GaS/GaSe heterostructures were constructed to investigate the presence of the Rashba effect and potential device applications. The heterostructures were constructed such that a region of each component flake was not covered by the other. This was done to

study each flake individually and obtain thickness measurements of each flake via PACBED patterns.

The electron dose for all imaging and EDX spectral imaging are summarised in Table 4.2. Figure 4.17(a) and (b) are HAADF-STEM images of a GaSe and GaS flake of the GaS/-GaSe heterostructure in Figure 4.21, respectively. The lattice parameters of the flakes are measured to be $a = b = 3.67$ Å and 3.48 Å, respectively, which are in line with their bulk lattice parameters [6, 8, 75–77]. The stacking order in each flake is different: the GaSe flake is in the ε-phase (2H') with AB stacking of the layers, while the GaS flake is in the β-phase (2H) with AA stacking of the layers. The thickness of each flake is approximated to be 7 - 8 layers (~ 6 - 7 nm) for GaSe, and 20 - 21 layers (~ 12 - 13 nm) for GaS from PACBED pattern simulations as shown in Figure 4.18. The best-fitting simulated PACBED patterns are shown alongside the experimental ones, while PACBED simulations of other layer amounts for the GaS and GaSe flakes are also shown. It should be noted that while the intensity of the simulated PACBED patterns is not fully commensurate with the experimental ones, the structure of the PACBED patterns is more important for thickness measurements and is in line with the experimental ones [119].

Units = e^- Å^{-2}	Figure 4.17		Figure 4.19	Figure 4.20	Figure 4.21
	(a)	(b)			
e^- Dose	1.79×10^4	1.79×10^4	5.41×10^6	8.67×10^5	1.79×10^4
Total e^- Dose (single frame)	4.69×10^9	4.69×10^9	2.82×10^9	6.48×10^8	4.69×10^9
Total e^- Dose (multi-frame)	9.38×10^{10}	2.35×10^{11}			2.35×10^{11}

Table 4.2 Table of electron doses and electron dose per image frame for the HAADF-STEM images and EDX spectral images in this Chapter. The total electron dose for multi-frame image stacks used in Figure 4.17 and 4.21 are also highlighted.

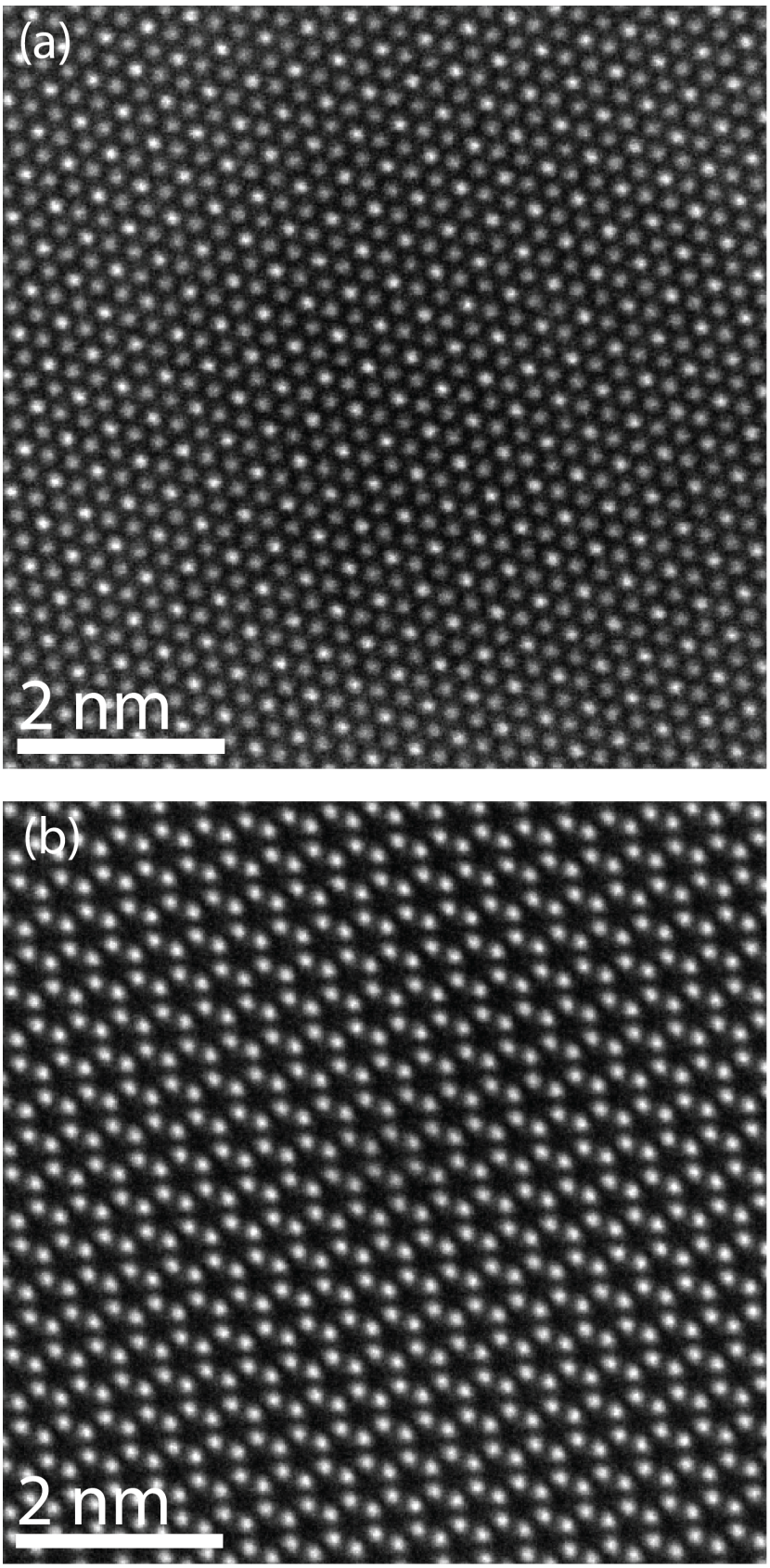

Fig. 4.17 HAADF-STEM images of GaSe (a) and GaS (b) flakes used to form the GaS/GaSe heterostructure in Figure 4.21.

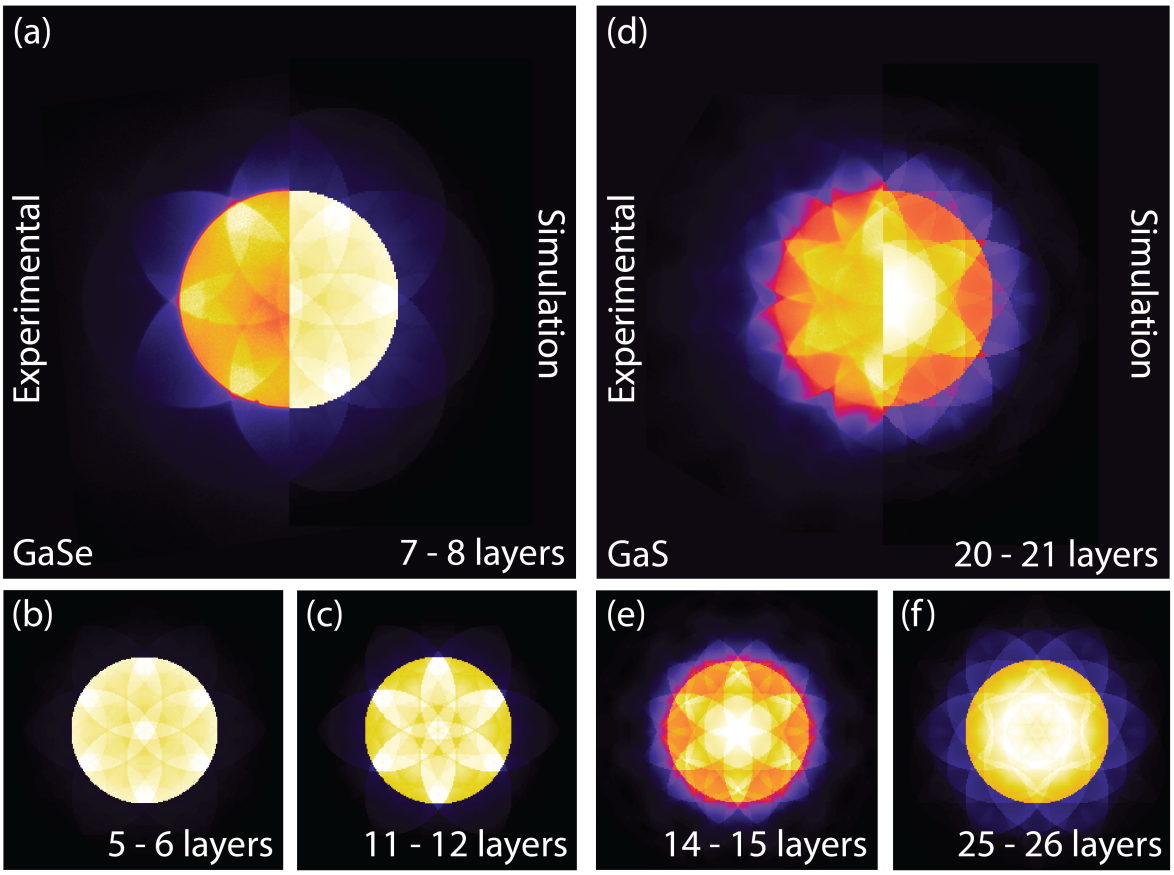

Fig. 4.18 Experimental and simulated PACBED patterns of GaSe (a) and GaS (d) flakes from Figure 4.17. A range of layer thicknesses for GaSe (b-c) and GaS (e-f) are shown to highlight the changes in PACBED patterns with thickness. False coloured for clarity.

Consistency in the exfoliation of flakes requires optimisation as there are thickness differences between the different heterostructures, as is also seen in the cross-sections of Figures 4.19 and 4.20, and it is also clear that these structures are not at the monolayer limit. As the properties of these structures are highly dependent on the interfacial contact between the layers [149], it is important to have clean surfaces. A facile method of doing so is vacuum baking which agglomerates the hydrocarbon contaminations into large, spaced-out bubbles while improving surface cohesion and leaving behind large enough surface areas for the active region [48]. This was done with all subsequent heterostructures, as seen in Figure 4.20.

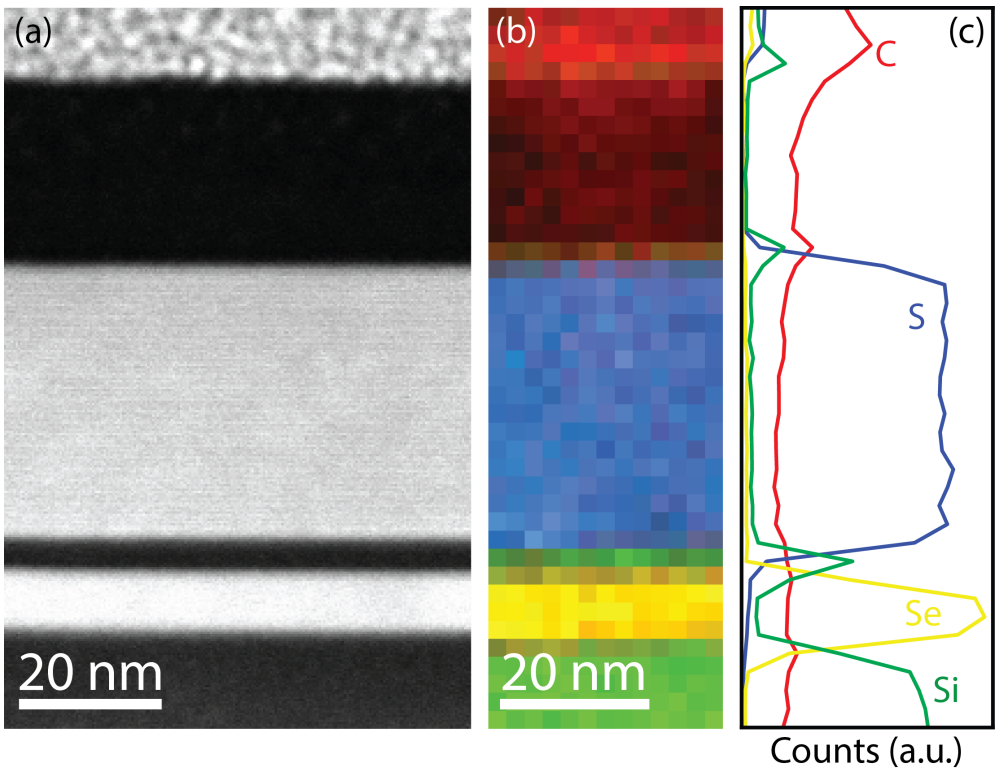

Fig. 4.19 (a) Cross-sectional HAADF-STEM image of hBN/GaS/GaSe heterostructure on SiO_2/Si substrate without vacuum baking. (b) EDX mapping of the heterostructure in (a) with S (blue), Se (yellow), C (red) and Si (green) highlighted. (c) Integrated counts of the elements highlighted in (b).

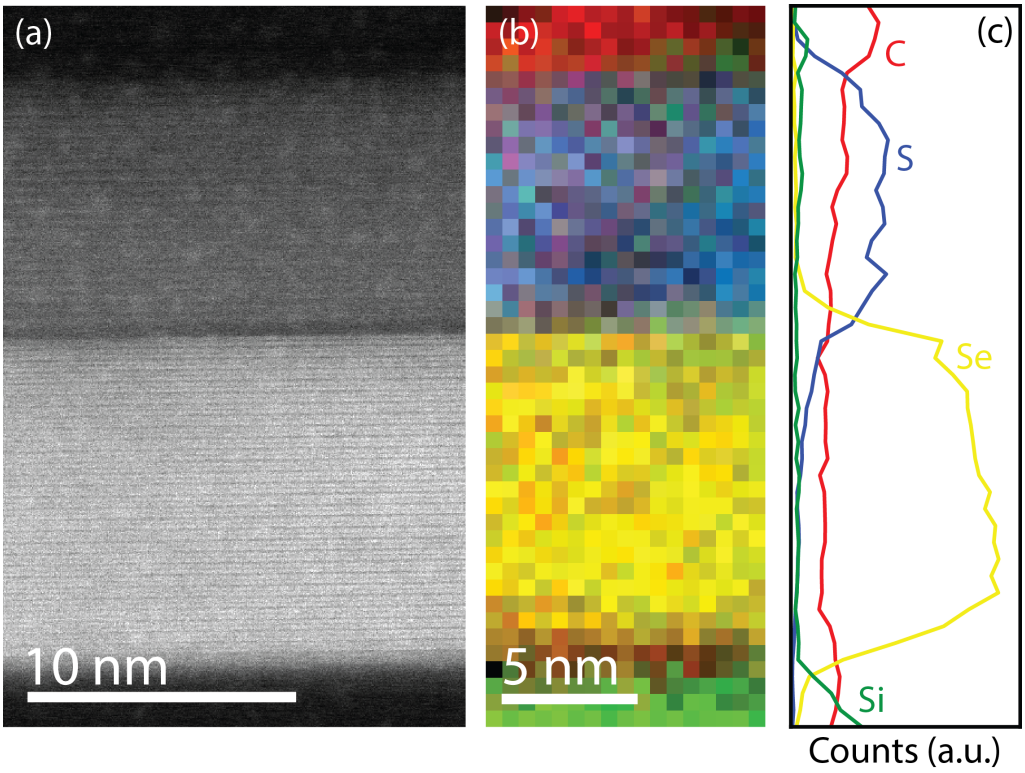

Fig. 4.20 (a) Cross-sectional HAADF-STEM image of hBN/GaS/GaSe heterostructure on SiO_2/Si substrate. (b) EDX mapping of the heterostructure in (a) with S (blue), Se (yellow), C (red) and Si (green) highlighted. (c) Integrated counts of the elements highlighted in (b).

Nonetheless, it has been demonstrated that GaS/GaSe heterostructures can be successfully assembled. The individual flakes of GaS and GaSe in Figure 4.17 come together to form the heterostructure in Figure 4.21(a). On first inspection, there appears to be no visible moiré pattern present, possibly due to the thickness of the structure and the small field of view. To study the moiré patterns of the structures, an FFT of the plan-view HAADF-STEM image in Figure 4.21(a) is performed in Figure 4.21(b). The slight difference in lattice parameter between GaS and GaSe allows one to allocate the correct points in the FFT to each, and to measure the twist angle between the layers. The superlattice spots in the centre of the FFT, highlighted in red, correspond to the moiré lattice from which the moiré lattice parameter can be measured [150]. From the FFT, the twist angle is measured to be $\sim 7.8°$ and the moiré lattice parameter is measured to be ~ 14 Å.

The band gaps and Rashba band splitting effect should be measurable using EELS spectral imaging, however, the simulations in this work were performed on bilayer heterostructures, not few layer/bulk heterostructures as in Figure 4.21, so the results would not be directly comparable in this context. Nonetheless, the Nion UltraSTEM 200 used in this work has an energy resolution of 0.35 eV [151], so it should be able to measurable discern the band gaps in these heterostructures. In order to measure the Rashba splitting, however, this energy resolution is not enough. A highly-monochromated system, such as the Nion UltraSTEM 100MC 'HERMES' at the SuperSTEM facility in Darsbury, England, can achieve energy resolutions of up to 5 meV [151, 152] which would be sufficient to measure such splitting. However, sample preparation requires optimisation before such experiments can be performed.

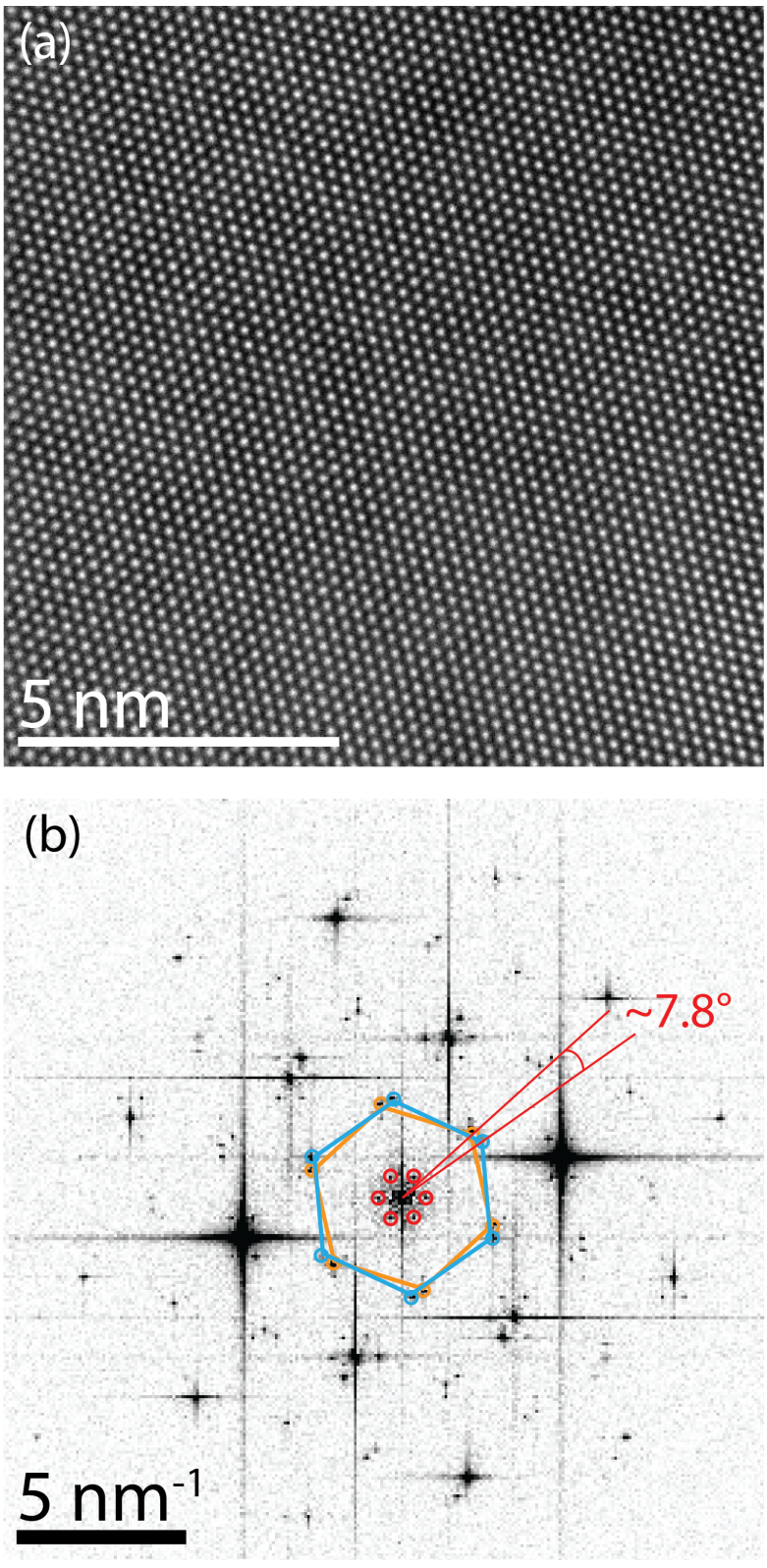

Fig. 4.21 HAADF-STEM image of a GaS/GaSe heterostructure (a) and its corresponding FFT pattern in (b). The FFT is inversed in colour to make it clearer for the reader. The GaS and GaSe reciprocal lattices are highlighted in orange and blue, respectively, along with the moiré lattice spots in red.

4.4 Conclusions

Through the use of first-principles calculations, GaS/GaSe heterostructures have been predicted to exhibit fascinating physical phenomena in the form of Rashba band splitting. The angular dependence of this splitting and of the band gap of the structure allows for many degrees of freedom which can be exploited for spintronic properties. These calculations also show the importance of including SOC effects in systems with broken symmetries, as much interesting material physics may be hidden in plain sight by not including it.

The construction of these heterostructures using mechanical exfoliation of their bulk crystals has also been shown to be successful in this work. Further optimisation of this technique is required to achieve monolayers of GaS and GaSe, and hence construct heterostructures which can be comparable to the theoretical calculations of this work. Low-loss EELS experiments would ideally be performed on a series of heterostructures, at different twist angles, to measure and confirm the trends seen in the band gaps and in the Rashba band splitting energies. Furthermore, multislice simulations of these heterostructures would also be performed to confirm the moiré patterns and moiré lattice spacings formed by their twist angles.

The large change in band gap values with twist angles also can allow for highly tunable optoelectronic devices. With further optimisation of sample preparation and suitable contacts, optical and electronic measurements can be performed to measure the device performance for use in photodetectors [153], for example.

References

[1] A. L.John Peter and T. Viraraghavan. “Thallium: a review of public health and environmental concerns”. In: *Environment International* 31.4 (2005), pp. 493–501. ISSN: 0160-4120. DOI: 10.1016/J.ENVINT.2004.09.003.

[2] Petra Cvjetko, Ivan Cvjetko, and Mirjana Pavlica. “Thallium toxicity in humans”. In: *Arhiv za Higijenu Rada i Toksikologiju* 61.1 (2010), pp. 111–119. ISSN: 00041254. DOI: 10.2478/10004-1254-61-2010-1976.

[3] Anders Lennartson. “Toxic thallium”. In: *Nature Chemistry* 7.7 (2015), pp. 610–610. ISSN: 1755-4349. DOI: 10.1038/nchem.2286.

[4] F. Withers et al. “Light-emitting diodes by band-structure engineering in van der Waals heterostructures”. In: *Nature Materials* 14.3 (2015), pp. 301–306. ISSN: 14764660. DOI: 10.1038/nmat4205.

[5] Yuan Cao et al. “Unconventional superconductivity in magic-angle graphene superlattices”. In: *Nature* 556.7699 (2018), pp. 43–50. ISSN: 14764687. DOI: 10.1038/nature26160.

[6] Pingan Hu et al. “Highly responsive ultrathin GaS nanosheet photodetectors on rigid and flexible substrates”. In: *Nano Letters* 13.4 (2013), pp. 1649–1654. ISSN: 15306984. DOI: 10.1021/nl400107k.

[7] Andrew Harvey et al. “Preparation of gallium sulfide nanosheets by liquid exfoliation and their application as hydrogen evolution catalysts”. In: *Chemistry of Materials* 27.9 (2015), pp. 3483–3493. ISSN: 15205002. DOI: 10.1021/acs.chemmater.5b00910.

[8] Yandong Ma et al. “Tunable electronic and dielectric behavior of GaS and GaSe monolayers”. In: *Physical Chemistry Chemical Physics* 15.19 (2013), pp. 7098–7105. ISSN: 14639076. DOI: 10.1039/c3cp50233c.

[9] Zeineb Ben Aziza et al. “Tunable quasiparticle band gap in few-layer GaSe/graphene van der Waals heterostructures”. In: *Physical Review B* 96.3 (2017), pp. 1–8. ISSN: 24699969. DOI: 10.1103/PhysRevB.96.035407.

[10] Wei Wei et al. “Electronic properties of two-dimensional van der Waals GaS/GaSe heterostructures”. In: *Journal of Materials Chemistry C* 3.43 (2015), pp. 11548–11554. ISSN: 20507526. DOI: 10.1039/c5tc02975a.

[11] K. S. Novoselov et al. “Electric field in atomically thin carbon films”. In: *Science* 306.5696 (2004), pp. 666–669. ISSN: 00368075. DOI: 10.1126/science.1102896.

[12] Andrea Splendiani et al. “Emerging Photoluminescence in Monolayer MoS 2”. In: *Nano Letters* 10.4 (2010), pp. 1271–1275. ISSN: 1530-6984. DOI: 10.1021/nl903868w.

[13] Hai Li et al. “Preparation and Applications of Mechanically Exfoliated Single-Layer and Multilayer MoS 2 and WSe 2 Nanosheets”. In: *Accounts of Chemical Research* 47.4 (2014), pp. 1067–1075. ISSN: 0001-4842. DOI: 10.1021/ar4002312.

[14] Yung Chang Lin et al. “Three-fold rotational defects in two-dimensional transition metal dichalcogenides”. In: *Nature Communications* 6 (2015). ISSN: 20411723. DOI: 10.1038/NCOMMS7736.

[15] Kin Fai Mak and Jie Shan. “Photonics and optoelectronics of 2D semiconductor transition metal dichalcogenides”. In: *Nature Photonics* 10.4 (2016), pp. 216–226. ISSN: 1749-4885. DOI: 10.1038/nphoton.2015.282.

[16] Clement Kok Yong Tan, Wei Fu, and Kian Ping Loh. “Polymorphism and Ferroelectricity in Indium(III) Selenide”. In: *Chemical Reviews* 123.13 (2023), pp. 8701–8717. ISSN: 0009-2665. DOI: 10.1021/acs.chemrev.3c00129.

[17] Zhaoyang Lin et al. “High-yield exfoliation of 2D semiconductor monolayers and reassembly of organic/inorganic artificial superlattices”. In: *Chem* 7.7 (2021), pp. 1887–1902. ISSN: 2451-9294. DOI: 10.1016/J.CHEMPR.2021.03.022.

[18] Weiran Shi et al. “Tin Selenide (SnSe): Growth, Properties, and Applications”. In: *Advanced Science* 5.4 (2018), p. 1700602. ISSN: 2198-3844. DOI: 10.1002/ADVS.201700602.

[19] Kai Chang et al. “Microscopic Manipulation of Ferroelectric Domains in SnSe Monolayers at Room Temperature”. In: *Nano Letters* 20.9 (2020), pp. 6590–6597. ISSN: 1530-6984. DOI: 10.1021/acs.nanolett.0c02357.

[20] Adriano Ambrosi et al. “Exfoliation of Layered Topological Insulators Bi2Se3 and Bi2Te3 via Electrochemistry”. In: *ACS Nano* 10.12 (2016), pp. 11442–11448. ISSN: 1936-0851. DOI: 10.1021/acsnano.6b07096.

[21] Liping Sun et al. “Preparation of Few-Layer Bismuth Selenide by Liquid-Phase-Exfoliation and Its Optical Absorption Properties”. In: *Scientific Reports* 4.1 (2014), p. 4794. ISSN: 2045-2322. DOI: 10.1038/srep04794.

[22] I V Antonova et al. “Electrochemically exfoliated thin Bi2Se3 films and van der Waals heterostructures Bi2Se3 /graphene”. In: *Nanotechnology* 31.12 (2020), p. 125602. ISSN: 0957-4484. DOI: 10.1088/1361-6528/ab5cd5.

[23] Johanna Zultak et al. “Ultra-thin van der Waals crystals as semiconductor quantum wells”. In: *Nature Communications* 11.1 (2020), pp. 1–6. ISSN: 20411723. DOI: 10.1038/s41467-019-13893-w. arXiv: 1910.04215.

[24] O. Del Pozo-Zamudio et al. “Electrically pumped WSe2-based light-emitting van der Waals heterostructures embedded in monolithic dielectric microcavities”. In: *2D Materials* 7.3 (2020), p. 031006. ISSN: 2053-1583. DOI: 10.1088/2053-1583/AB8542. arXiv: 1911.06808.

[25] Woo Jong Yu et al. “Vertically stacked multi-heterostructures of layered materials for logic transistors and complementary inverters”. In: *Nature Materials* 12.3 (2013), pp. 246–252. ISSN: 1476-1122. DOI: 10.1038/nmat3518.

[26] Rai Moriya et al. “Large current modulation in exfoliated-graphene/MoS2/metal vertical heterostructures”. In: *Applied Physics Letters* 105.8 (2014), p. 83119. ISSN: 0003-6951. DOI: 10.1063/1.4894256.

[27] Xiaowei Wang et al. “Van der Waals engineering of ferroelectric heterostructures for long-retention memory”. In: *Nature Communications 2021 12:1* 12.1 (2021), pp. 1–8. ISSN: 2041-1723. DOI: 10.1038/s41467-021-21320-2.

[28] Marco M. Furchi et al. “Photovoltaic Effect in an Electrically Tunable van der Waals Heterojunction”. In: *Nano Letters* 14.8 (2014), pp. 4785–4791. ISSN: 1530-6984. DOI: 10.1021/nl501962c.

[29] Yexin Deng et al. “Black Phosphorus–Monolayer MoS 2 van der Waals Heterojunction p–n Diode”. In: *ACS Nano* 8.8 (2014), pp. 8292–8299. ISSN: 1936-0851. DOI: 10.1021/nn5027388.

[30] Nengjie Huo et al. “Novel and Enhanced Optoelectronic Performances of Multilayer MoS2–WS2 Heterostructure Transistors”. In: *Advanced Functional Materials* 24.44 (2014), pp. 7025–7031. ISSN: 1616-3028. DOI: 10.1002/ADFM.201401504.

[31] Min Sup Choi et al. “Lateral MoS 2 p–n Junction Formed by Chemical Doping for Use in High-Performance Optoelectronics”. In: *ACS Nano* 8.9 (2014), pp. 9332–9340. ISSN: 1936-0851. DOI: 10.1021/nn503284n.

[32] Yichen Wang et al. “High-performance and broadband 2D ReS2/MoS2 semivertical heterojunction photodiodes”. In: *Materials Science in Semiconductor Processing* 165 (2023), p. 107650. ISSN: 1369-8001. DOI: 10.1016/J.MSSP.2023.107650.

[33] Nayereh Ghobadi and Mahdi Pourfath. “Vertical tunneling graphene heterostructure-based transistor for pressure sensing”. In: *IEEE Electron Device Letters* 36.3 (2015), pp. 280–282. ISSN: 07413106. DOI: 10.1109/LED.2014.2388452.

[34] Duy Thach Phan et al. “Black P/graphene hybrid: A fast response humidity sensor with good reversibility and stability”. In: *Scientific Reports* 7.1 (2017), pp. 1–7. ISSN: 2045-2322. DOI: 10.1038/s41598-017-10848-3.

[35] Ashok Chhetry et al. “Black Phosphorus@Laser-Engraved Graphene Heterostructure-Based Temperature–Strain Hybridized Sensor for Electronic-Skin Applications”. In: *Advanced Functional Materials* 31.10 (2021), p. 2007661. ISSN: 1616-3028. DOI: 10.1002/ADFM.202007661.

[36] Phan Thi Kim Loan et al. “Graphene/MoS2 Heterostructures for Ultrasensitive Detection of DNA Hybridisation”. In: *Advanced Materials* 26.28 (2014), pp. 4838–4844. ISSN: 1521-4095. DOI: 10.1002/ADMA.201401084.

[37] Jianwei Gao et al. “Graphene oxide-graphene Van der Waals heterostructure transistor biosensor for SARS-CoV-2 protein detection”. In: *Talanta* 240 (2022), p. 123197. ISSN: 0039-9140. DOI: 10.1016/J.TALANTA.2021.123197.

[38] A. K. Geim and I. V. Grigorieva. “Van der Waals heterostructures”. In: *Nature* 499.7459 (2013), pp. 419–425. ISSN: 00280836. DOI: 10.1038/nature12385. arXiv: 1307.6718.

[39] Valeria Nicolosi et al. “Liquid exfoliation of layered materials”. In: *Science* 340.6139 (2013), pp. 72–75. ISSN: 10959203. DOI: 10.1126/science.1226419.

[40] Jonathan N. Coleman. “Liquid exfoliation of defect-free graphene”. In: *Accounts of Chemical Research* 46.1 (2013), pp. 14–22. ISSN: 00014842. DOI: 10.1021/ar300009f.

[41] Junhao Lin et al. “Gentle transfer method for water- and acid/alkali-sensitive 2D materials for (S)TEM study”. In: *APL Materials* 4.11 (2016). ISSN: 2166532X. DOI: 10.1063/1.4967938.

[42] I. G. Rebollo et al. “Thin-suspended 2D materials: Facile, versatile, and deterministic transfer assembly”. In: *2D Materials* 8.3 (2021). ISSN: 20531583. DOI: 10.1088/2053-1583/abf98c. arXiv: 2011.14166.

[43] Qinghua Zhao et al. “An inexpensive system for the deterministic transfer of 2D materials”. In: *JPhys Materials* 3.1 (2020). ISSN: 25157639. DOI: 10.1088/2515-7639/ab6a72.

[44] Janis Köster et al. “Polymer-assisted TEM specimen preparation method for oxidation-sensitive 2D materials”. In: *Nanotechnology* 32.7 (2021). ISSN: 13616528. DOI: 10.1088/1361-6528/abc49e.

[45] Xu Dong Chen et al. “High-Precision Twist-Controlled Bilayer and Trilayer Graphene”. In: *Advanced Materials* 28.13 (2016), pp. 2563–2570. ISSN: 15214095. DOI: 10.1002/adma.201505129.

[46] Kyounghwan Kim et al. “Van der Waals Heterostructures with High Accuracy Rotational Alignment”. In: *Nano Letters* 16.3 (2016), pp. 1989–1995. ISSN: 15306992. DOI: 10.1021/acs.nanolett.5b05263.

[47] Adam J. Watson et al. “Transfer of large-scale two-dimensional semiconductors: challenges and developments”. In: *2D Materials* 8.3 (2021), p. 032001. ISSN: 2053-1583. DOI: 10.1088/2053-1583/ABF234. arXiv: 2101.03004.

[48] S. J. Haigh et al. “Cross-sectional imaging of individual layers and buried interfaces of graphene-based heterostructures and superlattices”. In: *Nature Materials* 11.9 (2012), pp. 764–767. ISSN: 14764660. DOI: 10.1038/nmat3386. arXiv: 1206.6698.

[49] Andres Castellanos-Gomez et al. “Van der Waals heterostructures”. In: *Nature Reviews Methods Primers* 2.1 (2022), pp. 1–19. ISSN: 26628449. DOI: 10.1038/s43586-022-00139-1.

[50] Shanshan Wang, Xiaochen Wang, and Jamie H. Warner. “All Chemical Vapor Deposition Growth of MoS 2 :h-BN Vertical van der Waals Heterostructures”. In: *ACS Nano* 9.5 (2015), pp. 5246–5254. ISSN: 1936-0851. DOI: 10.1021/acsnano.5b00655.

[51] Tao Zhang and Lei Fu. “Controllable Chemical Vapor Deposition Growth of Two-Dimensional Heterostructures”. In: *Chem* 4.4 (2018), pp. 671–689. ISSN: 2451-9294. DOI: 10.1016/J.CHEMPR.2017.12.006.

[52] Honglei Gao et al. “Van der Waals MoS2/PdSe2 Heterostructures Grown by Chemical Vapor Deposition for Broadband and Polarized Photodetection”. In: *Advanced Materials Interfaces* 9.12 (2022), p. 2102350. ISSN: 2196-7350. DOI: 10.1002/ADMI.202102350.

[53] Kate Reidy et al. “Direct imaging and electronic structure modulation of moiré superlattices at the 2D/3D interface”. In: *Nature Communications* 12.1 (2021), pp. 1–9. ISSN: 2041-1723. DOI: 10.1038/s41467-021-21363-5. arXiv: 2008.12215.

[54] Stephen Carr et al. “Twistronics: Manipulating the electronic properties of two-dimensional layered structures through their twist angle”. In: *Physical Review B* 95.7 (2017), p. 075420. ISSN: 2469-9950. DOI: 10.1103/PhysRevB.95.075420. arXiv: 1611.00649.

[55] Zachariah Hennighausen and Swastik Kar. “Twistronics: a turning point in 2D quantum materials”. In: *Electronic Structure* 3.1 (2021), p. 014004. ISSN: 2516-1075. DOI: 10.1088/2516-1075/ABD957. arXiv: 2101.04501.

[56] Rafi Bistritzer and Allan H. MacDonald. “Moiré bands in twisted double-layer graphene”. In: *Proceedings of the National Academy of Sciences* 108.30 (2011), pp. 12233–12237. ISSN: 0027-8424. DOI: 10.1073/pnas.1108174108. arXiv: 1009.4203.

[57] Xiaobo Lu et al. “Superconductors, orbital magnets and correlated states in magic-angle bilayer graphene”. In: *Nature* 574.7780 (2019), pp. 653–657. ISSN: 14764687. DOI: 10.1038/s41586-019-1695-0. arXiv: 1903.06513.

[58] Matthew Yankowitz et al. “Tuning superconductivity in twisted bilayer graphene”. In: *Science* 363.6431 (2019), pp. 1059–1064. ISSN: 0036-8075. DOI: 10.1126/science.aav1910. arXiv: 1808.07865.

[59] Aaron L. Sharpe et al. “Emergent ferromagnetism near three-quarters filling in twisted bilayer graphene”. In: *Science* 365.6453 (2019), pp. 605–608. ISSN: 0036-8075. DOI: 10.1126/science.aaw3780. arXiv: 1901.03520.

[60] Evgeny M. Alexeev et al. “Resonantly hybridized excitons in moiré superlattices in van der Waals heterostructures”. In: *Nature* 567.7746 (2019), pp. 81–86. ISSN: 0028-0836. DOI: 10.1038/s41586-019-0986-9. arXiv: 1904.06214.

[61] Kha Tran et al. “Evidence for moiré excitons in van der Waals heterostructures”. In: *Nature* 567.7746 (2019), pp. 71–75. ISSN: 0028-0836. DOI: 10.1038/s41586-019-0975-z.

[62] Chenhao Jin et al. “Observation of moiré excitons in WSe2/WS2 heterostructure superlattices”. In: *Nature* 567.7746 (2019), pp. 76–80. ISSN: 0028-0836. DOI: 10.1038/s41586-019-0976-y. arXiv: 1812.09815.

[63] Hongyi Yu et al. “Moiré excitons: From programmable quantum emitter arrays to spin-orbit–coupled artificial lattices”. In: *Science Advances* 3.11 (2017). ISSN: 2375-2548. DOI: 10.1126/sciadv.1701696. arXiv: 1710.07015.

[64] M. Serlin et al. “Intrinsic quantized anomalous Hall effect in a moiré heterostructure”. In: *Science* 367.6480 (2020), pp. 900–903. ISSN: 0036-8075. DOI: 10.1126/science.aay5533. arXiv: 1907.00261.

[65] Ya-Hui Zhang, Dan Mao, and T. Senthil. “Twisted bilayer graphene aligned with hexagonal boron nitride: Anomalous Hall effect and a lattice model”. In: *Physical Review Research* 1.3 (2019), p. 033126. ISSN: 2643-1564. DOI: 10.1103/PhysRevResearch.1.033126. arXiv: 1901.08209.

[66] C. R. Dean et al. “Hofstadter’s butterfly and the fractal quantum Hall effect in moiré superlattices”. In: *Nature* 497.7451 (2013), pp. 598–602. ISSN: 0028-0836. DOI: 10.1038/nature12186.

[67] Lei Wang et al. “Evidence for a fractional fractal quantum Hall effect in graphene superlattices”. In: *Science* 350.6265 (2015), pp. 1231–1234. ISSN: 0036-8075. DOI: 10.1126/science.aad2102.

[68] Dacen Waters et al. “Mixed-dimensional moiré systems of twisted graphitic thin films”. In: *Nature* 620.7975 (2023), pp. 750–755. ISSN: 0028-0836. DOI: 10.1038/s41586-023-06290-3.

[69] C. H. Ho and S. L. Lin. “Optical properties of the interband transitions of layered gallium sulfide”. In: *Journal of Applied Physics* 100.8 (2006). ISSN: 00218979. DOI: 10.1063/1.2358192.

[70] D. V. Rybkovskiy et al. “Size-induced effects in gallium selenide electronic structure: The influence of interlayer interactions”. In: *Physical Review B - Condensed Matter and Materials Physics* 84.8 (2011), pp. 1–7. ISSN: 10980121. DOI: 10.1103/PhysRevB.84.085314.

[71] Houlong L. Zhuang and Richard G. Hennig. “Single-layer group-III monochalcogenide photocatalysts for water splitting”. In: *Chemistry of Materials* 25.15 (2013), pp. 3232–3238. ISSN: 08974756. DOI: 10.1021/cm401661x.

[72] Yael Gutiérrez et al. “Layered gallium sulfide optical properties from monolayer to CVD crystalline thin films”. In: *Optics Express* 30.15 (2022), p. 27609. ISSN: 1094-4087. DOI: 10.1364/OE.459815.

[73] Si Zhou et al. “Monolayer group-III monochalcogenides by oxygen functionalization: a promising class of two-dimensional topological insulators”. In: *npj Quantum Materials* 3.1 (2018), p. 16. ISSN: 2397-4648. DOI: 10.1038/s41535-018-0089-0.

[74] Sahin Sorifi et al. “High-Temperature Performance of a GaSe Nanosheet-Based Broadband Photodetector”. In: *ACS Applied Electronic Materials* 2.3 (2020), pp. 670–676. ISSN: 2637-6113. DOI: 10.1021/acsaelm.9b00770.

[75] Yael Gutiérrez et al. “Exploring the Thickness-Dependence of the Properties of Layered Gallium Sulfide”. In: *Frontiers in Chemistry* 9.November (2021), pp. 1–8. ISSN: 22962646. DOI: 10.3389/fchem.2021.781467.

[76] A. Kuhn, A. Chevy, and R. Chevalier. “Refinement of the 2 H GaS β-type”. In: *Acta Crystallographica Section B Structural Crystallography and Crystal Chemistry* 32.3 (1976), pp. 983–984. ISSN: 0567-7408. DOI: 10.1107/S0567740876004445.

[77] A. Kuhn, A. Chevy, and R. Chevalier. “Crystal structure and interatomic distances in GaSe”. In: *Physica Status Solidi (a)* 31.2 (1975), pp. 469–475. ISSN: 00318965. DOI: 10.1002/pssa.2210310216.

[78] Leon Balents et al. “Superconductivity and strong correlations in moiré flat bands”. In: *Nature Physics* 16.7 (2020), pp. 725–733. ISSN: 1745-2473. DOI: 10.1038/s41567-020-0906-9.

[79] Matthew Yankowitz et al. “van der Waals heterostructures combining graphene and hexagonal boron nitride”. In: *Nature Reviews Physics* 1.2 (2019), pp. 112–125. ISSN: 2522-5820. DOI: 10.1038/s42254-018-0016-0.

[80] Stuart A. Wolf, Almadena Y. Chtchelkanova, and Daryl M. Treger. “Spintronics—A retrospective and perspective”. In: *IBM Journal of Research and Development* 50.1 (2006), pp. 101–110. ISSN: 0018-8646. DOI: 10.1147/rd.501.0101.

[81] Koichi Momma and Fujio Izumi. “VESTA 3 for three-dimensional visualization of crystal, volumetric and morphology data”. In: *Journal of Applied Crystallography* 44.6 (2011), pp. 1272–1276. ISSN: 00218898. DOI: 10.1107/S0021889811038970.

[82] G. Kresse and J. Furthmüller. “Efficient iterative schemes for ab initio total energy calculations using a plane wave basis set”. In: *Physical Review B - Condensed Matter and Materials Physics* 54.16 (1996), pp. 11169–11186. ISSN: 1550235X. DOI: 10.1103/PhysRevB.54.11169.

[83] G. Kresse and D. Joubert. “From ultrasoft pseudopotentials to the projector augmented wave method”. In: *Physical Review B* 59.3 (1999), pp. 1758–1775. ISSN: 0163-1829. DOI: 10.1103/PhysRevB.59.1758.

[84] John P. Perdew, Matthias Ernzerhof, and Kieron Burke. “Rationale for mixing exact exchange with density functional approximations”. In: *The Journal of Chemical Physics* 105.22 (1996), pp. 9982–9985. ISSN: 0021-9606. DOI: 10.1063/1.472933.

[85] Stefan Grimme. “Accurate description of van der Waals complexes by density functional theory including empirical corrections”. In: *Journal of Computational Chemistry* 25.12 (2004), pp. 1463–1473. ISSN: 01928651. DOI: 10.1002/jcc.20078.

[86] Stefan Grimme, Stephan Ehrlich, and Lars Goerigk. “Effect of the damping function in dispersion corrected density functional theory”. In: *Journal of Computational Chemistry* 32.7 (2011), pp. 1456–1465. ISSN: 01928651. DOI: 10.1002/jcc.21759.

[87] Irina V. Lebedeva et al. “Comparison of performance of van der Waals-corrected exchange-correlation functionals for interlayer interaction in graphene and hexagonal boron nitride”. In: *Computational Materials Science* 128 (2017), pp. 45–58. ISSN: 09270256. DOI: 10.1016/j.commatsci.2016.11.011. arXiv: 1708.01504.

[88] Jochen Heyd, Gustavo E. Scuseria, and Matthias Ernzerhof. “Hybrid functionals based on a screened Coulomb potential”. In: *The Journal of Chemical Physics* 118.18 (2003), pp. 8207–8215. ISSN: 0021-9606. DOI: 10.1063/1.1564060.

[89] G. P. Francis and M. C. Payne. “Finite basis set corrections to total energy pseudopotential calculations”. In: *Journal of Physics: Condensed Matter* 2.19 (1990), pp. 4395–4404. ISSN: 09538984. DOI: 10.1088/0953-8984/2/19/007.

[90] Tomasz Necio and Magdalena Birowska. “Supercell-core software: A useful tool to generate an optimal supercell for vertically stacked nanomaterials”. In: *AIP Advances* 10.10 (2020), p. 105105. ISSN: 2158-3226. DOI: 10.1063/5.0023984.

[91] Stephan Mohr et al. “Accurate and efficient linear scaling DFT calculations with universal applicability”. In: *Physical Chemistry Chemical Physics* 17.47 (2015), pp. 31360–31370. ISSN: 1463-9076. DOI: 10.1039/C5CP00437C. arXiv: 1501.05884.

[92] X. Gonze et al. “ABINIT: First-principles approach to material and nanosystem properties”. In: *Computer Physics Communications* 180.12 (2009), pp. 2582–2615. ISSN: 00104655. DOI: 10.1016/j.cpc.2009.07.007.

[93] Paolo Giannozzi et al. “QUANTUM ESPRESSO: a modular and open-source software project for quantum simulations of materials”. In: *Journal of Physics: Condensed Matter* 21.39 (2009), p. 395502. ISSN: 0953-8984. DOI: 10.1088/0953-8984/21/39/395502. arXiv: 0906.2569.

[94] M. D. Segall et al. “First-principles simulation: ideas, illustrations and the CASTEP code”. In: *Journal of Physics: Condensed Matter* 14.11 (2002), pp. 2717–2744. ISSN: 0953-8984. DOI: 10.1088/0953-8984/14/11/301.

[95] J. Almlöf, K. Faegri, and K. Korsell. “Principles for a direct SCF approach to LICAO-MO ab-initio calculations”. In: *Journal of Computational Chemistry* 3.3 (1982), pp. 385–399. ISSN: 0192-8651. DOI: 10.1002/jcc.540030314.

[96] Dieter Cremer and JüRgen Gauss. “An unconventional scf method for calculations on large molecules”. In: *Journal of Computational Chemistry* 7.3 (1986), pp. 274–282. ISSN: 0192-8651. DOI: 10.1002/jcc.540070305.

[97] Joseph C.A. Prentice et al. “The ONETEP linear-scaling density functional theory program”. In: *Journal of Chemical Physics* 152.17 (2020), p. 174111. ISSN: 10897690. DOI: 10.1063/5.0004445/198202.

[98] Daniel S. Koda et al. “Coincidence Lattices of 2D Crystals: Heterostructure Predictions and Applications”. In: *The Journal of Physical Chemistry C* 120.20 (2016), pp. 10895–10908. ISSN: 1932-7447. DOI: 10.1021/acs.jpcc.6b01496.

[99] Predrag Lazić. “CellMatch: Combining two unit cells into a common supercell with minimal strain”. In: *Computer Physics Communications* 197 (2015), pp. 324–334. ISSN: 00104655. DOI: 10.1016/j.cpc.2015.08.038.

[100] Davide Campi et al. “Expansion of the Materials Cloud 2D Database”. In: *ACS Nano* 17.12 (2023), pp. 11268–11278. ISSN: 1936-0851. DOI: 10.1021/acsnano.2c11510.

[101] Rui Dong et al. “High-throughput bandstructure simulations of van der Waals hetero-bilayers formed by 1T and 2H monolayers”. In: *npj 2D Materials and Applications* 5.1 (2021), p. 26. ISSN: 2397-7132. DOI: 10.1038/s41699-021-00200-9.

[102] Wendong Wang et al. “Clean assembly of van der Waals heterostructures using silicon nitride membranes”. In: *Nature Electronics* 6.12 (2023), pp. 981–990. ISSN: 2520-1131. DOI: 10.1038/s41928-023-01075-y.

[103] Achint Jain et al. “Minimizing residues and strain in 2D materials transferred from PDMS”. In: *Nanotechnology* 29.26 (2018), p. 265203. ISSN: 0957-4484. DOI: 10.1088/1361-6528/aabd90. arXiv: 1801.02971.

[104] Chan Kim et al. “Damage-free transfer mechanics of 2-dimensional materials: competition between adhesion instability and tensile strain”. In: *NPG Asia Materials* 13.1 (2021), p. 44. ISSN: 1884-4049. DOI: 10.1038/s41427-021-00311-1.

[105] Roman Kempt. *hetbuilder: Zenodo Release*. DOI: 10.5281/ZENODO.4721346.

[106] Zhiwei Peng et al. “Strain engineering of 2D semiconductors and graphene: from strain fields to band-structure tuning and photonic applications”. In: *Light: Science & Applications* 9.1 (2020), p. 190. ISSN: 2047-7538. DOI: 10.1038/s41377-020-00421-5.

[107] Yuling Yin, Hangyan Chen, and Qinghong Yuan. “Strain-induced bandgap engineering in C3N nanotubes”. In: *Chemical Physics Letters* 768 (2021), p. 138390. ISSN: 00092614. DOI: 10.1016/j.cplett.2021.138390.

[108] János Pető et al. “Moderate strain induced indirect bandgap and conduction electrons in MoS2 single layers”. In: *npj 2D Materials and Applications* 3.1 (2019), p. 39. ISSN: 2397-7132. DOI: 10.1038/s41699-019-0123-5.

[109] A. Chaves et al. “Bandgap engineering of two-dimensional semiconductor materials”. In: *npj 2D Materials and Applications* 4.1 (2020), p. 29. ISSN: 2397-7132. DOI: 10.1038/s41699-020-00162-4.

[110] Nathanael P. Kazmierczak et al. “Strain fields in twisted bilayer graphene”. In: *Nature Materials* 20.7 (2021), pp. 956–963. ISSN: 1476-1122. DOI: 10.1038/s41563-021-00973-w. arXiv: 2008.09761.

[111] Astrid Weston et al. “Interfacial ferroelectricity in marginally twisted 2D semiconductors”. In: *Nature Nanotechnology 2022 17:4* 17.4 (2022), pp. 390–395. ISSN: 1748-3395. DOI: 10.1038/s41565-022-01072-w. arXiv: 2108.06489.

[112] Álvaro Rodríguez et al. “Complex Strain Scapes in Reconstructed Transition-Metal Dichalcogenide Moiré Superlattices”. In: *ACS Nano* 17.8 (2023), pp. 7787–7796. ISSN: 1936-0851. DOI: 10.1021/acsnano.3c00609.

[113] En Li et al. “Lattice reconstruction induced multiple ultra-flat bands in twisted bilayer WSe2”. In: *Nature Communications* 12.1 (2021), p. 5601. ISSN: 2041-1723. DOI: 10.1038/s41467-021-25924-6. arXiv: 2103.06479.

[114] Chenhao Jin et al. “Observation of moiré excitons in WSe2/WS2 heterostructure superlattices”. In: *Nature* 567.7746 (2019), pp. 76–80. ISSN: 0028-0836. DOI: 10.1038/s41586-019-0976-y. arXiv: 1812.09815.

[115] Trond I. Andersen et al. “Excitons in a reconstructed moiré potential in twisted WSe2/WSe2 homobilayers”. In: *Nature Materials* 20.4 (2021), pp. 480–487. ISSN: 1476-1122. DOI: 10.1038/s41563-020-00873-5.

[116] Klaus Zollner, Eike Icking, and Jaroslav Fabian. “Electronic and spin-orbit properties of <math> <mi>h</mi> </math> -BN encapsulated bilayer graphene”. In: *Physical Review B* 108.12 (2023), p. 125126. ISSN: 2469-9950. DOI: 10.1103/PhysRevB.108.125126. arXiv: 2307.11697.

[117] Alex M Ganose, Adam J Jackson, and David O Scanlon. “sumo: Command-line tools for plotting and analysis of periodic ab initio calculations”. In: *Journal of Open Source Software* 3.28 (2018), p. 717. ISSN: 2475-9066. DOI: 10.21105/joss.00717.

[118] Uthpala Herath et al. “PyProcar: A Python library for electronic structure pre/post-processing”. In: *Computer Physics Communications* 251 (2020), p. 107080. ISSN: 00104655. DOI: 10.1016/j.cpc.2019.107080. arXiv: 1906.11387.

[119] James M. LeBeau et al. “Position averaged convergent beam electron diffraction: Theory and applications”. In: *Ultramicroscopy* 110.2 (2010), pp. 118–125. ISSN: 03043991. DOI: 10.1016/j.ultramic.2009.10.001.

[120] Yoichiro Ogata et al. “Refinement of the crystal structural parameters of the intermediate phase of h-BaTiO 3 using convergent-beam electron diffraction”. In: *Acta Crystallographica Section A Foundations of Crystallography* 60.6 (2004), pp. 525–531. ISSN: 0108-7673. DOI: 10.1107/S0108767304016307.

[121] Lewys Jones et al. “Smart Align-a new tool for robust non-rigid registration of scanning microscope data”. In: *Advanced Structural and Chemical Imaging* 1.1 (2015), pp. 1–16. ISSN: 21980926. DOI: 10.1186/s40679-015-0008-4.

[122] David J. Griffiths and Darrell F. Schroeter. *Introduction to Quantum Mechanics*. 3rd. Cambridge University Press, 2018. ISBN: 9781316995433. DOI: 10.1017/9781316995433.

[123] Alexander J. Browne, Aleksandra Krajewska, and Alexandra S. Gibbs. “Quantum materials with strong spin-orbit coupling: challenges and opportunities for materials chemists”. In: *Journal of Materials Chemistry C* 9.35 (2021), pp. 11640–11654. ISSN: 2050-7526. DOI: 10.1039/D1TC02070F.

[124] Daniel I. Khomskii. *Transition Metal Compounds*. Cambridge University Press, 2014. ISBN: 9781107020177. DOI: 10.1017/CBO9781139096782.

[125] Wahyu Setyawan and Stefano Curtarolo. “High-throughput electronic band structure calculations: Challenges and tools”. In: *Computational Materials Science* 49.2 (2010), pp. 299–312. ISSN: 09270256. DOI: 10.1016/j.commatsci.2010.05.010. arXiv: 1004.2974.

[126] A. Manchon et al. “New perspectives for Rashba spin–orbit coupling”. In: *Nature Materials* 14.9 (2015), pp. 871–882. ISSN: 1476-1122. DOI: 10.1038/nmat4360. arXiv: 1507.02408.

[127] Sara Varotto et al. “Direct visualization of Rashba-split bands and spin/orbital-charge interconversion at KTaO3 interfaces”. In: *Nature Communications* 13.1 (2022), p. 6165. ISSN: 2041-1723. DOI: 10.1038/s41467-022-33621-1. arXiv: 2207.08698.

[128] Zeineb Ben Aziza et al. “Valence band inversion and spin-orbit effects in the electronic structure of monolayer GaSe”. In: *Physical Review B* 98.11 (2018), p. 115405. ISSN: 2469-9950. DOI: 10.1103/PhysRevB.98.115405.

[129] Hideaki Iwasawa. “High-resolution angle-resolved photoemission spectroscopy and microscopy”. In: *Electronic Structure* 2.4 (2020), p. 043001. ISSN: 2516-1075. DOI: 10.1088/2516-1075/abb379.

[130] O.L. Krivanek et al. “Progress in ultrahigh energy resolution EELS”. In: *Ultramicroscopy* 203 (2019), pp. 60–67. ISSN: 03043991. DOI: 10.1016/j.ultramic.2018.12.006.

[131] K. Ishizaka et al. “Giant Rashba-type spin splitting in bulk BiTeI”. In: *Nature Materials* 10.7 (2011), pp. 521–526. ISSN: 1476-1122. DOI: 10.1038/nmat3051.

[132] Ya Feng et al. “Rashba-like spin splitting along three momentum directions in trigonal layered PtBi2”. In: *Nature Communications* 10.1 (2019), p. 4765. ISSN: 2041-1723. DOI: 10.1038/s41467-019-12805-2. arXiv: 1910.12671.

[133] Preeti Bhumla et al. “Origin of Rashba Spin Splitting and Strain Tunability in Ferroelectric Bulk CsPbF 3”. In: *The Journal of Physical Chemistry Letters* 12.39 (2021), pp. 9539–9546. ISSN: 1948-7185. DOI: 10.1021/acs.jpclett.1c02596. arXiv: 2108.03683.

[134] Sunny Gupta and Boris I. Yakobson. “What Dictates Rashba Splitting in 2D van der Waals Heterobilayers”. In: *Journal of the American Chemical Society* 143.9 (2021), pp. 3503–3508. ISSN: 0002-7863. DOI: 10.1021/jacs.0c12809.

[135] Dario Bercioux and Procolo Lucignano. “Quantum transport in Rashba spin–orbit materials: a review”. In: *Reports on Progress in Physics* 78.10 (2015), p. 106001. ISSN: 0034-4885. DOI: 10.1088/0034-4885/78/10/106001. arXiv: 1502.00570.

[136] M. Michiardi et al. “Optical manipulation of Rashba-split 2-dimensional electron gas”. In: *Nature Communications* 13.1 (2022), p. 3096. ISSN: 2041-1723. DOI: 10.1038/s41467-022-30742-5. arXiv: 2105.09320.

[137] Wencan Jin et al. “Tuning the electronic structure of monolayer graphene/MoS2 van der Waals heterostructures via interlayer twist”. In: *Physical Review B* 92.20 (2015), p. 201409. ISSN: 1098-0121. DOI: 10.1103/PhysRevB.92.201409.

[138] Jiajun Chen et al. “Twist-angle-dependent momentum-space direct and indirect interlayer excitons in WSe 2 /WS 2 heterostructure”. In: *RSC Advances* 13.26 (2023), pp. 18099–18107. ISSN: 2046-2069. DOI: 10.1039/D3RA02952B.

[139] Klaus Zollner, Paulo E. Faria Junior, and Jaroslav Fabian. “Strong manipulation of the valley splitting upon twisting and gating in MoSe2/CrI3 and WSe2/CrI3 van der Waals heterostructures”. In: *Physical Review B* 107.3 (2023), p. 035112. ISSN: 2469-9950. DOI: 10.1103/PhysRevB.107.035112. arXiv: 2210.13794.

[140] Sayantika Chowdhury, P. Venkateswaran, and D. Somvanshi. “Interlayer twist angle-dependent electronic structure and optical properties of InSe/WTe 2 van der Waals heterostructure”. In: *2022 IEEE International Conference of Electron Devices Society Kolkata Chapter (EDKCON)*. IEEE, 2022, pp. 325–328. ISBN: 978-1-6654-7205-0. DOI: 10.1109/EDKCON56221.2022.10032930.

[141] Shengxi Huang et al. “Probing the Interlayer Coupling of Twisted Bilayer MoS 2 Using Photoluminescence Spectroscopy”. In: *Nano Letters* 14.10 (2014), pp. 5500–5508. ISSN: 1530-6984. DOI: 10.1021/nl5014597.

[142] Chan Su Jung et al. “Red-to-Ultraviolet Emission Tuning of Two-Dimensional Gallium Sulfide/Selenide”. In: *ACS Nano* 9.10 (2015), pp. 9585–9593. ISSN: 1936-0851. DOI: 10.1021/acsnano.5b04876.

[143] Rik Brydson, ed. *Aberration-Corrected Analytical Transmission Electron Microscopy*. Wiley, 2011, p. 280. ISBN: 978-1-119-97990-6.

[144] Sobhit Singh and Aldo H. Romero. “Giant tunable Rashba spin splitting in a two-dimensional BiSb monolayer and in BiSb/AlN heterostructures”. In: *Physical Review B* 95.16 (2017), p. 165444. ISSN: 2469-9950. DOI: 10.1103/PhysRevB.95.165444. arXiv: 1701.06213.

[145] Samuel D. Stranks and Paulina Plochocka. “The influence of the Rashba effect”. In: *Nature Materials* 17.5 (2018), pp. 381–382. ISSN: 1476-1122. DOI: 10.1038/s41563-018-0067-8.

[146] Jiajia Chen et al. “Tunable Rashba Spin Splitting in Two-Dimensional Polar Perovskites”. In: *The Journal of Physical Chemistry Letters* 12.7 (2021), pp. 1932–1939. ISSN: 1948-7185. DOI: 10.1021/acs.jpclett.0c03668.

[147] Ryo Noguchi. “Revealing the Role of Wavefunctions in Rashba-Split States”. In: Springer, Singapore, 2022, pp. 39–76. ISBN: 978-981-19-1874-2. DOI: 10.1007/978-981-19-1874-2_4.

[148] Sara Varotto et al. “Direct visualization of Rashba-split bands and spin/orbital-charge interconversion at KTaO3 interfaces”. In: *Nature Communications* 13.1 (2022), p. 6165. ISSN: 2041-1723. DOI: 10.1038/s41467-022-33621-1. arXiv: 2207.08698.

[149] Takuya Iwasaki et al. “Bubble-Free Transfer Technique for High-Quality Graphene/hBN van der Waals Heterostructures”. In: *ACS Applied Materials & Interfaces* 12.7 (2020), pp. 8533–8538. ISSN: 1944-8244. DOI: 10.1021/acsami.9b19191.

[150] Zachariah Hennighausen et al. “Evidence of a purely electronic two-dimensional lattice at the interface of TMD/Bi 2 Se 3 heterostructures”. In: *Nanoscale* 11.34 (2019), pp. 15929–15938. ISSN: 2040-3364. DOI: 10.1039/C9NR04412D.

[151] *Results - Nion Inc. - https://www.nion.com/results.html.* (accessed 2023-12-13).

[152] *Instrumentation - SuperSTEM - https://www.superstem.org/facility/instrumentation.* (accessed 2023-12-18).

[153] Oriol Lopez-Sanchez et al. “Ultrasensitive photodetectors based on monolayer MoS2”. In: *Nature Nanotechnology* 8.7 (2013), pp. 497–501. ISSN: 1748-3387. DOI: 10.1038/nnano.2013.100.

5

Structural Characterization of $BaZrS_{(3-y)}Se_y$ Perovskite Thin Films

The world is not our facility
We have a responsibility
To use all of our abilities
To keep this place alive

– "Burning Too", *Margin Walker EP*, Fugazi

In the previous chapters, the role of stacking of 2-D chalcogenide layers was investigated, be it intrinsic stacking faults in $TlGaSe_2$ in Chapter 3, or assembly of GaS/GaSe twisted layers and heterostructures in Chapter 4. While these systems have interesting material properties, such as thermoelectricity or the Rashba effect, respectively, there are still major limitations preventing these materials from advancing into market-ready devices.

For $TlGaSe_2$, as mentioned at the start of Chapter 4, the toxicity of thallium would likely deter consumers from such devices (much to the efforts of the manufacturer's marketing department). As for the GaS/GaSe heterostructures, while the toxicity is not an issue here, it is a labour-intensive, multistep process to build each individual heterostructure which currently would be prohibitively expensive to do at scale. While there are efforts to grow van der Waals heterostructures directly [1–3] and mechanise the process [4], these methods are still not ready for en masse device manufacturing.

For more practical, safer, and environmentally conscious future use, chalcogenide systems that avoid the use of toxic elements and that can be scaled in the near future should be further investigated. One such class of chalcogenides which fulfils these criteria are chalcogenide perovskites. In this chapter, chalcogenide perovskites are introduced and discussed. The $BaZrS_{(3-y)}Se_y$ alloy system is characterised via STEM, coupled with EDX and EELS. These are used to understand the diffusion of defects, both point defects and planar defects, throughout the structure and their effects on optoelectronic properties.

The work in this Chapter was performed during a four-month placement at MIT in 2022. The HAADF-STEM imaging, spectroscopy and analysis for the y = 1 samples were performed by the author, while the y = 2 samples were studied by Michael Xu (MIT) after the author had returned from the placement. The DFT calculations were performed by the author, while all other experiments were performed by several members of Prof. Rafael Jaramillo's group at MIT (Ida Sadeghi, Jack Van Sambeek, Kevin Ye, and Tao Cai).

5.1 Introduction

Alternative sources of energy must be developed in order to address the rising threats from climate change. Of the most common types of renewable energy sources available, solar energy is by far one of the most promising given the abundance of sunlight impinging onto the Earth's surface [5].

Solar cells operate under the principle of the photovoltaic effect. This is where photons of energy larger than that of the band gap of a semiconducting device (often a *pn*-junction) are absorbed by the material. This forms electron-hole pairs, and with suitable contacts attached to the device, allows a photo-generated current to flow in a circuit [6, 7].

Most commercial photovoltaics (PVs) are based on crystalline silicon wafer technology, be it mono- or poly-crystalline [5]. Si-based PVs are quite brittle, have low absorption coefficients, and become less effective with increased temperature [8, 9]. Therefore, research is shifting towards thin-film-based PVs, such as perovskite PVs, due to their far lower manufacturing costs and relatively simpler synthesis methods [10].

The perovskite structure is in the form of ABX_3, where A and B are cations and X is either oxygen or chalcogen ions. These are arranged in an idealised cubic structure,

albeit variations such as orthogonal or tetragonal cells, and distorted cells do also exist [11]. Perovskites are used in PVs as a light-harvesting layer due to their relatively high absorption coefficients and direct correlation of efficiency with temperature [12–14]. Perovskite PVs are some of the highest cell efficiencies for single-junction PVs to date, as can be seen in Figure 5.1. Other added benefits include that they are far lighter and more flexible than wafer-based PVs, allowing for easier transportation and installation.

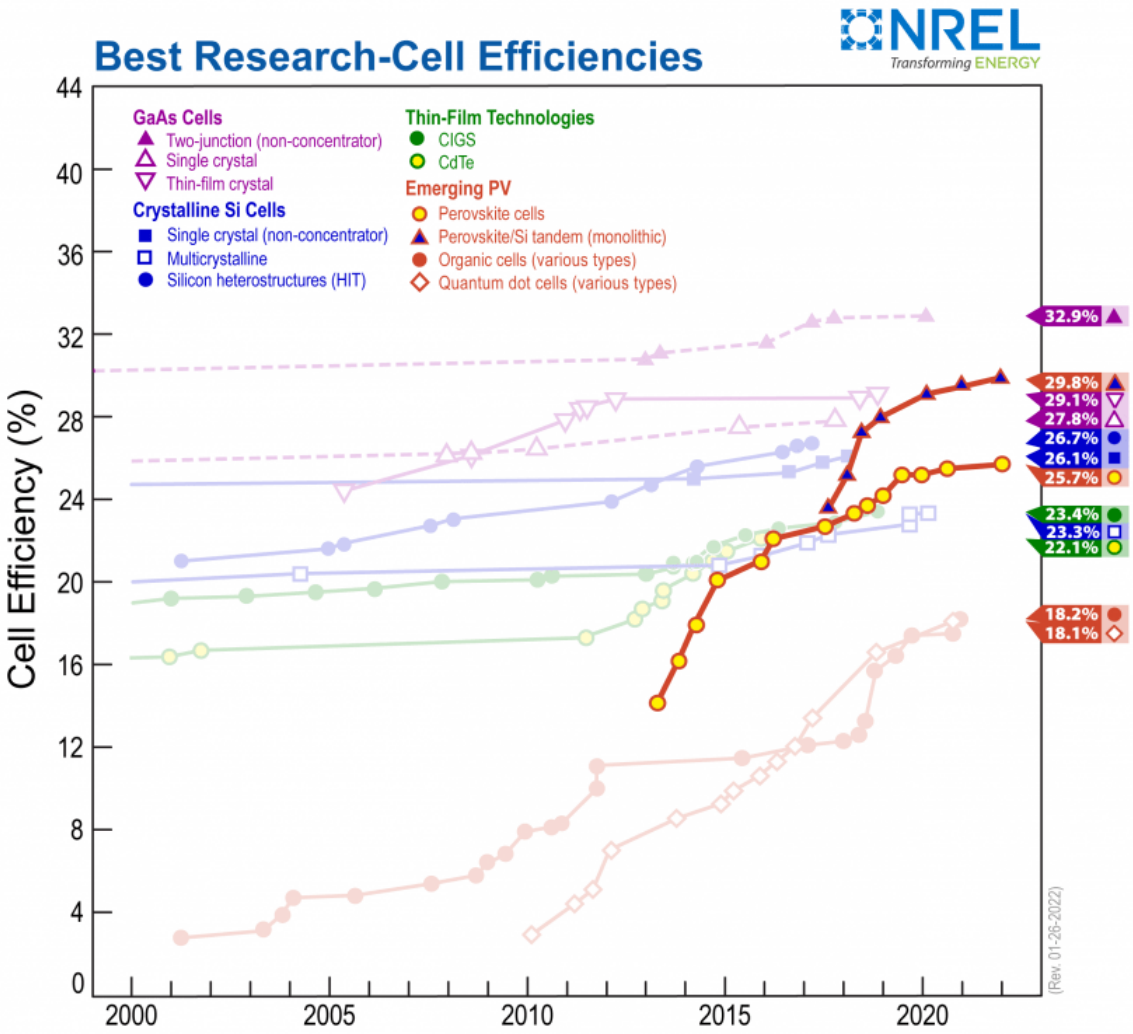

Fig. 5.1 Graph of photovoltaic cell efficiencies over time, with perovskite PVs highlighted in yellow circles and blue triangles. This plot is courtesy of the National Renewable Energy Laboratory, Golden, CO, USA [15].

However, many of the common perovskites used in PVs, such as $MAPbHa_3$ (where Ha = I, Cl or Br), contain toxic, scarce, and conflict minerals, making the ethical costs of using them outweigh their wider benefits [16]. One solution to these issues is to use chalcogenide perovskites instead. These chalcogenide perovskites have good chemical and thermal

stability compared to their halide perovskite counterparts [17–19] while avoiding the use of heavy and toxic elements.

Despite their merits, issues in chalcogenide perovskite synthesis persist and prevent their further device development. Most reported chalcogenide perovskites are a powder [17, 18, 20] or a bulk single crystal [21, 22], with limited reports of thin-films [23–27]. The rarity of thin film chalcogenide perovskites is owed to the poor quality of the layers produced. It often results in small, randomly orientated grains rather than a single continuous film [19]. This is due to difficulties in optimising the growth conditions from two contradictory conditions. Metals such as Zr and Hf are sluggish to form crystalline compounds due to their very low vapour pressures, and hence extremely high growth temperatures are required. However, at these high temperatures, chalcogen precursors can readily degas from the growth substrate and cause corrosion to the growth chamber [19, 28].

This dichotomy was recently overcome to grow high quality, epitaxial $BaZrS_3$ using molecular beam epitaxy (MBE) through a simple modification of the traditional MBE chamber shown in Figure 2.1. Rather than letting the gaseous precursors diffuse from their original valve openings at the back of the MBE chamber, these valves are extended via nozzles to just above the substrate. This has thus allowed for the growth of high quality, epitaxial $BaZrS_3$ to be realised [28] by ensuring a much higher vapour pressure throughout the growth and limiting degassing of the chalcogens, and corrosion to the (expensive) vacuum chamber.

The $BaZrS_3$ (BZS) system is by far the most studied chalcogenide perovskite [17–21, 28–31]. Its attractiveness is from its relatively low band gap of 1.9 eV and high light absorbance [28]. Theoretical studies have shown that by alloying with Se, the band gap decreases down to ~ 1.3 eV, which is the ideal band gap to reach the Shockley-Queisser limit for single junction solar cell efficiency of ~33% [32–34].

$BaZrSe_3$ (BZSe) comes with its own problems. DFT calculations predict that the most stable structure is a needle-like crystal with a band gap of ~ 1 eV [34], and any synthesis attempts to date have yielded hexagonal phases with metallic conductivity [35].

In this work, this limitation is overcome by first growing a $BaZrS_3$ template layer on a $LaAlO_3$ (LAO) substrate, as was done before [28], then mixing the H_2S gas flow with

H_2Se to allow growth of a perovskite $BaZrS_{(3-y)}Se_y$ (BZSSe) alloy. By controlling the ratio of H_2S/H_2Se gas flow, a variety of BZSSe alloys, with y = 1 - 3, were synthesised.

The BZSSe films were then characterised using various techniques. Band gaps of the films with varying S/Se ratios were measured using photoconductivity spectroscopy and correlated with DFT calculations. Structural characterisation of the films is carried out using STEM, and chemical analysis of the S/Se ratios was performed via EELS and EDX. Crystal structure features that were observed in the high-resolution XRD (HRXRD) spectra of the various films were correlated to the features and defects observed in HAADF-STEM images.

5.2 Methods

A modified gas-source MBE system (Mantis Deposition M500) was used to grow the films [28]. The $(001)_{PC}$-oriented $LaAlO_3$ (herein, PC stands for pseudo-cubic) single-crystal substrates (CrysTec GmbH) were outgassed in the MBE chamber at 1000 °C in H_2S gas. The substrates were then heated radiatively from a SiC filament and were rotated at 2 rpm. Ba metal was supplied from an effusion cell (Mantis Comcell 16-500), and Zr metal was from an electron beam evaporator (Telemark model 578). Sulphur and selenium were supplied in the form of H_2S and H_2Se gases (Matheson) from condensed, liquified sources of 99.9% and 99.998% purity, respectively. The gases are injected in close proximity to the substrate using custom-made gas lines and nozzles.

The growth temperature measured at the thermocouple in the chamber was 1000 °C. A template layer of $BaZrS_3$ of approximately 20 nm thick was first grown. The deposition was then interrupted to start the H_2Se flow, and then resume growth. The H_2S flow rate was 0.8 sccm during substrate outgassing and template layer growth. During $BaZrS_{(3-y)}Se_y$ film growth, the H_2S and H_2Se flow rates were adjusted to achieve the desired chalcogen ratios. For $BaZrSe_3$ (y = 3), a H_2Se flow rate of 0.5 sccm was used. The chamber pressure during film growth was approximately $8{\cdot}10^{-5}$ torr. The film growth rate was 0.1 Å s^{-1}. After growth, the H_2S and H_2Se gas flows were maintained during cooldown to avoid unwanted S and Se desorption.

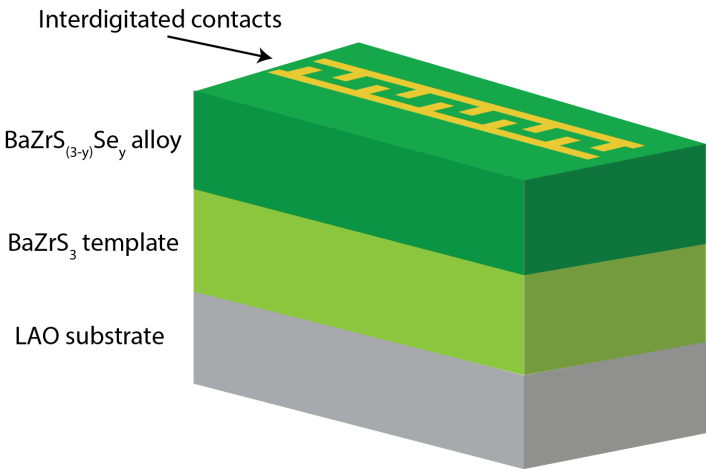

Fig. 5.2 Schematic diagram of a typical BZSSe thin-film, showing the LAO substrate, BZS template layer, BZSSe alloy layer, and interdigitated contacts on the surface for PCS measurements.

Out-of-plane XRD was performed using a Bruker D8 High-Resolution X-ray diffractometer. Photoconductivity spectroscopy (PCS) was performed on photodetector samples fabricated by sputtering 5 nm Ti/200 nm Au interdigitated contacts on the alloy films. These contacts had 8 individual 5 mm long fingers with finger spacing and width of 100 μm, as can be seen in Figure 5.2. A tunable light source with a 300 W Xe arc lamp (ScienceTech) was used to provide irradiance from 50 to 200 μW cm^{-2}, depending on the selected wavelength. A source-meter (Keithley 2400-C) was used to source a fixed bias of 4 V and measure the photocurrent.

Samples for STEM were prepared using nonaqueous wedge polishing using IPA, as mentioned in Chapter 2. EpoxyBond^{TM} 110 from Allied High Tech Products, Inc., USA, was used to glue the sectioned films together due to its robustness against plasma and quick curing time. The polishing wheel used was an Allied MultiPrep, and a wedge angle of 3° was achieved. This was followed by single-sector ion milling (Fischione 1051) using ion-beam energies of 3 kV, 2 kV, and then 1 kV.

HAADF-STEM imaging was conducted on an aberration-corrected Thermo-Fischer Scientific Themis Z, using an accelerating voltage of 200 kV, an 18.9 mrad convergence angle and a HAADF inner collection angle of 30 mrad. A beam current of 30 pA was used for the y = 1 sample and 50 pA for the y = 2 sample. Dwell time was set to 2 μs for y = 1 and 500 ns for y = 2. For the HAADF-STEM image of y = 2 shown in Figure 5.6, a series of 4 images were recorded of the same area, where the scan direction was changed by 90° for

each image. The images were then aligned with non-rigid registration using the RevSTEM software package [36].

STEM-EDX was performed using the Super X detectors, with a beam current of 100 pA for y = 1 and 50 pA for y = 2, and dwell time of 10 μs for y = 1 and 2 μs for y = 2. The sample was tilted just off the zone axis to minimised the effects of electron channelling on the quantification [37, 38]. This was then quantified via Thermo-Fisher Scientific Velox software, using both pre- and post-filtering (Gaussian blur, sigma = 1.6). The quantification of the S/Se ratio was based on Cliff-Lorimer method [39–41]. In this method, for elements A and B, their weight percentages (C_A and C_B, respectively) can be related to their above-background characteristic intensities by:

$$\frac{C_A}{C_B} = k_{AB}\frac{I_A}{I_B} \tag{5.1}$$

where k_{AB} is the Cliff-Lorimer sensitivity factor. This factor is based on the ionisation cross-section for each element, fluorescence yield (which is the ionisation fraction resulting in X-ray emission) and detector efficiency [39, 42]. However, the exact implementation and k-factors used in Velox are unknown to the user, and hence, depending on experimental requirements, this "black box" approach should be taken with care. Nonetheless, the default k-factors available in Velox were used as well as the Brown-Powell empirical ionization cross-section model [43].

STEM-EELS was performed using the same experimental parameters as for the STEM-EDX of the y = 1 sample. A Gatan Continuum spectrometer using a dispersion of 0.75 eV ch^{-1} was utilised, and the data was processed via the HyperSpy python package [44]. Peak fitting of the cation distances in Figure 5.11 was performed using in-house Python codes, based on the SciKit-Image package [45]. The peak-fitting algorithm fits the HAADF-STEM intensities with 2D-Gaussian peaks such as to find the centre of the peak. The distances from peak to peak are then calculated using a k-dimensional tree along the in-plane or out-of-plane directions. Subsequent statistical analysis was performed using Origin.

DFT calculations of the band gaps of the various alloys were performed via the VASP code with projector augmented wave (PAW) pseudopotentials [46, 47]. Atomic structures were optimised using the PBE functional and a Hellman-Feynman force criterion of 10^{-2}

eV/Å. Band gap calculations were subsequentially performed using the HSE06 functional [48]. A 9×7×9 and 6×4×6 k-point grid was used in the PBE and HSE06 calculations, respectively. A cut-off energy of 450 eV and 300 eV for the plane wave basis set was used for the structural optimisation and band gap calculations, respectively. The relaxed structural file for each alloy is shown in Appendix C.

5.3 Results & Discussion

5.3.1 Cho Plot Analysis of BZSSe Alloy Films

The PCS measurements of the films from y = 0 to y = 3 are shown in Figure 5.3(a) where the responsivity is plotted as a function of the impinging photon energy. The band gaps of the different films were determined by extrapolating the linear fits to the responsivity immediately above the onset energy in Figure 5.3(a), similar to a Tauc plot for determining the band gap of semiconductors from UV/Vis spectroscopy [49]. As is shown in Figure 5.3(b), there is a decrease in band gap energies as y increases. For the pure BZS films, the band gap was determined to be E_g = 1.82 ± 0.08 eV, in line with the value of 1.9 eV determined optically in the previous work on such films [28]. With increasing Se content, the value of the band gap of the alloys decreases in line with current and previous theoretical calculations [33, 50] all the way down to 1.4 ± 0.1 eV for the y = 3 films, indicating the successful growth of perovskite $BaZrSe_3$ (BZSe).

Out-of-plane HRXRD, as shown in Figure 5.4, for the various films highlights several key features. Notably, the films all align with perovskite structures of the pure BZS film (y = 1) indicating successful BZSSe perovskite alloy epitaxial growth. The films show out-of-plane (202) reflection pairs, aligning with the (012) family of LAO reflections, which corresponds to two sets of out-of-plane d-spacings. Finally, the two (202) reflections shift to smaller angles as y increases. This is due to lattice expansion as the BZSe lattice is larger than that of BZS [33, 50].

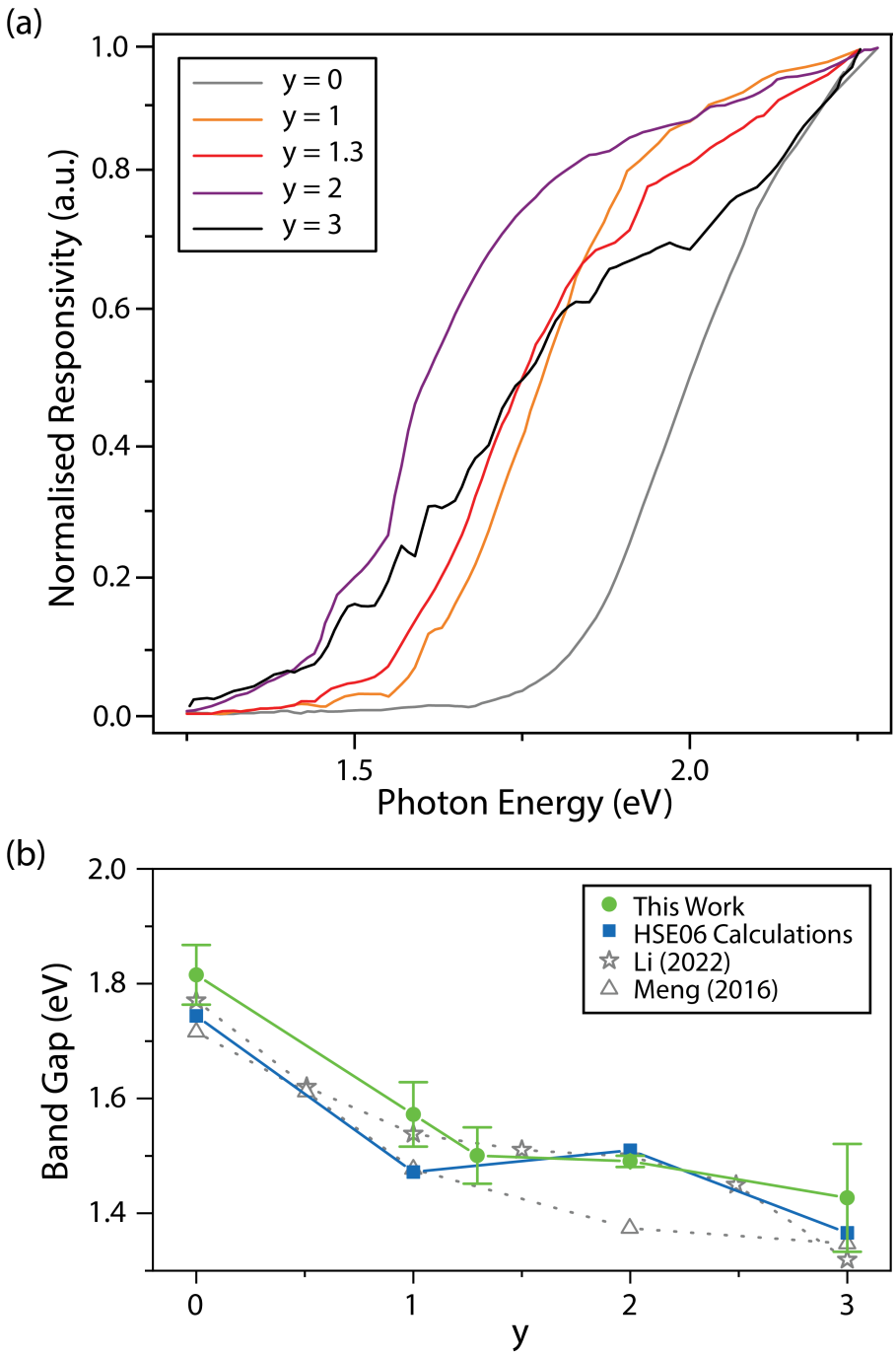

Fig. 5.3 (a) Photoconductivity spectroscopy measurements of epitaxial-grown BZSSe films on an LAO substrate, from y = 0 - 3. (b) Band gap energies, derived from (a), of the various films, along with HSE06 calculated band gaps and previous theoretical studies [33, 50]. Adapted from [51].

In Figure 5.5, the band gaps from the films (from Figure 5.3(b)) are plotted against their lattice constants from Figure 5.4. These lattice constants are the pseudocubic (a_{pc}) lattice constants determined from the (202) reflection in the HRXRD of the films. This type of plot, known here as a Cho plot (named after the developer of MBE [52]), acts as a starting point for designing optoelectronics, as one can look up the band gap of the required device,

find a suitable material in that band gap range, and find a substrate with a similar lattice constant to allow for epitaxial growth. Careful choice of a suitable substrate is also key as growth-induced strain can lead to deteriorating device properties [53], or if exploited, can enhance them [54, 55].

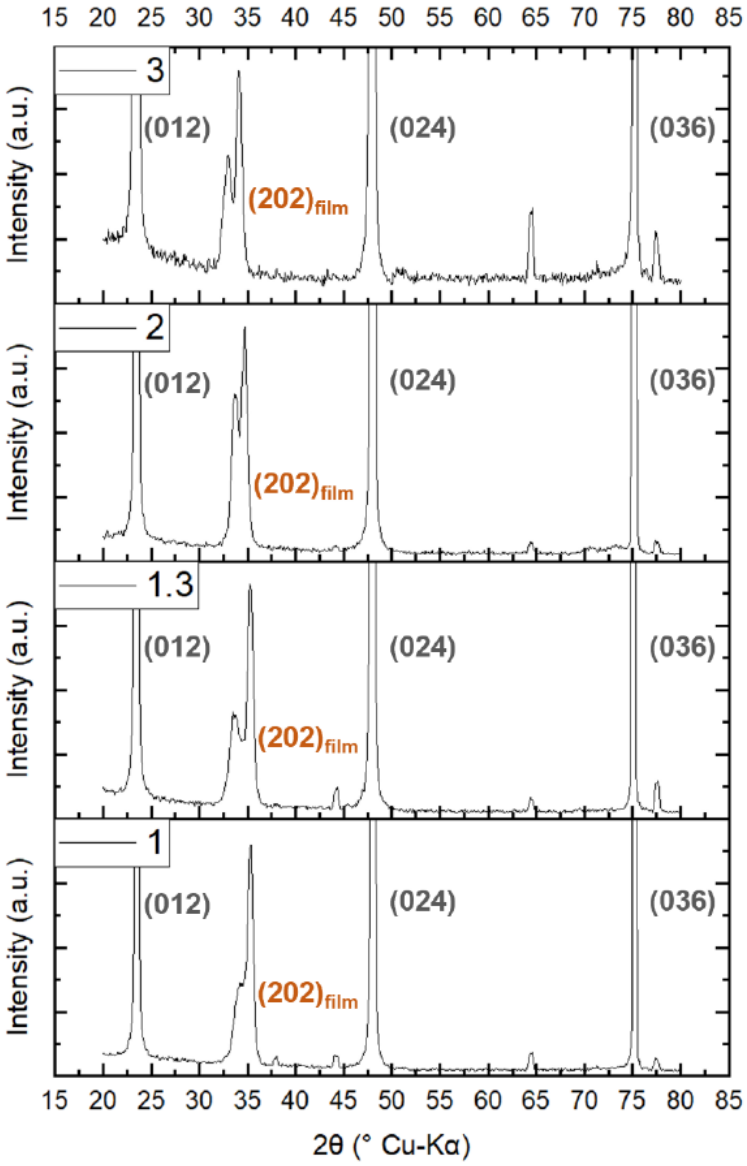

Fig. 5.4 HRXRD of various BZSSe films, from y = 0 - 3, with shifting of the out-of-plane (202) reflection pair to smaller angles as y increases. The (012), (024) and (036) reflections labelled in grey are from the LAO substrate. Adapted from [51].

In Figure 5.5, the light blue band highlights the range of band gaps that are suitable for single-junction PVs [32–34]. Multi-junction PVs, by having several layers which absorb different energy ranges of light, have been shown to have solar efficiencies of close to 50% (in specific lab conditions), exceeding that of single-junction PVs [56]. However, they are often more expensive to produce and less robust than of single-junction PVs, especially as

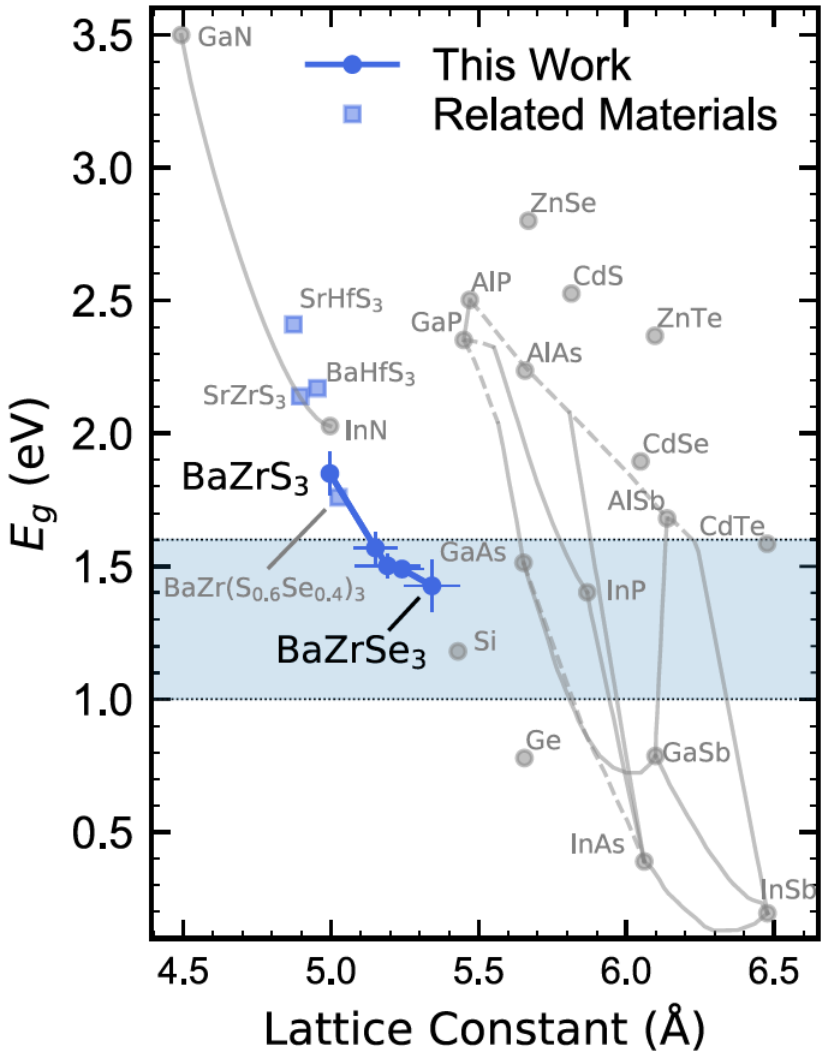

Fig. 5.5 Cho plot representing the band gaps (E_g) of various optoelectronic materials against their (pseudo)cubic lattice constants. BZSSe alloy series from this work is highlighted in dark blue, with related chalcogenide perovskites in light blue squares. The light blue band indicates range of E_g suitable for single-junction solar cells. Adapted from [51].

the number of layers increases [57]. Therefore, designing high-efficiency, robust single-junction PVs that can be produced at scale and at low cost would be far more advantageous to help address the current energy and environmental needs of society. The BZSSe alloy system is the ideal candidate to address this as it is within this "Goldilocks" range.

5.3.2 Defect Characterisation of BZSSe Alloy Films via STEM

It is expected that there will be some intermixing of the S and Se anions, with possible effects on the microstructure of the films, due to the high growth temperatures. The evidence of two d-spacings at the (202) out-of-plane reflection especially when Se is introduced,

as was shown in Figure 5.4, requires addressing also. It is important to understand such microstructural changes before proceeding with product development, in case these affect material or device properties. STEM was used to study the cross-sections of a representative sample of $BaZrS_2Se$ (y = 1) and $BaZrSSe_2$ (y = 2) films. The electron dose for all imaging and spectral imaging are summarised in Table 5.1.

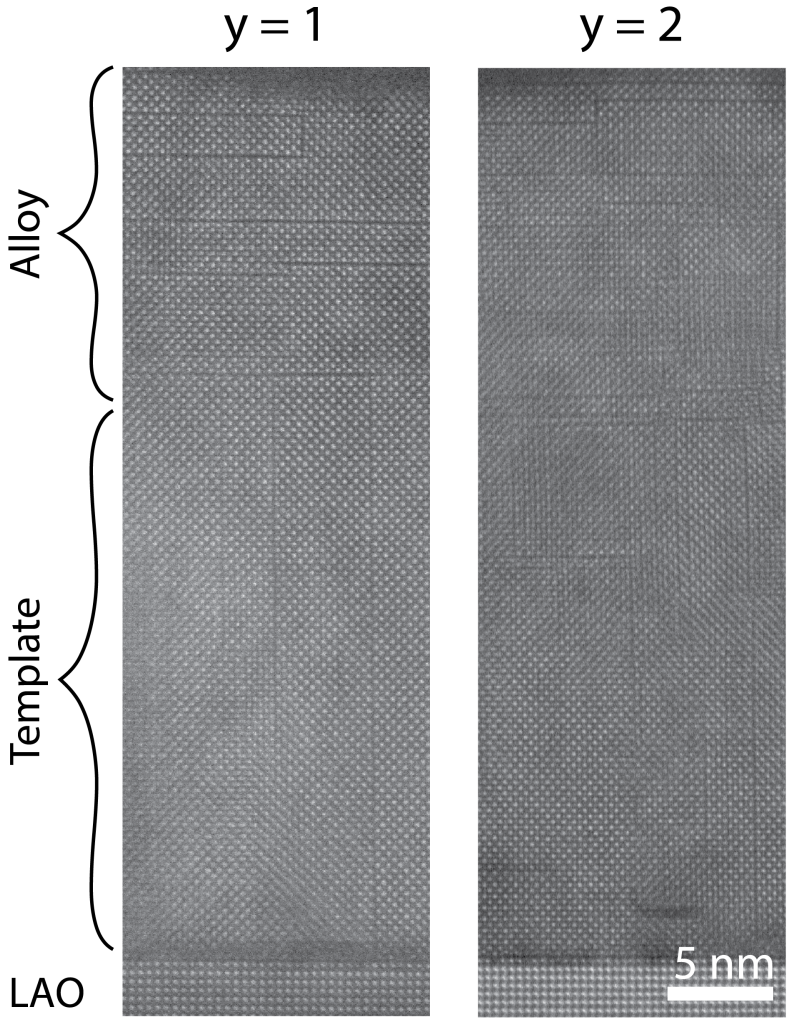

Fig. 5.6 HAADF-STEM image of BZSSe thin film cross-sections of both y = 1 and y = 2 films.

Units = e^- $Å^{-2}$	Figure 5.6		Figure 5.8		Figure 5.9
	y = 1	y = 2	(a)	(b)	
e^- Dose	6.34×10^3	2.60×10^3	825	661	7.62×10^4
Total e^- Dose (single frame)	6.65×10^9	1.09×10^{10}	1.44×10^7	6.93×10^8	5.21×10^7
Total e^- Dose (multi-frame)		4.36×10^{10}			

Table 5.1 Table of electron doses and electron dose per image frame for the HAADF-STEM images, EDX spectra and EELS spectral imaging in this Chapter. The total electron dose for multi-frame image stacks used in Figure 5.6 (y = 2) and are also highlighted.

In Figure 5.6, HAADF-STEM images of the y = 1 and y = 2 films show several immediately noticeable features. As was shown in the HRXRD analysis in Figure 5.4, the films are of a perovskite structure throughout, including in the alloy region. However, there are numerous rotational variants throughout each of these films, far more than what was observed in pure BZS films previously [28].

Present in the pure BZS films are two growth modes, buffered epitaxy and direct epitaxy, with the former far more dominant [28]. Buffered epitaxy involves a self-assembled interface layer that relieves the epitaxial strain between the substrate and the film, and direct epitaxy, with 45° rotated-cube-on-cube growth that accommodates the large lattice constant mismatch between the substrate and the film. The dominance of the buffered epitaxy, in both pure BZS films and the alloyed films present, is seen by the significant decrease in the HAADF intensity across the two atomic planes of the interface, suggesting a lack of coherency due to compositional or static displacements [58, 59].

The interface in pure BZS films is incommensurate with the substrate, with the coincident lattice alignment roughly every five substrate planes and four film planes where buffered epitaxy is present, and an extra misfit plane every 14 substrate planes where direct epitaxy is present [28]. In order to analyse the coincident lattice alignments of the BZSSe alloy films, a similar method for achieving this for the pure BZS films reported before was used herein [28]. Figure 5.7(a) and (b) show a representative interface between the y = 1 and y = 2 films, respectively, with the LAO substrate. To display only the out-of-plane components of each image, a fast Fourier transform (FFT) is performed. The out-of-plane components of each FFT are masked and an inverse FFT is performed to reveal the Fourier-filtered images of the y = 1 and y = 2 films, shown in Figure 5.7(c) and (d) respectively.

As can be seen in both of the inverse FFTs, there are 4 film planes for every 5 lattice planes in the region where buffered epitaxy is present, as was the case with the pure BZS films [28]. In the LAO region of the inverse FFTs, it should be noted that there is a plane of O/Al atomic columns between each visible plane of La atomic columns. However, only the La atomic columns are clearly seen (with faint signs of Al/O atomic columns) due to the much larger Z-contrast present in the HAADF images of Figure 5.7(a) and (b). Hence,

when filtering out the out-of-plane components, one needs to take the Al/O planes into account when analysing the coincident lattice alignments. Nonetheless, Figure 5.7 suggests minimal to no presence of direct epitaxial growth.

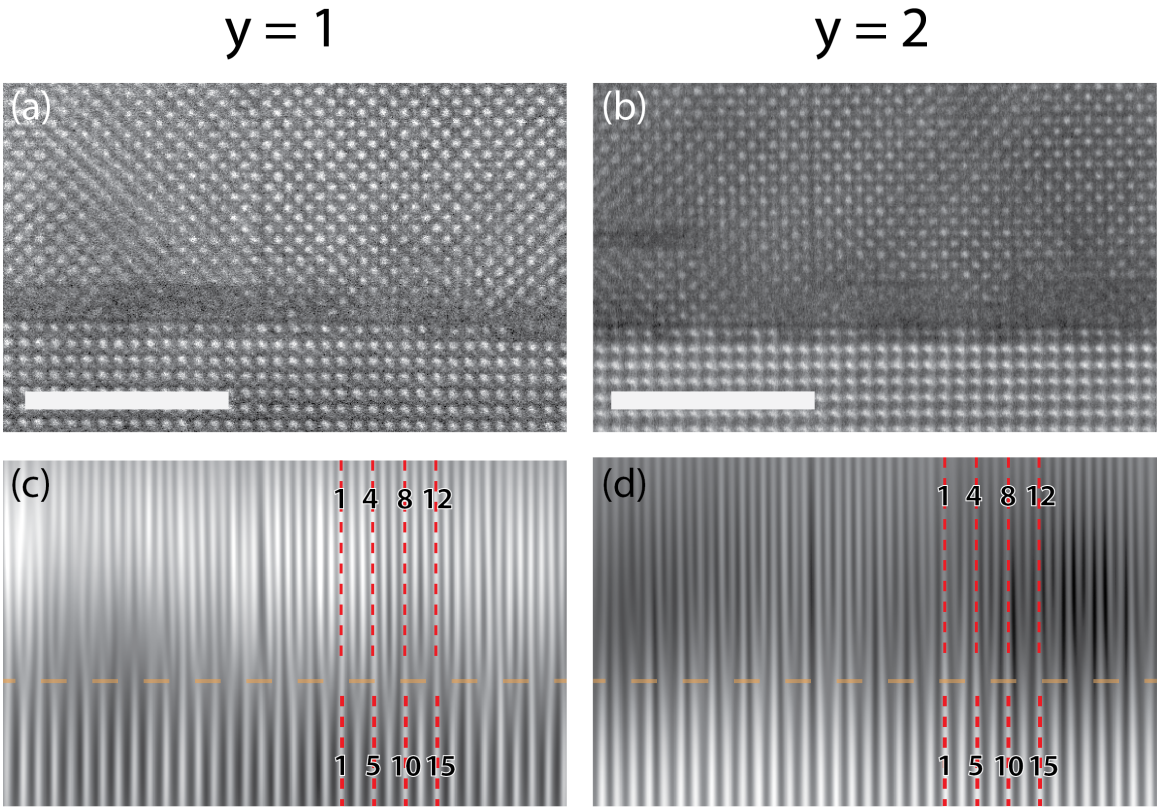

Fig. 5.7 (a, b) Representative interfaces of the BZSSe alloy films on LAO substrates, with y = 1 and y = 2, respectively. (c, d) Fourier-filtered images of (a) and (b), respectively, showing the out-of-plane components which highlight that for every 4 film planes, there are 5 substrate planes. Dashed orange line highlights the film/substrate interface. Scale bars are 5 nm.

This phenomenon is likely due to the inhomogeneities of the Se diffusion. To understand this, STEM-EDX was performed on the films and the S/Se at% ratio for the y = 1 and y = 2 films in Figure 5.8. It should be noted that the larger uncertainties in the y = 1 ratio compared to y = 2 is due to the fact that the y = 2 data was acquired by another TEM operator on behalf of the author (thanks Michael!); a larger total electron dose and hence X-ray counts, as shown in Table 5.1, and a larger area (1.31×10^3 nm^2 for y = 1 vs. 9.90×10^3 nm^2 for y = 2) was used, which would smooth out some inhomogeneities and noise. This results in smaller error bars and more consistent trends in the y = 2 ratios seen in Figure 5.8. Nonetheless, as is shown in both the y = 1 and y = 2 EDX data, Se has diffused down to the substrate interface and is present throughout the films.

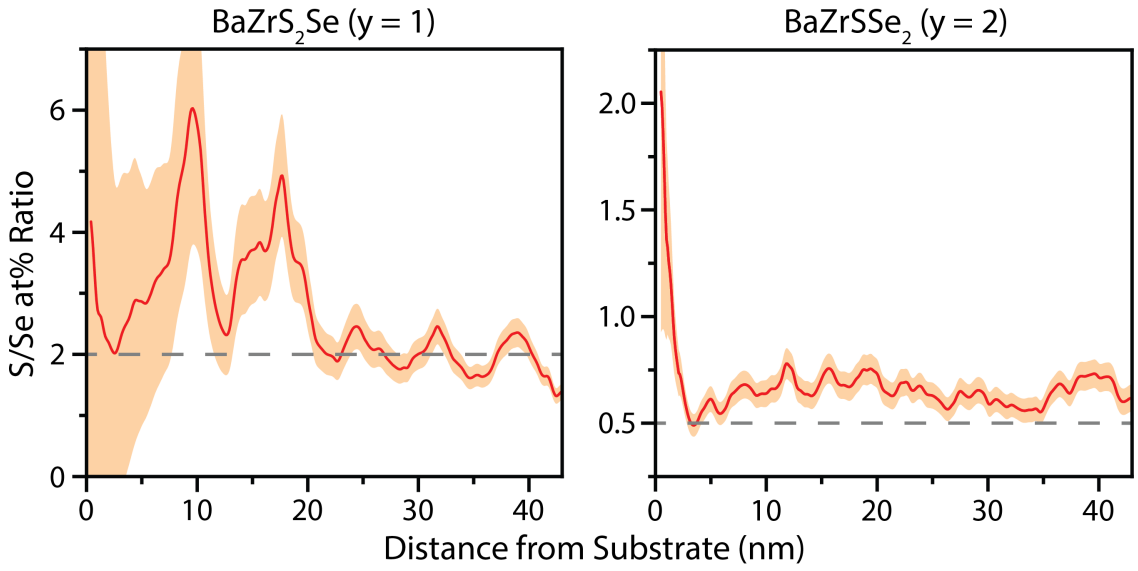

Fig. 5.8 S/Se at% ratio (red; uncertainty is in orange) along the out-of-plane direction from EDX mapping of the y = 1 and y = 2 films in Figure 5.6. The ideal ratio for each film is shown as a dashed grey line.

The ratio of S to Se concentrations throughout each film is mostly consistent from the substrate to the surface of the film. The ratios are also similar to the initial and ideal growth conditions, shown by the dashed grey lines in Figure 5.8, despite growing the BZS template layer first. This implies the diffusion of Se has displaced the S ions in the template layer and replaced the diffused Se in the alloy layer with the S ions from the template layer, with the equilibrium condition defined by the concentration of Se present in the growth of the alloy layer. However, inhomogeneities of the Se concentration are present, as seen in Figure 5.9 when the Se $L_{2,3}$ edge was mapped out across the y = 1 film using EELS. These inhomogeneities can cause localised strain throughout the film, hence explaining the large number of different rotation variants present [60].

The presence of Se also disrupts the rotated cube-on-cube lattice alignments of the direct epitaxial growth mode. Since this growth mode requires a lattice misfit plane for every 14 substrate planes to accommodate the lattice mismatch, the presence of Se at the interface inhibits such a large region from existing and hence to relieve the stress at this interface, it is preferential to form an incoherent buffer layer instead.

The other striking feature present in these films is the large number of planar defects. These anti-phase boundaries (APBs) appear in perovskites as rock-salt-like layers that disrupt the corner-sharing octahedra along a plane. APBs can also accommodate cation

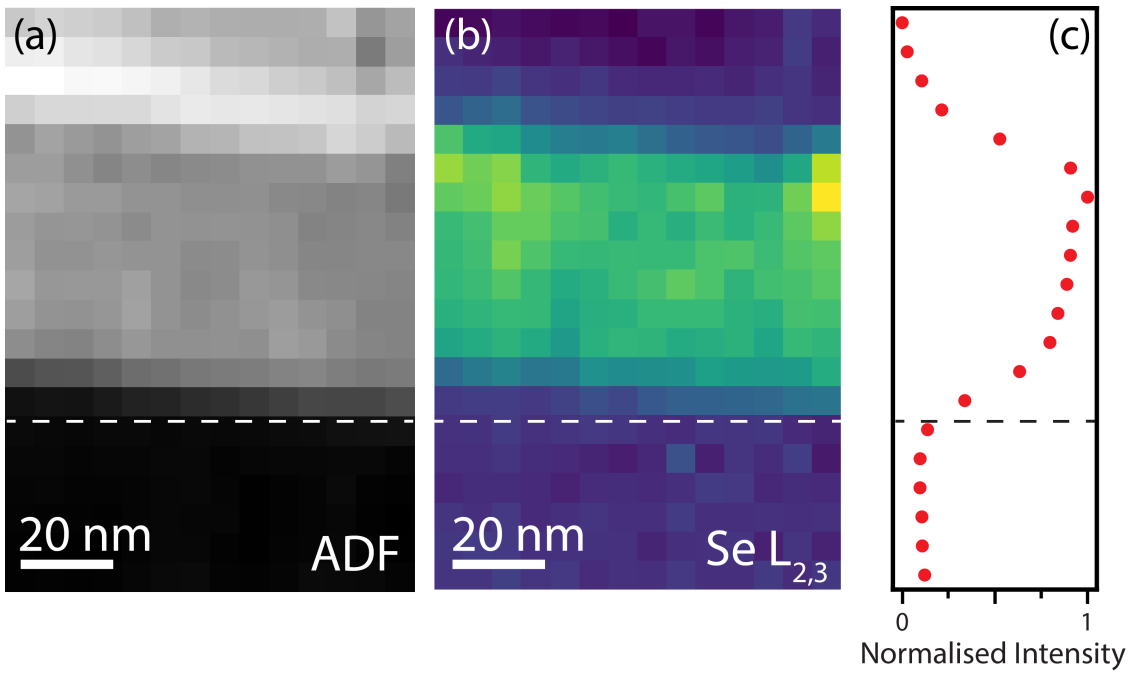

Fig. 5.9 (a) Annular dark field (ADF) image of y = 1 film. (b) EELS spectral image of the same area as (a), mapping out the intensity of the Se $L_{2,3}$ edge. (c) Normalised intensity values of (b) along the out-of-plane direction. The dashed line indicated the substrate-film interface.

off-stoichometry and, along with the buffered interface, relieve strain [61, 62]. APBs were observed in previous BZS thin films, due to step-edges [28]. Difficulties in maintaining the exact Ba:Zr ratio of 1:1 during the synthesis without a clear pathway to growth by self-limiting adsorption, can also result in the formation of APBs [63]. In the BZSSe alloys, an additional effect is present: vertical, out-of-plane APBs appear to be concentrated in the template layer, while horizontal, in-plane APBs are concentrated in the alloy region. Since the Ba:Zr ratios are not changed throughout the growth of the films, the presence of these APBs is thought to accommodate the strain from lattice expansion due to the introduction of Se.

In Figure 5.10, the out-of-plane and in-plane A-site cation distances are mapped out for a typical region of the y = 1 film. The lattice parameters of perovskite BZSe are larger than that of BZS and hence the alloy layer places the template layer into tensile strain, which is relieved via out-of-plane APBs in the template layer. Conversely, the template layer places the alloy layer under compressive strain and this is relieved via in-plane APBs. Despite the intermixing of S and Se ions throughout the film as was shown in the EDX profiles of Figure 5.8, it is clear from Figure 5.10 that the in-plane APBs are concentrated in the alloy layer,

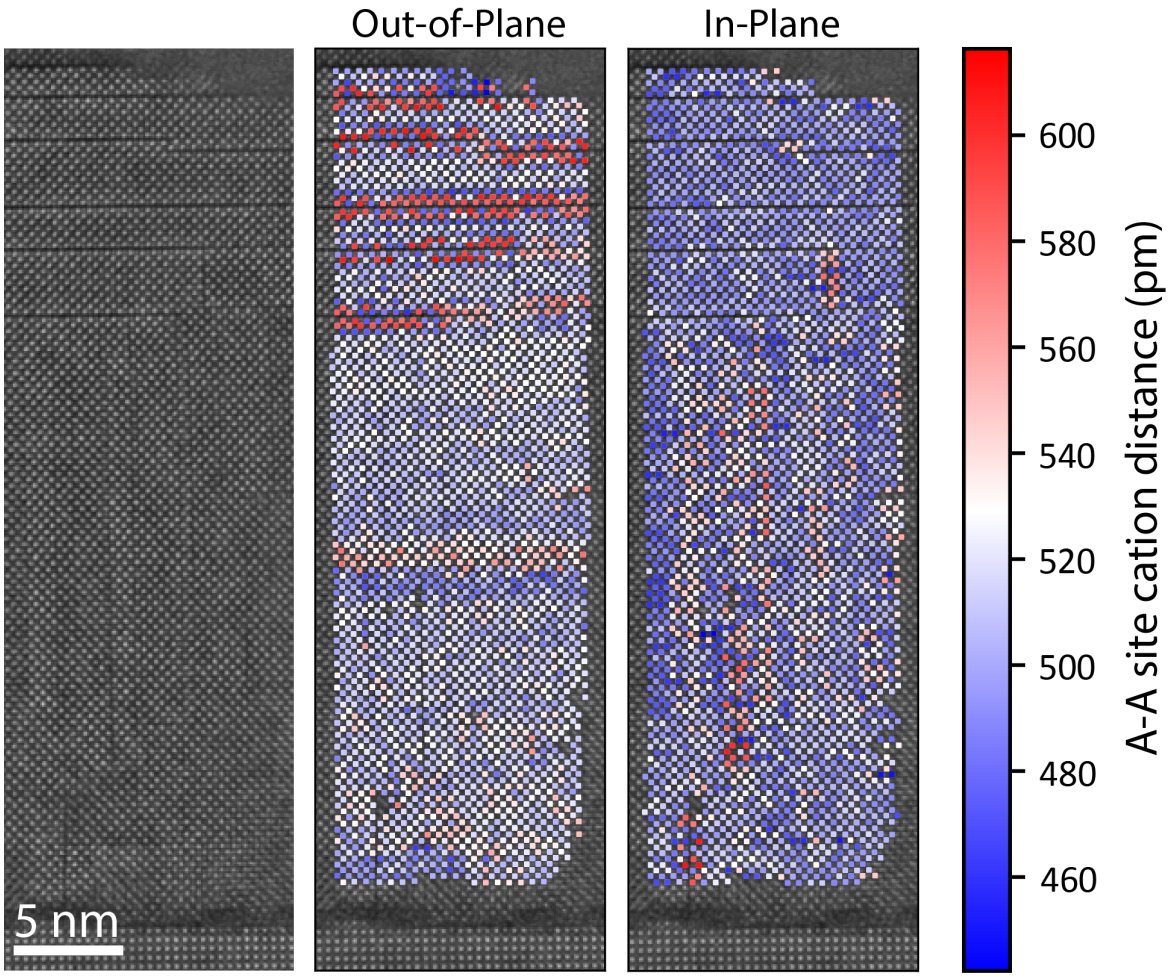

Fig. 5.10 Out-of-plane and in-plane A-site cation distances for BZSSe (y = 1) from Figure 5.8(a)

and out-of-plane APBs concentrated in the template layer. This is understandable as the diffusion of extended, 2D planar defects is far more difficult than that of individual ions. Therefore, the APBs nucleate and grow simultaneously as the ad-atoms are attached, while the chalcogen ions can migrate throughout the film during growth.

The in-plane and out-of-plane A-site cation distances seen in Figure 5.10 are plotted and fitted in Figure 5.11. While more obvious in the y = 2 case seen in Figure 5.12, the out-of-plane spacing distributions are broader for the alloy layers than for the template layers, due to the presence of horizontal APBs in the top layers. Similarly, the in-plane spacing distributions are broader for the template layers than for the alloy layers, due to the presence of vertical APBs in the alloy layers. However, for the in-plane distances, the peak values in the template and alloy layers align for both the y = 1 and y = 2 cases.

Unlike the in-plane distances, the peak values for the out-of-plane distances are shifted towards larger d-spacings in the alloy as compared to the template layers, in both y = 1

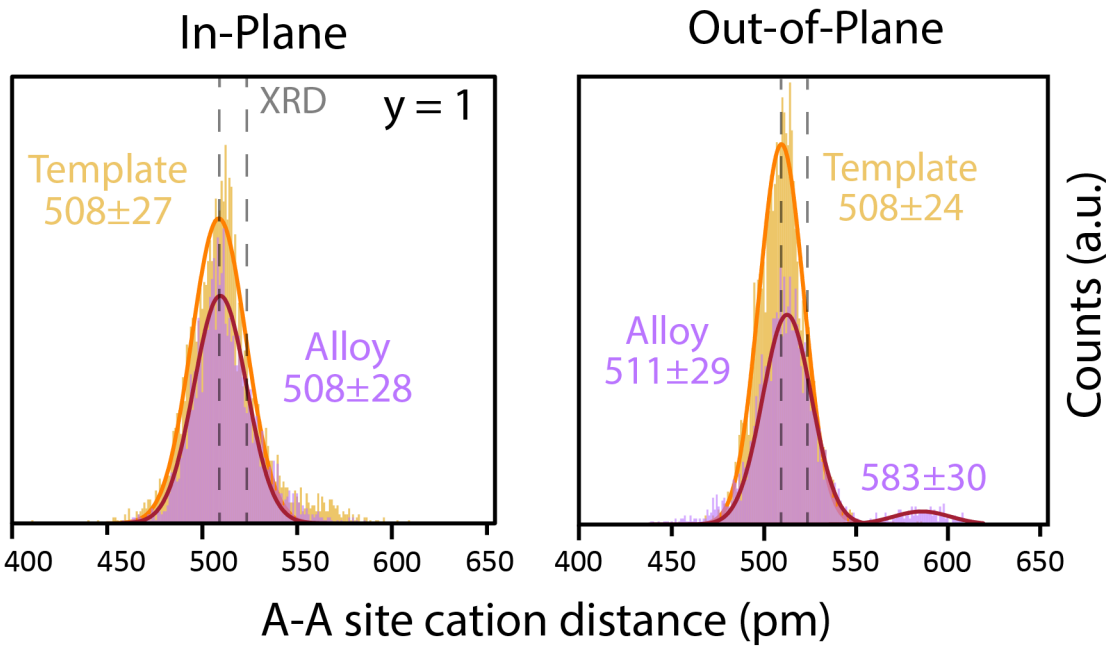

Fig. 5.11 Histogram analysis of in-plane and out-of-plane distances from (a), along with (202) reflection pairs from the HRXRD for the y = 1 film from Figure 5.4.

and y = 2 cases. These peak shifts align with the values of the (202) reflection pairs seen in the HRXRD in Figure 5.4. It can also be seen that there is a tripartite of peaks in the out-of-plane distances in both films.

The third peak in out-of-plane distances in Figure 5.11 for y = 1, faintly seen before the main 511±29 pm peak, was statistically not significant enough to fit and is hence not shown. Only the A-site cations are considered for the y = 1 analysis. This is because, while some B-site cations are visible, especially at APB boundaries, the noise in the HAADF images was too high for the peak-finding algorithm to discern them. However, for the y = 2 case, shown in Figure 5.12(b), this third out-of-plane peak is clearly visible as all cation atomic column distances are considered. This is because, while this data set was acquired by another user (again, thanks Michael!), several images were acquired in series and post-processed to align and average them [36], which increased the signal-to-noise, allowing for the peak finding algorithm to discern the B-site atomic columns in the HAADF images. This summation of images can also minimised scan distortions which would affect the statistics of the peak-to-peak distances. For example, there is no out-of-plane APB in the template region in Figure 5.10(a), however in the out-of-plane cation distances in Figure 5.10(b), there appears to be one. This is most likely a scan distortion perhaps caused by environmental factors, such as a door opening as the image was being acquired [64].

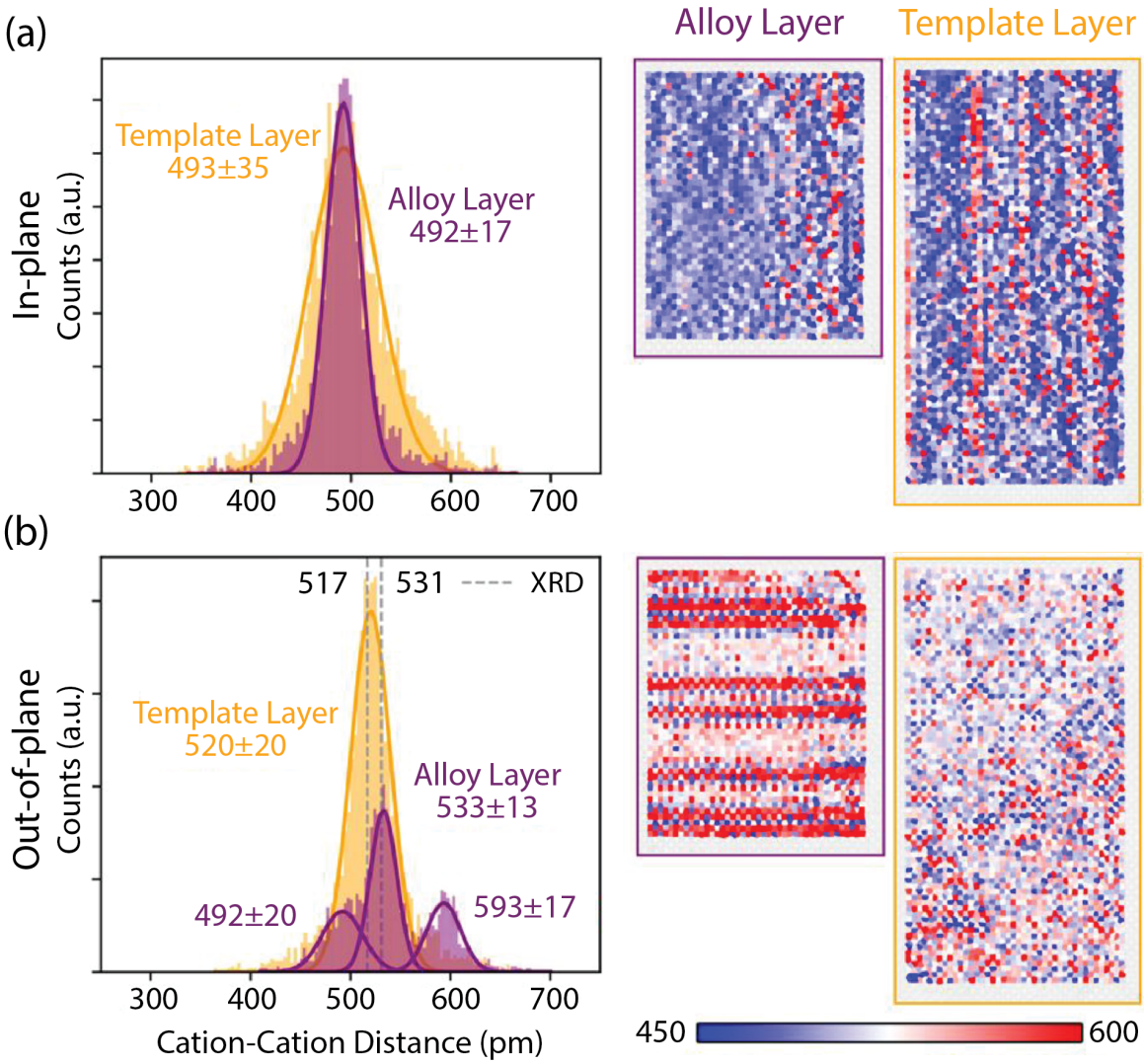

Fig. 5.12 Cation-cation distances from HAADF-STEM images of a typical region of $BaZrSSe_2$ (y = 2). The in-plane (a) and out-of-plane (b) distribution of the distances are shown, alongside the colour-maps of both the alloy and template regions of the film. Adapted from [51].

Due to the limited time the author had at MIT and only noticing such a feature in the analysis after they had returned to the Emerald Isle, such frame-averaging was not conducted for the y = 1 case. Had it been done, the third peak would be more clearly seen and fitted. Regardless, the tripartite of out-of-plane distances in the alloy layer of the films corresponds to an expansion in the APB core (583±30 pm for y = 1, 593±17 pm for y = 2), compression immediately adjacent to the APB core (492±20 pm for y = 2), and an intermediate value away from the APBs (511±29 pm for y = 1, 533±13 pm for y = 2). The films result in a variation in d-spacing in certain regions, despite the nearly uniform composition as was shown in the EDX in Figure 5.8. In spite of this, the film only differentiates by at most 5 pm in the out-of-plane distances from substrate to surface,

which is a < 1 % strain, further indicating that the film as a whole is relaxed, with the strain relived via the interface and the APBs.

5.4 Conclusions

The growth of perovskite $BaZrS_{(3-y)}Se_y$ alloy films was successfully demonstrated via the use of a $BaZrS_3$ template layer on a $LaAlO_3$ substrate. Adjusting the S/Se ratio during the MBE growth allows for the careful adjustment of the film's S/Se concentration in line with the initial conditions, with the S/Se concentration in the film mostly consistent from the substrate to the surface. Optical properties of the subsequent films via the measurement of the band gaps via PCS align with previous and current theoretical predictions. APBs were seen throughout the film, with out-of-plane APBs mostly concentrated in the template region, while in-plane APBs were mostly concentrated in the alloy region. Regardless, the films are relaxed as any residual strain is relieved via the APBs and the mostly incoherent buffered interface.

While this chapter showed the successful growth of chalcogenide perovskite thin films, its use on an industrial scale may be still limited due to the stringent growth conditions in molecular beam epitaxy. Other more scalable methods, such as chemical vapour deposition, would need to be employed if such materials are to make an impact. Hence, further research into adapting the growth conditions for the BZSSe perovskite films to more scalable manufacturing methods is key and is currently being undertaken, along with exploring other chalcogenide perovskite families.

References

[1] Junlei Qi et al. “Fabrication and applications of van der Waals heterostructures”. In: *International Journal of Extreme Manufacturing* 5.2 (2023), p. 022007. ISSN: 2631-8644. DOI: 10.1088/2631-7990/acc8a1.

[2] Can Liu et al. “Designed growth of large bilayer graphene with arbitrary twist angles”. In: *Nature Materials* 21.11 (2022), pp. 1263–1268. ISSN: 1476-1122. DOI: 10.1038/s41563-022-01361-8.

[3] Zhengwei Zhang et al. “Robust epitaxial growth of two-dimensional heterostructures, multiheterostructures, and superlattices”. In: *Science* 357.6353 (2017), pp. 788–792. ISSN: 0036-8075. DOI: 10.1126/science.aan6814.

[4] Satoru Masubuchi et al. “Autonomous robotic searching and assembly of two-dimensional crystals to build van der Waals superlattices”. In: *Nature Communications* 9.1 (2018), p. 1413. ISSN: 2041-1723. DOI: 10.1038/s41467-018-03723-w.

[5] International Energy Agency. *Executive summary - Renewables 2022 - Analysis - IEA*. Tech. rep. International Energy Agency.

[6] Simon. Sze and Ming-Kwei Lee. *Semiconductor Devices: Physics and Technology*. 3rd. Wiley, 2016. ISBN: 978-0-470-53794-7.

[7] Britney Spears. *p-n Junctions, Diodes - Britney Spears Guide to Semiconductor Physics - https://britneyspears.ac/physics/pn/pnjunct.htm*. (accessed 2023-11-06).

[8] Moshsin Ijaz et al. “Perovskite solar cells: importance, challenges, and plasmonic enhancement”. In: *International Journal of Green Energy* 17.15 (2020), pp. 1022–1035. ISSN: 1543-5075. DOI: 10.1080/15435075.2020.1818567.

[9] Sarat Kumar Sahoo, Balamurugan Manoharan, and Narendiran Sivakumar. “Chapter 1 - Introduction: Why Perovskite and Perovskite Solar Cells?” In: *Perovskite Photovoltaics*. Elsevier, 2018, pp. 1–24. ISBN: 9780128129159. DOI: 10.1016/B978-0-12-812915-9.00001-0.

[10] Pavel Čulík et al. “Design and Cost Analysis of 100 MW Perovskite Solar Panel Manufacturing Process in Different Locations”. In: *ACS Energy Letters* 7.9 (2022), pp. 3039–3044. ISSN: 2380-8195. DOI: 10.1021/acsenergylett.2c01728.

[11] Mats Johnsson and Peter Lemmens. “Crystallography and Chemistry of Perovskites”. In: *Handbook of Magnetism and Advanced Magnetic Materials*. Wiley, 2007. DOI: 10.1002/9780470022184.hmm411. arXiv: 0506606 [cond-mat].

[12] Dong Shin and Suk-Ho Choi. “Recent Studies of Semitransparent Solar Cells”. In: *Coatings* 8.10 (2018), p. 329. ISSN: 2079-6412. DOI: 10.3390/coatings8100329.

[13] Mingming Liu et al. “Suppression of temperature quenching in perovskite nanocrystals for efficient and thermally stable light-emitting diodes”. In: *Nature Photonics* 15.5 (2021), pp. 379–385. ISSN: 1749-4885. DOI: 10.1038/s41566-021-00766-2.

[14] Zijing Dong et al. “High-Temperature Perovskite Solar Cells”. In: *Solar RRL* 5.9 (2021), p. 2100370. ISSN: 2367-198X. DOI: 10.1002/solr.202100370.

[15] NREL. *Best Research-Cell Efficiency Chart*. Golden, CO, 2023.

[16] Aleydis Nissen. *The European Union, emerging global business and human rights*. Cambridge University Press, 2022, p. 288. ISBN: 9781009284301.

[17] Shanyuan Niu et al. “Crystal growth and structural analysis of perovskite chalcogenide BaZrS3 and Ruddlesden–Popper phase Ba3Zr2S7”. In: *Journal of Materials Research* 34.22 (2019), pp. 3819–3826. ISSN: 0884-2914. DOI: 10.1557/JMR.2019.348. arXiv: 1904.11523.

[18] Vikash Kumar Ravi et al. “Colloidal BaZrS3 chalcogenide perovskite nanocrystals for thin film device fabrication”. In: *Nanoscale* 13.3 (2021), pp. 1616–1623. ISSN: 2040-3372. DOI: 10.1039/D0NR08078K.

[19] Kostiantyn V. Sopiha et al. “Chalcogenide Perovskites: Tantalizing Prospects, Challenging Materials”. In: *Advanced Optical Materials* 10.3 (2022), p. 2101704. ISSN: 2195-1071. DOI: 10.1002/ADOM.202101704.

[20] Shanyuan Niu et al. “Bandgap Control via Structural and Chemical Tuning of Transition Metal Perovskite Chalcogenides”. In: *Advanced Materials* 29.9 (2017), p. 1604733. ISSN: 1521-4095. DOI: 10.1002/ADMA.201604733.

[21] Yukinori Nishigaki et al. “Extraordinary Strong Band-Edge Absorption in Distorted Chalcogenide Perovskites”. In: *Solar RRL* 4.5 (2020), p. 1900555. ISSN: 2367-198X. DOI: 10.1002/SOLR.201900555.

[22] Antonio Cabas-Vidani et al. “High-Efficiency (LixCu1-x)2ZnSn(S,Se)4 Kesterite Solar Cells with Lithium Alloying”. In: *Advanced Energy Materials* 8.34 (2018), p. 1801191. ISSN: 1614-6840. DOI: 10.1002/AENM.201801191.

[23] Andrea Crovetto et al. “Shining Light on Sulfide Perovskites: LaYS 3 Material Properties and Solar Cells”. In: *Chemistry of Materials* 31.9 (2019), pp. 3359–3369. ISSN: 0897-4756. DOI: 10.1021/acs.chemmater.9b00478.

[24] Corrado Comparotto et al. “Chalcogenide Perovskite BaZrS 3 : Thin Film Growth by Sputtering and Rapid Thermal Processing”. In: *ACS Applied Energy Materials* 3.3 (2020), pp. 2762–2770. ISSN: 2574-0962. DOI: 10.1021/acsaem.9b02428.

[25] Xiucheng Wei et al. “Realization of BaZrS3 chalcogenide perovskite thin films for optoelectronics”. In: *Nano Energy* 68 (2020), p. 104317. ISSN: 2211-2855. DOI: 10.1016/J.NANOEN.2019.104317. arXiv: 1910.04978.

[26] José A. Márquez et al. “BaZrS 3 Chalcogenide Perovskite Thin Films by H 2 S Sulfurization of Oxide Precursors”. In: *The Journal of Physical Chemistry Letters* 12.8 (2021), pp. 2148–2153. ISSN: 1948-7185. DOI: 10.1021/acs.jpclett.1c00177.

[27] Hamza Shaili et al. “Synthesis of the Sn-based CaSnS3 chalcogenide perovskite thin film as a highly stable photoabsorber for optoelectronic applications”. In: *Journal of Alloys and Compounds* 851 (2021), p. 156790. ISSN: 0925-8388. DOI: 10.1016/J.JALLCOM.2020.156790.

[28] Ida Sadeghi et al. “Making BaZrS3 Chalcogenide Perovskite Thin Films by Molecular Beam Epitaxy”. In: *Advanced Functional Materials* 31.45 (2021), p. 2105563. ISSN: 1616-3028. DOI: 10.1002/ADFM.202105563. arXiv: 2105.10258.

[29] Joseph W. Bennett, Ilya Grinberg, and Andrew M. Rappe. “Effect of substituting of S for O: The sulfide perovskite BaZrS3 investigated with density functional theory”. In: *Physical Review B* 79.23 (2009), p. 235115. ISSN: 1098-0121. DOI: 10.1103/PhysRevB.79.235115.

[30] Shanyuan Niu et al. “Thermal stability study of transition metal perovskite sulfides”. In: *Journal of Materials Research* 33.24 (2018), pp. 4135–4143. ISSN: 0884-2914. DOI: 10.1557/jmr.2018.419.

[31] Shanyuan Niu et al. “Crystal growth and structural analysis of perovskite chalcogenide BaZrS 3 and Ruddlesden–Popper phase Ba 3 Zr 2 S 7”. In: *Journal of Materials Research* 34.22 (2019), pp. 3819–3826. ISSN: 0884-2914. DOI: 10.1557/jmr.2019.348. arXiv: 1904.11523.

[32] Yi-Yang Sun et al. “Chalcogenide Perovskites for Photovoltaics”. In: *Nano Letters* 15.1 (2015), pp. 581–585. ISSN: 1530-6984. DOI: 10.1021/nl504046x.

[33] Weiwei Meng et al. “Alloying and Defect Control within Chalcogenide Perovskites for Optimized Photovoltaic Application”. In: *Chemistry of Materials* 28.3 (2016), pp. 821–829. ISSN: 0897-4756. DOI: 10.1021/acs.chemmater.5b04213.

[34] Marc Ong et al. “BaZrSe3: Ab initio study of anion substitution for bandgap tuning in a chalcogenide material”. In: *Journal of Applied Physics* 125.23 (2019), p. 235702. ISSN: 0021-8979. DOI: 10.1063/1.5097940.

[35] Louis J. Tranchitella et al. “Commensurate Columnar Composite Compounds: Synthesis and Structure of Ba 15 Zr 14 Se 42 and Sr 21 Ti 19 Se 57”. In: *Journal of the American Chemical Society* 120.30 (1998), pp. 7639–7640. ISSN: 0002-7863. DOI: 10.1021/ja972442p.

[36] Xiahan Sang and James M. LeBeau. “Revolving scanning transmission electron microscopy: Correcting sample drift distortion without prior knowledge”. In: *Ultramicroscopy* 138 (2014), pp. 28–35. ISSN: 18792723. DOI: 10.1016/j.ultramic.2013.12.004.

[37] Katherine E. MacArthur, Marc Heggen, and Rafal E. Dunin-Borkowski. “Differentiating the structure of PtNi octahedral nanoparticles through combined ADF–EDX simulations”. In: *Advanced Structural and Chemical Imaging* 4.1 (2018), p. 2. ISSN: 2198-0926. DOI: 10.1186/s40679-018-0053-x.

[38] Katherine E. MacArthur et al. “Probing the Effects of Electron Channelling on EDX Quantification”. In: *Microscopy and Microanalysis* 23.S1 (2017), pp. 392–393. ISSN: 1431-9276. DOI: 10.1017/S1431927617002641.

[39] G. Cliff and G. W. Lorimer. “The quantitative analysis of thin specimens”. In: *Journal of Microscopy* 103.2 (1975), pp. 203–207. ISSN: 0022-2720. DOI: 10.1111/j.1365-2818.1975.tb03895.x.

[40] Rik Brydson, ed. *Aberration-Corrected Analytical Transmission Electron Microscopy*. Wiley, 2011, p. 280. ISBN: 978-1-119-97990-6.

[41] David B. Williams and C. Barry Carter. *Transmission electron microscopy: A textbook for materials science*. 2009, pp. 1–760. ISBN: 9780387765006. DOI: 10.1007/978-0-387-76501-3.

[42] David M. Longo, James M. Howe, and William C. Johnson. “Experimental method for determining Cliff–Lorimer factors in transmission electron microscopy (TEM) utilizing stepped wedge-shaped specimens prepared by focused ion beam (FIB) thinning”. In: *Ultramicroscopy* 80.2 (1999), pp. 85–97. ISSN: 03043991. DOI: 10.1016/S0304-3991(99)00082-0.

[43] C. J. Powell. “Cross sections for ionization of inner-shell electrons by electrons”. In: *Reviews of Modern Physics* 48.1 (1976), pp. 33–47. ISSN: 0034-6861. DOI: 10.1103/RevModPhys.48.33.

[44] “hyperspy/hyperspy: v2.0.1”. In: (). DOI: 10.5281/ZENODO.10709941.

[45] Stéfan van der Walt et al. “scikit-image: image processing in Python”. In: *PeerJ* 2.1 (2014), e453. ISSN: 2167-8359. DOI: 10.7717/peerj.453.

[46] G. Kresse and J. Furthmüller. “Efficient iterative schemes for ab initio total energy calculations using a plane wave basis set”. In: *Physical Review B - Condensed Matter*

and Materials Physics 54.16 (1996), pp. 11169–11186. ISSN: 1550235X. DOI: 10.1103/PhysRevB.54.11169.

[47] G. Kresse and D. Joubert. "From ultrasoft pseudopotentials to the projector augmented wave method". In: *Physical Review B* 59.3 (1999), pp. 1758–1775. ISSN: 0163-1829. DOI: 10.1103/PhysRevB.59.1758.

[48] Jochen Heyd, Gustavo E. Scuseria, and Matthias Ernzerhof. "Hybrid functionals based on a screened Coulomb potential". In: *The Journal of Chemical Physics* 118.18 (2003), pp. 8207–8215. ISSN: 0021-9606. DOI: 10.1063/1.1564060.

[49] J. Tauc. "Optical properties and electronic structure of amorphous Ge and Si". In: *Materials Research Bulletin* 3.1 (1968), pp. 37–46. ISSN: 00255408. DOI: 10.1016/0025-5408(68)90023-8.

[50] Qiao Qiao Li et al. "Control of Polaronic Behavior and Carrier Lifetimes via Metal and Anion Alloying in Chalcogenide Perovskites". In: *Journal of Physical Chemistry Letters* 13.22 (2022), pp. 4955–4962. ISSN: 19487185. DOI: 10.1021/acs.jpclett.2c00880.

[51] Ida Sadeghi et al. "Expanding the Perovskite Periodic Table to Include Chalcogenide Alloys with Tunable Band Gap Spanning 1.5-1.9 eV". In: *Advanced Functional Materials* 33.41 (2023). (author contributed to this work), p. 2304575. ISSN: 1616-301X. DOI: 10.1002/adfm.202304575.

[52] A. Y. Cho and J. R. Arthur. "Molecular beam epitaxy". In: *Progress in Solid State Chemistry* 10.PART 3 (1975), pp. 157–191. ISSN: 00796786. DOI: 10.1016/0079-6786(75)90005-9.

[53] Takeaki Hamachi et al. "Comprehensive analysis of current leakage at individual screw and mixed threading dislocations in freestanding GaN substrates". In: *Scientific Reports* 13.1 (2023), p. 2436. ISSN: 2045-2322. DOI: 10.1038/s41598-023-29458-3.

[54] J.L. Hoyt et al. "Strained silicon MOSFET technology". In: *Digest. International Electron Devices Meeting,* IEEE, 2002, pp. 23–26. ISBN: 0-7803-7462-2. DOI: 10.1109/IEDM.2002.1175770.

[55] Tara Peña et al. “Strain engineering 2D MoS 2 with thin film stress capping layers”. In: *2D Materials* 8.4 (2021), p. 045001. ISSN: 2053-1583. DOI: 10.1088/2053-1583/ac08f2. arXiv: 2009.10626.

[56] John F. Geisz et al. “Six-junction III–V solar cells with 47.1% conversion efficiency under 143 Suns concentration”. In: *Nature Energy* 5.4 (2020), pp. 326–335. ISSN: 20587546. DOI: 10.1038/s41560-020-0598-5.

[57] Ian Marius Peters et al. “Practical limits of multijunction solar cells”. In: *Progress in Photovoltaics: Research and Applications* April (2023), pp. 1–10. ISSN: 1099159X. DOI: 10.1002/pip.3705.

[58] Tim Grieb et al. “Determination of the chemical composition of GaNAs using STEM HAADF imaging and STEM strain state analysis”. In: *Ultramicroscopy* 117 (2012), pp. 15–23. ISSN: 03043991. DOI: 10.1016/j.ultramic.2012.03.014.

[59] V. Grillo, E. Carlino, and F. Glas. “Influence of the static atomic displacement on atomic resolution Z-contrast imaging”. In: *Physical Review B - Condensed Matter and Materials Physics* 77.5 (2008), pp. 1–6. ISSN: 10980121. DOI: 10.1103/PhysRevB.77.054103.

[60] Joshua Young and James M. Rondinelli. “Octahedral Rotation Preferences in Perovskite Iodides and Bromides”. In: *The Journal of Physical Chemistry Letters* 7.5 (2016), pp. 918–922. ISSN: 1948-7185. DOI: 10.1021/acs.jpclett.6b00094.

[61] Hong Mei Jing et al. “Formation of Ruddlesden-Popper Faults and Their Effect on the Magnetic Properties in Pr0.5Sr0.5CoO3 Thin Films”. In: *ACS Applied Materials and Interfaces* 10.1 (2018), pp. 1428–1433. ISSN: 19448252. DOI: 10.1021/acsami.7b16341.

[62] Jumi Bak et al. “Effect of Lattice Strain on the Formation of Ruddlesden-Popper Faults in Heteroepitaxial LaNiO3for Oxygen Evolution Electrocatalysis”. In: *Journal of Physical Chemistry Letters* 11.17 (2020), pp. 7253–7260. ISSN: 19487185. DOI: 10.1021/acs.jpclett.0c01426.

[63] Stephen A. Filippone, Yi Yang Sun, and R. Jaramillo. “The effect of an improved density functional on the thermodynamics and adsorption-controlled growth windows of chalcogenide perovskites”. In: *MRS Advances* 3.55 (2018), pp. 3249–3254. ISSN: 20598521. DOI: 10.1557/adv.2018.497.

[64] A. Muller and J. Grazul. “Optimizing the environment for sub-0.2 nm scanning transmission electron microscopy”. In: *Journal of Electron Microscopy* 50.3 (2001), pp. 219–226. ISSN: 00220744. DOI: 10.1093/jmicro/50.3.219.

6

Conclusions & Future Work

Where will it end? Where will it end?

Where will it end? Where will it end?!?!?

– "Day of the Lords", *Unknown Pleasures*, Joy Divison

In this work, the significance of establishing structure-property relationships in chalcogenide-based materials was shown through the use of electron microscopy and computational methods. It was shown that it was not an either/or situation with these methods; the techniques are highly complementary and were required to study the several novel chalcogenide systems in this work.

In studying these different chalcogenide systems, each with different material properties and applications, a wide range of topics are covered in this work. Chapter 3 concerns the thermoelectric properties of $TlGaSe_2$. Here, the stacking faults of TlGaSe2 were imaged with HAADF-STEM and compared to multislice calculations to confirm the imaging. Diffraction studies of the material using SAED revealed streaking along the (*hhl*) directions of the material, which were confirmed using diffraction simulations to be due to the short- to medium-range disorder of the material due to the stacking faults. DFT calculations revealed the negative stacking fault energies of the system of ~ -25 mJ m^{-2}. This implied that these faults are intrinsic to the system and that there is no equilibrium distance between the stacking faults, which was evident from the lack of long-range stacking order seen in the characterisation studies. Therefore, to study the thermoelectric properties,

experimentation would prove to be far too cumbersome, hence the need to use DFT to qualitatively study the role of these stacking faults in the thermoelectric properties.

To study this, electron transport and phonon calculations of the bulk system (*AA*-stacking) and a faulted system (*AB*-stacking) were performed. This is because it was predicted that the stacking faults would suppress the phonon transport through the stacking direction, as is the case in other thermoelectric systems [1, 2], while the electrical characteristics would mostly remain the same. From the preliminary electron transport calculations, it can be seen that minimal, if not negligible, change is seen between the bulk and faulted systems, especially around the VBM. It should be noted that these calculations were done at a PBE-level of theory, so the band gap of the systems is underestimated (~ 1.3 eV for the bulk stacking and ~ 1.2 eV for the *AB*-stacking, compared to 1.95 - 2.2 eV in literature [3–7]). It is also assumed that these are undoped systems, which is not the case as $TlGaSe_2$ exhibits *p*-type conductivity [8]. While calculations using experimentally measured and predicted doping values are being conducted, it is predicted that the general trend that a negligible change in the electron transport between the systems will remain.

On the other hand, preliminary phonon calculations do show some differences between the two structures. There appears to be suppression of some of the optical phonons when the stacking fault is induced, indicating a lower thermal transport through the system. This could confirm the relationship between the stacking faults and the thermoelectric properties of $TlGaSe_2$. However, more work is ongoing on these calculations, as the presence of negative phonons in both systems at the same high symmetry points indicates instability in both, which is more likely a calculation error rather than a physical property. Raman spectroscopy measurements are planned to correlate any shifts in the phonon DOS obtained in the calculations with the presence of stacking faults in the system.

While $TlGaSe_2$ is an interesting chalcogenide system, its commercial prospects are hampered by the high toxicity of thallium [9, 10]. The lack of control of stacking also poses a challenge as this reduces the material's ability to be tuned for specific applications. As such, the topic of van der Waals heterostructures and twisted bilayers are explored in Chapter 4. Here, the system of GaS/GaSe-based heterostructures is studied first by DFT calculations and then experimentally via HAADF-STEM and EDX. In line with previous

first-principles calculations, the electronic band structure of the system possesses splitting of the VBM along momentum space rather than in energy space when SOC is included, in a process known as Rashba splitting. However, shown in this work, this splitting is asymmetrical along different high symmetry points and sinusoidally changes with respect to the twist angle. The band gap of these heterostructures is also calculated to be sinusoidal with respect to the twist angle. While this feature is not unique to this system, as other van der Waals heterostructures also have angular-dependent band gaps [11–13], what is unique is the extreme change in band gap value of up to ~ 1 eV every 30°. This excellent tunability and several degrees of freedom allow for optoelectronic devices which cover a wide range of wavelengths and spintronic applications.

Experimentally, it was shown that these GaS/GaSe heterostructures can be constructed using mechanical exfoliation and a (relatively) cheap transfer stage and microscope [14]. Using FFTs of HAADF-STEM images of the plan-view heterostructures, it revealed the presence of a moiré lattice with a lattice parameter of ~ 14 Å due to the ~ 7.8° twist angle between the GaS and GaSe layers. However, PACBED patterns from its constituent flakes and cross-sectional imaging of other heterostructures revealed that the structures are not at the monolayer limit, so comparing them to simulation results is not appropriate. However, with further optimisation of the sample preparation, the band gaps of these structures can be revealed with the Nion UltraSTEM 200 that was used in this work. Yet, to probe the Rashba splitting, more energy resolution is required so these structures would also be examined at a facility such as SuperSTEM in Darsbury, England which has a highly-monochromated Nion UltraSTEM 100MC "HERMES" microscope. Device preparation is also planned, to probe the optoelectronic applications of these heterostructures using suitable contacts and a range of wavelengths from an optical source.

Despite the merits of such chalcogenide-based heterostructures, their market viability is currently limited as producing van der Waals heterostructures at arbitrary twist angles and at scale is currently not feasible. Thus, materials which can address current short- to medium-term environmental and market needs, such as chalcogenide perovskites, were investigated in Chapter 5. Here the $BaZrS_{(3-y)}Se_y$ alloy system was investigated due to its ideal band gap ranges for single junction photovoltaics [15–18]. By using a $BaZrS_3$

template layer grown on a $LaAlO_3$ substrate, the $BaZrS_{(3-y)}Se_y$ structure could be forced into growing into its perovskite form, rather than its more stable needle-like structure [16, 19]. While it was shown with cross-sectional HAADF-STEM imaging that the structure is indeed perovskite, the slight lattice mismatch between $BaZrS_3$ and $BaZrSe_3$ causes internal strain which is relieved through the interface with the substrate and the large number of APBs seen throughout. It was shown that as the ratio of Se/S increased, the number of APBs also increased, but out-of-plane APBs were mostly isolated to the template region, while in-plane APBs were predominantly seen in the alloy region. EDX spectral imaging of the samples showed that Se had diffused all the way down to the interface, while the S/Se ratio remained the same throughout the sample and was the same as the initial growth conditions. Mapping of the in-plane and out-of-plane A-site cation distances revealed a tripartite of out-of-plane spacings that were in line with the (202) reflection pairs seen in the HRXRD spectra. Additionally, the mapping revealed a < 1% strain from the substrate to the surface of the films, highlighting that the films were relaxed, and the relaxation mechanism was via the APBs and the buffered interface. Photoconductivity spectroscopy measurements revealed that the band gaps of the films dropped with increasing Se content, in line with previous and current theoretical modelling [20, 21].

This bespoke control of the band gap by simple adjustment of initial growth conditions allows for the development of photovoltaic devices for a wide range of wavelengths. However, these films were grown by collaborators via gas-flow MBE [17], which is a slow but precise growth process. Work is currently ongoing to transition this process to more commercially viable CVD processes and explore other chalcogenide perovskite systems.

Throughout the various chalcogenide systems in this work, the author hopes that they have instilled into the reader that chalcogenide-based materials are immensely interesting. They hope that the importance of establishing structure-property relationships before such systems can be made into consumer-ready devices has been highlighted. The author also hopes that crucial role of both electron microscopy and computational modelling and analysis cannot be understated for these systems, as without these techniques, key findings such as the Rashba splitting in GaS/GaSe heterostructure in Chapter 4 or the thermoelectric properties of $TlGaSe_2$ in Chapter 3 could not be practically investigated.

Finally, the author would like to thank the reader for making it this far into this tome of chalcogen knowledge, and now ...

I'll meet you

At the exit.

– "Exit Only", *Steady Diet of Nothing*, Fugazi

References

[1] Bingchao Qin, Dongyang Wang, and Li-Dong Zhao. “Slowing down the heat in thermoelectrics”. In: *InfoMat* 3.7 (2021), pp. 755–789. ISSN: 2567-3165. DOI: 10.1002/inf2.12217.

[2] Li Xie et al. “Stacking faults modulation for scattering optimization in GeTe-based thermoelectric materials”. In: *Nano Energy* 68 (2020), p. 104347. ISSN: 22112855. DOI: 10.1016/j.nanoen.2019.104347.

[3] S Duman and B Gürbulak. “ Urbach Tail and Optical Absorption in Layered Semiconductor TlGaSe 2(1- x) S 2 x Single Crystals ”. In: *Physica Scripta* 72.1 (2005), pp. 79–86. ISSN: 0031-8949. DOI: 10.1238/physica.regular.072a00079.

[4] H.T. Shaban. “Characterization of TlGaSe2 single crystals”. In: *Physica B: Condensed Matter* 405.8 (2010), pp. 1951–1954. ISSN: 09214526. DOI: 10.1016/j.physb.2009.08.018.

[5] Simon Johnsen et al. “Thallium chalcogenide-based wide-band-gap semiconductors: TlGaSe 2 for radiation detectors”. In: *Chemistry of Materials* 23.12 (2011), pp. 3120–3128. ISSN: 08974756. DOI: 10.1021/cm200946y.

[6] Shengxue Yang et al. “Ultrathin ternary semiconductor TlGaSe2 phototransistors with Broad-spectral response”. In: *2D Materials* 4.3 (2017). ISSN: 20531583. DOI: 10.1088/2053-1583/aa80c7.

[7] Asuman Cengiz et al. “Origin of the optical absorption of TlGaSe2 layered semiconductor in the visible range”. In: *Semiconductor Science and Technology* 33.7 (2018). ISSN: 13616641. DOI: 10.1088/1361-6641/aac97b.

[8] A. M. Panich. “Electronic properties and phase transitions in low-dimensional semiconductors”. In: *Journal of Physics Condensed Matter* 20.29 (2008). ISSN: 09538984. DOI: 10.1088/0953-8984/20/29/293202.

[9] Petra Cvjetko, Ivan Cvjetko, and Mirjana Pavlica. “Thallium toxicity in humans”. In: *Arhiv za Higijenu Rada i Toksikologiju* 61.1 (2010), pp. 111–119. ISSN: 00041254. DOI: 10.2478/10004-1254-61-2010-1976.

[10] Anders Lennartson. “Toxic thallium”. In: *Nature Chemistry* 7.7 (2015), pp. 610–610. ISSN: 1755-4349. DOI: 10.1038/nchem.2286.

[11] Shengxi Huang et al. “Probing the Interlayer Coupling of Twisted Bilayer MoS 2 Using Photoluminescence Spectroscopy”. In: *Nano Letters* 14.10 (2014), pp. 5500–5508. ISSN: 1530-6984. DOI: 10.1021/nl5014597.

[12] Wencan Jin et al. “Tuning the electronic structure of monolayer graphene/MoS2 van der Waals heterostructures via interlayer twist”. In: *Physical Review B* 92.20 (2015), p. 201409. ISSN: 1098-0121. DOI: 10.1103/PhysRevB.92.201409.

[13] Sayantika Chowdhury, P. Venkateswaran, and D. Somvanshi. “Interlayer twist angle-dependent electronic structure and optical properties of InSe/WTe 2 van der Waals heterostructure”. In: *2022 IEEE International Conference of Electron Devices Society Kolkata Chapter (EDKCON)*. IEEE, 2022, pp. 325–328. ISBN: 978-1-6654-7205-0. DOI: 10.1109/EDKCON56221.2022.10032930.

[14] Qinghua Zhao et al. “An inexpensive system for the deterministic transfer of 2D materials”. In: *JPhys Materials* 3.1 (2020). ISSN: 25157639. DOI: 10.1088/2515-7639/ab6a72.

[15] Yi-Yang Sun et al. “Chalcogenide Perovskites for Photovoltaics”. In: *Nano Letters* 15.1 (2015), pp. 581–585. ISSN: 1530-6984. DOI: 10.1021/nl504046x.

[16] Marc Ong et al. “BaZrSe3: Ab initio study of anion substitution for bandgap tuning in a chalcogenide material”. In: *Journal of Applied Physics* 125.23 (2019), p. 235702. ISSN: 0021-8979. DOI: 10.1063/1.5097940.

[17] Ida Sadeghi et al. “Making BaZrS3 Chalcogenide Perovskite Thin Films by Molecular Beam Epitaxy”. In: *Advanced Functional Materials* 31.45 (2021), p. 2105563. ISSN: 1616-3028. DOI: 10.1002/ADFM.202105563. arXiv: 2105.10258.

[18] Ida Sadeghi et al. “Expanding the Perovskite Periodic Table to Include Chalcogenide Alloys with Tunable Band Gap Spanning 1.5-1.9 eV”. In: *Advanced Functional Materials* 33.41 (2023). (author contributed to this work), p. 2304575. ISSN: 1616-301X. DOI: 10.1002/adfm.202304575.

[19] Louis J. Tranchitella et al. “Commensurate Columnar Composite Compounds: Synthesis and Structure of Ba 15 Zr 14 Se 42 and Sr 21 Ti 19 Se 57”. In: *Journal of the American Chemical Society* 120.30 (1998), pp. 7639–7640. ISSN: 0002-7863. DOI: 10.1021/ja972442p.

[20] Weiwei Meng et al. “Alloying and Defect Control within Chalcogenide Perovskites for Optimized Photovoltaic Application”. In: *Chemistry of Materials* 28.3 (2016), pp. 821–829. ISSN: 0897-4756. DOI: 10.1021/acs.chemmater.5b04213.

[21] Qiao Qiao Li et al. “Control of Polaronic Behavior and Carrier Lifetimes via Metal and Anion Alloying in Chalcogenide Perovskites”. In: *Journal of Physical Chemistry Letters* 13.22 (2022), pp. 4955–4962. ISSN: 19487185. DOI: 10.1021/acs.jpclett.2c00880.

Appendix A

Structure of $TlGaSe_2$ Used in SAED Simulations

For the simulation of the SAED pattern in Figure 3.6(a), the stacking order of $TlGaSe_2$ from Figure 3.3(a) was used as both imaging and diffraction patterns were collected from the same area. A 24-unit cell stacked structure was first created using the ASE. The structure was then created using the ATOMMAN python package [1]. Below is the *BBBBAAABABABBBBAAABBAAAA*-stacking order structure seen in Figure 3.3(a) in the Crystallographic Information File (.cif) format [2]:

```
#======================================================================
# CRYSTAL DATA
#----------------------------------------------------------------------
data_VESTA_phase_1

_chemical_name_common                  'tlgase2 24 AB'
_cell_length_a                         10.771000
_cell_length_b                         10.772000
_cell_length_c                         369.495605
_cell_angle_alpha                      89.857513
_cell_angle_beta                       90.000000
_cell_angle_gamma                      90.000000
_cell_volume                           42870.674272
_space_group_name_H-M_alt              'P 1'
_space_group_IT_number                 1

loop_
_space_group_symop_operation_xyz
   'x, y, z'

loop_
   _atom_site_label
   _atom_site_occupancy
   _atom_site_fract_x
   _atom_site_fract_y
   _atom_site_fract_z
```

```
_atom_site_adp_type
_atom_site_U_iso_or_equiv
_atom_site_type_symbol
Ga1     1.0     0.312000     0.936340     0.805740     Uiso  ? Ga
Ga2     1.0     0.688000     0.061320     0.826570     Uiso  ? Ga
Ga3     1.0     0.936100     0.061300     0.819200     Uiso  ? Ga
Ga4     1.0     0.063900     0.936320     0.798370     Uiso  ? Ga
Ga5     1.0     0.938000     0.061340     0.868240     Uiso  ? Ga
Ga6     1.0     0.938000     0.063620     0.735920     Uiso  ? Ga
Ga7     1.0     0.438000     0.563620     0.735920     Uiso  ? Ga
Ga8     1.0     0.686100     0.563700     0.743300     Uiso  ? Ga
Ga9     1.0     0.186100     0.063700     0.743300     Uiso  ? Ga
Ga10    1.0     0.812000     0.938660     0.756760     Uiso  ? Ga
Ga11    1.0     0.312000     0.438660     0.756760     Uiso  ? Ga
Ga12    1.0     0.936100     0.563660     0.784960     Uiso  ? Ga
Ga13    1.0     0.063900     0.438680     0.764130     Uiso  ? Ga
Ga14    1.0     0.563900     0.938680     0.764130     Uiso  ? Ga
Ga15    1.0     0.188000     0.561320     0.826570     Uiso  ? Ga
Ga16    1.0     0.436100     0.561300     0.819200     Uiso  ? Ga
Ga17    1.0     0.062000     0.436360     0.847410     Uiso  ? Ga
Ga18    1.0     0.062000     0.188640     0.840090     Uiso  ? Ga
Ga19    1.0     0.186100     0.061320     0.860870     Uiso  ? Ga
Ga20    1.0     0.686100     0.313700     0.868300     Uiso  ? Ga
Ga21    1.0     0.062000     0.686320     0.889070     Uiso  ? Ga
Ga22    1.0     0.438000     0.811360     0.909910     Uiso  ? Ga
Ga23    1.0     0.938000     0.063640     0.902590     Uiso  ? Ga
Ga24    1.0     0.186100     0.063660     0.909960     Uiso  ? Ga
Ga25    1.0     0.186100     0.311340     0.902540     Uiso  ? Ga
Ga26    1.0     0.686100     0.811340     0.902540     Uiso  ? Ga
Ga27    1.0     0.813900     0.686300     0.881700     Uiso  ? Ga
Ga28    1.0     0.813900     0.438680     0.889130     Uiso  ? Ga
Ga29    1.0     0.438000     0.813660     0.944260     Uiso  ? Ga
Ga30    1.0     0.562000     0.436340     0.930740     Uiso  ? Ga
Ga31    1.0     0.562000     0.188620     0.923420     Uiso  ? Ga
Ga32    1.0     0.938000     0.313660     0.944260     Uiso  ? Ga
Ga33    1.0     0.938000     0.561320     0.951570     Uiso  ? Ga
Ga34    1.0     0.186100     0.313680     0.951630     Uiso  ? Ga
Ga35    1.0     0.186100     0.561300     0.944200     Uiso  ? Ga
Ga36    1.0     0.313900     0.436320     0.923370     Uiso  ? Ga
Ga37    1.0     0.313900     0.188700     0.930800     Uiso  ? Ga
Ga38    1.0     0.686100     0.813680     0.951630     Uiso  ? Ga
Ga39    1.0     0.062000     0.186360     0.972410     Uiso  ? Ga
Ga40    1.0     0.062000     0.938640     0.965090     Uiso  ? Ga
Ga41    1.0     0.438000     0.063620     0.985920     Uiso  ? Ga
Ga42    1.0     0.438000     0.311340     0.993240     Uiso  ? Ga
Ga43    1.0     0.562000     0.686360     0.972410     Uiso  ? Ga
Ga44    1.0     0.562000     0.438640     0.965090     Uiso  ? Ga
Ga45    1.0     0.938000     0.563620     0.985920     Uiso  ? Ga
Ga46    1.0     0.938000     0.811340     0.993240     Uiso  ? Ga
Ga47    1.0     0.186100     0.563700     0.993300     Uiso  ? Ga
Ga48    1.0     0.186100     0.811320     0.985870     Uiso  ? Ga
Ga49    1.0     0.686100     0.063700     0.993300     Uiso  ? Ga
Ga50    1.0     0.686100     0.311320     0.985870     Uiso  ? Ga
```

Ga51	1.0	0.813900	0.186340	0.965040	Uiso	?	Ga
Ga52	1.0	0.813900	0.938660	0.972460	Uiso	?	Ga
Ga53	1.0	0.562000	0.936340	0.680740	Uiso	?	Ga
Ga54	1.0	0.938000	0.061320	0.701570	Uiso	?	Ga
Ga55	1.0	0.186100	0.061300	0.694200	Uiso	?	Ga
Ga56	1.0	0.313900	0.936320	0.673370	Uiso	?	Ga
Ga57	1.0	0.436100	0.311340	0.777540	Uiso	?	Ga
Ga58	1.0	0.812000	0.436340	0.805740	Uiso	?	Ga
Ga59	1.0	0.563900	0.436320	0.798370	Uiso	?	Ga
Ga60	1.0	0.438000	0.313620	0.860920	Uiso	?	Ga
Ga61	1.0	0.062000	0.438660	0.881760	Uiso	?	Ga
Ga62	1.0	0.686100	0.563660	0.909960	Uiso	?	Ga
Ga63	1.0	0.062000	0.688620	0.923420	Uiso	?	Ga
Ga64	1.0	0.813900	0.688700	0.930800	Uiso	?	Ga
Ga65	1.0	0.438000	0.561320	0.701570	Uiso	?	Ga
Ga66	1.0	0.686100	0.561300	0.694200	Uiso	?	Ga
Ga67	1.0	0.062000	0.686360	0.722410	Uiso	?	Ga
Ga68	1.0	0.688000	0.811360	0.784910	Uiso	?	Ga
Ga69	1.0	0.936100	0.811340	0.777540	Uiso	?	Ga
Ga70	1.0	0.186100	0.563660	0.659960	Uiso	?	Ga
Ga71	1.0	0.562000	0.688640	0.840090	Uiso	?	Ga
Ga72	1.0	0.938000	0.813620	0.860920	Uiso	?	Ga
Ga73	1.0	0.186100	0.813700	0.868300	Uiso	?	Ga
Ga74	1.0	0.313900	0.688660	0.847460	Uiso	?	Ga
Ga75	1.0	0.438000	0.061320	0.951570	Uiso	?	Ga
Ga76	1.0	0.686100	0.061300	0.944200	Uiso	?	Ga
Ga77	1.0	0.812000	0.188640	0.465090	Uiso	?	Ga
Ga78	1.0	0.688000	0.063640	0.527590	Uiso	?	Ga
Ga79	1.0	0.936100	0.063660	0.534960	Uiso	?	Ga
Ga80	1.0	0.312000	0.188620	0.548420	Uiso	?	Ga
Ga81	1.0	0.063900	0.188700	0.555800	Uiso	?	Ga
Ga82	1.0	0.812000	0.186360	0.597410	Uiso	?	Ga
Ga83	1.0	0.188000	0.311340	0.618240	Uiso	?	Ga
Ga84	1.0	0.436100	0.311320	0.610870	Uiso	?	Ga
Ga85	1.0	0.563900	0.186340	0.590040	Uiso	?	Ga
Ga86	1.0	0.562000	0.186320	0.889070	Uiso	?	Ga
Ga87	1.0	0.188000	0.313660	0.819260	Uiso	?	Ga
Ga88	1.0	0.436100	0.313680	0.826630	Uiso	?	Ga
Ga89	1.0	0.813900	0.188660	0.847460	Uiso	?	Ga
Ga90	1.0	0.938000	0.311360	0.909910	Uiso	?	Ga
Ga91	1.0	0.313900	0.186300	0.881700	Uiso	?	Ga
Ga92	1.0	0.313900	0.438660	0.972460	Uiso	?	Ga
Ga93	1.0	0.062000	0.938660	0.631760	Uiso	?	Ga
Ga94	1.0	0.438000	0.063640	0.652590	Uiso	?	Ga
Ga95	1.0	0.686100	0.063660	0.659960	Uiso	?	Ga
Ga96	1.0	0.813900	0.938680	0.639130	Uiso	?	Ga
Ga97	1.0	0.562000	0.186360	0.722410	Uiso	?	Ga
Ga98	1.0	0.313900	0.186340	0.715040	Uiso	?	Ga
Ga99	1.0	0.188000	0.311360	0.784910	Uiso	?	Ga
Ga100	1.0	0.688000	0.313660	0.569260	Uiso	?	Ga
Ga101	1.0	0.936100	0.313680	0.576630	Uiso	?	Ga
Ga102	1.0	0.688000	0.061340	0.493240	Uiso	?	Ga
Ga103	1.0	0.936100	0.061320	0.485870	Uiso	?	Ga

Ga104	1.0	0.312000	0.186380	0.514080	Uiso	?	Ga
Ga105	1.0	0.063900	0.186300	0.506700	Uiso	?	Ga
Ga106	1.0	0.562000	0.188620	0.423420	Uiso	?	Ga
Ga107	1.0	0.938000	0.313660	0.444260	Uiso	?	Ga
Ga108	1.0	0.186100	0.313680	0.451630	Uiso	?	Ga
Ga109	1.0	0.313900	0.188700	0.430800	Uiso	?	Ga
Ga110	1.0	0.563900	0.188660	0.472460	Uiso	?	Ga
Ga111	1.0	0.938000	0.061340	0.368240	Uiso	?	Ga
Ga112	1.0	0.186100	0.061320	0.360870	Uiso	?	Ga
Ga113	1.0	0.562000	0.686320	0.639070	Uiso	?	Ga
Ga114	1.0	0.562000	0.938640	0.715090	Uiso	?	Ga
Ga115	1.0	0.313900	0.938660	0.722460	Uiso	?	Ga
Ga116	1.0	0.688000	0.563640	0.777590	Uiso	?	Ga
Ga117	1.0	0.312000	0.688620	0.798420	Uiso	?	Ga
Ga118	1.0	0.063900	0.688700	0.805800	Uiso	?	Ga
Ga119	1.0	0.438000	0.561340	0.868240	Uiso	?	Ga
Ga120	1.0	0.686100	0.561320	0.860870	Uiso	?	Ga
Ga121	1.0	0.813900	0.436340	0.840040	Uiso	?	Ga
Ga122	1.0	0.313900	0.686340	0.965040	Uiso	?	Ga
Ga123	1.0	0.188000	0.811360	0.534910	Uiso	?	Ga
Ga124	1.0	0.436100	0.811340	0.527540	Uiso	?	Ga
Ga125	1.0	0.188000	0.813660	0.569260	Uiso	?	Ga
Ga126	1.0	0.436100	0.813680	0.576630	Uiso	?	Ga
Ga127	1.0	0.812000	0.938640	0.590090	Uiso	?	Ga
Ga128	1.0	0.188000	0.063620	0.610920	Uiso	?	Ga
Ga129	1.0	0.436100	0.063700	0.618300	Uiso	?	Ga
Ga130	1.0	0.563900	0.938660	0.597460	Uiso	?	Ga
Ga131	1.0	0.938000	0.811360	0.659910	Uiso	?	Ga
Ga132	1.0	0.186100	0.811340	0.652540	Uiso	?	Ga
Ga133	1.0	0.313900	0.686300	0.631700	Uiso	?	Ga
Ga134	1.0	0.438000	0.563640	0.902590	Uiso	?	Ga
Ga135	1.0	0.438000	0.811340	0.743240	Uiso	?	Ga
Ga136	1.0	0.686100	0.811320	0.735870	Uiso	?	Ga
Ga137	1.0	0.813900	0.686340	0.715040	Uiso	?	Ga
Ga138	1.0	0.312000	0.686320	0.764070	Uiso	?	Ga
Ga139	1.0	0.063900	0.686300	0.756700	Uiso	?	Ga
Ga140	1.0	0.688000	0.811340	0.618240	Uiso	?	Ga
Ga141	1.0	0.938000	0.563640	0.652590	Uiso	?	Ga
Ga142	1.0	0.562000	0.688620	0.673420	Uiso	?	Ga
Ga143	1.0	0.938000	0.813660	0.694260	Uiso	?	Ga
Ga144	1.0	0.186100	0.813680	0.701630	Uiso	?	Ga
Ga145	1.0	0.313900	0.688700	0.680800	Uiso	?	Ga
Ga146	1.0	0.688000	0.813660	0.819260	Uiso	?	Ga
Ga147	1.0	0.936100	0.813680	0.826630	Uiso	?	Ga
Ga148	1.0	0.936100	0.811320	0.610870	Uiso	?	Ga
Ga149	1.0	0.688000	0.061380	0.326580	Uiso	?	Ga
Ga150	1.0	0.936100	0.061300	0.319200	Uiso	?	Ga
Ga151	1.0	0.688000	0.813680	0.485930	Uiso	?	Ga
Ga152	1.0	0.936100	0.813700	0.493300	Uiso	?	Ga
Ga153	1.0	0.312000	0.938660	0.506760	Uiso	?	Ga
Ga154	1.0	0.063900	0.938680	0.514130	Uiso	?	Ga
Ga155	1.0	0.188000	0.061320	0.576570	Uiso	?	Ga
Ga156	1.0	0.436100	0.061300	0.569200	Uiso	?	Ga

Ga157	1.0	0.812000	0.188620	0.298420	Uiso	?	Ga
Ga158	1.0	0.563900	0.188700	0.305800	Uiso	?	Ga
Ga159	1.0	0.188000	0.061360	0.409910	Uiso	?	Ga
Ga160	1.0	0.436100	0.061340	0.402540	Uiso	?	Ga
Ga161	1.0	0.438000	0.061360	0.284910	Uiso	?	Ga
Ga162	1.0	0.686100	0.061340	0.277540	Uiso	?	Ga
Ga163	1.0	0.812000	0.936340	0.555740	Uiso	?	Ga
Ga164	1.0	0.563900	0.936320	0.548370	Uiso	?	Ga
Ga165	1.0	0.938000	0.063620	0.235920	Uiso	?	Ga
Ga166	1.0	0.186100	0.063700	0.243300	Uiso	?	Ga
Ga167	1.0	0.562000	0.188660	0.256760	Uiso	?	Ga
Ga168	1.0	0.313900	0.188680	0.264130	Uiso	?	Ga
Ga169	1.0	0.188000	0.313660	0.319260	Uiso	?	Ga
Ga170	1.0	0.436100	0.313680	0.326630	Uiso	?	Ga
Ga171	1.0	0.062000	0.188640	0.340090	Uiso	?	Ga
Ga172	1.0	0.686100	0.313700	0.368300	Uiso	?	Ga
Ga173	1.0	0.813900	0.188660	0.347460	Uiso	?	Ga
Ga174	1.0	0.063900	0.188680	0.389130	Uiso	?	Ga
Ga175	1.0	0.438000	0.061380	0.451580	Uiso	?	Ga
Ga176	1.0	0.686100	0.061300	0.444200	Uiso	?	Ga
Ga177	1.0	0.312000	0.936360	0.472410	Uiso	?	Ga
Ga178	1.0	0.063900	0.936340	0.465040	Uiso	?	Ga
Ga179	1.0	0.188000	0.061380	0.076580	Uiso	?	Ga
Ga180	1.0	0.436100	0.061300	0.069200	Uiso	?	Ga
Ga181	1.0	0.188000	0.063680	0.110930	Uiso	?	Ga
Ga182	1.0	0.436100	0.063700	0.118300	Uiso	?	Ga
Ga183	1.0	0.688000	0.061360	0.159910	Uiso	?	Ga
Ga184	1.0	0.936100	0.061340	0.152540	Uiso	?	Ga
Ga185	1.0	0.938000	0.061380	0.201580	Uiso	?	Ga
Ga186	1.0	0.186100	0.061300	0.194200	Uiso	?	Ga
Ga187	1.0	0.562000	0.186360	0.222410	Uiso	?	Ga
Ga188	1.0	0.313900	0.186340	0.215040	Uiso	?	Ga
Ga189	1.0	0.438000	0.313620	0.360920	Uiso	?	Ga
Ga190	1.0	0.312000	0.188660	0.381760	Uiso	?	Ga
Ga191	1.0	0.688000	0.313640	0.402590	Uiso	?	Ga
Ga192	1.0	0.936100	0.313660	0.409960	Uiso	?	Ga
Ga193	1.0	0.686100	0.311340	0.652540	Uiso	?	Ga
Ga194	1.0	0.062000	0.436340	0.680740	Uiso	?	Ga
Ga195	1.0	0.813900	0.436320	0.673370	Uiso	?	Ga
Ga196	1.0	0.562000	0.936360	0.847410	Uiso	?	Ga
Ga197	1.0	0.313900	0.936340	0.840040	Uiso	?	Ga
Ga198	1.0	0.062000	0.438640	0.715090	Uiso	?	Ga
Ga199	1.0	0.188000	0.063640	0.777590	Uiso	?	Ga
Ga200	1.0	0.436100	0.063660	0.784960	Uiso	?	Ga
Ga201	1.0	0.562000	0.938660	0.881760	Uiso	?	Ga
Ga202	1.0	0.313900	0.938680	0.889130	Uiso	?	Ga
Ga203	1.0	0.062000	0.936340	0.930740	Uiso	?	Ga
Ga204	1.0	0.813900	0.936320	0.923370	Uiso	?	Ga
Ga205	1.0	0.812000	0.688660	0.381760	Uiso	?	Ga
Ga206	1.0	0.436100	0.813660	0.409960	Uiso	?	Ga
Ga207	1.0	0.563900	0.688680	0.389130	Uiso	?	Ga
Ga208	1.0	0.812000	0.436360	0.472410	Uiso	?	Ga
Ga209	1.0	0.312000	0.438640	0.590090	Uiso	?	Ga

Ga210	1.0	0.936100	0.563700	0.618300	Uiso	?	Ga
Ga211	1.0	0.313900	0.438680	0.639130	Uiso	?	Ga
Ga212	1.0	0.936100	0.311340	0.527540	Uiso	?	Ga
Ga213	1.0	0.312000	0.436340	0.555740	Uiso	?	Ga
Ga214	1.0	0.688000	0.561320	0.576570	Uiso	?	Ga
Ga215	1.0	0.936100	0.561300	0.569200	Uiso	?	Ga
Ga216	1.0	0.063900	0.436320	0.548370	Uiso	?	Ga
Ga217	1.0	0.312000	0.686360	0.597410	Uiso	?	Ga
Ga218	1.0	0.688000	0.563620	0.610920	Uiso	?	Ga
Ga219	1.0	0.562000	0.438660	0.631760	Uiso	?	Ga
Ga220	1.0	0.936100	0.561340	0.402540	Uiso	?	Ga
Ga221	1.0	0.562000	0.436340	0.430740	Uiso	?	Ga
Ga222	1.0	0.938000	0.561380	0.451580	Uiso	?	Ga
Ga223	1.0	0.186100	0.561300	0.444200	Uiso	?	Ga
Ga224	1.0	0.313900	0.436320	0.423370	Uiso	?	Ga
Ga225	1.0	0.188000	0.313680	0.485930	Uiso	?	Ga
Ga226	1.0	0.436100	0.313700	0.493300	Uiso	?	Ga
Ga227	1.0	0.812000	0.438660	0.506760	Uiso	?	Ga
Ga228	1.0	0.436100	0.563660	0.534960	Uiso	?	Ga
Ga229	1.0	0.563900	0.438680	0.514130	Uiso	?	Ga
Ga230	1.0	0.062000	0.186320	0.639070	Uiso	?	Ga
Ga231	1.0	0.438000	0.311360	0.659910	Uiso	?	Ga
Ga232	1.0	0.813900	0.186300	0.631700	Uiso	?	Ga
Ga233	1.0	0.438000	0.313660	0.694260	Uiso	?	Ga
Ga234	1.0	0.686100	0.313680	0.701630	Uiso	?	Ga
Ga235	1.0	0.813900	0.438660	0.722460	Uiso	?	Ga
Ga236	1.0	0.812000	0.188620	0.798420	Uiso	?	Ga
Ga237	1.0	0.563900	0.188700	0.805800	Uiso	?	Ga
Ga238	1.0	0.062000	0.188620	0.673420	Uiso	?	Ga
Ga239	1.0	0.813900	0.188700	0.680800	Uiso	?	Ga
Ga240	1.0	0.938000	0.311340	0.743240	Uiso	?	Ga
Ga241	1.0	0.186100	0.311320	0.735870	Uiso	?	Ga
Ga242	1.0	0.812000	0.186320	0.764070	Uiso	?	Ga
Ga243	1.0	0.563900	0.186300	0.756700	Uiso	?	Ga
Ga244	1.0	0.063900	0.438660	0.597460	Uiso	?	Ga
Ga245	1.0	0.938000	0.313640	0.277590	Uiso	?	Ga
Ga246	1.0	0.186100	0.313660	0.284960	Uiso	?	Ga
Ga247	1.0	0.688000	0.311360	0.534910	Uiso	?	Ga
Ga248	1.0	0.936100	0.063660	0.034960	Uiso	?	Ga
Ga249	1.0	0.812000	0.186360	0.097410	Uiso	?	Ga
Ga250	1.0	0.812000	0.188660	0.131760	Uiso	?	Ga
Ga251	1.0	0.436100	0.313660	0.159960	Uiso	?	Ga
Ga252	1.0	0.563900	0.188680	0.139130	Uiso	?	Ga
Ga253	1.0	0.062000	0.188620	0.173420	Uiso	?	Ga
Ga254	1.0	0.438000	0.313660	0.194260	Uiso	?	Ga
Ga255	1.0	0.686100	0.313680	0.201630	Uiso	?	Ga
Ga256	1.0	0.813900	0.188700	0.180800	Uiso	?	Ga
Ga257	1.0	0.938000	0.311340	0.243240	Uiso	?	Ga
Ga258	1.0	0.186100	0.311320	0.235870	Uiso	?	Ga
Ga259	1.0	0.813900	0.438660	0.222460	Uiso	?	Ga
Ga260	1.0	0.562000	0.436380	0.264080	Uiso	?	Ga
Ga261	1.0	0.938000	0.561360	0.284910	Uiso	?	Ga
Ga262	1.0	0.313900	0.436300	0.256700	Uiso	?	Ga

Ga263	1.0	0.812000	0.436340	0.305740	Uiso	?	Ga
Ga264	1.0	0.188000	0.561380	0.326580	Uiso	?	Ga
Ga265	1.0	0.436100	0.561300	0.319200	Uiso	?	Ga
Ga266	1.0	0.563900	0.436320	0.298370	Uiso	?	Ga
Ga267	1.0	0.062000	0.436360	0.347410	Uiso	?	Ga
Ga268	1.0	0.438000	0.561340	0.368240	Uiso	?	Ga
Ga269	1.0	0.686100	0.561320	0.360870	Uiso	?	Ga
Ga270	1.0	0.813900	0.436340	0.340040	Uiso	?	Ga
Ga271	1.0	0.313900	0.688660	0.347460	Uiso	?	Ga
Ga272	1.0	0.312000	0.436380	0.389080	Uiso	?	Ga
Ga273	1.0	0.688000	0.561360	0.409910	Uiso	?	Ga
Ga274	1.0	0.063900	0.436300	0.381700	Uiso	?	Ga
Ga275	1.0	0.562000	0.936360	0.347410	Uiso	?	Ga
Ga276	1.0	0.313900	0.936340	0.340040	Uiso	?	Ga
Ga277	1.0	0.438000	0.813660	0.444260	Uiso	?	Ga
Ga278	1.0	0.686100	0.813680	0.451630	Uiso	?	Ga
Ga279	1.0	0.188000	0.813640	0.402590	Uiso	?	Ga
Ga280	1.0	0.062000	0.688620	0.423420	Uiso	?	Ga
Ga281	1.0	0.813900	0.688700	0.430800	Uiso	?	Ga
Ga282	1.0	0.188000	0.561340	0.493240	Uiso	?	Ga
Ga283	1.0	0.436100	0.561320	0.485870	Uiso	?	Ga
Ga284	1.0	0.563900	0.436340	0.465040	Uiso	?	Ga
Ga285	1.0	0.812000	0.686380	0.514080	Uiso	?	Ga
Ga286	1.0	0.563900	0.686300	0.506700	Uiso	?	Ga
Ga287	1.0	0.812000	0.688620	0.548420	Uiso	?	Ga
Ga288	1.0	0.563900	0.688700	0.555800	Uiso	?	Ga
Ga289	1.0	0.063900	0.686340	0.590040	Uiso	?	Ga
Ga290	1.0	0.688000	0.063640	0.027590	Uiso	?	Ga
Ga291	1.0	0.188000	0.311340	0.118240	Uiso	?	Ga
Ga292	1.0	0.436100	0.311320	0.110870	Uiso	?	Ga
Ga293	1.0	0.563900	0.186340	0.090040	Uiso	?	Ga
Ga294	1.0	0.188000	0.313640	0.152590	Uiso	?	Ga
Ga295	1.0	0.062000	0.436340	0.180740	Uiso	?	Ga
Ga296	1.0	0.438000	0.561380	0.201580	Uiso	?	Ga
Ga297	1.0	0.686100	0.561300	0.194200	Uiso	?	Ga
Ga298	1.0	0.813900	0.436320	0.173370	Uiso	?	Ga
Ga299	1.0	0.062000	0.438640	0.215090	Uiso	?	Ga
Ga300	1.0	0.438000	0.563620	0.235920	Uiso	?	Ga
Ga301	1.0	0.686100	0.563700	0.243300	Uiso	?	Ga
Ga302	1.0	0.062000	0.688660	0.256760	Uiso	?	Ga
Ga303	1.0	0.438000	0.813640	0.277590	Uiso	?	Ga
Ga304	1.0	0.186100	0.561340	0.277540	Uiso	?	Ga
Ga305	1.0	0.686100	0.813660	0.284960	Uiso	?	Ga
Ga306	1.0	0.813900	0.688680	0.264130	Uiso	?	Ga
Ga307	1.0	0.312000	0.688620	0.298420	Uiso	?	Ga
Ga308	1.0	0.688000	0.813660	0.319260	Uiso	?	Ga
Ga309	1.0	0.936100	0.813680	0.326630	Uiso	?	Ga
Ga310	1.0	0.063900	0.688700	0.305800	Uiso	?	Ga
Ga311	1.0	0.562000	0.688640	0.340090	Uiso	?	Ga
Ga312	1.0	0.938000	0.813620	0.360920	Uiso	?	Ga
Ga313	1.0	0.186100	0.813700	0.368300	Uiso	?	Ga
Ga314	1.0	0.188000	0.563640	0.527590	Uiso	?	Ga
Ga315	1.0	0.812000	0.936380	0.389080	Uiso	?	Ga

Ga316	1.0	0.312000	0.688640	0.465090	Uiso	?	Ga
Ga317	1.0	0.063900	0.688660	0.472460	Uiso	?	Ga
Ga318	1.0	0.563900	0.936300	0.381700	Uiso	?	Ga
Ga319	1.0	0.062000	0.936340	0.430740	Uiso	?	Ga
Ga320	1.0	0.813900	0.936320	0.423370	Uiso	?	Ga
Ga321	1.0	0.312000	0.188620	0.048420	Uiso	?	Ga
Ga322	1.0	0.063900	0.188700	0.055800	Uiso	?	Ga
Ga323	1.0	0.812000	0.436380	0.139080	Uiso	?	Ga
Ga324	1.0	0.188000	0.561360	0.159910	Uiso	?	Ga
Ga325	1.0	0.436100	0.561340	0.152540	Uiso	?	Ga
Ga326	1.0	0.563900	0.436300	0.131700	Uiso	?	Ga
Ga327	1.0	0.062000	0.686360	0.222410	Uiso	?	Ga
Ga328	1.0	0.438000	0.811340	0.243240	Uiso	?	Ga
Ga329	1.0	0.686100	0.811320	0.235870	Uiso	?	Ga
Ga330	1.0	0.813900	0.686340	0.215040	Uiso	?	Ga
Ga331	1.0	0.062000	0.936380	0.264080	Uiso	?	Ga
Ga332	1.0	0.813900	0.936300	0.256700	Uiso	?	Ga
Ga333	1.0	0.312000	0.936340	0.305740	Uiso	?	Ga
Ga334	1.0	0.063900	0.936320	0.298370	Uiso	?	Ga
Ga335	1.0	0.562000	0.688620	0.173420	Uiso	?	Ga
Ga336	1.0	0.313900	0.688700	0.180800	Uiso	?	Ga
Ga337	1.0	0.688000	0.313660	0.069260	Uiso	?	Ga
Ga338	1.0	0.936100	0.313680	0.076630	Uiso	?	Ga
Ga339	1.0	0.312000	0.438640	0.090090	Uiso	?	Ga
Ga340	1.0	0.936100	0.563700	0.118300	Uiso	?	Ga
Ga341	1.0	0.063900	0.438660	0.097460	Uiso	?	Ga
Ga342	1.0	0.063900	0.688680	0.139130	Uiso	?	Ga
Ga343	1.0	0.938000	0.813660	0.194260	Uiso	?	Ga
Ga344	1.0	0.186100	0.813680	0.201630	Uiso	?	Ga
Ga345	1.0	0.562000	0.938640	0.215090	Uiso	?	Ga
Ga346	1.0	0.313900	0.938660	0.222460	Uiso	?	Ga
Ga347	1.0	0.812000	0.686380	0.014080	Uiso	?	Ga
Ga348	1.0	0.812000	0.438660	0.006760	Uiso	?	Ga
Ga349	1.0	0.188000	0.563640	0.027590	Uiso	?	Ga
Ga350	1.0	0.188000	0.811360	0.034910	Uiso	?	Ga
Ga351	1.0	0.312000	0.186380	0.014080	Uiso	?	Ga
Ga352	1.0	0.312000	0.938660	0.006760	Uiso	?	Ga
Ga353	1.0	0.688000	0.311360	0.034910	Uiso	?	Ga
Ga354	1.0	0.936100	0.311340	0.027540	Uiso	?	Ga
Ga355	1.0	0.063900	0.186300	0.006700	Uiso	?	Ga
Ga356	1.0	0.063900	0.938680	0.014130	Uiso	?	Ga
Ga357	1.0	0.436100	0.563660	0.034960	Uiso	?	Ga
Ga358	1.0	0.436100	0.811340	0.027540	Uiso	?	Ga
Ga359	1.0	0.563900	0.686300	0.006700	Uiso	?	Ga
Ga360	1.0	0.563900	0.438680	0.014130	Uiso	?	Ga
Ga361	1.0	0.812000	0.936340	0.055740	Uiso	?	Ga
Ga362	1.0	0.812000	0.688620	0.048420	Uiso	?	Ga
Ga363	1.0	0.188000	0.813660	0.069260	Uiso	?	Ga
Ga364	1.0	0.312000	0.436340	0.055740	Uiso	?	Ga
Ga365	1.0	0.688000	0.561380	0.076580	Uiso	?	Ga
Ga366	1.0	0.936100	0.561300	0.069200	Uiso	?	Ga
Ga367	1.0	0.063900	0.436320	0.048370	Uiso	?	Ga
Ga368	1.0	0.436100	0.813680	0.076630	Uiso	?	Ga

Ga369	1.0	0.563900	0.936320	0.048370	Uiso	?	Ga
Ga370	1.0	0.563900	0.688700	0.055800	Uiso	?	Ga
Ga371	1.0	0.812000	0.938640	0.090090	Uiso	?	Ga
Ga372	1.0	0.312000	0.686360	0.097410	Uiso	?	Ga
Ga373	1.0	0.688000	0.811340	0.118240	Uiso	?	Ga
Ga374	1.0	0.936100	0.811320	0.110870	Uiso	?	Ga
Ga375	1.0	0.063900	0.686340	0.090040	Uiso	?	Ga
Ga376	1.0	0.563900	0.938660	0.097460	Uiso	?	Ga
Ga377	1.0	0.312000	0.936380	0.139080	Uiso	?	Ga
Ga378	1.0	0.063900	0.936300	0.131700	Uiso	?	Ga
Ga379	1.0	0.562000	0.936340	0.180740	Uiso	?	Ga
Ga380	1.0	0.313900	0.936320	0.173370	Uiso	?	Ga
Ga381	1.0	0.688000	0.563680	0.110930	Uiso	?	Ga
Ga382	1.0	0.312000	0.688660	0.131760	Uiso	?	Ga
Ga383	1.0	0.688000	0.813640	0.152590	Uiso	?	Ga
Ga384	1.0	0.936100	0.813660	0.159960	Uiso	?	Ga
Se1	1.0	0.937600	0.564180	0.711380	Uiso	?	Se
Se2	1.0	0.563000	0.937320	0.788770	Uiso	?	Se
Se3	1.0	0.437000	0.812340	0.767940	Uiso	?	Se
Se4	1.0	0.437600	0.814180	0.836380	Uiso	?	Se
Se5	1.0	0.437600	0.064200	0.878050	Uiso	?	Se
Se6	1.0	0.062400	0.189180	0.898880	Uiso	?	Se
Se7	1.0	0.062400	0.439200	0.940550	Uiso	?	Se
Se8	1.0	0.820500	0.687480	0.739580	Uiso	?	Se
Se9	1.0	0.679500	0.562500	0.718750	Uiso	?	Se
Se10	1.0	0.320500	0.187480	0.739580	Uiso	?	Se
Se11	1.0	0.179500	0.062500	0.718750	Uiso	?	Se
Se12	1.0	0.303200	0.687480	0.739580	Uiso	?	Se
Se13	1.0	0.196800	0.562500	0.718750	Uiso	?	Se
Se14	1.0	0.803200	0.187480	0.739580	Uiso	?	Se
Se15	1.0	0.696800	0.062500	0.718750	Uiso	?	Se
Se16	1.0	0.437600	0.060820	0.726120	Uiso	?	Se
Se17	1.0	0.062400	0.185800	0.746950	Uiso	?	Se
Se18	1.0	0.937600	0.560820	0.726120	Uiso	?	Se
Se19	1.0	0.562400	0.685800	0.746950	Uiso	?	Se
Se20	1.0	0.563000	0.437680	0.773730	Uiso	?	Se
Se21	1.0	0.437000	0.312700	0.752900	Uiso	?	Se
Se22	1.0	0.063000	0.937680	0.773730	Uiso	?	Se
Se23	1.0	0.063000	0.437320	0.788770	Uiso	?	Se
Se24	1.0	0.937000	0.812700	0.752900	Uiso	?	Se
Se25	1.0	0.811800	0.428880	0.781280	Uiso	?	Se
Se26	1.0	0.811800	0.946120	0.781220	Uiso	?	Se
Se27	1.0	0.188200	0.821080	0.760380	Uiso	?	Se
Se28	1.0	0.188200	0.303900	0.760450	Uiso	?	Se
Se29	1.0	0.311800	0.928880	0.781280	Uiso	?	Se
Se30	1.0	0.311800	0.446120	0.781220	Uiso	?	Se
Se31	1.0	0.688200	0.321080	0.760380	Uiso	?	Se
Se32	1.0	0.688200	0.803900	0.760450	Uiso	?	Se
Se33	1.0	0.437000	0.562660	0.794560	Uiso	?	Se
Se34	1.0	0.937000	0.562300	0.809600	Uiso	?	Se
Se35	1.0	0.188200	0.553920	0.802120	Uiso	?	Se
Se36	1.0	0.688200	0.571100	0.802050	Uiso	?	Se
Se37	1.0	0.179500	0.812500	0.843750	Uiso	?	Se

Se38	1.0	0.696800	0.812500	0.843750	Uiso	?	Se
Se39	1.0	0.313000	0.687300	0.872100	Uiso	?	Se
Se40	1.0	0.061800	0.678920	0.864620	Uiso	?	Se
Se41	1.0	0.561800	0.696100	0.864550	Uiso	?	Se
Se42	1.0	0.562400	0.439220	0.857220	Uiso	?	Se
Se43	1.0	0.437600	0.810820	0.851120	Uiso	?	Se
Se44	1.0	0.320500	0.187500	0.906250	Uiso	?	Se
Se45	1.0	0.179500	0.062520	0.885420	Uiso	?	Se
Se46	1.0	0.820500	0.687500	0.906250	Uiso	?	Se
Se47	1.0	0.803200	0.187500	0.906250	Uiso	?	Se
Se48	1.0	0.696800	0.062520	0.885420	Uiso	?	Se
Se49	1.0	0.303200	0.687500	0.906250	Uiso	?	Se
Se50	1.0	0.813000	0.437320	0.913770	Uiso	?	Se
Se51	1.0	0.687000	0.312340	0.892940	Uiso	?	Se
Se52	1.0	0.313000	0.437680	0.898730	Uiso	?	Se
Se53	1.0	0.187000	0.812340	0.892940	Uiso	?	Se
Se54	1.0	0.187000	0.312700	0.877900	Uiso	?	Se
Se55	1.0	0.061800	0.446120	0.906220	Uiso	?	Se
Se56	1.0	0.438200	0.321080	0.885380	Uiso	?	Se
Se57	1.0	0.561800	0.428880	0.906280	Uiso	?	Se
Se58	1.0	0.938200	0.303900	0.885450	Uiso	?	Se
Se59	1.0	0.562400	0.685820	0.913620	Uiso	?	Se
Se60	1.0	0.562400	0.689180	0.898880	Uiso	?	Se
Se61	1.0	0.437600	0.060780	0.892780	Uiso	?	Se
Se62	1.0	0.062400	0.185820	0.913620	Uiso	?	Se
Se63	1.0	0.320500	0.437520	0.947920	Uiso	?	Se
Se64	1.0	0.820500	0.937520	0.947920	Uiso	?	Se
Se65	1.0	0.679500	0.812480	0.927080	Uiso	?	Se
Se66	1.0	0.803200	0.437520	0.947920	Uiso	?	Se
Se67	1.0	0.303200	0.937520	0.947920	Uiso	?	Se
Se68	1.0	0.196800	0.812480	0.927080	Uiso	?	Se
Se69	1.0	0.813000	0.187700	0.940400	Uiso	?	Se
Se70	1.0	0.687000	0.562300	0.934600	Uiso	?	Se
Se71	1.0	0.687000	0.062660	0.919560	Uiso	?	Se
Se72	1.0	0.313000	0.187340	0.955440	Uiso	?	Se
Se73	1.0	0.187000	0.062300	0.934600	Uiso	?	Se
Se74	1.0	0.187000	0.562660	0.919560	Uiso	?	Se
Se75	1.0	0.061800	0.178900	0.947950	Uiso	?	Se
Se76	1.0	0.438200	0.571100	0.927050	Uiso	?	Se
Se77	1.0	0.438200	0.053920	0.927120	Uiso	?	Se
Se78	1.0	0.561800	0.196080	0.947880	Uiso	?	Se
Se79	1.0	0.938200	0.071100	0.927050	Uiso	?	Se
Se80	1.0	0.938200	0.553920	0.927120	Uiso	?	Se
Se81	1.0	0.937600	0.814220	0.919720	Uiso	?	Se
Se82	1.0	0.937600	0.810800	0.934450	Uiso	?	Se
Se83	1.0	0.562400	0.935780	0.955280	Uiso	?	Se
Se84	1.0	0.562400	0.939200	0.940550	Uiso	?	Se
Se85	1.0	0.062400	0.435780	0.955280	Uiso	?	Se
Se86	1.0	0.320500	0.687480	0.989580	Uiso	?	Se
Se87	1.0	0.179500	0.562500	0.968750	Uiso	?	Se
Se88	1.0	0.820500	0.187480	0.989580	Uiso	?	Se
Se89	1.0	0.679500	0.062500	0.968750	Uiso	?	Se
Se90	1.0	0.803200	0.687480	0.989580	Uiso	?	Se

Se91	1.0	0.696800	0.562500	0.968750	Uiso	?	Se
Se92	1.0	0.303200	0.187480	0.989580	Uiso	?	Se
Se93	1.0	0.196800	0.062500	0.968750	Uiso	?	Se
Se94	1.0	0.813000	0.437660	0.982060	Uiso	?	Se
Se95	1.0	0.813000	0.937300	0.997100	Uiso	?	Se
Se96	1.0	0.687000	0.812320	0.976270	Uiso	?	Se
Se97	1.0	0.687000	0.312680	0.961230	Uiso	?	Se
Se98	1.0	0.313000	0.937660	0.982060	Uiso	?	Se
Se99	1.0	0.313000	0.437300	0.997100	Uiso	?	Se
Se100	1.0	0.187000	0.312320	0.976270	Uiso	?	Se
Se101	1.0	0.061800	0.428920	0.989620	Uiso	?	Se
Se102	1.0	0.061800	0.946100	0.989550	Uiso	?	Se
Se103	1.0	0.438200	0.821120	0.968720	Uiso	?	Se
Se104	1.0	0.438200	0.303880	0.968780	Uiso	?	Se
Se105	1.0	0.561800	0.928920	0.989620	Uiso	?	Se
Se106	1.0	0.561800	0.446100	0.989550	Uiso	?	Se
Se107	1.0	0.938200	0.321120	0.968720	Uiso	?	Se
Se108	1.0	0.938200	0.803880	0.968780	Uiso	?	Se
Se109	1.0	0.937600	0.064180	0.961380	Uiso	?	Se
Se110	1.0	0.937600	0.060820	0.976120	Uiso	?	Se
Se111	1.0	0.562400	0.185800	0.996950	Uiso	?	Se
Se112	1.0	0.437600	0.564180	0.961380	Uiso	?	Se
Se113	1.0	0.437600	0.560820	0.976120	Uiso	?	Se
Se114	1.0	0.062400	0.685800	0.996950	Uiso	?	Se
Se115	1.0	0.062400	0.689220	0.982220	Uiso	?	Se
Se116	1.0	0.313000	0.937680	0.648730	Uiso	?	Se
Se117	1.0	0.813000	0.937320	0.663770	Uiso	?	Se
Se118	1.0	0.561800	0.928880	0.656280	Uiso	?	Se
Se119	1.0	0.061800	0.946120	0.656220	Uiso	?	Se
Se120	1.0	0.437600	0.064180	0.711380	Uiso	?	Se
Se121	1.0	0.062400	0.189220	0.732220	Uiso	?	Se
Se122	1.0	0.937000	0.312340	0.767940	Uiso	?	Se
Se123	1.0	0.570500	0.437520	0.822920	Uiso	?	Se
Se124	1.0	0.053200	0.437520	0.822920	Uiso	?	Se
Se125	1.0	0.312400	0.435780	0.830280	Uiso	?	Se
Se126	1.0	0.312400	0.439200	0.815550	Uiso	?	Se
Se127	1.0	0.820500	0.437480	0.864580	Uiso	?	Se
Se128	1.0	0.679500	0.312500	0.843750	Uiso	?	Se
Se129	1.0	0.303200	0.437480	0.864580	Uiso	?	Se
Se130	1.0	0.196800	0.312500	0.843750	Uiso	?	Se
Se131	1.0	0.937600	0.314180	0.836380	Uiso	?	Se
Se132	1.0	0.937600	0.310820	0.851120	Uiso	?	Se
Se133	1.0	0.562400	0.435800	0.871950	Uiso	?	Se
Se134	1.0	0.187000	0.812680	0.961230	Uiso	?	Se
Se135	1.0	0.187000	0.562300	0.684600	Uiso	?	Se
Se136	1.0	0.687000	0.562660	0.669560	Uiso	?	Se
Se137	1.0	0.938200	0.571100	0.677050	Uiso	?	Se
Se138	1.0	0.438200	0.553920	0.677120	Uiso	?	Se
Se139	1.0	0.562400	0.689220	0.732220	Uiso	?	Se
Se140	1.0	0.187600	0.814220	0.794720	Uiso	?	Se
Se141	1.0	0.812400	0.939200	0.815550	Uiso	?	Se
Se142	1.0	0.070500	0.937520	0.822920	Uiso	?	Se
Se143	1.0	0.929500	0.812480	0.802080	Uiso	?	Se

Se144	1.0	0.553200	0.937520	0.822920	Uiso	?	Se
Se145	1.0	0.446800	0.812480	0.802080	Uiso	?	Se
Se146	1.0	0.187600	0.810800	0.809450	Uiso	?	Se
Se147	1.0	0.812400	0.935780	0.830280	Uiso	?	Se
Se148	1.0	0.813000	0.687660	0.857060	Uiso	?	Se
Se149	1.0	0.687000	0.812700	0.877900	Uiso	?	Se
Se150	1.0	0.438200	0.803900	0.885450	Uiso	?	Se
Se151	1.0	0.938200	0.821080	0.885380	Uiso	?	Se
Se152	1.0	0.562400	0.189220	0.982220	Uiso	?	Se
Se153	1.0	0.062400	0.439200	0.440550	Uiso	?	Se
Se154	1.0	0.320500	0.437520	0.447920	Uiso	?	Se
Se155	1.0	0.803200	0.437520	0.447920	Uiso	?	Se
Se156	1.0	0.062400	0.435780	0.455280	Uiso	?	Se
Se157	1.0	0.187600	0.060780	0.517780	Uiso	?	Se
Se158	1.0	0.063000	0.187340	0.580440	Uiso	?	Se
Se159	1.0	0.937000	0.062300	0.559600	Uiso	?	Se
Se160	1.0	0.563000	0.187700	0.565400	Uiso	?	Se
Se161	1.0	0.437000	0.062660	0.544560	Uiso	?	Se
Se162	1.0	0.311800	0.196080	0.572880	Uiso	?	Se
Se163	1.0	0.688200	0.071100	0.552050	Uiso	?	Se
Se164	1.0	0.811800	0.178900	0.572950	Uiso	?	Se
Se165	1.0	0.188200	0.053920	0.552120	Uiso	?	Se
Se166	1.0	0.937000	0.312320	0.601270	Uiso	?	Se
Se167	1.0	0.437000	0.312680	0.586230	Uiso	?	Se
Se168	1.0	0.688200	0.321120	0.593720	Uiso	?	Se
Se169	1.0	0.188200	0.303880	0.593780	Uiso	?	Se
Se170	1.0	0.312400	0.189220	0.607220	Uiso	?	Se
Se171	1.0	0.937600	0.064200	0.628050	Uiso	?	Se
Se172	1.0	0.437600	0.314220	0.919720	Uiso	?	Se
Se173	1.0	0.679500	0.062520	0.635420	Uiso	?	Se
Se174	1.0	0.196800	0.062520	0.635420	Uiso	?	Se
Se175	1.0	0.813000	0.187300	0.872100	Uiso	?	Se
Se176	1.0	0.687000	0.062320	0.851270	Uiso	?	Se
Se177	1.0	0.313000	0.187660	0.857060	Uiso	?	Se
Se178	1.0	0.187000	0.062680	0.836230	Uiso	?	Se
Se179	1.0	0.061800	0.196100	0.864550	Uiso	?	Se
Se180	1.0	0.438200	0.071120	0.843720	Uiso	?	Se
Se181	1.0	0.561800	0.178920	0.864620	Uiso	?	Se
Se182	1.0	0.938200	0.053880	0.843780	Uiso	?	Se
Se183	1.0	0.179500	0.312480	0.927080	Uiso	?	Se
Se184	1.0	0.696800	0.312480	0.927080	Uiso	?	Se
Se185	1.0	0.437600	0.310800	0.934450	Uiso	?	Se
Se186	1.0	0.570500	0.187480	0.614580	Uiso	?	Se
Se187	1.0	0.053200	0.187480	0.614580	Uiso	?	Se
Se188	1.0	0.312400	0.185800	0.621950	Uiso	?	Se
Se189	1.0	0.937600	0.060780	0.642780	Uiso	?	Se
Se190	1.0	0.313000	0.187700	0.690400	Uiso	?	Se
Se191	1.0	0.187000	0.062660	0.669560	Uiso	?	Se
Se192	1.0	0.813000	0.187340	0.705440	Uiso	?	Se
Se193	1.0	0.687000	0.062300	0.684600	Uiso	?	Se
Se194	1.0	0.561800	0.178900	0.697950	Uiso	?	Se
Se195	1.0	0.938200	0.053920	0.677120	Uiso	?	Se
Se196	1.0	0.061800	0.196080	0.697880	Uiso	?	Se

Se197	1.0	0.438200	0.071100	0.677050	Uiso	?	Se
Se198	1.0	0.429500	0.312480	0.802080	Uiso	?	Se
Se199	1.0	0.946800	0.312480	0.802080	Uiso	?	Se
Se200	1.0	0.687600	0.314220	0.794720	Uiso	?	Se
Se201	1.0	0.687600	0.310800	0.809450	Uiso	?	Se
Se202	1.0	0.812400	0.185820	0.538620	Uiso	?	Se
Se203	1.0	0.563000	0.187300	0.497100	Uiso	?	Se
Se204	1.0	0.437000	0.062320	0.476270	Uiso	?	Se
Se205	1.0	0.311800	0.178920	0.489620	Uiso	?	Se
Se206	1.0	0.688200	0.053880	0.468780	Uiso	?	Se
Se207	1.0	0.811800	0.196100	0.489550	Uiso	?	Se
Se208	1.0	0.188200	0.071120	0.468720	Uiso	?	Se
Se209	1.0	0.070500	0.187500	0.531250	Uiso	?	Se
Se210	1.0	0.929500	0.062520	0.510420	Uiso	?	Se
Se211	1.0	0.553200	0.187500	0.531250	Uiso	?	Se
Se212	1.0	0.446800	0.062520	0.510420	Uiso	?	Se
Se213	1.0	0.187600	0.064200	0.503050	Uiso	?	Se
Se214	1.0	0.812400	0.189180	0.523880	Uiso	?	Se
Se215	1.0	0.437600	0.314220	0.419720	Uiso	?	Se
Se216	1.0	0.179500	0.312480	0.427080	Uiso	?	Se
Se217	1.0	0.696800	0.312480	0.427080	Uiso	?	Se
Se218	1.0	0.437600	0.310800	0.434450	Uiso	?	Se
Se219	1.0	0.063000	0.187660	0.482060	Uiso	?	Se
Se220	1.0	0.937000	0.062680	0.461230	Uiso	?	Se
Se221	1.0	0.320500	0.937520	0.697920	Uiso	?	Se
Se222	1.0	0.179500	0.812480	0.677080	Uiso	?	Se
Se223	1.0	0.803200	0.937520	0.697920	Uiso	?	Se
Se224	1.0	0.696800	0.812480	0.677080	Uiso	?	Se
Se225	1.0	0.437600	0.814220	0.669720	Uiso	?	Se
Se226	1.0	0.437600	0.810800	0.684450	Uiso	?	Se
Se227	1.0	0.062400	0.935780	0.705280	Uiso	?	Se
Se228	1.0	0.062400	0.939200	0.690550	Uiso	?	Se
Se229	1.0	0.187600	0.560780	0.767780	Uiso	?	Se
Se230	1.0	0.563000	0.687700	0.815400	Uiso	?	Se
Se231	1.0	0.063000	0.687340	0.830440	Uiso	?	Se
Se232	1.0	0.811800	0.678900	0.822950	Uiso	?	Se
Se233	1.0	0.311800	0.696080	0.822880	Uiso	?	Se
Se234	1.0	0.687000	0.562680	0.836230	Uiso	?	Se
Se235	1.0	0.187000	0.562320	0.851270	Uiso	?	Se
Se236	1.0	0.438200	0.553880	0.843780	Uiso	?	Se
Se237	1.0	0.938200	0.571120	0.843720	Uiso	?	Se
Se238	1.0	0.679500	0.562520	0.885420	Uiso	?	Se
Se239	1.0	0.196800	0.562520	0.885420	Uiso	?	Se
Se240	1.0	0.937600	0.564200	0.878050	Uiso	?	Se
Se241	1.0	0.813000	0.687340	0.955440	Uiso	?	Se
Se242	1.0	0.313000	0.687700	0.940400	Uiso	?	Se
Se243	1.0	0.061800	0.696080	0.947880	Uiso	?	Se
Se244	1.0	0.561800	0.678900	0.947950	Uiso	?	Se
Se245	1.0	0.687600	0.814220	0.544720	Uiso	?	Se
Se246	1.0	0.312400	0.939200	0.565550	Uiso	?	Se
Se247	1.0	0.570500	0.937520	0.572920	Uiso	?	Se
Se248	1.0	0.429500	0.812480	0.552080	Uiso	?	Se
Se249	1.0	0.053200	0.937520	0.572920	Uiso	?	Se

Se250	1.0	0.946800	0.812480	0.552080	Uiso	?	Se
Se251	1.0	0.687600	0.810800	0.559450	Uiso	?	Se
Se252	1.0	0.312400	0.935780	0.580280	Uiso	?	Se
Se253	1.0	0.063000	0.937660	0.607060	Uiso	?	Se
Se254	1.0	0.937000	0.812680	0.586230	Uiso	?	Se
Se255	1.0	0.563000	0.937300	0.622100	Uiso	?	Se
Se256	1.0	0.437000	0.812320	0.601270	Uiso	?	Se
Se257	1.0	0.311800	0.928920	0.614620	Uiso	?	Se
Se258	1.0	0.688200	0.803880	0.593780	Uiso	?	Se
Se259	1.0	0.811800	0.946100	0.614550	Uiso	?	Se
Se260	1.0	0.188200	0.821120	0.593720	Uiso	?	Se
Se261	1.0	0.187000	0.812700	0.627900	Uiso	?	Se
Se262	1.0	0.687000	0.812340	0.642940	Uiso	?	Se
Se263	1.0	0.938200	0.803900	0.635450	Uiso	?	Se
Se264	1.0	0.438200	0.821080	0.635380	Uiso	?	Se
Se265	1.0	0.937600	0.560780	0.892780	Uiso	?	Se
Se266	1.0	0.313000	0.687340	0.705440	Uiso	?	Se
Se267	1.0	0.813000	0.687700	0.690400	Uiso	?	Se
Se268	1.0	0.561800	0.696080	0.697880	Uiso	?	Se
Se269	1.0	0.061800	0.678900	0.697950	Uiso	?	Se
Se270	1.0	0.313000	0.937300	0.747100	Uiso	?	Se
Se271	1.0	0.187000	0.812320	0.726270	Uiso	?	Se
Se272	1.0	0.561800	0.946100	0.739550	Uiso	?	Se
Se273	1.0	0.938200	0.821120	0.718720	Uiso	?	Se
Se274	1.0	0.061800	0.928920	0.739620	Uiso	?	Se
Se275	1.0	0.438200	0.803880	0.718780	Uiso	?	Se
Se276	1.0	0.187600	0.564200	0.753050	Uiso	?	Se
Se277	1.0	0.812400	0.689180	0.773880	Uiso	?	Se
Se278	1.0	0.320500	0.687500	0.656250	Uiso	?	Se
Se279	1.0	0.179500	0.562520	0.635420	Uiso	?	Se
Se280	1.0	0.803200	0.687500	0.656250	Uiso	?	Se
Se281	1.0	0.696800	0.562520	0.635420	Uiso	?	Se
Se282	1.0	0.437600	0.564200	0.628050	Uiso	?	Se
Se283	1.0	0.437600	0.560780	0.642780	Uiso	?	Se
Se284	1.0	0.062400	0.685820	0.663620	Uiso	?	Se
Se285	1.0	0.062400	0.689180	0.648880	Uiso	?	Se
Se286	1.0	0.813000	0.937660	0.732060	Uiso	?	Se
Se287	1.0	0.687000	0.812680	0.711230	Uiso	?	Se
Se288	1.0	0.070500	0.687500	0.781250	Uiso	?	Se
Se289	1.0	0.929500	0.562520	0.760420	Uiso	?	Se
Se290	1.0	0.553200	0.687500	0.781250	Uiso	?	Se
Se291	1.0	0.446800	0.562520	0.760420	Uiso	?	Se
Se292	1.0	0.812400	0.685820	0.788620	Uiso	?	Se
Se293	1.0	0.070500	0.937480	0.489580	Uiso	?	Se
Se294	1.0	0.929500	0.812500	0.468750	Uiso	?	Se
Se295	1.0	0.553200	0.937480	0.489580	Uiso	?	Se
Se296	1.0	0.446800	0.812500	0.468750	Uiso	?	Se
Se297	1.0	0.187600	0.810820	0.476120	Uiso	?	Se
Se298	1.0	0.812400	0.935800	0.496950	Uiso	?	Se
Se299	1.0	0.063000	0.937320	0.538770	Uiso	?	Se
Se300	1.0	0.563000	0.937680	0.523730	Uiso	?	Se
Se301	1.0	0.437000	0.812700	0.502900	Uiso	?	Se
Se302	1.0	0.311800	0.946120	0.531220	Uiso	?	Se

Se303	1.0	0.688200	0.821080	0.510380	Uiso	?	Se
Se304	1.0	0.811800	0.928880	0.531280	Uiso	?	Se
Se305	1.0	0.188200	0.803900	0.510450	Uiso	?	Se
Se306	1.0	0.063000	0.187700	0.315400	Uiso	?	Se
Se307	1.0	0.937000	0.062660	0.294560	Uiso	?	Se
Se308	1.0	0.563000	0.187340	0.330440	Uiso	?	Se
Se309	1.0	0.437000	0.062300	0.309600	Uiso	?	Se
Se310	1.0	0.311800	0.178900	0.322950	Uiso	?	Se
Se311	1.0	0.688200	0.053920	0.302120	Uiso	?	Se
Se312	1.0	0.811800	0.196080	0.322880	Uiso	?	Se
Se313	1.0	0.188200	0.071100	0.302050	Uiso	?	Se
Se314	1.0	0.187000	0.062680	0.336230	Uiso	?	Se
Se315	1.0	0.813000	0.187300	0.372100	Uiso	?	Se
Se316	1.0	0.687000	0.062320	0.351270	Uiso	?	Se
Se317	1.0	0.561800	0.178920	0.364620	Uiso	?	Se
Se318	1.0	0.938200	0.053880	0.343780	Uiso	?	Se
Se319	1.0	0.061800	0.196100	0.364550	Uiso	?	Se
Se320	1.0	0.438200	0.071120	0.343720	Uiso	?	Se
Se321	1.0	0.937000	0.062340	0.392940	Uiso	?	Se
Se322	1.0	0.187600	0.814180	0.461380	Uiso	?	Se
Se323	1.0	0.187000	0.062340	0.267940	Uiso	?	Se
Se324	1.0	0.937000	0.812340	0.517940	Uiso	?	Se
Se325	1.0	0.687600	0.064180	0.586380	Uiso	?	Se
Se326	1.0	0.429500	0.062500	0.593750	Uiso	?	Se
Se327	1.0	0.946800	0.062500	0.593750	Uiso	?	Se
Se328	1.0	0.687600	0.060820	0.601120	Uiso	?	Se
Se329	1.0	0.313000	0.187320	0.288770	Uiso	?	Se
Se330	1.0	0.320500	0.187480	0.239580	Uiso	?	Se
Se331	1.0	0.179500	0.062500	0.218750	Uiso	?	Se
Se332	1.0	0.803200	0.187480	0.239580	Uiso	?	Se
Se333	1.0	0.696800	0.062500	0.218750	Uiso	?	Se
Se334	1.0	0.437600	0.060820	0.226120	Uiso	?	Se
Se335	1.0	0.062400	0.185800	0.246950	Uiso	?	Se
Se336	1.0	0.813000	0.187680	0.273730	Uiso	?	Se
Se337	1.0	0.687000	0.062700	0.252900	Uiso	?	Se
Se338	1.0	0.061800	0.178880	0.281280	Uiso	?	Se
Se339	1.0	0.438200	0.053900	0.260450	Uiso	?	Se
Se340	1.0	0.561800	0.196120	0.281220	Uiso	?	Se
Se341	1.0	0.938200	0.071080	0.260380	Uiso	?	Se
Se342	1.0	0.313000	0.187660	0.357060	Uiso	?	Se
Se343	1.0	0.563000	0.187680	0.398730	Uiso	?	Se
Se344	1.0	0.437000	0.062700	0.377900	Uiso	?	Se
Se345	1.0	0.063000	0.187320	0.413770	Uiso	?	Se
Se346	1.0	0.811800	0.178880	0.406280	Uiso	?	Se
Se347	1.0	0.188200	0.053900	0.385450	Uiso	?	Se
Se348	1.0	0.311800	0.196120	0.406220	Uiso	?	Se
Se349	1.0	0.688200	0.071080	0.385380	Uiso	?	Se
Se350	1.0	0.813000	0.187700	0.440400	Uiso	?	Se
Se351	1.0	0.687000	0.062660	0.419560	Uiso	?	Se
Se352	1.0	0.313000	0.187340	0.455440	Uiso	?	Se
Se353	1.0	0.187000	0.062300	0.434600	Uiso	?	Se
Se354	1.0	0.061800	0.178900	0.447950	Uiso	?	Se
Se355	1.0	0.438200	0.053920	0.427120	Uiso	?	Se

Se356	1.0	0.561800	0.196080	0.447880	Uiso	?	Se
Se357	1.0	0.938200	0.071100	0.427050	Uiso	?	Se
Se358	1.0	0.812400	0.939220	0.482220	Uiso	?	Se
Se359	1.0	0.429500	0.062500	0.093750	Uiso	?	Se
Se360	1.0	0.946800	0.062500	0.093750	Uiso	?	Se
Se361	1.0	0.687600	0.064180	0.086380	Uiso	?	Se
Se362	1.0	0.687600	0.060820	0.101120	Uiso	?	Se
Se363	1.0	0.437000	0.062340	0.142940	Uiso	?	Se
Se364	1.0	0.937000	0.062700	0.127900	Uiso	?	Se
Se365	1.0	0.188200	0.071080	0.135380	Uiso	?	Se
Se366	1.0	0.688200	0.053900	0.135450	Uiso	?	Se
Se367	1.0	0.813000	0.187340	0.205440	Uiso	?	Se
Se368	1.0	0.687000	0.062300	0.184600	Uiso	?	Se
Se369	1.0	0.313000	0.187700	0.190400	Uiso	?	Se
Se370	1.0	0.187000	0.062660	0.169560	Uiso	?	Se
Se371	1.0	0.061800	0.196080	0.197880	Uiso	?	Se
Se372	1.0	0.438200	0.071100	0.177050	Uiso	?	Se
Se373	1.0	0.561800	0.178900	0.197950	Uiso	?	Se
Se374	1.0	0.938200	0.053920	0.177120	Uiso	?	Se
Se375	1.0	0.437600	0.064180	0.211380	Uiso	?	Se
Se376	1.0	0.062400	0.189220	0.232220	Uiso	?	Se
Se377	1.0	0.937600	0.314180	0.336380	Uiso	?	Se
Se378	1.0	0.187600	0.314200	0.378050	Uiso	?	Se
Se379	1.0	0.679500	0.312500	0.343750	Uiso	?	Se
Se380	1.0	0.196800	0.312500	0.343750	Uiso	?	Se
Se381	1.0	0.937600	0.310820	0.351120	Uiso	?	Se
Se382	1.0	0.929500	0.312520	0.385420	Uiso	?	Se
Se383	1.0	0.446800	0.312520	0.385420	Uiso	?	Se
Se384	1.0	0.187600	0.310780	0.392780	Uiso	?	Se
Se385	1.0	0.187000	0.312340	0.642940	Uiso	?	Se
Se386	1.0	0.562400	0.439200	0.690550	Uiso	?	Se
Se387	1.0	0.062400	0.939220	0.857220	Uiso	?	Se
Se388	1.0	0.820500	0.437520	0.697920	Uiso	?	Se
Se389	1.0	0.303200	0.437520	0.697920	Uiso	?	Se
Se390	1.0	0.562400	0.435780	0.705280	Uiso	?	Se
Se391	1.0	0.563000	0.187340	0.830440	Uiso	?	Se
Se392	1.0	0.437000	0.062300	0.809600	Uiso	?	Se
Se393	1.0	0.063000	0.187700	0.815400	Uiso	?	Se
Se394	1.0	0.937000	0.062660	0.794560	Uiso	?	Se
Se395	1.0	0.811800	0.196080	0.822880	Uiso	?	Se
Se396	1.0	0.188200	0.071100	0.802050	Uiso	?	Se
Se397	1.0	0.311800	0.178900	0.822950	Uiso	?	Se
Se398	1.0	0.688200	0.053920	0.802120	Uiso	?	Se
Se399	1.0	0.320500	0.937480	0.864580	Uiso	?	Se
Se400	1.0	0.803200	0.937480	0.864580	Uiso	?	Se
Se401	1.0	0.062400	0.935800	0.871950	Uiso	?	Se
Se402	1.0	0.687000	0.562300	0.434600	Uiso	?	Se
Se403	1.0	0.187000	0.562660	0.419560	Uiso	?	Se
Se404	1.0	0.438200	0.571100	0.427050	Uiso	?	Se
Se405	1.0	0.938200	0.553920	0.427120	Uiso	?	Se
Se406	1.0	0.313000	0.437320	0.663770	Uiso	?	Se
Se407	1.0	0.813000	0.437680	0.648730	Uiso	?	Se
Se408	1.0	0.687000	0.312700	0.627900	Uiso	?	Se

Se409	1.0	0.561800	0.446120	0.656220	Uiso	?	Se
Se410	1.0	0.938200	0.321080	0.635380	Uiso	?	Se
Se411	1.0	0.061800	0.428880	0.656280	Uiso	?	Se
Se412	1.0	0.438200	0.303900	0.635450	Uiso	?	Se
Se413	1.0	0.563000	0.437320	0.538770	Uiso	?	Se
Se414	1.0	0.437000	0.312340	0.517940	Uiso	?	Se
Se415	1.0	0.070500	0.437520	0.572920	Uiso	?	Se
Se416	1.0	0.553200	0.437520	0.572920	Uiso	?	Se
Se417	1.0	0.812400	0.435780	0.580280	Uiso	?	Se
Se418	1.0	0.812400	0.439200	0.565550	Uiso	?	Se
Se419	1.0	0.070500	0.687480	0.614580	Uiso	?	Se
Se420	1.0	0.929500	0.562500	0.593750	Uiso	?	Se
Se421	1.0	0.553200	0.687480	0.614580	Uiso	?	Se
Se422	1.0	0.446800	0.562500	0.593750	Uiso	?	Se
Se423	1.0	0.187600	0.564180	0.586380	Uiso	?	Se
Se424	1.0	0.187600	0.560820	0.601120	Uiso	?	Se
Se425	1.0	0.812400	0.685800	0.621950	Uiso	?	Se
Se426	1.0	0.812400	0.689220	0.607220	Uiso	?	Se
Se427	1.0	0.813000	0.937680	0.898730	Uiso	?	Se
Se428	1.0	0.313000	0.937320	0.913770	Uiso	?	Se
Se429	1.0	0.061800	0.928880	0.906280	Uiso	?	Se
Se430	1.0	0.561800	0.946120	0.906220	Uiso	?	Se
Se431	1.0	0.563000	0.687320	0.413770	Uiso	?	Se
Se432	1.0	0.437000	0.562340	0.392940	Uiso	?	Se
Se433	1.0	0.063000	0.687680	0.398730	Uiso	?	Se
Se434	1.0	0.937000	0.562700	0.377900	Uiso	?	Se
Se435	1.0	0.811800	0.696120	0.406220	Uiso	?	Se
Se436	1.0	0.188200	0.571080	0.385380	Uiso	?	Se
Se437	1.0	0.311800	0.678880	0.406280	Uiso	?	Se
Se438	1.0	0.688200	0.553900	0.385450	Uiso	?	Se
Se439	1.0	0.687600	0.314180	0.461380	Uiso	?	Se
Se440	1.0	0.312400	0.439220	0.482220	Uiso	?	Se
Se441	1.0	0.570500	0.437480	0.489580	Uiso	?	Se
Se442	1.0	0.429500	0.312500	0.468750	Uiso	?	Se
Se443	1.0	0.053200	0.437480	0.489580	Uiso	?	Se
Se444	1.0	0.946800	0.312500	0.468750	Uiso	?	Se
Se445	1.0	0.687600	0.310820	0.476120	Uiso	?	Se
Se446	1.0	0.312400	0.435800	0.496950	Uiso	?	Se
Se447	1.0	0.063000	0.437680	0.523730	Uiso	?	Se
Se448	1.0	0.937000	0.312700	0.502900	Uiso	?	Se
Se449	1.0	0.311800	0.428880	0.531280	Uiso	?	Se
Se450	1.0	0.688200	0.303900	0.510450	Uiso	?	Se
Se451	1.0	0.811800	0.446120	0.531220	Uiso	?	Se
Se452	1.0	0.188200	0.321080	0.510380	Uiso	?	Se
Se453	1.0	0.937000	0.562660	0.544560	Uiso	?	Se
Se454	1.0	0.437000	0.562300	0.559600	Uiso	?	Se
Se455	1.0	0.688200	0.553920	0.552120	Uiso	?	Se
Se456	1.0	0.188200	0.571100	0.552050	Uiso	?	Se
Se457	1.0	0.063000	0.437300	0.622100	Uiso	?	Se
Se458	1.0	0.311800	0.446100	0.614550	Uiso	?	Se
Se459	1.0	0.811800	0.428920	0.614620	Uiso	?	Se
Se460	1.0	0.562400	0.189180	0.648880	Uiso	?	Se
Se461	1.0	0.937600	0.314220	0.669720	Uiso	?	Se

Se462	1.0	0.820500	0.187500	0.656250	Uiso	?	Se
Se463	1.0	0.303200	0.187500	0.656250	Uiso	?	Se
Se464	1.0	0.562400	0.185820	0.663620	Uiso	?	Se
Se465	1.0	0.679500	0.312480	0.677080	Uiso	?	Se
Se466	1.0	0.196800	0.312480	0.677080	Uiso	?	Se
Se467	1.0	0.937600	0.310800	0.684450	Uiso	?	Se
Se468	1.0	0.313000	0.437660	0.732060	Uiso	?	Se
Se469	1.0	0.687600	0.060780	0.767780	Uiso	?	Se
Se470	1.0	0.312400	0.185820	0.788620	Uiso	?	Se
Se471	1.0	0.187000	0.312680	0.711230	Uiso	?	Se
Se472	1.0	0.813000	0.437300	0.747100	Uiso	?	Se
Se473	1.0	0.687000	0.312320	0.726270	Uiso	?	Se
Se474	1.0	0.561800	0.428920	0.739620	Uiso	?	Se
Se475	1.0	0.938200	0.303880	0.718780	Uiso	?	Se
Se476	1.0	0.061800	0.446100	0.739550	Uiso	?	Se
Se477	1.0	0.438200	0.321120	0.718720	Uiso	?	Se
Se478	1.0	0.570500	0.187500	0.781250	Uiso	?	Se
Se479	1.0	0.429500	0.062520	0.760420	Uiso	?	Se
Se480	1.0	0.053200	0.187500	0.781250	Uiso	?	Se
Se481	1.0	0.946800	0.062520	0.760420	Uiso	?	Se
Se482	1.0	0.687600	0.064200	0.753050	Uiso	?	Se
Se483	1.0	0.312400	0.189180	0.773880	Uiso	?	Se
Se484	1.0	0.563000	0.437660	0.607060	Uiso	?	Se
Se485	1.0	0.437600	0.310780	0.267780	Uiso	?	Se
Se486	1.0	0.062400	0.435820	0.288620	Uiso	?	Se
Se487	1.0	0.929500	0.312480	0.552080	Uiso	?	Se
Se488	1.0	0.446800	0.312480	0.552080	Uiso	?	Se
Se489	1.0	0.187600	0.314220	0.544720	Uiso	?	Se
Se490	1.0	0.187600	0.310800	0.559450	Uiso	?	Se
Se491	1.0	0.437000	0.062660	0.044560	Uiso	?	Se
Se492	1.0	0.937000	0.062300	0.059600	Uiso	?	Se
Se493	1.0	0.188200	0.053920	0.052120	Uiso	?	Se
Se494	1.0	0.688200	0.071100	0.052050	Uiso	?	Se
Se495	1.0	0.570500	0.187480	0.114580	Uiso	?	Se
Se496	1.0	0.053200	0.187480	0.114580	Uiso	?	Se
Se497	1.0	0.312400	0.185800	0.121950	Uiso	?	Se
Se498	1.0	0.312400	0.189220	0.107220	Uiso	?	Se
Se499	1.0	0.563000	0.187320	0.163770	Uiso	?	Se
Se500	1.0	0.063000	0.187680	0.148730	Uiso	?	Se
Se501	1.0	0.811800	0.196120	0.156220	Uiso	?	Se
Se502	1.0	0.311800	0.178880	0.156280	Uiso	?	Se
Se503	1.0	0.679500	0.312480	0.177080	Uiso	?	Se
Se504	1.0	0.196800	0.312480	0.177080	Uiso	?	Se
Se505	1.0	0.937600	0.314220	0.169720	Uiso	?	Se
Se506	1.0	0.937600	0.310800	0.184450	Uiso	?	Se
Se507	1.0	0.813000	0.437300	0.247100	Uiso	?	Se
Se508	1.0	0.687000	0.312320	0.226270	Uiso	?	Se
Se509	1.0	0.313000	0.437660	0.232060	Uiso	?	Se
Se510	1.0	0.187000	0.312680	0.211230	Uiso	?	Se
Se511	1.0	0.061800	0.446100	0.239550	Uiso	?	Se
Se512	1.0	0.438200	0.321120	0.218720	Uiso	?	Se
Se513	1.0	0.561800	0.428920	0.239620	Uiso	?	Se
Se514	1.0	0.938200	0.303880	0.218780	Uiso	?	Se

Se515	1.0	0.437600	0.314200	0.253050	Uiso	?	Se
Se516	1.0	0.062400	0.439180	0.273880	Uiso	?	Se
Se517	1.0	0.937000	0.562300	0.309600	Uiso	?	Se
Se518	1.0	0.437000	0.562660	0.294560	Uiso	?	Se
Se519	1.0	0.688200	0.571100	0.302050	Uiso	?	Se
Se520	1.0	0.188200	0.553920	0.302120	Uiso	?	Se
Se521	1.0	0.687600	0.314220	0.294720	Uiso	?	Se
Se522	1.0	0.312400	0.439200	0.315550	Uiso	?	Se
Se523	1.0	0.313000	0.687300	0.372100	Uiso	?	Se
Se524	1.0	0.187000	0.562320	0.351270	Uiso	?	Se
Se525	1.0	0.813000	0.687660	0.357060	Uiso	?	Se
Se526	1.0	0.687000	0.562680	0.336230	Uiso	?	Se
Se527	1.0	0.561800	0.696100	0.364550	Uiso	?	Se
Se528	1.0	0.938200	0.571120	0.343720	Uiso	?	Se
Se529	1.0	0.061800	0.678920	0.364620	Uiso	?	Se
Se530	1.0	0.438200	0.553880	0.343780	Uiso	?	Se
Se531	1.0	0.562400	0.439220	0.357220	Uiso	?	Se
Se532	1.0	0.812400	0.439180	0.398880	Uiso	?	Se
Se533	1.0	0.320500	0.437500	0.281250	Uiso	?	Se
Se534	1.0	0.179500	0.312520	0.260420	Uiso	?	Se
Se535	1.0	0.803200	0.437500	0.281250	Uiso	?	Se
Se536	1.0	0.696800	0.312520	0.260420	Uiso	?	Se
Se537	1.0	0.570500	0.437520	0.322920	Uiso	?	Se
Se538	1.0	0.429500	0.312480	0.302080	Uiso	?	Se
Se539	1.0	0.053200	0.437520	0.322920	Uiso	?	Se
Se540	1.0	0.946800	0.312480	0.302080	Uiso	?	Se
Se541	1.0	0.687600	0.310800	0.309450	Uiso	?	Se
Se542	1.0	0.312400	0.435780	0.330280	Uiso	?	Se
Se543	1.0	0.820500	0.437480	0.364580	Uiso	?	Se
Se544	1.0	0.303200	0.437480	0.364580	Uiso	?	Se
Se545	1.0	0.562400	0.435800	0.371950	Uiso	?	Se
Se546	1.0	0.070500	0.437500	0.406250	Uiso	?	Se
Se547	1.0	0.553200	0.437500	0.406250	Uiso	?	Se
Se548	1.0	0.812400	0.435820	0.413620	Uiso	?	Se
Se549	1.0	0.062400	0.939220	0.357220	Uiso	?	Se
Se550	1.0	0.570500	0.937500	0.406250	Uiso	?	Se
Se551	1.0	0.429500	0.812520	0.385420	Uiso	?	Se
Se552	1.0	0.053200	0.937500	0.406250	Uiso	?	Se
Se553	1.0	0.946800	0.812520	0.385420	Uiso	?	Se
Se554	1.0	0.687600	0.814200	0.378050	Uiso	?	Se
Se555	1.0	0.312400	0.935820	0.413620	Uiso	?	Se
Se556	1.0	0.312400	0.939180	0.398880	Uiso	?	Se
Se557	1.0	0.563000	0.687660	0.482060	Uiso	?	Se
Se558	1.0	0.320500	0.937480	0.364580	Uiso	?	Se
Se559	1.0	0.179500	0.812500	0.343750	Uiso	?	Se
Se560	1.0	0.803200	0.937480	0.364580	Uiso	?	Se
Se561	1.0	0.696800	0.812500	0.343750	Uiso	?	Se
Se562	1.0	0.437600	0.814180	0.336380	Uiso	?	Se
Se563	1.0	0.437600	0.810820	0.351120	Uiso	?	Se
Se564	1.0	0.062400	0.935800	0.371950	Uiso	?	Se
Se565	1.0	0.687600	0.810780	0.392780	Uiso	?	Se
Se566	1.0	0.813000	0.687340	0.455440	Uiso	?	Se
Se567	1.0	0.313000	0.687700	0.440400	Uiso	?	Se

Se568	1.0	0.061800	0.696080	0.447880	Uiso	?	Se
Se569	1.0	0.561800	0.678900	0.447950	Uiso	?	Se
Se570	1.0	0.063000	0.687300	0.497100	Uiso	?	Se
Se571	1.0	0.937000	0.562320	0.476270	Uiso	?	Se
Se572	1.0	0.437000	0.562680	0.461230	Uiso	?	Se
Se573	1.0	0.311800	0.696100	0.489550	Uiso	?	Se
Se574	1.0	0.688200	0.571120	0.468720	Uiso	?	Se
Se575	1.0	0.811800	0.678920	0.489620	Uiso	?	Se
Se576	1.0	0.188200	0.553880	0.468780	Uiso	?	Se
Se577	1.0	0.687600	0.564200	0.503050	Uiso	?	Se
Se578	1.0	0.312400	0.689180	0.523880	Uiso	?	Se
Se579	1.0	0.570500	0.687500	0.531250	Uiso	?	Se
Se580	1.0	0.429500	0.562520	0.510420	Uiso	?	Se
Se581	1.0	0.053200	0.687500	0.531250	Uiso	?	Se
Se582	1.0	0.946800	0.562520	0.510420	Uiso	?	Se
Se583	1.0	0.687600	0.560780	0.517780	Uiso	?	Se
Se584	1.0	0.312400	0.685820	0.538620	Uiso	?	Se
Se585	1.0	0.563000	0.187700	0.065400	Uiso	?	Se
Se586	1.0	0.063000	0.187340	0.080440	Uiso	?	Se
Se587	1.0	0.811800	0.178900	0.072950	Uiso	?	Se
Se588	1.0	0.311800	0.196080	0.072880	Uiso	?	Se
Se589	1.0	0.570500	0.437500	0.156250	Uiso	?	Se
Se590	1.0	0.429500	0.312520	0.135420	Uiso	?	Se
Se591	1.0	0.053200	0.437500	0.156250	Uiso	?	Se
Se592	1.0	0.946800	0.312520	0.135420	Uiso	?	Se
Se593	1.0	0.687600	0.314200	0.128050	Uiso	?	Se
Se594	1.0	0.687600	0.310780	0.142780	Uiso	?	Se
Se595	1.0	0.312400	0.435820	0.163620	Uiso	?	Se
Se596	1.0	0.312400	0.439180	0.148880	Uiso	?	Se
Se597	1.0	0.820500	0.437520	0.197920	Uiso	?	Se
Se598	1.0	0.303200	0.437520	0.197920	Uiso	?	Se
Se599	1.0	0.562400	0.435780	0.205280	Uiso	?	Se
Se600	1.0	0.562400	0.439200	0.190550	Uiso	?	Se
Se601	1.0	0.820500	0.687480	0.239580	Uiso	?	Se
Se602	1.0	0.679500	0.562500	0.218750	Uiso	?	Se
Se603	1.0	0.303200	0.687480	0.239580	Uiso	?	Se
Se604	1.0	0.196800	0.562500	0.218750	Uiso	?	Se
Se605	1.0	0.937600	0.564180	0.211380	Uiso	?	Se
Se606	1.0	0.937600	0.560820	0.226120	Uiso	?	Se
Se607	1.0	0.562400	0.685800	0.246950	Uiso	?	Se
Se608	1.0	0.562400	0.689220	0.232220	Uiso	?	Se
Se609	1.0	0.813000	0.687320	0.288770	Uiso	?	Se
Se610	1.0	0.687000	0.562340	0.267940	Uiso	?	Se
Se611	1.0	0.313000	0.687680	0.273730	Uiso	?	Se
Se612	1.0	0.187000	0.562700	0.252900	Uiso	?	Se
Se613	1.0	0.061800	0.696120	0.281220	Uiso	?	Se
Se614	1.0	0.438200	0.571080	0.260380	Uiso	?	Se
Se615	1.0	0.561800	0.678880	0.281280	Uiso	?	Se
Se616	1.0	0.938200	0.553900	0.260450	Uiso	?	Se
Se617	1.0	0.070500	0.937520	0.322920	Uiso	?	Se
Se618	1.0	0.929500	0.812480	0.302080	Uiso	?	Se
Se619	1.0	0.553200	0.937520	0.322920	Uiso	?	Se
Se620	1.0	0.446800	0.812480	0.302080	Uiso	?	Se

Se621	1.0	0.063000	0.687340	0.330440	Uiso	?	Se
Se622	1.0	0.563000	0.687700	0.315400	Uiso	?	Se
Se623	1.0	0.311800	0.696080	0.322880	Uiso	?	Se
Se624	1.0	0.811800	0.678900	0.322950	Uiso	?	Se
Se625	1.0	0.187600	0.814220	0.294720	Uiso	?	Se
Se626	1.0	0.187600	0.810800	0.309450	Uiso	?	Se
Se627	1.0	0.812400	0.935780	0.330280	Uiso	?	Se
Se628	1.0	0.812400	0.939200	0.315550	Uiso	?	Se
Se629	1.0	0.063000	0.687700	0.565400	Uiso	?	Se
Se630	1.0	0.563000	0.687340	0.580440	Uiso	?	Se
Se631	1.0	0.311800	0.678900	0.572950	Uiso	?	Se
Se632	1.0	0.811800	0.696080	0.572880	Uiso	?	Se
Se633	1.0	0.820500	0.937520	0.447920	Uiso	?	Se
Se634	1.0	0.679500	0.812480	0.427080	Uiso	?	Se
Se635	1.0	0.303200	0.937520	0.447920	Uiso	?	Se
Se636	1.0	0.196800	0.812480	0.427080	Uiso	?	Se
Se637	1.0	0.937600	0.814220	0.419720	Uiso	?	Se
Se638	1.0	0.937600	0.810800	0.434450	Uiso	?	Se
Se639	1.0	0.562400	0.935780	0.455280	Uiso	?	Se
Se640	1.0	0.562400	0.939200	0.440550	Uiso	?	Se
Se641	1.0	0.187600	0.060780	0.017780	Uiso	?	Se
Se642	1.0	0.437000	0.312680	0.086230	Uiso	?	Se
Se643	1.0	0.063000	0.437300	0.122100	Uiso	?	Se
Se644	1.0	0.937000	0.312320	0.101270	Uiso	?	Se
Se645	1.0	0.811800	0.428920	0.114620	Uiso	?	Se
Se646	1.0	0.188200	0.303880	0.093780	Uiso	?	Se
Se647	1.0	0.311800	0.446100	0.114550	Uiso	?	Se
Se648	1.0	0.688200	0.321120	0.093720	Uiso	?	Se
Se649	1.0	0.937000	0.562340	0.142940	Uiso	?	Se
Se650	1.0	0.813000	0.687700	0.190400	Uiso	?	Se
Se651	1.0	0.687000	0.562660	0.169560	Uiso	?	Se
Se652	1.0	0.313000	0.687340	0.205440	Uiso	?	Se
Se653	1.0	0.187000	0.562300	0.184600	Uiso	?	Se
Se654	1.0	0.061800	0.678900	0.197950	Uiso	?	Se
Se655	1.0	0.438200	0.553920	0.177120	Uiso	?	Se
Se656	1.0	0.561800	0.696080	0.197880	Uiso	?	Se
Se657	1.0	0.938200	0.571100	0.177050	Uiso	?	Se
Se658	1.0	0.313000	0.937300	0.247100	Uiso	?	Se
Se659	1.0	0.187000	0.812320	0.226270	Uiso	?	Se
Se660	1.0	0.061800	0.928920	0.239620	Uiso	?	Se
Se661	1.0	0.438200	0.803880	0.218780	Uiso	?	Se
Se662	1.0	0.561800	0.946100	0.239550	Uiso	?	Se
Se663	1.0	0.938200	0.821120	0.218720	Uiso	?	Se
Se664	1.0	0.820500	0.937500	0.281250	Uiso	?	Se
Se665	1.0	0.679500	0.812520	0.260420	Uiso	?	Se
Se666	1.0	0.303200	0.937500	0.281250	Uiso	?	Se
Se667	1.0	0.196800	0.812520	0.260420	Uiso	?	Se
Se668	1.0	0.937600	0.814200	0.253050	Uiso	?	Se
Se669	1.0	0.937600	0.810780	0.267780	Uiso	?	Se
Se670	1.0	0.562400	0.935820	0.288620	Uiso	?	Se
Se671	1.0	0.562400	0.939180	0.273880	Uiso	?	Se
Se672	1.0	0.687000	0.812680	0.211230	Uiso	?	Se
Se673	1.0	0.812400	0.185820	0.038620	Uiso	?	Se

Se674	1.0	0.563000	0.437660	0.107060	Uiso	?	Se
Se675	1.0	0.563000	0.687680	0.148730	Uiso	?	Se
Se676	1.0	0.437000	0.562700	0.127900	Uiso	?	Se
Se677	1.0	0.063000	0.687320	0.163770	Uiso	?	Se
Se678	1.0	0.811800	0.678880	0.156280	Uiso	?	Se
Se679	1.0	0.188200	0.553900	0.135450	Uiso	?	Se
Se680	1.0	0.311800	0.696120	0.156220	Uiso	?	Se
Se681	1.0	0.688200	0.571080	0.135380	Uiso	?	Se
Se682	1.0	0.437600	0.814220	0.169720	Uiso	?	Se
Se683	1.0	0.062400	0.939200	0.190550	Uiso	?	Se
Se684	1.0	0.320500	0.937520	0.197920	Uiso	?	Se
Se685	1.0	0.179500	0.812480	0.177080	Uiso	?	Se
Se686	1.0	0.803200	0.937520	0.197920	Uiso	?	Se
Se687	1.0	0.696800	0.812480	0.177080	Uiso	?	Se
Se688	1.0	0.437600	0.810800	0.184450	Uiso	?	Se
Se689	1.0	0.062400	0.935780	0.205280	Uiso	?	Se
Se690	1.0	0.813000	0.937660	0.232060	Uiso	?	Se
Se691	1.0	0.570500	0.687500	0.031250	Uiso	?	Se
Se692	1.0	0.429500	0.562520	0.010420	Uiso	?	Se
Se693	1.0	0.053200	0.687500	0.031250	Uiso	?	Se
Se694	1.0	0.946800	0.562520	0.010420	Uiso	?	Se
Se695	1.0	0.563000	0.937680	0.023730	Uiso	?	Se
Se696	1.0	0.563000	0.437320	0.038770	Uiso	?	Se
Se697	1.0	0.437000	0.312340	0.017940	Uiso	?	Se
Se698	1.0	0.437000	0.812700	0.002900	Uiso	?	Se
Se699	1.0	0.063000	0.437680	0.023730	Uiso	?	Se
Se700	1.0	0.063000	0.937320	0.038770	Uiso	?	Se
Se701	1.0	0.937000	0.812340	0.017940	Uiso	?	Se
Se702	1.0	0.937000	0.312700	0.002900	Uiso	?	Se
Se703	1.0	0.811800	0.928880	0.031280	Uiso	?	Se
Se704	1.0	0.811800	0.446120	0.031220	Uiso	?	Se
Se705	1.0	0.188200	0.321080	0.010380	Uiso	?	Se
Se706	1.0	0.188200	0.803900	0.010450	Uiso	?	Se
Se707	1.0	0.311800	0.428880	0.031280	Uiso	?	Se
Se708	1.0	0.311800	0.946120	0.031220	Uiso	?	Se
Se709	1.0	0.688200	0.821080	0.010380	Uiso	?	Se
Se710	1.0	0.688200	0.303900	0.010450	Uiso	?	Se
Se711	1.0	0.687600	0.564200	0.003050	Uiso	?	Se
Se712	1.0	0.687600	0.560780	0.017780	Uiso	?	Se
Se713	1.0	0.312400	0.685820	0.038620	Uiso	?	Se
Se714	1.0	0.312400	0.689180	0.023880	Uiso	?	Se
Se715	1.0	0.187600	0.064200	0.003050	Uiso	?	Se
Se716	1.0	0.812400	0.189180	0.023880	Uiso	?	Se
Se717	1.0	0.570500	0.937520	0.072920	Uiso	?	Se
Se718	1.0	0.429500	0.812480	0.052080	Uiso	?	Se
Se719	1.0	0.053200	0.937520	0.072920	Uiso	?	Se
Se720	1.0	0.946800	0.812480	0.052080	Uiso	?	Se
Se721	1.0	0.563000	0.687340	0.080440	Uiso	?	Se
Se722	1.0	0.437000	0.562300	0.059600	Uiso	?	Se
Se723	1.0	0.063000	0.687700	0.065400	Uiso	?	Se
Se724	1.0	0.937000	0.562660	0.044560	Uiso	?	Se
Se725	1.0	0.811800	0.696080	0.072880	Uiso	?	Se
Se726	1.0	0.188200	0.571100	0.052050	Uiso	?	Se

Se727	1.0	0.311800	0.678900	0.072950	Uiso	?	Se
Se728	1.0	0.688200	0.553920	0.052120	Uiso	?	Se
Se729	1.0	0.687600	0.814220	0.044720	Uiso	?	Se
Se730	1.0	0.687600	0.810800	0.059450	Uiso	?	Se
Se731	1.0	0.312400	0.935780	0.080280	Uiso	?	Se
Se732	1.0	0.312400	0.939200	0.065550	Uiso	?	Se
Se733	1.0	0.187600	0.314220	0.044720	Uiso	?	Se
Se734	1.0	0.812400	0.439200	0.065550	Uiso	?	Se
Se735	1.0	0.563000	0.937300	0.122100	Uiso	?	Se
Se736	1.0	0.437000	0.812320	0.101270	Uiso	?	Se
Se737	1.0	0.063000	0.937660	0.107060	Uiso	?	Se
Se738	1.0	0.937000	0.812680	0.086230	Uiso	?	Se
Se739	1.0	0.811800	0.946100	0.114550	Uiso	?	Se
Se740	1.0	0.188200	0.821120	0.093720	Uiso	?	Se
Se741	1.0	0.311800	0.928920	0.114620	Uiso	?	Se
Se742	1.0	0.688200	0.803880	0.093780	Uiso	?	Se
Se743	1.0	0.187600	0.564180	0.086380	Uiso	?	Se
Se744	1.0	0.812400	0.689220	0.107220	Uiso	?	Se
Se745	1.0	0.187600	0.814200	0.128050	Uiso	?	Se
Se746	1.0	0.812400	0.939180	0.148880	Uiso	?	Se
Se747	1.0	0.070500	0.187500	0.031250	Uiso	?	Se
Se748	1.0	0.929500	0.062520	0.010420	Uiso	?	Se
Se749	1.0	0.553200	0.187500	0.031250	Uiso	?	Se
Se750	1.0	0.446800	0.062520	0.010420	Uiso	?	Se
Se751	1.0	0.070500	0.437520	0.072920	Uiso	?	Se
Se752	1.0	0.929500	0.312480	0.052080	Uiso	?	Se
Se753	1.0	0.553200	0.437520	0.072920	Uiso	?	Se
Se754	1.0	0.446800	0.312480	0.052080	Uiso	?	Se
Se755	1.0	0.187600	0.310800	0.059450	Uiso	?	Se
Se756	1.0	0.812400	0.435780	0.080280	Uiso	?	Se
Se757	1.0	0.070500	0.687480	0.114580	Uiso	?	Se
Se758	1.0	0.929500	0.562500	0.093750	Uiso	?	Se
Se759	1.0	0.553200	0.687480	0.114580	Uiso	?	Se
Se760	1.0	0.446800	0.562500	0.093750	Uiso	?	Se
Se761	1.0	0.187600	0.560820	0.101120	Uiso	?	Se
Se762	1.0	0.812400	0.685800	0.121950	Uiso	?	Se
Se763	1.0	0.070500	0.937500	0.156250	Uiso	?	Se
Se764	1.0	0.929500	0.812520	0.135420	Uiso	?	Se
Se765	1.0	0.553200	0.937500	0.156250	Uiso	?	Se
Se766	1.0	0.446800	0.812520	0.135420	Uiso	?	Se
Se767	1.0	0.187600	0.810780	0.142780	Uiso	?	Se
Se768	1.0	0.812400	0.935820	0.163620	Uiso	?	Se
Tl1	1.0	0.438500	0.563720	0.712820	Uiso	?	Tl
Tl2	1.0	0.938700	0.812360	0.766010	Uiso	?	Tl
Tl3	1.0	0.938500	0.813720	0.837820	Uiso	?	Tl
Tl4	1.0	0.561500	0.188720	0.900320	Uiso	?	Tl
Tl5	1.0	0.938500	0.063740	0.879490	Uiso	?	Tl
Tl6	1.0	0.561500	0.438740	0.941990	Uiso	?	Tl
Tl7	1.0	0.938500	0.563780	0.962830	Uiso	?	Tl
Tl8	1.0	0.561500	0.186260	0.745510	Uiso	?	Tl
Tl9	1.0	0.938500	0.061280	0.724680	Uiso	?	Tl
Tl10	1.0	0.938500	0.063720	0.712820	Uiso	?	Tl
Tl11	1.0	0.061500	0.686260	0.745510	Uiso	?	Tl

Tl12	1.0	0.438500	0.561280	0.724680	Uiso	?	Tl
Tl13	1.0	0.938700	0.312620	0.754820	Uiso	?	Tl
Tl14	1.0	0.061300	0.937340	0.786840	Uiso	?	Tl
Tl15	1.0	0.061300	0.437660	0.775660	Uiso	?	Tl
Tl16	1.0	0.438700	0.812620	0.754820	Uiso	?	Tl
Tl17	1.0	0.561300	0.437340	0.786840	Uiso	?	Tl
Tl18	1.0	0.561300	0.937660	0.775660	Uiso	?	Tl
Tl19	1.0	0.938700	0.562640	0.796490	Uiso	?	Tl
Tl20	1.0	0.438700	0.562320	0.807670	Uiso	?	Tl
Tl21	1.0	0.061500	0.438760	0.858660	Uiso	?	Tl
Tl22	1.0	0.938500	0.811220	0.849670	Uiso	?	Tl
Tl23	1.0	0.811300	0.687320	0.870170	Uiso	?	Tl
Tl24	1.0	0.061500	0.688720	0.900320	Uiso	?	Tl
Tl25	1.0	0.061500	0.686220	0.912170	Uiso	?	Tl
Tl26	1.0	0.561500	0.186220	0.912170	Uiso	?	Tl
Tl27	1.0	0.938500	0.061240	0.891340	Uiso	?	Tl
Tl28	1.0	0.188700	0.312360	0.891010	Uiso	?	Tl
Tl29	1.0	0.311300	0.437340	0.911840	Uiso	?	Tl
Tl30	1.0	0.688700	0.312620	0.879820	Uiso	?	Tl
Tl31	1.0	0.688700	0.812360	0.891010	Uiso	?	Tl
Tl32	1.0	0.811300	0.437660	0.900660	Uiso	?	Tl
Tl33	1.0	0.061500	0.938740	0.941990	Uiso	?	Tl
Tl34	1.0	0.061500	0.936240	0.953840	Uiso	?	Tl
Tl35	1.0	0.438500	0.811260	0.933010	Uiso	?	Tl
Tl36	1.0	0.438500	0.813760	0.921160	Uiso	?	Tl
Tl37	1.0	0.561500	0.436240	0.953840	Uiso	?	Tl
Tl38	1.0	0.188700	0.062640	0.921490	Uiso	?	Tl
Tl39	1.0	0.188700	0.562320	0.932670	Uiso	?	Tl
Tl40	1.0	0.311300	0.187620	0.942320	Uiso	?	Tl
Tl41	1.0	0.688700	0.562640	0.921490	Uiso	?	Tl
Tl42	1.0	0.688700	0.062320	0.932670	Uiso	?	Tl
Tl43	1.0	0.811300	0.187360	0.953510	Uiso	?	Tl
Tl44	1.0	0.061500	0.186260	0.995510	Uiso	?	Tl
Tl45	1.0	0.438500	0.061220	0.974670	Uiso	?	Tl
Tl46	1.0	0.438500	0.063780	0.962830	Uiso	?	Tl
Tl47	1.0	0.561500	0.688760	0.983660	Uiso	?	Tl
Tl48	1.0	0.561500	0.686260	0.995510	Uiso	?	Tl
Tl49	1.0	0.938500	0.561220	0.974670	Uiso	?	Tl
Tl50	1.0	0.188700	0.312660	0.963160	Uiso	?	Tl
Tl51	1.0	0.188700	0.812340	0.974340	Uiso	?	Tl
Tl52	1.0	0.311300	0.937320	0.995170	Uiso	?	Tl
Tl53	1.0	0.311300	0.437640	0.983990	Uiso	?	Tl
Tl54	1.0	0.688700	0.812660	0.963160	Uiso	?	Tl
Tl55	1.0	0.688700	0.312340	0.974340	Uiso	?	Tl
Tl56	1.0	0.811300	0.437320	0.995170	Uiso	?	Tl
Tl57	1.0	0.811300	0.937640	0.983990	Uiso	?	Tl
Tl58	1.0	0.811300	0.937660	0.650660	Uiso	?	Tl
Tl59	1.0	0.311300	0.937340	0.661840	Uiso	?	Tl
Tl60	1.0	0.561500	0.188760	0.733660	Uiso	?	Tl
Tl61	1.0	0.438700	0.312360	0.766010	Uiso	?	Tl
Tl62	1.0	0.811500	0.438740	0.816990	Uiso	?	Tl
Tl63	1.0	0.811500	0.436240	0.828840	Uiso	?	Tl
Tl64	1.0	0.061500	0.436260	0.870510	Uiso	?	Tl

Tl65	1.0	0.438500	0.311220	0.849670	Uiso	?	Tl
Tl66	1.0	0.438500	0.313720	0.837820	Uiso	?	Tl
Tl67	1.0	0.688700	0.562380	0.682680	Uiso	?	Tl
Tl68	1.0	0.188700	0.562640	0.671490	Uiso	?	Tl
Tl69	1.0	0.061500	0.688760	0.733660	Uiso	?	Tl
Tl70	1.0	0.311500	0.938740	0.816990	Uiso	?	Tl
Tl71	1.0	0.688500	0.813760	0.796160	Uiso	?	Tl
Tl72	1.0	0.311500	0.936240	0.828840	Uiso	?	Tl
Tl73	1.0	0.688500	0.811260	0.808010	Uiso	?	Tl
Tl74	1.0	0.311300	0.687640	0.858990	Uiso	?	Tl
Tl75	1.0	0.188700	0.812620	0.879820	Uiso	?	Tl
Tl76	1.0	0.061500	0.188760	0.983660	Uiso	?	Tl
Tl77	1.0	0.561500	0.438740	0.441990	Uiso	?	Tl
Tl78	1.0	0.561500	0.436240	0.453840	Uiso	?	Tl
Tl79	1.0	0.688500	0.061240	0.516340	Uiso	?	Tl
Tl80	1.0	0.438700	0.062320	0.557670	Uiso	?	Tl
Tl81	1.0	0.561300	0.187360	0.578510	Uiso	?	Tl
Tl82	1.0	0.938700	0.062640	0.546490	Uiso	?	Tl
Tl83	1.0	0.061300	0.187620	0.567320	Uiso	?	Tl
Tl84	1.0	0.811500	0.188760	0.608660	Uiso	?	Tl
Tl85	1.0	0.438700	0.312340	0.599340	Uiso	?	Tl
Tl86	1.0	0.938700	0.312660	0.588160	Uiso	?	Tl
Tl87	1.0	0.438500	0.063740	0.629490	Uiso	?	Tl
Tl88	1.0	0.938500	0.313760	0.921160	Uiso	?	Tl
Tl89	1.0	0.188700	0.062340	0.849340	Uiso	?	Tl
Tl90	1.0	0.311300	0.187320	0.870170	Uiso	?	Tl
Tl91	1.0	0.688700	0.062660	0.838160	Uiso	?	Tl
Tl92	1.0	0.811300	0.187640	0.858990	Uiso	?	Tl
Tl93	1.0	0.938500	0.311260	0.933010	Uiso	?	Tl
Tl94	1.0	0.811500	0.186260	0.620510	Uiso	?	Tl
Tl95	1.0	0.438500	0.061240	0.641340	Uiso	?	Tl
Tl96	1.0	0.688700	0.062640	0.671490	Uiso	?	Tl
Tl97	1.0	0.811300	0.187620	0.692320	Uiso	?	Tl
Tl98	1.0	0.188700	0.062380	0.682680	Uiso	?	Tl
Tl99	1.0	0.311300	0.187360	0.703510	Uiso	?	Tl
Tl100	1.0	0.188500	0.311260	0.808010	Uiso	?	Tl
Tl101	1.0	0.188500	0.313760	0.796160	Uiso	?	Tl
Tl102	1.0	0.438700	0.062660	0.463160	Uiso	?	Tl
Tl103	1.0	0.938700	0.062340	0.474340	Uiso	?	Tl
Tl104	1.0	0.061300	0.187380	0.495180	Uiso	?	Tl
Tl105	1.0	0.311500	0.188780	0.525330	Uiso	?	Tl
Tl106	1.0	0.311500	0.186220	0.537170	Uiso	?	Tl
Tl107	1.0	0.688500	0.063740	0.504490	Uiso	?	Tl
Tl108	1.0	0.938500	0.313760	0.421160	Uiso	?	Tl
Tl109	1.0	0.938500	0.311260	0.433010	Uiso	?	Tl
Tl110	1.0	0.561300	0.187640	0.483990	Uiso	?	Tl
Tl111	1.0	0.561500	0.938740	0.691990	Uiso	?	Tl
Tl112	1.0	0.561500	0.936240	0.703840	Uiso	?	Tl
Tl113	1.0	0.938500	0.811260	0.683010	Uiso	?	Tl
Tl114	1.0	0.938500	0.813760	0.671160	Uiso	?	Tl
Tl115	1.0	0.688500	0.561240	0.766340	Uiso	?	Tl
Tl116	1.0	0.061300	0.687620	0.817320	Uiso	?	Tl
Tl117	1.0	0.561300	0.687360	0.828510	Uiso	?	Tl

Tl118	1.0	0.188700	0.562660	0.838160	Uiso	?	Tl
Tl119	1.0	0.688700	0.562340	0.849340	Uiso	?	Tl
Tl120	1.0	0.438500	0.563740	0.879490	Uiso	?	Tl
Tl121	1.0	0.311300	0.687360	0.953510	Uiso	?	Tl
Tl122	1.0	0.811300	0.687620	0.942320	Uiso	?	Tl
Tl123	1.0	0.811500	0.938740	0.566990	Uiso	?	Tl
Tl124	1.0	0.188500	0.813760	0.546160	Uiso	?	Tl
Tl125	1.0	0.811500	0.936240	0.578840	Uiso	?	Tl
Tl126	1.0	0.188500	0.811260	0.558010	Uiso	?	Tl
Tl127	1.0	0.438700	0.812660	0.588160	Uiso	?	Tl
Tl128	1.0	0.561300	0.937640	0.608990	Uiso	?	Tl
Tl129	1.0	0.938700	0.812340	0.599340	Uiso	?	Tl
Tl130	1.0	0.061300	0.937320	0.620170	Uiso	?	Tl
Tl131	1.0	0.688700	0.812620	0.629820	Uiso	?	Tl
Tl132	1.0	0.188700	0.812360	0.641010	Uiso	?	Tl
Tl133	1.0	0.438500	0.561240	0.891340	Uiso	?	Tl
Tl134	1.0	0.811300	0.687360	0.703510	Uiso	?	Tl
Tl135	1.0	0.311300	0.687620	0.692320	Uiso	?	Tl
Tl136	1.0	0.688700	0.812340	0.724340	Uiso	?	Tl
Tl137	1.0	0.811300	0.937380	0.745180	Uiso	?	Tl
Tl138	1.0	0.188700	0.812660	0.713160	Uiso	?	Tl
Tl139	1.0	0.311500	0.688720	0.775320	Uiso	?	Tl
Tl140	1.0	0.688500	0.563740	0.754490	Uiso	?	Tl
Tl141	1.0	0.561500	0.688720	0.650320	Uiso	?	Tl
Tl142	1.0	0.561500	0.686220	0.662170	Uiso	?	Tl
Tl143	1.0	0.938500	0.561240	0.641340	Uiso	?	Tl
Tl144	1.0	0.938500	0.563740	0.629490	Uiso	?	Tl
Tl145	1.0	0.311300	0.937640	0.733990	Uiso	?	Tl
Tl146	1.0	0.311500	0.686220	0.787170	Uiso	?	Tl
Tl147	1.0	0.311500	0.936260	0.495510	Uiso	?	Tl
Tl148	1.0	0.688500	0.811220	0.474670	Uiso	?	Tl
Tl149	1.0	0.688500	0.813720	0.462820	Uiso	?	Tl
Tl150	1.0	0.561300	0.937340	0.536840	Uiso	?	Tl
Tl151	1.0	0.938700	0.812620	0.504820	Uiso	?	Tl
Tl152	1.0	0.061300	0.937660	0.525660	Uiso	?	Tl
Tl153	1.0	0.438700	0.062640	0.296490	Uiso	?	Tl
Tl154	1.0	0.561300	0.187620	0.317320	Uiso	?	Tl
Tl155	1.0	0.938700	0.062320	0.307670	Uiso	?	Tl
Tl156	1.0	0.061300	0.187360	0.328510	Uiso	?	Tl
Tl157	1.0	0.688700	0.062660	0.338160	Uiso	?	Tl
Tl158	1.0	0.188700	0.062340	0.349340	Uiso	?	Tl
Tl159	1.0	0.311300	0.187320	0.370170	Uiso	?	Tl
Tl160	1.0	0.438700	0.062360	0.391010	Uiso	?	Tl
Tl161	1.0	0.688700	0.062360	0.266010	Uiso	?	Tl
Tl162	1.0	0.438700	0.812360	0.516010	Uiso	?	Tl
Tl163	1.0	0.188500	0.063720	0.587820	Uiso	?	Tl
Tl164	1.0	0.188500	0.061220	0.599670	Uiso	?	Tl
Tl165	1.0	0.938500	0.063780	0.212830	Uiso	?	Tl
Tl166	1.0	0.561500	0.186260	0.245510	Uiso	?	Tl
Tl167	1.0	0.938500	0.061220	0.224670	Uiso	?	Tl
Tl168	1.0	0.188700	0.062680	0.254830	Uiso	?	Tl
Tl169	1.0	0.311300	0.187660	0.275660	Uiso	?	Tl
Tl170	1.0	0.811300	0.187340	0.286840	Uiso	?	Tl

Tl171	1.0	0.811300	0.187640	0.358990	Uiso	?	Tl
Tl172	1.0	0.938700	0.062680	0.379830	Uiso	?	Tl
Tl173	1.0	0.061300	0.187660	0.400660	Uiso	?	Tl
Tl174	1.0	0.561300	0.187340	0.411840	Uiso	?	Tl
Tl175	1.0	0.188700	0.062640	0.421490	Uiso	?	Tl
Tl176	1.0	0.311300	0.187680	0.442330	Uiso	?	Tl
Tl177	1.0	0.688700	0.062320	0.432670	Uiso	?	Tl
Tl178	1.0	0.811300	0.187360	0.453510	Uiso	?	Tl
Tl179	1.0	0.311500	0.938760	0.483660	Uiso	?	Tl
Tl180	1.0	0.188500	0.061220	0.099670	Uiso	?	Tl
Tl181	1.0	0.188500	0.063720	0.087820	Uiso	?	Tl
Tl182	1.0	0.938700	0.062360	0.141010	Uiso	?	Tl
Tl183	1.0	0.438700	0.062620	0.129820	Uiso	?	Tl
Tl184	1.0	0.188700	0.062380	0.182680	Uiso	?	Tl
Tl185	1.0	0.311300	0.187360	0.203510	Uiso	?	Tl
Tl186	1.0	0.688700	0.062640	0.171490	Uiso	?	Tl
Tl187	1.0	0.811300	0.187620	0.192320	Uiso	?	Tl
Tl188	1.0	0.561500	0.188760	0.233660	Uiso	?	Tl
Tl189	1.0	0.438500	0.313720	0.337820	Uiso	?	Tl
Tl190	1.0	0.688500	0.313740	0.379490	Uiso	?	Tl
Tl191	1.0	0.438500	0.311280	0.349680	Uiso	?	Tl
Tl192	1.0	0.688500	0.311240	0.391340	Uiso	?	Tl
Tl193	1.0	0.688700	0.312360	0.641010	Uiso	?	Tl
Tl194	1.0	0.061500	0.438740	0.691990	Uiso	?	Tl
Tl195	1.0	0.561500	0.938760	0.858660	Uiso	?	Tl
Tl196	1.0	0.061500	0.436240	0.703840	Uiso	?	Tl
Tl197	1.0	0.938700	0.062320	0.807670	Uiso	?	Tl
Tl198	1.0	0.061300	0.187360	0.828510	Uiso	?	Tl
Tl199	1.0	0.438700	0.062640	0.796490	Uiso	?	Tl
Tl200	1.0	0.561300	0.187620	0.817320	Uiso	?	Tl
Tl201	1.0	0.561500	0.936260	0.870510	Uiso	?	Tl
Tl202	1.0	0.188700	0.562320	0.432670	Uiso	?	Tl
Tl203	1.0	0.688700	0.562640	0.421490	Uiso	?	Tl
Tl204	1.0	0.811300	0.437340	0.661840	Uiso	?	Tl
Tl205	1.0	0.188700	0.312620	0.629820	Uiso	?	Tl
Tl206	1.0	0.311300	0.437660	0.650660	Uiso	?	Tl
Tl207	1.0	0.938700	0.312360	0.516010	Uiso	?	Tl
Tl208	1.0	0.311500	0.438740	0.566990	Uiso	?	Tl
Tl209	1.0	0.311500	0.436240	0.578840	Uiso	?	Tl
Tl210	1.0	0.311500	0.688760	0.608660	Uiso	?	Tl
Tl211	1.0	0.311500	0.686260	0.620510	Uiso	?	Tl
Tl212	1.0	0.688500	0.561220	0.599670	Uiso	?	Tl
Tl213	1.0	0.688500	0.563720	0.587820	Uiso	?	Tl
Tl214	1.0	0.311300	0.937660	0.900660	Uiso	?	Tl
Tl215	1.0	0.811300	0.937340	0.911840	Uiso	?	Tl
Tl216	1.0	0.938700	0.562360	0.391010	Uiso	?	Tl
Tl217	1.0	0.061300	0.687340	0.411840	Uiso	?	Tl
Tl218	1.0	0.438700	0.562680	0.379830	Uiso	?	Tl
Tl219	1.0	0.561300	0.687660	0.400660	Uiso	?	Tl
Tl220	1.0	0.811500	0.438760	0.483660	Uiso	?	Tl
Tl221	1.0	0.188500	0.313720	0.462820	Uiso	?	Tl
Tl222	1.0	0.811500	0.436260	0.495510	Uiso	?	Tl
Tl223	1.0	0.188500	0.311220	0.474670	Uiso	?	Tl

Tl224	1.0	0.438700	0.312620	0.504820	Uiso	?	Tl
Tl225	1.0	0.561300	0.437660	0.525660	Uiso	?	Tl
Tl226	1.0	0.061300	0.437340	0.536840	Uiso	?	Tl
Tl227	1.0	0.438700	0.562640	0.546490	Uiso	?	Tl
Tl228	1.0	0.938700	0.562320	0.557670	Uiso	?	Tl
Tl229	1.0	0.561300	0.437320	0.620170	Uiso	?	Tl
Tl230	1.0	0.061500	0.188720	0.650320	Uiso	?	Tl
Tl231	1.0	0.438500	0.313760	0.671160	Uiso	?	Tl
Tl232	1.0	0.061500	0.186220	0.662170	Uiso	?	Tl
Tl233	1.0	0.438500	0.311260	0.683010	Uiso	?	Tl
Tl234	1.0	0.811300	0.437640	0.733990	Uiso	?	Tl
Tl235	1.0	0.188500	0.061240	0.766340	Uiso	?	Tl
Tl236	1.0	0.688700	0.312660	0.713160	Uiso	?	Tl
Tl237	1.0	0.188700	0.312340	0.724340	Uiso	?	Tl
Tl238	1.0	0.311300	0.437380	0.745180	Uiso	?	Tl
Tl239	1.0	0.811500	0.188720	0.775320	Uiso	?	Tl
Tl240	1.0	0.811500	0.186220	0.787170	Uiso	?	Tl
Tl241	1.0	0.188500	0.063740	0.754490	Uiso	?	Tl
Tl242	1.0	0.061300	0.437640	0.608990	Uiso	?	Tl
Tl243	1.0	0.938500	0.311240	0.266340	Uiso	?	Tl
Tl244	1.0	0.688500	0.311260	0.558010	Uiso	?	Tl
Tl245	1.0	0.688500	0.313760	0.546160	Uiso	?	Tl
Tl246	1.0	0.938700	0.062640	0.046490	Uiso	?	Tl
Tl247	1.0	0.438700	0.062320	0.057670	Uiso	?	Tl
Tl248	1.0	0.811500	0.188760	0.108660	Uiso	?	Tl
Tl249	1.0	0.811500	0.186260	0.120510	Uiso	?	Tl
Tl250	1.0	0.061300	0.187340	0.161840	Uiso	?	Tl
Tl251	1.0	0.561300	0.187660	0.150660	Uiso	?	Tl
Tl252	1.0	0.438500	0.311260	0.183010	Uiso	?	Tl
Tl253	1.0	0.438500	0.313760	0.171160	Uiso	?	Tl
Tl254	1.0	0.188700	0.312340	0.224340	Uiso	?	Tl
Tl255	1.0	0.311300	0.437380	0.245180	Uiso	?	Tl
Tl256	1.0	0.688700	0.312660	0.213160	Uiso	?	Tl
Tl257	1.0	0.811300	0.437640	0.233990	Uiso	?	Tl
Tl258	1.0	0.561500	0.438720	0.275320	Uiso	?	Tl
Tl259	1.0	0.938500	0.313740	0.254490	Uiso	?	Tl
Tl260	1.0	0.811500	0.438740	0.316990	Uiso	?	Tl
Tl261	1.0	0.188500	0.313760	0.296160	Uiso	?	Tl
Tl262	1.0	0.438700	0.562320	0.307670	Uiso	?	Tl
Tl263	1.0	0.938700	0.562640	0.296490	Uiso	?	Tl
Tl264	1.0	0.061500	0.438760	0.358660	Uiso	?	Tl
Tl265	1.0	0.688700	0.562340	0.349340	Uiso	?	Tl
Tl266	1.0	0.811300	0.687320	0.370170	Uiso	?	Tl
Tl267	1.0	0.188700	0.562660	0.338160	Uiso	?	Tl
Tl268	1.0	0.311300	0.687640	0.358990	Uiso	?	Tl
Tl269	1.0	0.311500	0.438720	0.400320	Uiso	?	Tl
Tl270	1.0	0.561500	0.436220	0.287170	Uiso	?	Tl
Tl271	1.0	0.811500	0.436240	0.328840	Uiso	?	Tl
Tl272	1.0	0.188500	0.311260	0.308010	Uiso	?	Tl
Tl273	1.0	0.061500	0.436260	0.370510	Uiso	?	Tl
Tl274	1.0	0.311500	0.436280	0.412180	Uiso	?	Tl
Tl275	1.0	0.561500	0.938760	0.358660	Uiso	?	Tl
Tl276	1.0	0.811500	0.938720	0.400320	Uiso	?	Tl

Tl277	1.0	0.811500	0.936280	0.412180	Uiso	?	Tl
Tl278	1.0	0.188500	0.813740	0.379490	Uiso	?	Tl
Tl279	1.0	0.061300	0.687640	0.483990	Uiso	?	Tl
Tl280	1.0	0.561500	0.936260	0.370510	Uiso	?	Tl
Tl281	1.0	0.938500	0.811280	0.349680	Uiso	?	Tl
Tl282	1.0	0.938500	0.813720	0.337820	Uiso	?	Tl
Tl283	1.0	0.188500	0.811240	0.391340	Uiso	?	Tl
Tl284	1.0	0.311300	0.687360	0.453510	Uiso	?	Tl
Tl285	1.0	0.811300	0.687680	0.442330	Uiso	?	Tl
Tl286	1.0	0.438700	0.562340	0.474340	Uiso	?	Tl
Tl287	1.0	0.561300	0.687380	0.495180	Uiso	?	Tl
Tl288	1.0	0.938700	0.562660	0.463160	Uiso	?	Tl
Tl289	1.0	0.811500	0.688780	0.525330	Uiso	?	Tl
Tl290	1.0	0.188500	0.563740	0.504490	Uiso	?	Tl
Tl291	1.0	0.811500	0.686220	0.537170	Uiso	?	Tl
Tl292	1.0	0.188500	0.561240	0.516340	Uiso	?	Tl
Tl293	1.0	0.061300	0.187620	0.067320	Uiso	?	Tl
Tl294	1.0	0.561300	0.187360	0.078510	Uiso	?	Tl
Tl295	1.0	0.811500	0.438720	0.150320	Uiso	?	Tl
Tl296	1.0	0.811500	0.436280	0.162180	Uiso	?	Tl
Tl297	1.0	0.188500	0.311240	0.141340	Uiso	?	Tl
Tl298	1.0	0.188500	0.313740	0.129490	Uiso	?	Tl
Tl299	1.0	0.061500	0.438740	0.191990	Uiso	?	Tl
Tl300	1.0	0.061500	0.436240	0.203840	Uiso	?	Tl
Tl301	1.0	0.061500	0.688760	0.233660	Uiso	?	Tl
Tl302	1.0	0.061500	0.686260	0.245510	Uiso	?	Tl
Tl303	1.0	0.438500	0.561220	0.224670	Uiso	?	Tl
Tl304	1.0	0.438500	0.563780	0.212830	Uiso	?	Tl
Tl305	1.0	0.188700	0.562360	0.266010	Uiso	?	Tl
Tl306	1.0	0.311300	0.687340	0.286840	Uiso	?	Tl
Tl307	1.0	0.688700	0.562680	0.254830	Uiso	?	Tl
Tl308	1.0	0.811300	0.687660	0.275660	Uiso	?	Tl
Tl309	1.0	0.311500	0.938740	0.316990	Uiso	?	Tl
Tl310	1.0	0.311500	0.936240	0.328840	Uiso	?	Tl
Tl311	1.0	0.688500	0.811260	0.308010	Uiso	?	Tl
Tl312	1.0	0.688500	0.813760	0.296160	Uiso	?	Tl
Tl313	1.0	0.561300	0.687360	0.328510	Uiso	?	Tl
Tl314	1.0	0.061300	0.687620	0.317320	Uiso	?	Tl
Tl315	1.0	0.561300	0.687620	0.567320	Uiso	?	Tl
Tl316	1.0	0.061300	0.687360	0.578510	Uiso	?	Tl
Tl317	1.0	0.061500	0.938740	0.441990	Uiso	?	Tl
Tl318	1.0	0.061500	0.936240	0.453840	Uiso	?	Tl
Tl319	1.0	0.438500	0.811260	0.433010	Uiso	?	Tl
Tl320	1.0	0.438500	0.813760	0.421160	Uiso	?	Tl
Tl321	1.0	0.688500	0.061240	0.016340	Uiso	?	Tl
Tl322	1.0	0.938700	0.312660	0.088160	Uiso	?	Tl
Tl323	1.0	0.438700	0.312340	0.099340	Uiso	?	Tl
Tl324	1.0	0.561300	0.437320	0.120170	Uiso	?	Tl
Tl325	1.0	0.438700	0.562360	0.141010	Uiso	?	Tl
Tl326	1.0	0.188700	0.562640	0.171490	Uiso	?	Tl
Tl327	1.0	0.311300	0.687620	0.192320	Uiso	?	Tl
Tl328	1.0	0.688700	0.562380	0.182680	Uiso	?	Tl
Tl329	1.0	0.811300	0.687360	0.203510	Uiso	?	Tl

Tl330	1.0	0.188700	0.812660	0.213160	Uiso	?	Tl
Tl331	1.0	0.688700	0.812340	0.224340	Uiso	?	Tl
Tl332	1.0	0.811300	0.937380	0.245180	Uiso	?	Tl
Tl333	1.0	0.061500	0.938720	0.275320	Uiso	?	Tl
Tl334	1.0	0.061500	0.936220	0.287170	Uiso	?	Tl
Tl335	1.0	0.438500	0.811240	0.266340	Uiso	?	Tl
Tl336	1.0	0.438500	0.813740	0.254490	Uiso	?	Tl
Tl337	1.0	0.061300	0.437640	0.108990	Uiso	?	Tl
Tl338	1.0	0.938700	0.562620	0.129820	Uiso	?	Tl
Tl339	1.0	0.061300	0.687660	0.150660	Uiso	?	Tl
Tl340	1.0	0.561300	0.687340	0.161840	Uiso	?	Tl
Tl341	1.0	0.561500	0.938740	0.191990	Uiso	?	Tl
Tl342	1.0	0.938500	0.813760	0.171160	Uiso	?	Tl
Tl343	1.0	0.561500	0.936240	0.203840	Uiso	?	Tl
Tl344	1.0	0.938500	0.811260	0.183010	Uiso	?	Tl
Tl345	1.0	0.311300	0.937640	0.233990	Uiso	?	Tl
Tl346	1.0	0.811500	0.688780	0.025330	Uiso	?	Tl
Tl347	1.0	0.811500	0.686220	0.037170	Uiso	?	Tl
Tl348	1.0	0.188500	0.561240	0.016340	Uiso	?	Tl
Tl349	1.0	0.188500	0.563740	0.004490	Uiso	?	Tl
Tl350	1.0	0.311500	0.188780	0.025330	Uiso	?	Tl
Tl351	1.0	0.688500	0.063740	0.004490	Uiso	?	Tl
Tl352	1.0	0.938700	0.812680	0.004830	Uiso	?	Tl
Tl353	1.0	0.938700	0.312360	0.016010	Uiso	?	Tl
Tl354	1.0	0.061300	0.437340	0.036840	Uiso	?	Tl
Tl355	1.0	0.061300	0.937660	0.025660	Uiso	?	Tl
Tl356	1.0	0.438700	0.312680	0.004830	Uiso	?	Tl
Tl357	1.0	0.438700	0.812360	0.016010	Uiso	?	Tl
Tl358	1.0	0.561300	0.937340	0.036840	Uiso	?	Tl
Tl359	1.0	0.561300	0.437660	0.025660	Uiso	?	Tl
Tl360	1.0	0.811500	0.938740	0.066990	Uiso	?	Tl
Tl361	1.0	0.811500	0.936240	0.078840	Uiso	?	Tl
Tl362	1.0	0.188500	0.811260	0.058010	Uiso	?	Tl
Tl363	1.0	0.188500	0.813760	0.046160	Uiso	?	Tl
Tl364	1.0	0.311500	0.438740	0.066990	Uiso	?	Tl
Tl365	1.0	0.688500	0.313760	0.046160	Uiso	?	Tl
Tl366	1.0	0.938700	0.562320	0.057670	Uiso	?	Tl
Tl367	1.0	0.061300	0.687360	0.078510	Uiso	?	Tl
Tl368	1.0	0.438700	0.562640	0.046490	Uiso	?	Tl
Tl369	1.0	0.561300	0.687620	0.067320	Uiso	?	Tl
Tl370	1.0	0.311500	0.688760	0.108660	Uiso	?	Tl
Tl371	1.0	0.688500	0.563720	0.087820	Uiso	?	Tl
Tl372	1.0	0.938700	0.812340	0.099340	Uiso	?	Tl
Tl373	1.0	0.061300	0.937320	0.120170	Uiso	?	Tl
Tl374	1.0	0.438700	0.812660	0.088160	Uiso	?	Tl
Tl375	1.0	0.561300	0.937640	0.108990	Uiso	?	Tl
Tl376	1.0	0.311500	0.938720	0.150320	Uiso	?	Tl
Tl377	1.0	0.688500	0.813740	0.129490	Uiso	?	Tl
Tl378	1.0	0.311500	0.186220	0.037170	Uiso	?	Tl
Tl379	1.0	0.311500	0.436240	0.078840	Uiso	?	Tl
Tl380	1.0	0.688500	0.311260	0.058010	Uiso	?	Tl
Tl381	1.0	0.311500	0.686260	0.120510	Uiso	?	Tl
Tl382	1.0	0.688500	0.561220	0.099670	Uiso	?	Tl

Tl383	1.0	0.311500	0.936280	0.162180	Uiso	?	Tl
Tl384	1.0	0.688500	0.811240	0.141340	Uiso	?	Tl

References

[1] Lucas M. Hale, Zachary T. Trautt, and Chandler A. Becker. “Evaluating variability with atomistic simulations: the effect of potential and calculation methodology on the modeling of lattice and elastic constants”. In: *Modelling and Simulation in Materials Science and Engineering* 26.5 (2018), p. 055003. ISSN: 0965-0393. DOI: 10.1088/1361-651X/AABC05.

[2] S. R. Hall and B. McMahon, eds. *International Tables for Crystallography*. Vol. G. International Tables for Crystallography. Chester, England: International Union of Crystallography, 2006. ISBN: 978-1-4020-5411-2. DOI: 10.1107/97809553602060000107.

Appendix B

GaS/GaSe Heterostructures Structural Files

The structural files for each of the GaS/GaSe heterostructures, seen in Figure 4.3, are shown below in the POSCAR file format. These structures have been relaxed via DFT using the parameters in Chapter 4.

0°

```
 Gas/GaSe bilayer (0deg) with 20 angstrom vacuum
   1.00000000000000
     3.7047498935669338     0.0000000000005454     0.0000000000000000
    -1.8523749467324928     3.2084075225202726     0.0000000000000000
     0.0000000000000000    -0.0000000000000001   105.3075920469432702
   Ga    S     Se
     4     2     2
Direct
  0.3333333729901611  0.6666667459985050  0.2368663538102445
  0.3333333729901611  0.6666667459985050  0.2602045344564231
 -0.0000000000000000  0.0000000000000000  0.3118664326446204
  0.0000000000000000 -0.0000000000000000  0.3350680336260292
  0.6666667462394003  0.3333333731566555  0.2700077234038012
  0.6666667462394003  0.3333333731566555  0.2270106086487871
  0.3333333731978030  0.6666666270007511  0.3465921069723732
  0.3333333731978030  0.6666666270007511  0.3003990206999687

  0.00000000E+00  0.00000000E+00  0.00000000E+00
  0.00000000E+00  0.00000000E+00  0.00000000E+00
  0.00000000E+00  0.00000000E+00  0.00000000E+00
  0.00000000E+00  0.00000000E+00  0.00000000E+00
  0.00000000E+00  0.00000000E+00  0.00000000E+00
  0.00000000E+00  0.00000000E+00  0.00000000E+00
  0.00000000E+00  0.00000000E+00  0.00000000E+00
  0.00000000E+00  0.00000000E+00  0.00000000E+00
```

30°

```
Gas/GaSe bilayer (28deg basically 30) with 20 angstrom vacuum
   1.00000000000000
     6.9731951704259290    -0.0002297124619176     0.0002008037897167
    -3.4867964752673895     6.0392682657490218     0.0000612551034350
     0.0017944216992347     0.0018598641200753    55.6252724527712914
   Ga    S     Se
    14     8     6
Direct
  0.1114213425977013  0.1671404700667054  0.4482788780865832
  0.1115958708488520  0.1674483388061248  0.4923066331464625
  0.1105692308612518  0.6651663444424116  0.4482925781710492
  0.6116707068174492  0.1671179365081557  0.4482803787440091
  0.6113800288484583  0.6668445752820276  0.4483644688313433
  0.1099755843297316  0.6638939387787133  0.4923426159148718
  0.6118333246071614  0.1674045127331283  0.4923057474499473
  0.6114936735418368  0.6670604873315398  0.4924726359695697
  0.9991350362378242  0.1116107269995510  0.5944336941979529
  0.9992325578195107  0.1112636401635996  0.6386760920232817
  0.6674519933013272  0.4454927259507429  0.5945437629998693
  0.3330022615588888  0.7771183117884064  0.5944146574495335
  0.6671960788107256  0.4450874206245885  0.6387265462917640
  0.3329912496849445  0.7775041269331453  0.6386674834189776
  0.2770392944119848  0.9981391345586346  0.5124391335558443
  0.2776469933619410  0.9993515398656712  0.4279154019568523
  0.2785899489103230  0.4998117439759895  0.5130295069376061
  0.7786644363235951  0.0013922724609685  0.5128205315149117
  0.7771493240955891  0.4998216608808690  0.5130125147268387
  0.2784816074904555  0.5001500707872495  0.4277305946698178
  0.7779816616446453  0.0000206620882892  0.4277994410162833
  0.7775957586269584  0.5001492232929579  0.4277361995886793
  0.3329516221828186  0.1110740364651690  0.6576666054398217
  0.3340827773676835  0.1128290043862847  0.5757215954971997
  0.0001278079232137  0.4445696630626017  0.6578584023245497
  0.6663171156225971  0.7779877277160949  0.6578161155485844
  0.9993902844910636  0.4444429655181921  0.5751812088132624
  0.6661436218193089  0.7767733951279325  0.5752860897521828

  0.00000000E+00  0.00000000E+00  0.00000000E+00
  0.00000000E+00  0.00000000E+00  0.00000000E+00
  0.00000000E+00  0.00000000E+00  0.00000000E+00
  0.00000000E+00  0.00000000E+00  0.00000000E+00
  0.00000000E+00  0.00000000E+00  0.00000000E+00
  0.00000000E+00  0.00000000E+00  0.00000000E+00
  0.00000000E+00  0.00000000E+00  0.00000000E+00
  0.00000000E+00  0.00000000E+00  0.00000000E+00
  0.00000000E+00  0.00000000E+00  0.00000000E+00
  0.00000000E+00  0.00000000E+00  0.00000000E+00
  0.00000000E+00  0.00000000E+00  0.00000000E+00
  0.00000000E+00  0.00000000E+00  0.00000000E+00
  0.00000000E+00  0.00000000E+00  0.00000000E+00
  0.00000000E+00  0.00000000E+00  0.00000000E+00
  0.00000000E+00  0.00000000E+00  0.00000000E+00
  0.00000000E+00  0.00000000E+00  0.00000000E+00
```

```
  0.00000000E+00  0.00000000E+00  0.00000000E+00
  0.00000000E+00  0.00000000E+00  0.00000000E+00
  0.00000000E+00  0.00000000E+00  0.00000000E+00
  0.00000000E+00  0.00000000E+00  0.00000000E+00
  0.00000000E+00  0.00000000E+00  0.00000000E+00
  0.00000000E+00  0.00000000E+00  0.00000000E+00
  0.00000000E+00  0.00000000E+00  0.00000000E+00
  0.00000000E+00  0.00000000E+00  0.00000000E+00
  0.00000000E+00  0.00000000E+00  0.00000000E+00
  0.00000000E+00  0.00000000E+00  0.00000000E+00
  0.00000000E+00  0.00000000E+00  0.00000000E+00
  0.00000000E+00  0.00000000E+00  0.00000000E+00
```

60°

```
GaS/GaSe bilayer (59deg basically 60) with 20 angstrom vacuum
   1.00000000000000
     3.7040323853565424     0.0000159397721340     0.0071595113799047
    -1.8520109408144703     3.2077378199553910     0.0076121793222945
     0.0668186655815320     0.1206485911268231    34.7660793720527224
   Ga   Se   S
    4    2    2
Direct
  0.3339282290178937  0.6674288189105978  0.0810984177411515
  0.3286311718354837  0.6620297488180231  0.1513703089782157
  0.6443185856701619  0.3108170372174645  0.3795708971860961
  0.6496540376254660  0.3162564297234721  0.3088616918808808
  0.6593965345112726  0.3260739195564110  0.1861546681473714
  0.6698423511933949  0.3367281146959057  0.0461914175371533
  0.3185165166647557  0.6518322683796084  0.2791231897176889
  0.3087790665734626  0.6419002723489967  0.4094530811937708

  0.00000000E+00  0.00000000E+00  0.00000000E+00
  0.00000000E+00  0.00000000E+00  0.00000000E+00
  0.00000000E+00  0.00000000E+00  0.00000000E+00
  0.00000000E+00  0.00000000E+00  0.00000000E+00
  0.00000000E+00  0.00000000E+00  0.00000000E+00
  0.00000000E+00  0.00000000E+00  0.00000000E+00
  0.00000000E+00  0.00000000E+00  0.00000000E+00
  0.00000000E+00  0.00000000E+00  0.00000000E+00
```

90°

```
GaS/GaSe hetero (90 deg) with 20 ang vac
   1.00000000000000
     6.9730924803157759     0.0000599730790824     0.0000260288090190
    -3.4864942678864916     6.0388515044731577    -0.0003452573988373
     0.0004189091522426    -0.0016731968717207    32.5553890274577498
   Ga   S    Se
   14    8    6
```

```
Direct
  0.2232413442566994   0.2782692715769102   0.0599017412761782
  0.2240356166070825   0.2786559942423708   0.1353054408054533
  0.2225697722282973   0.7779740380543601   0.0598178711350812
  0.7216006077932562   0.2766292879792687   0.0597396221134758
  0.7216270748062286   0.7783238536097059   0.0597418947409167
  0.2224307859217731   0.7779244837966033   0.1351272491417461
  0.7210461488322437   0.2757397136684645   0.1349917692831966
  0.7211082185400457   0.7787103498659960   0.1349895719924277
  0.0002055730934316   0.0010663177146171   0.3086907193002517
  0.9999143248543803   0.0005727510978630   0.3842765635931045
  0.6657224776339632   0.3325309776754466   0.3086342341616017
  0.3342739952163285   0.6664598986541890   0.3088977670970721
  0.6661599352216641   0.3329761779931033   0.3842450944889109
  0.3338675933980326   0.6664057659601426   0.3843844492458999
  0.3888798602851153   0.1102524568505743   0.1704714713857598
  0.3886262205846833   0.1108781287336669   0.0246133135069968
  0.3888899511722741   0.6120116556448849   0.1704392763204723
  0.8906502904690399   0.1120346500863150   0.1700695867962523
  0.8869572547329199   0.6101769668921762   0.1693459213550383
  0.3886247143944814   0.6110508017666731   0.0246253529947822
  0.8899137477200227   0.1116122701004940   0.0247261543018311
  0.8885291182405410   0.6109158263228949   0.0249892865470756
  0.3333461035097116   0.3330045777136803   0.4170581225826453
  0.3330665385865288   0.3335847352458288   0.2758225247476176
  0.9998365551175823   0.6667079769816127   0.4166928426158947
  0.6667622567981013   0.0002861658565934   0.4169931396278486
  0.0015501513471676   0.6672812987321279   0.2767902596854483
  0.6654532603569194   0.9990748011172954   0.2759826894355584

  0.00000000E+00   0.00000000E+00   0.00000000E+00
  0.00000000E+00   0.00000000E+00   0.00000000E+00
  0.00000000E+00   0.00000000E+00   0.00000000E+00
  0.00000000E+00   0.00000000E+00   0.00000000E+00
  0.00000000E+00   0.00000000E+00   0.00000000E+00
  0.00000000E+00   0.00000000E+00   0.00000000E+00
  0.00000000E+00   0.00000000E+00   0.00000000E+00
  0.00000000E+00   0.00000000E+00   0.00000000E+00
  0.00000000E+00   0.00000000E+00   0.00000000E+00
  0.00000000E+00   0.00000000E+00   0.00000000E+00
  0.00000000E+00   0.00000000E+00   0.00000000E+00
  0.00000000E+00   0.00000000E+00   0.00000000E+00
  0.00000000E+00   0.00000000E+00   0.00000000E+00
  0.00000000E+00   0.00000000E+00   0.00000000E+00
  0.00000000E+00   0.00000000E+00   0.00000000E+00
  0.00000000E+00   0.00000000E+00   0.00000000E+00
  0.00000000E+00   0.00000000E+00   0.00000000E+00
  0.00000000E+00   0.00000000E+00   0.00000000E+00
  0.00000000E+00   0.00000000E+00   0.00000000E+00
  0.00000000E+00   0.00000000E+00   0.00000000E+00
  0.00000000E+00   0.00000000E+00   0.00000000E+00
  0.00000000E+00   0.00000000E+00   0.00000000E+00
  0.00000000E+00   0.00000000E+00   0.00000000E+00
  0.00000000E+00   0.00000000E+00   0.00000000E+00
  0.00000000E+00   0.00000000E+00   0.00000000E+00
  0.00000000E+00   0.00000000E+00   0.00000000E+00
  0.00000000E+00   0.00000000E+00   0.00000000E+00
  0.00000000E+00   0.00000000E+00   0.00000000E+00
  0.00000000E+00   0.00000000E+00   0.00000000E+00
```

```
 0.00000000E+00  0.00000000E+00  0.00000000E+00
 0.00000000E+00  0.00000000E+00  0.00000000E+00
 0.00000000E+00  0.00000000E+00  0.00000000E+00
 0.00000000E+00  0.00000000E+00  0.00000000E+00
 0.00000000E+00  0.00000000E+00  0.00000000E+00
```

Appendix C

$BaZrS_{(3-y)}Se_y$ Alloy Structural Files

The structural files for each of the $BaZrS_{(3-y)}Se_y$ alloys used in the DFT calculations of their band gaps, as shown in Figure 5.5, are shown below in the POSCAR file format. These structures have been relaxed via DFT using the parameters in Chapter 5.

$BaZrS_3$ (y = 0)

```
BaZrS3
   1.00000000000000
     7.0598998069999999     0.0000000000000000     0.0000000000000000
     0.0000000000000000     9.9813003540000000     0.0000000000000000
     0.0000000000000000     0.0000000000000000     7.0251002311999997
   Ba    Zr    S
     4     4     12
Direct
  0.0481092729967882   0.2500000000000000   0.0099119442877394
  0.9518907450032134   0.7500000000000000   0.9900880437122596
  0.4518907150032109   0.7500000000000000   0.5099119562877404
  0.5481092549967866   0.2500000000000000   0.4900880437122596
  0.0000000000000000   0.0000000000000000   0.5000000000000000
  0.5000000000000000   0.0000000000000000   0.0000000000000000
  0.0000000000000000   0.5000000000000000   0.5000000000000000
  0.5000000000000000   0.5000000000000000   0.0000000000000000
  0.9960845905550237   0.2500000000000000   0.5660516824963081
  0.0039154374449786   0.7500000000000000   0.4339483175036921
  0.5039154094449763   0.7500000000000000   0.0660516824963080
  0.4960845605550213   0.2500000000000000   0.9339483175036919
  0.2100258364044326   0.9657056464316246   0.7897626404158075
  0.7899741635955674   0.0342943805683812   0.2102373595841927
  0.2899741635955674   0.0342943805683812   0.2897626404158074
  0.7100258364044326   0.9657056464316246   0.7102373595841925
  0.7899741635955674   0.4657056164316221   0.2102373595841927
  0.2100258364044326   0.5342943535683754   0.7897626404158075
  0.7100258364044326   0.5342943535683754   0.7102373595841925
  0.2899741635955674   0.4657056164316221   0.2897626404158074
```

```
  0.00000000E+00   0.00000000E+00   0.00000000E+00
  0.00000000E+00   0.00000000E+00   0.00000000E+00
  0.00000000E+00   0.00000000E+00   0.00000000E+00
  0.00000000E+00   0.00000000E+00   0.00000000E+00
  0.00000000E+00   0.00000000E+00   0.00000000E+00
  0.00000000E+00   0.00000000E+00   0.00000000E+00
  0.00000000E+00   0.00000000E+00   0.00000000E+00
  0.00000000E+00   0.00000000E+00   0.00000000E+00
  0.00000000E+00   0.00000000E+00   0.00000000E+00
  0.00000000E+00   0.00000000E+00   0.00000000E+00
  0.00000000E+00   0.00000000E+00   0.00000000E+00
  0.00000000E+00   0.00000000E+00   0.00000000E+00
  0.00000000E+00   0.00000000E+00   0.00000000E+00
  0.00000000E+00   0.00000000E+00   0.00000000E+00
  0.00000000E+00   0.00000000E+00   0.00000000E+00
  0.00000000E+00   0.00000000E+00   0.00000000E+00
  0.00000000E+00   0.00000000E+00   0.00000000E+00
  0.00000000E+00   0.00000000E+00   0.00000000E+00
  0.00000000E+00   0.00000000E+00   0.00000000E+00
```

$BaZrS_2Se$ (y = 1)

```
BaZrS2Se  y=1
   1.00000000000000
     7.3256342064340627    -0.0144845974197732     0.0462017612106119
    -0.0205368875296626    10.1842824475392195     0.0086549544187588
     0.0467187935540026     0.0061662392240658     7.1595228229641723
   Ba    Zr    S     Se
     4     4     8     4
Direct
  0.0625424378152251   0.2479385188357446   0.0052976552013237
  0.9492086242434369   0.7504317657538850   0.9933953290018732
  0.4443424441637220   0.7529235838070349   0.5227620296012772
  0.5600848492945766   0.2423662583583271   0.4905299833782570
  0.0125896567069421   0.0051137553079668   0.5036757778681068
  0.4987999130692095   0.0051741888512012  -0.0131063256469815
 -0.0023459960899731   0.5035163692918685   0.5090570945237859
  0.4961204821941333   0.4952626843687786  -0.0157893347831400
  0.9880111113132265   0.2501210302200738   0.5707901302509607
  0.0122348053261252   0.7513503102527745   0.4433042126301796
  0.4917747846700514   0.2496564704833573   0.9269238372074968
  0.2084161341852378   0.9690270190978365   0.7911318392676484
  0.2884106662229611   0.0382113385120910   0.2882879618357986
  0.7112572412235328   0.9653269480984163   0.7105300170797236
  0.2038204005643741   0.5312608350807789   0.7937896537449322
  0.7048633223913761   0.5352896293646836   0.7051292626256278
  0.2941911515192029   0.4591744528488735   0.2971385900766101
  0.4915719849668848   0.7500233169032038   0.0657552237411981
  0.7906378730596161   0.0336239381751829   0.2081858002532372
  0.7934680991601375   0.4642075803879267   0.2032112501420832
```

```
  0.00000000E+00   0.00000000E+00   0.00000000E+00
  0.00000000E+00   0.00000000E+00   0.00000000E+00
  0.00000000E+00   0.00000000E+00   0.00000000E+00
  0.00000000E+00   0.00000000E+00   0.00000000E+00
  0.00000000E+00   0.00000000E+00   0.00000000E+00
  0.00000000E+00   0.00000000E+00   0.00000000E+00
  0.00000000E+00   0.00000000E+00   0.00000000E+00
  0.00000000E+00   0.00000000E+00   0.00000000E+00
  0.00000000E+00   0.00000000E+00   0.00000000E+00
  0.00000000E+00   0.00000000E+00   0.00000000E+00
  0.00000000E+00   0.00000000E+00   0.00000000E+00
  0.00000000E+00   0.00000000E+00   0.00000000E+00
  0.00000000E+00   0.00000000E+00   0.00000000E+00
  0.00000000E+00   0.00000000E+00   0.00000000E+00
  0.00000000E+00   0.00000000E+00   0.00000000E+00
  0.00000000E+00   0.00000000E+00   0.00000000E+00
  0.00000000E+00   0.00000000E+00   0.00000000E+00
  0.00000000E+00   0.00000000E+00   0.00000000E+00
  0.00000000E+00   0.00000000E+00   0.00000000E+00
```

$BaZrSSe_2$ (y = 2)

```
BaZrSSe2  y=2
    1.00000000000000
      7.4879267315361560      0.0028949063879382     -0.0126497583456525
      0.0039209367729551     10.2766040983004459      0.0036358940968862
     -0.0124232057219105      0.0026512577280662      7.2547104690433688
   Ba    Zr    S     Se
     4     4     4     8
Direct
  0.0647013251027886   0.2513358556866292   0.0017536466098379
  0.9363624132876072   0.7419949095052225   0.9812051966411955
  0.4349273477251305   0.7511874732451791   0.5206463957197409
  0.5656138298095631   0.2448355233181800   0.4971668664053854
  0.0236501578104610   0.0127616974200290   0.4886658360345115
  0.5056620903039832   0.0098715406602564  -0.0031634033037936
  0.0081131120716566   0.4955933533602297   0.5085175751208810
  0.4950005988454914   0.4957926869964474  -0.0024237716108918
  0.9915049693268788   0.2508177727757248   0.5701761450568628
  0.4829126473526250   0.2507072291294069   0.9306281194671679
  0.2942757398913641   0.0431598723371900   0.2928491382674552
  0.2055963285165769   0.5313703319806536   0.7927863928373277
  0.7020552765188732   0.5322653328812076   0.7028169897330304
  0.2933530943880016   0.4567765057314264   0.2975456654263824
  0.0037509057846372   0.7512637995486418   0.4304048556182528
  0.4967110158955247   0.7507523305117808   0.0721157425708335
  0.2019214210099076   0.9644838702931302   0.8002902858572736
  0.7942218555514982   0.0422438467455362   0.2066891942396308
  0.7082066348925511   0.9660207444761759   0.7062389185024522
  0.7914592219148782   0.4567653173969589   0.2050901988064628
```

```
  0.00000000E+00   0.00000000E+00   0.00000000E+00
  0.00000000E+00   0.00000000E+00   0.00000000E+00
  0.00000000E+00   0.00000000E+00   0.00000000E+00
  0.00000000E+00   0.00000000E+00   0.00000000E+00
  0.00000000E+00   0.00000000E+00   0.00000000E+00
  0.00000000E+00   0.00000000E+00   0.00000000E+00
  0.00000000E+00   0.00000000E+00   0.00000000E+00
  0.00000000E+00   0.00000000E+00   0.00000000E+00
  0.00000000E+00   0.00000000E+00   0.00000000E+00
  0.00000000E+00   0.00000000E+00   0.00000000E+00
  0.00000000E+00   0.00000000E+00   0.00000000E+00
  0.00000000E+00   0.00000000E+00   0.00000000E+00
  0.00000000E+00   0.00000000E+00   0.00000000E+00
  0.00000000E+00   0.00000000E+00   0.00000000E+00
  0.00000000E+00   0.00000000E+00   0.00000000E+00
  0.00000000E+00   0.00000000E+00   0.00000000E+00
  0.00000000E+00   0.00000000E+00   0.00000000E+00
  0.00000000E+00   0.00000000E+00   0.00000000E+00
```

$BaZrSe_3$ (y = 3)

```
BaZrSe3  y=3
   1.00000000000000
     7.5709628134575091      0.0000000000000000     -0.0000000000000000
     0.0000000000000000     10.5161372452153472      0.0000000000000000
     0.0000000000000000      0.0000000000000000      7.2977681668428076
   Ba    Zr    Se
     4     4    12
Direct
  0.0684327078875226   0.2500000000000000   0.0190038672512725
  0.9315673101124791   0.7500000000000000   0.9809961207487268
  0.4315672801124763   0.7500000000000000   0.5190038792512732
  0.5684326898875209   0.2500000000000000   0.4809961207487264
  0.0000000000000000   0.0000000000000000   0.5000000000000000
  0.5000000000000000   0.0000000000000000  -0.0000000000000000
  0.0000000000000000   0.5000000000000000   0.5000000000000000
  0.5000000000000000   0.5000000000000000  -0.0000000000000000
  0.9953459765145903   0.2500000000000000   0.5731842238910732
  0.0046540514854119   0.7500000000000000   0.4268157761089267
  0.5046540234854097   0.7500000000000000   0.0731842238910732
  0.4953459465145879   0.2500000000000000   0.9268157761089268
  0.2028803623558299   0.9622530463880092   0.7991659644111756
  0.7971196376441700   0.0377469806119964   0.2008340355888244
  0.2971196376441702   0.0377469806119964   0.2991659644111756
  0.7028803623558300   0.9622530463880093   0.7008340355888244
  0.7971196376441700   0.4622530163880069   0.2008340355888244
  0.2028803623558299   0.5377469536119908   0.7991659644111756
  0.7028803623558300   0.5377469536119908   0.7008340355888244
  0.2971196376441702   0.4622530163880069   0.2991659644111756
```

```
0.00000000E+00   0.00000000E+00   0.00000000E+00
0.00000000E+00   0.00000000E+00   0.00000000E+00
0.00000000E+00   0.00000000E+00   0.00000000E+00
0.00000000E+00   0.00000000E+00   0.00000000E+00
0.00000000E+00   0.00000000E+00   0.00000000E+00
0.00000000E+00   0.00000000E+00   0.00000000E+00
0.00000000E+00   0.00000000E+00   0.00000000E+00
0.00000000E+00   0.00000000E+00   0.00000000E+00
0.00000000E+00   0.00000000E+00   0.00000000E+00
0.00000000E+00   0.00000000E+00   0.00000000E+00
0.00000000E+00   0.00000000E+00   0.00000000E+00
0.00000000E+00   0.00000000E+00   0.00000000E+00
0.00000000E+00   0.00000000E+00   0.00000000E+00
0.00000000E+00   0.00000000E+00   0.00000000E+00
0.00000000E+00   0.00000000E+00   0.00000000E+00
0.00000000E+00   0.00000000E+00   0.00000000E+00
0.00000000E+00   0.00000000E+00   0.00000000E+00
0.00000000E+00   0.00000000E+00   0.00000000E+00
0.00000000E+00   0.00000000E+00   0.00000000E+00
0.00000000E+00   0.00000000E+00   0.00000000E+00
0.00000000E+00   0.00000000E+00   0.00000000E+00
0.00000000E+00   0.00000000E+00   0.00000000E+00
```